Prospects of Colloidal Nanocrystals for Electronic and Optoelectronic Applications

Dmitri V. Talapin,*,†,‡ Jong-Soo Lee,† Maksym V. Kovalenko,† and Elena V. Shevchenko‡

Department of Chemistry, The University of Chicago, Chicago, Illinois 60637, and Center for Nanoscale Materials, Argonne National Lab, Argonne, Illinois 60439

Received April 5, 2009

Contents

1. Introduction

Nanocrystals (NCs) discussed in this Review are tiny crystals of metals, semiconductors, and magnetic material consisting of hundreds to a few thousand atoms each. Their size ranges from 2−3 to about 20 nm. What is special about this size regime that placed NCs among the hottest research topics of the last decades? The quantum mechanical coupling

* To whom correspondence should be addressed. E-mail: dvtalapin@uchicago.edu.
† The University of Chicago.
‡ Argonne National Lab.

10.1021/cr900137k
Published on Web 12/03/2009

Dmitri V. Talapin is an Assistant Professor in the Department of Chemistry at the University of Chicago. He received his doctorate degree from the University of Hamburg, Germany, in 2002 under the supervision of Horst Weller. In 2003, he joined the IBM Research Division at the T. J. Watson Research Center as a postdoctoral fellow to work with Chris Murray on the synthesis and electronic properties of semiconductor nanostructures. In 2005, he moved to the Lawrence Berkeley National Laboratory as a staff scientist at the Molecular Foundry, newly founded DOE Center for Nanoscience and Nanotechnology. In 2007, he accepted a faculty position at the University of Chicago. His research interests revolve around colloidal inorganic nanomaterials, spanning from synthetic methodology to device fabrication, with the desire of turning colloidal nanostructures into useful electronic materials.

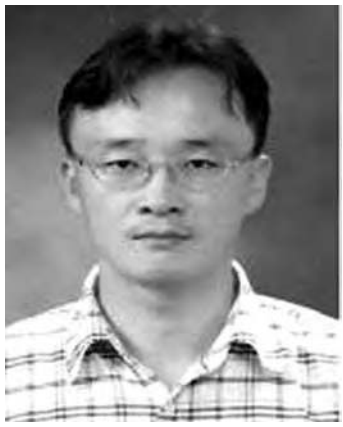

Jong-Soo Lee received a Ph.D. in the Department of Metallurgical Engineering from Chonbuk National University in South Korea in 1999. From 2001 to 2004, he worked in the Department of Electrical Engineering at Korea University in South Korea as a research assistant professor. In 2006−2007, he worked as a postdoctoral researcher at the Molecular Foundry in the Lawrence Berkeley National Laboratory with Dmitri V. Talapin and A. Paul Alivisatos. In 2007, he joined the Talapin group as a senior research technologist. His research interests include synthesis and charge transport studies in colloidal inorganic NCs and multifunctional nanostructures for electronic, photovoltaic, and thermoelectronic applications.

Maksym V. Kovalenko received his doctorate degree from the University of Linz (Austria) in 2007 under the supervision of Prof. Wolfgang Heiss. His doctoral thesis was focused on the synthesis and device applications of infrared-active colloidal semiconductor nanocrystals. In 2008, he joined the group of Prof. Dmitri Talapin at the University of Chicago as a postdoctoral scholar. He is currently working on the functionalization of inorganic nanocrystals with inorganic ligands and integration of these novel materials into electronic, optoelectronic, and thermoelectric devices. His other scientific interests include magnetism and self-assembly of nanocrystals.

Elena V. Shevchenko received her first degree in chemistry at the Belorussian State University and her Ph.D. from the University of Hamburg in 2003 with Horst Weller. From 2003 to 2005, she was a joint postdoctoral fellow between Columbia University (with Stephen O'Brien) and the T. J. Watson Research Center IBM (with Christopher Murray). In 2005, she moved to the Molecular Foundry, Lawrence Berkeley National Laboratory, as a staff scientist. Since 2007, she is a scientist at the Center for Nanoscale Materials at Argonne National Laboratory. Her primary research interests are in the design of nanoscale functional materials and understanding their fundamental properties.

of over hundreds to thousands atoms is necessary to develop the band structure of metals, semiconductors, and magnetic materials.[1−4] In this regime, the electronic structure, optical, and magnetic properties of materials can be tuned by varying the physical size of the crystal, leading to new phenomena, such as superparamagnetism of magnetic NCs, surface plasmon resonance in Au and Ag nanoparticles,[1] and the size-dependent band gap of semiconductor NCs.[2,3] These open interesting opportunities for device applications, for example, tailoring the electronic structure without introducing any changes in the chemical composition. Formerly, lithographic techniques aggressively invaded the nanoworld; nowadays, electronic circuits with features as small as 45 nm are used for commercial applications, with good prospects for 32 and 22 nm technologies that are on the way from laboratories to fabrication facilities.[5] Because of similarities in feature size, the knowledge obtained from electronic studies of nanoscale materials should help in understanding the design rules for next generations of electronic circuits.

Inorganic semiconductors have a proven track record in electronics and optoelectronics; they offer superior carrier mobilities, light absorption, photo, and thermal stability.[5] However, they are difficult to form by low cost processes. Crystallization of inorganic semiconductors requires high temperature treatments, which force trade-offs between device performance, fabrication costs, and compatibility with flexible plastic substrates. The development of applications ranging from photovoltaics and light-emitting devices to "smart cards", radio frequency tags, and sensors could be accelerated by introducing lower cost alternatives to conventional technologies that rely on single crystals.[5,6] Here,

the nanometer size crystals can find commercial use as the building blocks for inexpensive manufacturing of low cost and large area devices. Solution-based processes such as spin coating, dip coating, or inkjet printing offer substantial cost reductions for the fabrication of electronic and optoelectronic devices when combined with novel materials like organic semiconductors,[6,7] carbon nanotubes,[8] nanowires,[9] or hybrid organic−inorganic films.[10] Properly designed NCs can ideally fit the requirements for solution-processed electronic and optoelectronic devices because they form thermodynamically stable and easy-to-handle colloidal solutions. Moreover, NCs can self-assemble from colloidal solutions into ordered structures called "superlattices" or "NC solids", which will be an important subject of this review. Tunable electronic structure combined with small exciton binding energy, high luminescence efficiency,[11] and very low thermal conductivity[12] make NC solids especially attractive for photovoltaic, lighting, and thermoelectric applications. Efforts to harness the quantum tunability of semiconductor NCs have led to many successes in optical and optoelectronic applications, such as light emitting devices,[13−16] luminescent tags,[13] and lasers.[14−16] NCs have a variety of biological and biomedical applications.[17−21] Semiconductor NCs can serve as stable fluorescence probes.[18] Magnetic NCs can be used as efficient diagnostic tools in magnetic resonance imaging and magnetic separation of biological targets[20] and therapeutic agents for hyperthermic tumor treatments,[19] drug, and gene delivery.[21] Plasmonic properties of noble metal NCs are utilized in molecular-specific imaging and sensing, as well as in photodiagnostic and photothermal therapy.[17]

At the same time, realizing solid-state electronic applications (e.g., field-effect devices) of these nanoscale building blocks has been more challenging. The confinement of carriers inside the NCs imparts their fascinating size tunable properties, but, until recently, frustrated the efforts to efficiently contact and integrate them into devices that switch with useful speeds.[22−25] Charge transport in NCs relies on the electrons traveling between individual particles and is, therefore, dependent on the electronic communication and collective phenomena in NC arrays. In this respect, NCs are different from their cousins, nanowires and nanotubes, which can be directly connected to the electrodes.

2. Solution-Phase Synthesis of Metallic, Semiconducting, Magnetic, and Multicomponent Nanoparticles

Colloidal synthesis of inorganic nanostructures is developing into a new branch of synthetic chemistry. Starting with preparations of simple objects like monodisperse spherical nanoparticles,[26−29] the field is now moving toward more and more sophisticated structures where size, shape, and connectivity of multiple parts of a multicomponent structure can be tailored in an independent and predictable manner.[30−36] Many technologically important metals, semiconductors, and magnetic materials can be synthesized as uniform sub-20 nm crystals; multiple materials can be combined in the form of the core−shell, dumbbell, or more complex morphologies.[37] Although the general methodology of colloidal synthesis of multicomponent structures is much less developed as compared to the conventional synthesis of molecular compounds, impressive progress has been achieved in the past years, which introduced totally novel approaches to materials design. For example, the band gap of semiconductor nanostructures can be precisely tuned by size and shape control, electron and hole can be spatially separated within the NC by introducing heterostructures with staggered band offsets,[35] different confined regimes can be achieved for electrons and holes,[33] etc. Growing heterostructures built of semiconductor and plasmonic materials allow coupling excitons and surface plasmon resonance generated by semiconductor and metal components, respectively.[24,38] Below, we briefly describe the methodology of colloidal synthesis. For more detailed information, we should address the readers to numerous comprehensive reviews on the synthesis of inorganic nanomaterials.[28,37,39−45]

2.1. Basics of Colloidal Synthesis: Nucleation and Growth

Among the appeals of solution-based colloidal synthesis, we should mention the excellent control over size and shape of prepared nanostructures and applicability to a broad range of materials. Moreover, the use of relatively simple experimental equipment and chemicals allows one to obtain high-quality materials and tailor their properties at surprisingly low cost.[46] Typically, colloidal nanomaterials are synthesized by reacting appropriate molecular precursors, that is, inorganic salts or organometallic compounds. The colloidal synthesis generally involves several consecutive stages: nucleation from initially homogeneous solution, growth of the preformed nuclei, isolation of particles reaching the desired size from the reaction mixture, postpreparative treatments, etc. As a rule, temporal separation of the nucleation event from the growth of the nuclei is required for narrow size distribution.[26,47,48] The so-called hot-injection technique, when the precursors are rapidly injected into a hot solvent with subsequent temperature drop, satisfies this requirement.[26,48,49] The separation of nucleation and growth stages can also be achieved upon steady heating of the reaction mixture.[46]

Nucleation and growth of NCs occurs in the solution phase in the presence of organic surfactant molecules, which dynamically adhere to the surface of growing crystals.[30,46] Typical surfactants include long-chain carboxylic and phosphonic acids (e.g., oleic acid and *n*-octadecylphosphonic acid), alkanethiols (e.g., dodecanethiol), alkyl phosphines, alkylphosphine oxides (classical examples are trioctylphosphine, TOP, and trioctylphosphine oxide, TOPO), and alkylamines such as hexadecylmine. The surfactant molecules play the key role in tuning the kinetics of nucleation and growth,[39,47] which should be kinetically balanced because if the nanoparticle nucleation rate is either too slow or too fast with respect to the growth rate, the reaction will generate either bulk crystals or molecular clusters. Achieving proper balance of these intrinsically different processes is an important and sometimes challenging problem, which is usually addressed empirically by searching for a good combination of molecular precursors, surfactants, solvent, and the reaction conditions (temperature regime, etc.). Development of reproducible synthetic approaches leading to nanoparticles with uniform size, shape, composition, and surface morphology is extremely important for further progress in fundamental studies and practical applications.

Figure 1 shows several examples of metal nanocrystals synthesized by colloidal chemistry. Metal nanoparticles can be synthesized by reducing the metal ions using reductant such as borohydride, amines, or 1,2-diols in the presence of stabilizing agents, typically long-chain alkanethiols (e.g.,

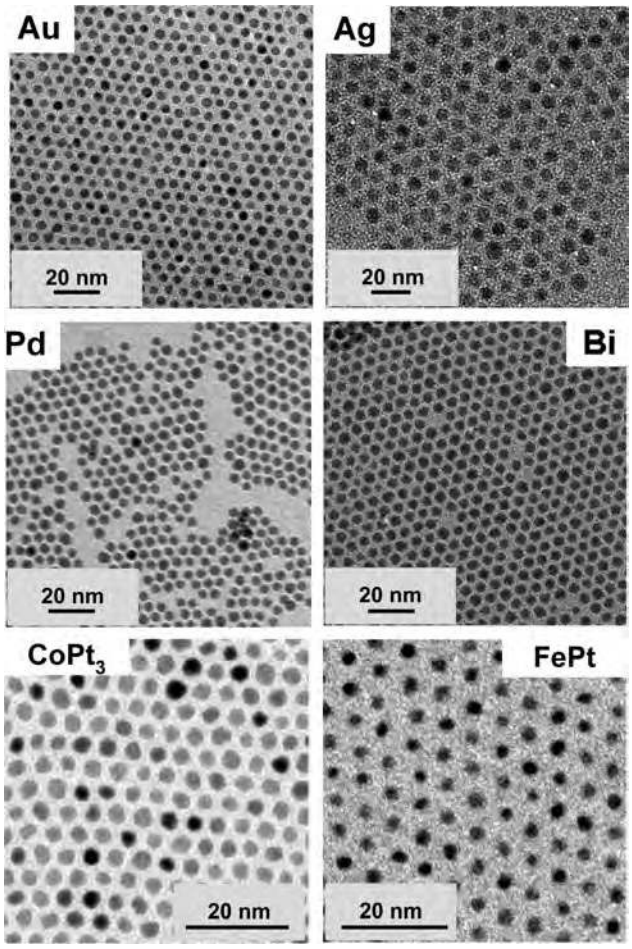

Figure 1. Examples of colloidally synthesized metal and metal alloy nanoparticles.

dodecanethiol), amines, or fatty acids. This approach works quite well for noble metals (Au,[50−53] Ag,[54−56] Pt,[57−59] Pd[60]) and their alloys (e.g., Au−Ag[61]). Current developments in the synthesis of these materials have been extensively reviewed by Xia et al.,[44] Yang et al.,[62] and Liz-Marzan.[63]

More reactive transition and main group metals (Co,[4,64] Fe,[4,65−67] Cr,[68] Bi,[69] Pb[70]) require rigorous control of the reaction conditions and are synthesized under inert atmosphere. High temperatures, up to 300 °C, are often necessary to anneal out the defects in crystalline lattice and form highly crystalline particles.[47] High boiling solvents are used to provide a wide window of reaction temperatures. The choice of solvent limits the range of possible molecular precursors. For example, solvents with low polarity such as dioctyl ether or 1-octadecene require precursors soluble in this medium. Among metal salts, acetylacetonates or carboxylates are frequently used[27,29,47] in the synthesis of metal nanoparticles. Alternatively, metal NCs can be generated by thermal decomposition of molecules containing zerovalent metal, such as metal carbonyls.[4,27,47] For example, cobalt nanoparticles can be synthesized either by reduction of Co(II) ions in solution or by thermal decomposition of $Co_2(CO)_8$.[4] Long-chain carboxylic acids or alkylamines are the typical surfactants for metal NCs. In addition to size and shape, precursors and surfactants can control the crystalline phase of the nanoparticle. Thus, three different polymorphs of cobalt NCs (hexagonal close-packed, face-centered cubic, and epsilon phase) were selectively synthesized by adjusting reaction parameters.[47] Combining two or more metal precursors, for example, $Pt(acac)_2$ and $Fe(CO)_5$, in a one-pot reaction allows one to obtain nanoparticles of metal alloys.[27,71] Among a variety of possible metal combinations, the alloys of magnetic metals (Fe, Co, and Ni) with Pt and Pd have been studied most extensively because in these systems alloying helped to overcome a serious drawback of elemental magnetic nanoparticles, their low stability against oxidation.

Several methods can be used to tune the size of metal nanoparticles during synthesis. Usually, the metal nanoparticles nucleate and grow very quickly, and it is difficult to terminate the reaction at the desired stage of particle growth. Instead, the particle size can be adjusted by first making small nanoparticles, which are then used as seeds for further growth by adding controllable amounts of molecular precursors. For example, this method was applied to vary the size of FePt[27] NCs. Another approach is based on tuning the relative rates of nanoparticle nucleation and growth. If the total amount of molecular precursors used in the reaction is constant, the fast nucleation provides high concentration of nuclei and yields smaller NCs. Instead, slow nucleation provides low concentration of seeds consuming the same amount of precursors, thus resulting in larger particles.[47] The balance between nucleation and growth rates can be tuned via changing of the reaction temperature because the activation energy for the homogeneous nucleation is usually much higher than that for particle growth.[72] Typically, the increase of reaction temperature allowed one to obtain smaller NCs for different materials.[47] Besides the reaction temperature, there are a number of other methods to control particle size, such as nature and concentration of capping molecules, molar ratios of precursors, etc. For example, lowering the concentration of surfactants in reaction mixture can also lead to smaller nanoparticles.[47]

Significant success was achieved in the synthesis of NCs of different technologically important semiconductors. Some examples of colloidal semiconductor NCs are shown in Figure 2. Typical reactions used for the synthesis of II−VI (CdSe, CdTe, CdS),[26,49,73−77] III−V (InP, InAs),[78−81] and IV−VI (PbS,[82−86] PbSe,[23] PbTe[87]) semiconductor NCs are outlined by reactions 1−3. The syntheses are carried out at high temperatures, and in the presence of long-chain alkylphosphines (e.g., trioctylphosphine, TOP), alkylphosphine oxides (e.g., trioctylphosphine oxide, TOPO), alkylamines (e.g., hexadecylamine, HDA), and alkylphosphonic acids as the stabilizing agents.

$$Cd(CH_3)_2 + (C_8H_{17})_3PSe \xrightarrow{300°C,\ HDA-TOPO-TOP} \text{CdSe nanocrystals} \quad (1)$$

$$InCl_3 + [(CH_3)_3Si]_3P \xrightarrow{260°C,\ TOP} \text{InP nanocrystals} \quad (2)$$

$$Pb(CH_3COO)_2 + (C_8H_{17})_3PSe \xrightarrow{180°C,\ \text{oleic acid}} \text{PbSe nanocrystals} \quad (3)$$

In many cases, the size of semiconductor NCs can be tuned by adjusting the concentrations of surfactants, reaction temperature, and duration of the particle growth. In a

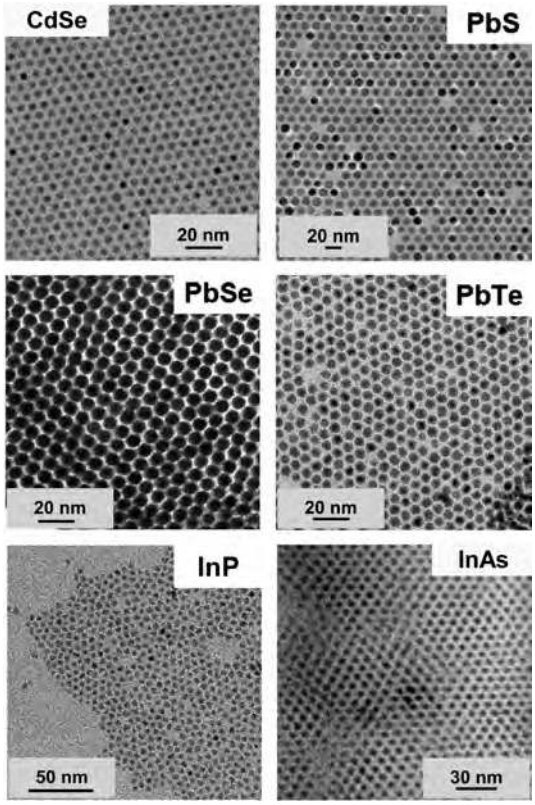

Figure 2. Examples of colloidal semiconductor nanocrystals of different materials.

colloidal solution, semiconductor NCs often grow through the Ostwald ripening mechanism, where the largest particles in solution grow at the expense of dissolving smaller ones. As a result, average particle size increases with time,[72] and the particle concentration decreases. A number of studies investigated the kinetics of nanoparticle growth and dissolution to model this self-consistent growth process and understand the parameters that control particle size distribution during the synthesis of semiconductor NCs.[80] Two regimes, so-called "focusing" and "defocusing" of size distribution during nanoparticle growth, were described by Peng et al.[88,89] "Nano-Ostwald ripening" model was proposed to describe the evolution of an ensemble of nanoscale particles.[90]

One of the most important manifestations of quantum confinement in semiconductors is the relationship between the electronic structure and particle size.[2,3] In semiconductor NCs, it gives rise to discrete electron and hole states that can be precisely tuned by varying particle size (Figure 3).[2,3] The proper control of surface chemistry can eliminate the midgap states associated with surface dangling bonds. As a result of reduced probability of carrier trapping and nonradiative recombination, high (>80%) luminescence quantum efficiencies were achieved for semiconductor NCs.[11,91−94]

Discussion of solution-phase synthesis of inorganic nanomaterials would be incomplete without mentioning other methodologies, complementary to above-described high-temperature synthesis in nonpolar organic solvents. Thus, there are several examples of high-quality semiconductor nanoparticles synthesized in aqueous medium.[96−98] For example, quite monodisperse samples of highly luminescent CdTe NCs can be prepared by reacting a cadmium salt (e.g., cadmium perchlorate) with H_2Te gas in aqueous solution containing thiol molecules with polar groups (e.g., thioglycolic acid, cysteamine). It is commonly accepted that the thiol group binds to the NC surface, whereas the deprotonated carboxylic group (or protonated amino group) provides colloidal stability due to electrostatic repulsion of charged NCs.[96,99] This approach has been successfully applied to different II−VI semiconductors: CdS,[100] CdSe,[101] CdTe,[102] HgTe,[103] etc. Generally, the NCs made in aqueous medium are not as monodisperse as those prepared in organic solvents, but in other aspects, such as luminescence efficiency, colloidal stability, and, especially, cost per gram, they can be very competitive. We may expect a revival of interest in the aqueous synthesis of colloidal NCs for large-scale manufacturing purposes.

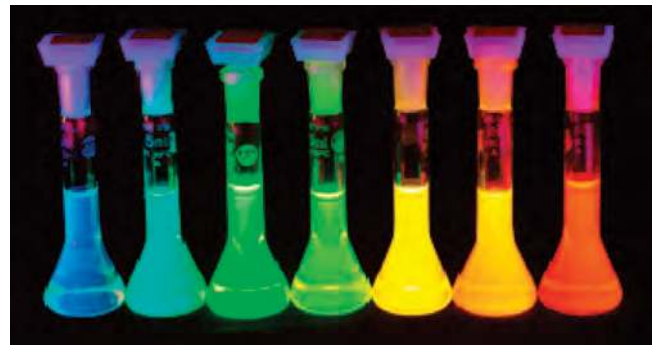

Figure 3. Size-dependent change of the emission color for colloidal solutions of CdSe/ZnS core−shell nanocrystals. The particles with the smallest (~1.7 nm) CdSe core emit blue; the particles with the largest (~5 nm) core emit red. Reprinted with permission from reference 95. Copyright 2002 Wiley.

The other prominent methodology is the so-called sol−gel technique that has been widely studied as one of the most popular routes for synthesis of oxide materials.[104,105] Typical precursors for sol−gel process are metal alkoxides and metal chlorides, which undergo hydrolysis and polycondensation reactions to form a colloid. Traditional sol−gel processes include a series of hydrolysis and condensation reactions of the precursors in acidic or basic aqueous or alcohol media, forming first nanoparticles (colloidal sols) controllably aggregating into a wet network (gel). The sol−gel process can be divided into several stages: (i) formation of stable solutions of the metal alkoxide (the sol); (ii) gelation resulting from the formation of an oxide- or alcohol-bridged network by a polycondensation reaction (the gel); (iii) aging of the gel (syneresis) accompanied by contraction of the gel network and expulsion of solvent from the gel pores; (iv) drying to remove water and other volatile liquids from the gel network; (v) dehydration for removing surface-bound M−OH groups; and (vi) thermal decomposition of the gels at high temperatures. From this process, the pores of the gel network are collapsed, and the remaining organic precursors are decomposed.

Depending upon how the wet gel is dried, the density and extent of porosity of the network can be effectively tuned, consequently impacting the bulk physical properties. Solvent removal can have a huge effect on the gel structure and is a critical step for creating nanostructures with desired functionality.[106] During thermal drying or room-temperature solvent evaporation, capillary forces induce stresses on the gel that induce collapse of the network, eventually leading to so-called xerogels with a collapsed but still porous form of the original gel network. On the other hand, the supercritical extraction of solvent from a gel does not induce capillary stresses due to the lack of solvent−vapor inter-

faces.[106] Obtained aerogels retain a much stronger resemblance to their original gel network structure than do xerogels. For more details on sol−gel synthesis, we address the reader to several recent review articles.[105,107−111]

Brock et al. reported the synthesis of xerogels and aerogels assembled from CdS, ZnS, PbS, CdSe, and CdSe/ZnS core/shell nanoparticles.[112,113] Primary nanoparticles were aggregated to the wet gels and then dried under ambient conditions or in supercritical CO_2 to produce nanoparticle xerogels and aerogels, respectively.

2.2. Nanoparticle Shape and Morphology Engineering

In analogy with bulk crystals, the nanoparticles are terminated by facets that expose different crystallographic planes. Selective adhesion of surfactant molecules allows for tuning the growth kinetics of different crystal facets and tailoring the NC shape from nearly spherical to highly anisotropic[30] (Figure 4). Strong binding of capping molecules suppresses the growth of certain facets, leading to a variety of NC shapes. The multicomponent mixtures of stabilizing agents are often employed to provide the difference in growth rate in different crystallographic directions. For example, depending on the length of alkyl chain and concentration of alkylphosphonic acid and the heating regime, the rod-, arrow-, rise-, teardrop-, and tetrapod-shaped CdSe NCs can be synthesized.[4,32] Possible nanoparticle shapes are determined by symmetry of underlying crystal lattice; for example, PbSe NCs with rocksalt atomic lattice can be synthesized in the form of spheres, cubes (Figure 4a), octahedrons, or star-shaped NCs.[31]

Tetrapods of ZnO,[114] iron oxide,[115] Pt,[116] CdSe,[35,117,118] CdTe (Figure 4b),[119] ZnSe,[120,121] and ZnS[121] are the examples of nanomaterials with higher level of morphological complexity. Two models were adopted to explain the formation of the tetrapods. The nucleation of seeds with zinc-blende crystal structure followed by the growth of four wurtzite-phase arms was originally proposed to explain the morphology of CdTe nanotetrapods.[117,119,122] The alternative octahedral multiple twin model is based on the assumption that the center of tetrapod consists of eight tetrahedral domains enclosed by low-index, high-atomic-density planes and three twin planes at the common edges.[114,121,123−125] The further growth of octa-twin core results in decohesion of the twin boundaries to relieve the strain energy accumulated at the common edges of the twins. Preferential growth along the *c*-axis for wurzite domains leads to the formation of a tetrapod. Formation of the twin planes is also known to be a reason of complex faceting and unusual anisotropic structures for noble metal nanostructures, for example, Au and Ag nanowires with 5-fold cross sections.[126]

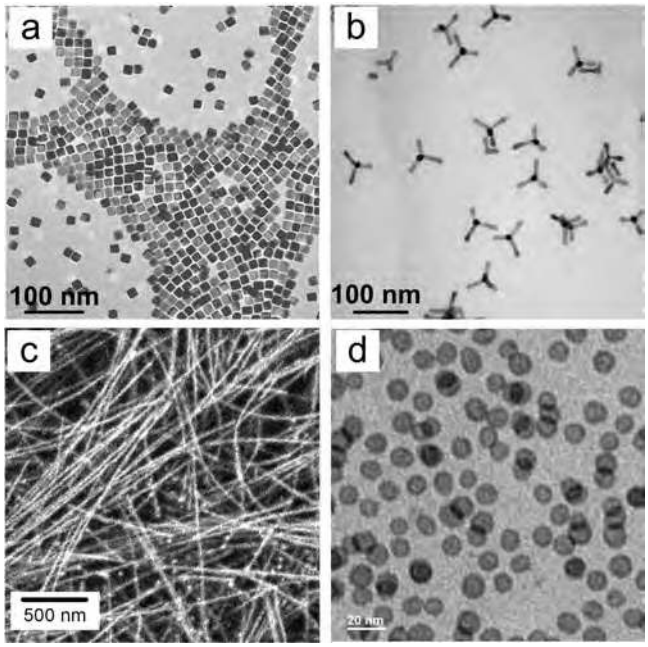

Figure 4. Examples of inorganic nanomaterials with different shapes and morphologies synthesized by colloidal chemistry: (a) PbSe cubes;[31] (b) CdTe tetrapods;[119] (c) PbSe nanowires;[31] and (d) hollow iron oxide nanoparticles. Reprinted with permission from ref 31. Copyright 2005 American Chemical Society. Reprinted with permission from ref 119. Copyright 2003 Nature Publishing Group.

There are a number of other techniques that can be applied to engineer the shape of colloidal NCs. Thus, long uniform colloidal nanowires (Figure 4c) can be synthesized by the oriented attachment[127−130] or solution−liquid−solid[131] growth mechanisms. In oriented attachment, individual nanoparticles attach and fuse along identical crystal faces forming oriented chains.[128] Such anisotropic assembly along one direction followed by subsequent fusion and annealing of surface defects has been reported for a number of systems including Ag,[132] CdTe,[133] CdSe,[134] PbSe,[31] ZnO,[135] ZnS,[136] ZnTe,[137] and In_2O_3.[138] To explain anisotropic growth, the concept of dipole−dipole interparticle interactions as a driving force of chain formation was proposed.[31,127,133] Synthesis through the oriented attachment allows one to control the nanowire morphology. In addition to straight wires, zigzag, helical, branched, and tapered nanowires could all be prepared by adjustment of the reaction conditions.[31] Solution liquid solid growth (SLS) of nanowires[131,139] involves the stages analogous to vapor−liquid−solid growth,[140−142] but nanowires grow in a colloidal solution in the presence of surfactant molecules, which prevent aggregation and precipitation of nanowires. In this approach, metal nanoparticles are used as catalysts to initiate and direct the nanowire growth; the droplets of melted metal function as a liquid phase catalyst for the growth of solid phase through intermediate formation of supersaturated eutectic solution of semiconductor in metal.[131] Nanoparticles of low-melting point metals such as Bi or In were used as the catalysts for solution-phase synthesis of different group IV, II−VI, III−V, and IV−VI semiconductor nanowires, freely suspended in solution.[139,143−146]

Hollow nanomaterials (Figure 4d) were synthesized through the nanoscale Kirkendall effect based on the difference in diffusion rates of two species resulting in accumulation and condensation of vacancies.[147] During gentle oxidation of metal nanoparticles, the outward diffusion of metal is much faster in formed oxide layer than the inward diffusion of oxygen, leading to the formation of a nanoscale void in the center of a nanoparticle.[148] This phenomenon was originally discovered by Yin et al.[148] and was observed for a variety of materials including hollow magnetic iron oxide (Figure 4d)[149] and cobalt sulfide[148] nanoparticles. Galvanic displacement reactions have been also employed for the synthesis of hollow nanostructures.[150] Thus, Xia et al. reported the formation of hollow Au nanoboxes by reacting ∼100 nm Ag cubes with Au^{3+} ions.[151,152] The hollow Au structure formed because in the course of galvanic displacement reduction of each Au^{3+} ion required the oxidation and dissolution of three silver atoms in the nanoparticle core.

Formation of hollow Au NCs allowed one to engineer their optical properties because the frequency of surface plasmon resonance in a hollow NC was strongly dependent on the shell thickness and shape.[153]

2.3. Multicomponent Colloidal Nanostructures

One of the most exciting aspects of colloidally synthesized nanomaterials is the possibility to prepare various multicomponent nanostructures. Combining materials at the nanoscale opens up additional opportunities for manipulating wave functions, Plasmon resonances, spins, and other materials properties.[36,37,154] Thus, bringing together components of intrinsically different functionality constitutes a particularly powerful route to creating novel functional materials with synergetic properties found in neither of the constituents. Multicomponent nanostructures can be prepared via multistep syntheses where presynthesized NCs are used as seeds for nucleation and growth of other inorganic phase. Significant progress has been achieved in the synthesis of core−shell NCs combining two different semiconductors,[49,94,155−157] metals,[158,159] or a metal and a semiconductor[160] in the form of a concentric core and shell (Figure 5a). Such morphology can be obtained by growing a uniform layer of a shell material around colloidal particles. In the case of epitaxial semiconductor−semiconductor core−shell NCs, the choice of materials for the core and the shell allows for controlling the confinement of electron and hole wave functions, which, in turn, determines their optical and electronic properties. If a narrow gap semiconductor is covered by a shell of semiconductor with wide band gap, both electron and hole wave functions will be strongly confined to the core (Figure 5b, left). This confinement regime called type-I heterostructure is observed, for example, in CdSe/ZnS,[49,155] InAs/ZnSe,[161,162] InP/ZnS,[163] and other systems. It is favorable for achieving high quantum efficiency and stability of photo- and electroluminescence, protecting emitting core from oxidation. In some cases, the band gap of the shell material is not wide enough to confine both electron and hole wave functions. For example, in CdSe/CdS core−shell NCs, electron can freely move between CdSe and CdS phases, whereas the hole is confined to the CdSe core because of its large effective mass and substantial offset of the valence band energies (Figure 5b, middle). It is possible to independently engineer symmetry of electron and hole wave functions by varying shapes of CdSe and CdS parts of the nanostructure. For example, one can prepare nanomaterials of "mixed dimensionality" with three-dimensionally confined holes and two-dimensionally confined electrons (Figures 5c and 6a).[33,34,164] Different behavior is observed when core and shell form heterostructure with staggered band offset (Figure 5b, right), the so-called type-II heterostructure.[165−167] In the lowest excited state, the electron and hole wave functions are spatially separated, slowing the radiative recombination rate and facilitating separation of photogenerated carriers.[167] Chemically synthesized type-II nanoheterostructures are considered promising candidates for photovoltaic[168] and

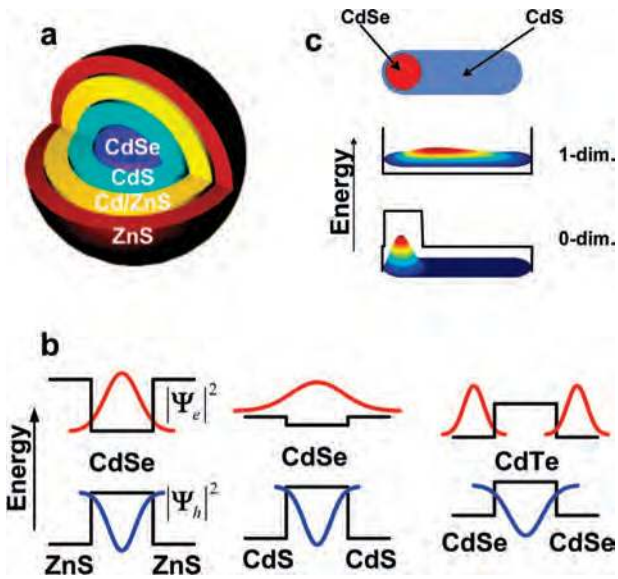

Figure 5. (a) Structure of a core−shell nanocrystal optimized for high luminescence efficiency and stability. Reproduced with permission from ref 171. (b) Schematic representation of the band structure of (left) CdSe/ZnS, (middle) CdSe/CdS, and (right) CdTe/CdSe core shell nanocrystals. The radial probability functions for the lowest energy electron and hole wave functions are schematically shown as red and blue curves, respectively. (c) An example of a nanostructure where electron and hole have different confinement regimes: the electron and hole are confined in two and three dimensions, respectively.

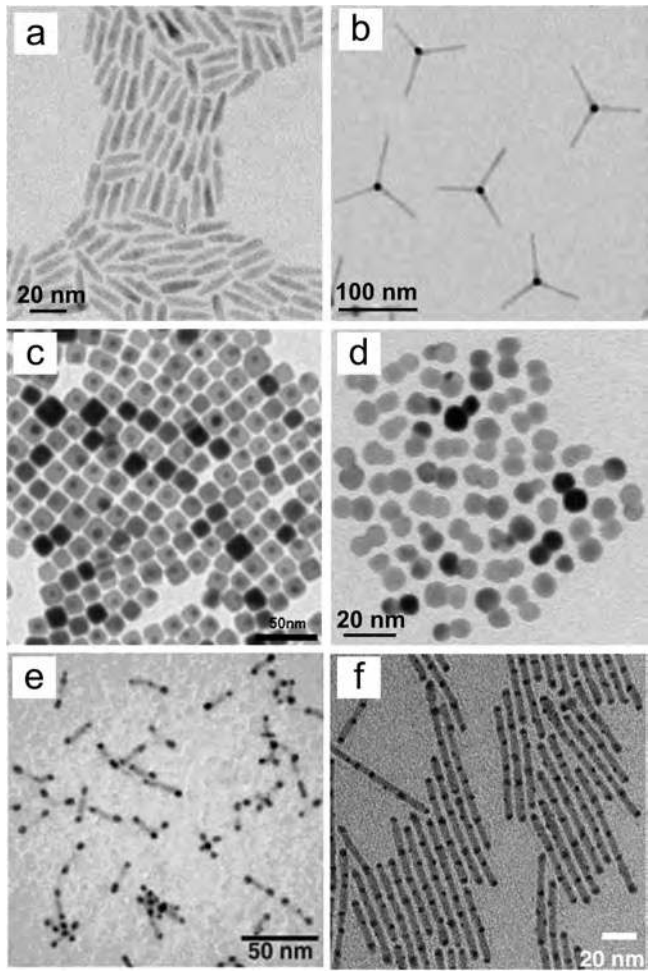

Figure 6. TEM images showing different examples of multicomponent nanostructures: (a) CdSe/CdS nanorods;[33,34] (b) CdSe/CdS tetrapods;[33] (c) Au/PbS core−shells;[24] (d) $CoPt_3$−Au dumbbells;[174] (e) Au−CdSe−Au rods;[38] (f) CdS-Au_2S segmented nanoheterostructures.[175] (a,b) Reprinted with permission from ref 33. Copyright 2007 American Chemical Society. (c) Reprinted with permission from ref 24. Copyright 2008 American Chemical Society. (e) Reprinted with permission from ref 38. Copyright 2004 American Association for Advancement of Science. (f) Reprinted with permission from ref 175. Copyright 2007 American Association for Advancement of Science.

lasing[16] applications. The confinement regime can depend on the diameter of the core and thickness of the shell. For example, ZnSe/CdSe core−shell nanoparticles can exhibit either type-I or type-II behavior, depending on CdSe shell thickness.[165,169] If core and shell materials have a difference in lattice parameters (i.e., lattice mismatch) larger than a few percent, the addition of an intermediate "wetting" layer helps to relax the interfacial strain and prevent accumulation of structural defects at the interface.[11,170]

The seeded growth can be used to fabricate a large variety of core−shell structures, including some very unusual material combinations such as Co/CdSe,[160] FePt/CdSe,[172] PtFe/CdS[172] magnetic core−semiconductor shell, or Au/PbS plasmonic core−semiconductor shell[24] (Figure 6c). Depending on the interfacial energy, lattice matching, and the reaction conditions, multicomponent nanostructures can range from uniformly covered core−shells to dumbbells (Figure 6d) and even highly anisotropic heterostructures like tetrapods shown in Figure 6b.

The use of seeds other than spherical nanoparticle, such as nanorods and tetrapods, may result in highly anisotropic structures where the new phase is selectively deposited on the tips of nanorods or tetrapod arms. Thus, PbSe/CdSe/PbSe,[173] CdTe/CdSe/CdTe,[35] and metal−semiconductor−metal Au/CdSe/Au heterostructures[38] (Figure 6e) were synthesized from CdSe nanorods.

Robinson et al. used partial exchange of Cd^{2+} ions in CdS nanorods with Ag^{+} via cation exchange reaction[175] to prepare beautiful periodic CdS/Ag_2S nanoheterostructures (Figure 6f). This approach is considered as a promising route to create modulated structures, interesting for thermoelectronic applications. Among other examples of multicomponent nanostructures, Au/PbS,[24] $CoPt_3$/Au dumbbells,[174] PbSe/Au_x,[176] gold/iron oxide dumbbells,[177] solid core−shell[178] and core−hollow shell structures,[32] TiO_2/Fe_2O_3,[179] PtFe/iron oxide,[180] and ZnO/Ag,[181] and many others have been reported during the last several years. The recent advances in the synthesis of hybrid structures were reviewed by Cozzoli et al.[37] and Zeng et al.[36]

The toolbox of synthetic techniques is quickly expanding, and many novel structures are reported every year. No doubt, this progress will further continue, providing scientists and engineers with novel potential functional building blocks for electronics and optoelectronics.

3. Nanocrystal Solids

When considering chemically synthesized nanoparticles for electronic and optoelectronic applications, we should keep in mind that the actual active element of most devices will be not individual nanoparticles but their macroscopic arrays. In analogy with conventional solids, the assemblies of nanoparticles should conduct charge carriers and perform other useful actions such as light absorption and carrier separation in solar cells, light emission in LEDs, etc. The ability to tailor size, shape, and compositions of individual nanoparticles provides means for fine-tuning material properties. At the same time, the behavior of nanoparticle ensembles depends not only on the properties of individual elements, but on the electronic and optical communication between the nanoparticles, on the interparticle medium, packing density, and mutual orientations of NCs, etc. All of these issues add new levels of complexity to the problem of designing electronic materials from nanoparticle building blocks. At the same time, understanding and utilizing self-assembly of nanoparticles can provide routes to multifunctional materials of unprecedented precision, complexity, and aesthetic beauty.[182]

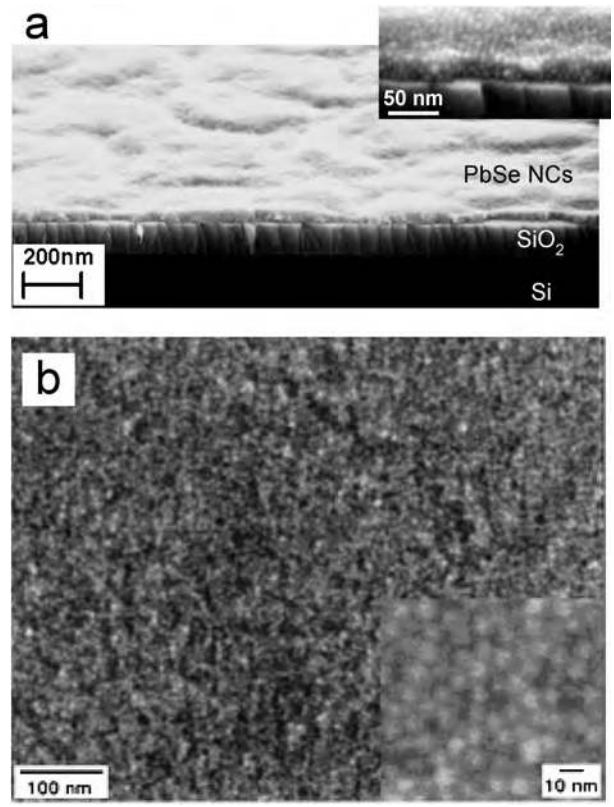

Figure 7. (a) High-resolution cross-section SEM image of a drop-cast film assembled from PbSe nanocrystals. Thickness of SiO_2 layer is 100 nm. Reprinted with permission from ref 23. Copyright 2005 American Association for Advancement of Science. (b) SEM micrographs of a glassy solid prepared from 5.6 nm CdSe nanoparticles. Reprinted with permission from ref 39. Copyright 2000 Annual Reviews.

NCs can be brought together in a form of an amorphous (glassy) or ordered periodic structures. Glassy NC solids can be defined as isotropic materials with only short-range order among the NCs (Figure 7). Several factors, such as polydispersity of NCs, their poor solubility in a given solvent, and fast solvent evaporation, favor the formation of disordered structures or assemblies with short-range order (Figure 7). Also, if repulsive forces dominate the particle−particle interactions and other interactions are weak, there is no significant energy driving the formation of an ordered lattice.[39]

Ordered NC solids (also referred to as "superlattices") are anisotropic materials that are characterized by three-dimensional periodicity with or without preferential orientation of individual nanoparticles.[39,183] In the case of periodic assemblies, the positions of particles and, as a result, packing density and chemical composition are uniform throughout the entire structure. This uniformity makes periodic nanoparticle arrays (films, 3D crystals) especially attractive for practical applications and for fundamental studies. However, there are a number of technical challenges in reproducible preparation of large nanoparticle superlattices, such as lack of control over their dimensions and structural defects.

3.1. Short-Range Ordered Nanoparticle Assemblies

As-synthesized nanoparticles form stable colloidal solutions convenient for processing and deposition (Figure 3). Close-packed NC films can be easily obtained by spin-coating or drop-casting of the colloidal solution. Typically, the films obtained this way show short-range ordering (i.e., each NC is surrounded by the same number of the nearest neighbors),[1] as can be seen in Figure 7. As with any kind of solution deposition, the proper choice of solvents and preparation of substrate surface are important for obtaining uniform continuous films. For example, a hexane:octane (9:1 by volume) solvent mixture can provide very uniform drop-cast films of NC with hydrophobic surface ligands, such as TOPO−TOP capped CdSe and InP[39] or oleic acid capped PbSe NCs.[23] Hydrophobization of substrate surface with hexamethyldisilazane (HMDS) treatment also helps obtaining good uniformity of nanoparticle films.[23] Solvents such as chloroform[184] and chlorobenzene were used for making close-packed films of CdSe and PbS NCs by spin-coating. Different solvents should be used for deposition of nanoparticles with polar surface groups. Thus, Yu et al. used a mixture of pyridine and ethanol (1:3 by volume) to prepare films of pyridine capped CdSe NCs.[185] Besides spin-coating and drop-casting, other approaches such as Langmuir−Blodgett,[186−189] layer-by-layer deposition,[190−194] doctor blading, and inkjet printing[195] have been employed to prepare close-packed films of nanoparticles. Combining solution deposition with photo- or e-beam lithography allows patterning of NC films with different levels of precision.[196,197] Thick nanoparticle films sometimes tend to crack upon drying, which negatively affects the performance of the nanoparticle-based devices. It can be hard to avoid the cracking of the drying films; however, the cracks can be filled by infiltration or other techniques.[23] More detailed information on the preparation of nanoparticle films can be found in several review articles.[39,198−200]

3.2. Nanoparticle Superlattices

NCs with narrow size distribution (<10% standard deviation) can self-assemble into long-range ordered superlattices upon slow evaporation of carrier solvent[39,183] or gentle destabilization of the colloidal solution.[95,201−203] Some examples of self-assembled NC superlattices are shown in Figure 8. The lateral size of long-range ordered domains can approach hundreds of micrometers. NCs with spherical shape usually form face centered cubic (fcc) lattice.[183] However, even minor NC shape anisotropy or dipolar interactions can lead to other packing symmetries, such as hexagonal close-packed (hcp) or simple hexagonal phases.[204] Ordering of spherical particles has been extensively studied both theoretically and experimentally. Entropy can drive the ordering of noninteracting hard spheres because of the increased local free space available for each sphere in the fcc lattice as compared to the disordered state.[205] Theoretical calculations and simulations of hard sphere colloids predict that the fcc structure should be slightly more stable as compared to the hcp structure.[206,207] In agreement with this prediction, monodisperse micrometer size latex and silica spheres whose behavior is similar to hard spheres exhibit predominantly fcc superlattices, also known as synthetic opals.[208] However, the free energy difference between fcc and hcp structures with identical packing density (~0.7405) is very small, about 10^{-3} k_BT per particle.

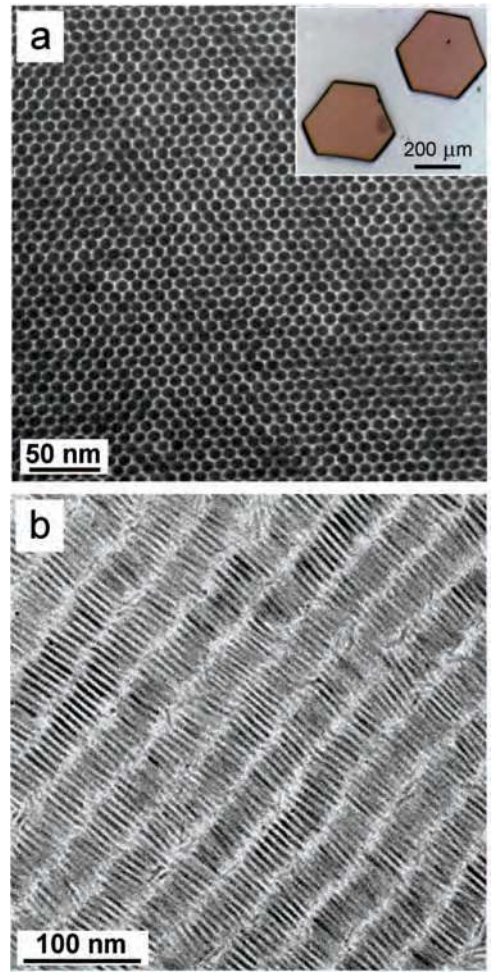

Figure 8. TEM images of self-assembled nanocrystal superstructures: (a) 7.5 nm PbS nanocrystals; inset shows optical micrographs of "supercrystals" grown from PbS nanocrystals. (b) Smectic ordering of 29 nm long, 4.5 nm diameter CdS nanorods. Image courtesy of M. Bodnarchuk.

In the case of nanoparticles, Coulombic, van der Waals, charge−dipole, dipole−dipole, entropic, capillary, convective, shear, and other forces contribute to the paprticle−particle and particle−substrate interactions.[198] The contributions of these forces depend on the nature of inorganic core and surface ligands, charging of nanoparticles, surrounding media, temperature, etc. The electrostatic interactions between nanoparticle can originate from static electric charges, static, and induced dipole moments.[209−212] van der Waals interactions take place between both "hard" inorganic cores[213,214] and "soft" organic shells.[215] In the case of magnetic particles, magnetic dipolar interactions can lead to ring- and pearl-like structures.[216] At the nanoscale, the magnitudes of all of these interactions are often comparable to each other, providing flexibility to the interparticle potentials.[217] In a superlattice, the nanoparticles can exhibit preferential orientation (alignment) of their atomic lattices.[39,182] However, the proper control of arrangement of atomic lattices throughout the entire periodic structure is difficult to predict and achieve on demand.

Shape of NCs plays an important role; self-assembly of NCs with shape anisotropy can lead to the formation of liquid crystalline (nematic and smectic)[218] and crystalline[34,65,182,218,219] phases (e.g., Figure 8b).

3.3. Multicomponent Nanoparticle Superstructures

Mixing two colloidal solutions of NCs with different size and functionality (e.g., transition metals, semiconductors, oxides, etc.) can lead to the formation of ordered binary nanoparticle superlattices (BNSLs) (Figures 9−11).[215,220−224] Multicomponent nanoparticle superlattices naturally provide a much broader range of compositions and structures as compared to the assemblies of one type of NCs. When particles of different sizes and types are brought together, they must adjust themselves to space constrains in a certain way. Many efforts were made to predict the formation of various ordered binary structures and evaluate their stability.[225−231] In the simplest mechanistic approach based on space filling, the formation of a binary assembly of hard (noninteracting) spheres is expected only if its packing density exceeds the packing density of single-component crystals in fcc or in hcp structure (~0.7405).[232] According to this principle, the key factors determining the structure of superlattices are particle size ratio ($\gamma = R_{small}/R_{large}$) and relative concentrations. Each structure has its own γ range of stability.[232] Taking into account geometrical considerations only, we can expect the formation of superlattices isostructural with NaCl, $NaZn_{13}$, and AlB_2. Indeed, $NaZn_{13}$- and AlB_2-type assemblies of silica particles were first found in natural Brazilian opals[233] and later grown from latex spheres.[234,235] Packing density in the stable γ range usually exceeds 0.7405, the packing density for fcc single component lattices. In other words, the higher is the packing density, the larger is the entropy gain achieved during crystallization of the NC superlattice.[233] Detailed computer simulations showed that the formation of NaCl-, AlB_2-, and $NaZn_{13}$-type structures of hard spheres can be driven by entropy alone without any specific energetic interactions between the particles.[228−230] However, the intrinsic entropy of binary superlattice also affects its stability. For example, the maximum packing density of $NaZn_{13}$-type superlattice is slightly below 0.74, whereas the detailed entropy calculations predict the stability of this structure in a rather broad range of γ.[230]

Self-assembly of two types of nanoparticles gives rise to amazing diversity of binary superlattices (Figure 10). Superlattices with AB, AB_2, AB_3, AB_4, AB_5, AB_6, and AB_{13} particle stoichiometry with cubic, hexagonal, tetragonal, and orthorhombic symmetries have been identified.[182,215,220−224] Assemblies with the same stoichiometry can be produced in several polymorphous forms by tailoring the particle size and deposition conditions. Thus, BNSLs isostructural with NaCl, NiAs, CuAu, AlB_2, $MgZn_2$, $MgNi_2$, Cu_3Au, Fe_4C, $CaCu_5$, CaB_6, $NaZn_{13}$, and *cub*-AB_{13} compounds were made using various nanoparticle combinations.[182,220] The observed structural diversity is rather challenging to understand. Currently, the structural diversity of BNSLs is explained by the interplay of multiple factors such as entropy, Coulombic, van der Waals, charge−dipole, dipole−dipole, and other interactions, which all contribute to stabilization of BNSL's in a rather complex way, allowing the superlattice formation to be dependent on a number of tunable parameters. Even

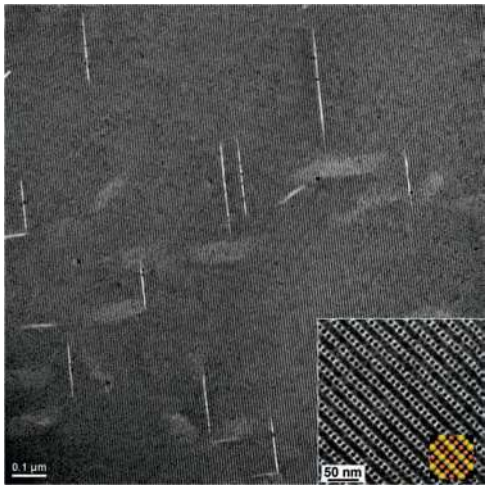

Figure 9. TEM image of (100) projection of a binary superlattice isostructural with AuCu intermetallic compound, self-assembled from 5.8 nm PbSe and 3.4 nm Ag nanoparticles; inset shows the same structure under higher magnification.

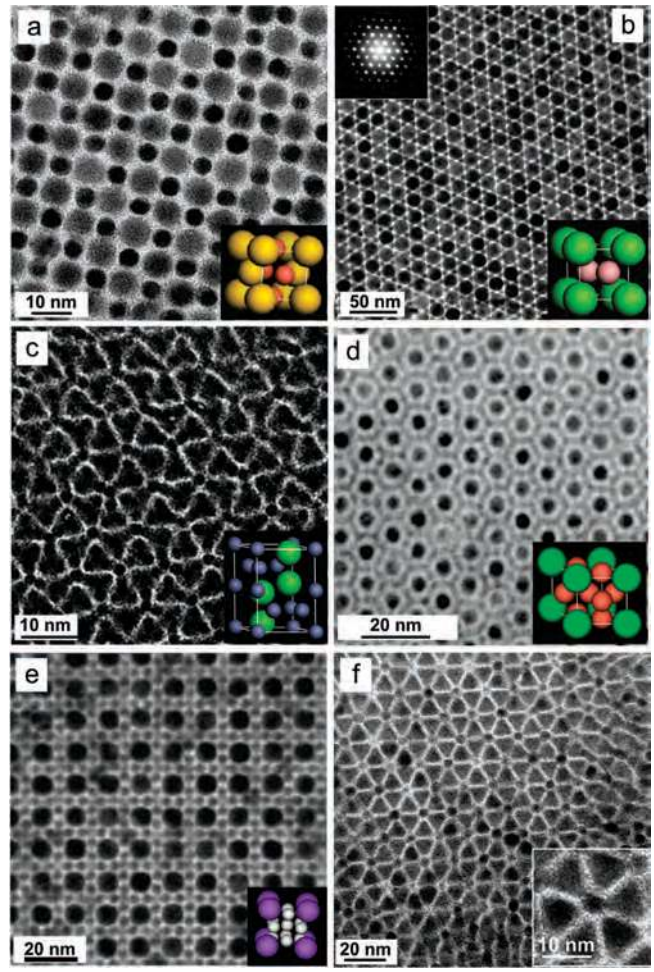

Figure 10. TEM images of binary nanoparticle superlattices (BNSLs) self-assembled from various semiconductor, metallic, and magnetic nanocrystals. The bottom-left corner insets show the unit cells of corresponding structures. (a) (001) projection of AuCu-type BNSL formed by 7.6 nm PbSe and 5.0 nm Au NCs. (b) (001) projection of AlB_2-type BNSL assembled from 13.4 nm Fe_2O_3 and 5.8 nm PbSe NCs. The top-left corner inset shows small-angle electron diffraction pattern. (c) (001) projection of Laves phase $MgZn_2$-type BNSL formed by 6.2 nm PbSe and 3.0 nm Pd nanocrystals. (d) (001) projection of $CaCu_5$ type BNSL formed by 3.4 nm CdSe and 7.3 nm PbSe nm NCs. (e) (100) plane of cub-AB_{13} type BNSL formed by 8.1 nm CdTe and 4.4 nm CdSe nanocrystals. (f) BNSL self-assembled from LaF_3 triangular nanoplates (9.0 nm side) and 5.0 nm spherical Au NCs. (a,b,c,f) Reprinted with permission from ref 182. Copyright 2006 Nature Publishing Group. (d) Reprinted with permission from ref 215. Copyright 2007 American Chemical Society. (e) Reprinted with permission from ref 224. Copyright 2008 American Chemical Society.

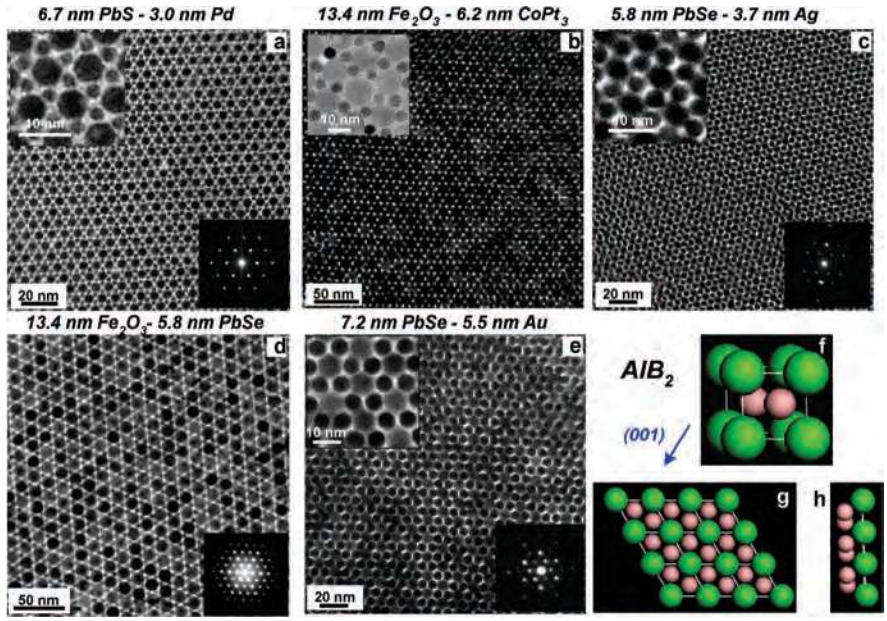

Figure 11. Binary superlattices combining different functional building blocks (magnetic, semiconducting, metallic). (a−e) TEM micrographs of (001) planes of binary superlattices isostructural with AlB_2 compound. (f) Sketch of AlB_2 unit cell. (g,h) Depictions of the front and side views of the superlattice (001) plane, correspondingly. Reprinted with permission from ref 220. Copyright 2006 American Chemical Society.

though the complex nature of particle−particle and particle−substrate interactions slows the progress in control of nanoparticle self-assembly, it also provides an amazing platform to synthesize structures fascinating our imagination. It should probably be possible to coassemble more than two nanoparticle components, forming ternary and quaternary superlattices. However, even preliminary studies show that the phase analysis of such structures will be very challenging. Using multicomponent (e.g., core−shell or dumbbell) NCs as BNSL building blocks is an alternative way to combine more than two inorganic components in a long-range ordered superlattice.[236] Different types of BNSLs can form simultaneously on the same substrate,[220] and, as a result, a smooth "epitaxial" transition between two BNSL phases can form a "super-heterostructure".[220]

As compared to atomic solids, the nanoparticle superlattices can possess extra degrees of freedom such as adjustable particle size and shape. The ability to mix and match different nanoparticles and assemble them systematically into ordered binary superlattices, with precisely controlled stoichiometry and symmetry, can provide a general and inexpensive path to a large variety of novel materials with precisely controlled chemical composition and tight placement of the components. In perspective, BNSLs could make possible a modular approach to create multifunctional materials by combining independently tailored functional components.

3.4. Theoretical Insight into the Electronic Structure of Nanocrystal Solids: From Insulated Dots to Three-Dimensional Minibands

Unlike atomic and molecular crystals where atoms, lattice geometry, and interatomic distances are fixed entities, the NC solids represent ensembles of designer atoms with potential for tuning their transport and optical properties. Generally speaking, NC assemblies can be considered as a novel type of condensed matter, whose behavior depend both on the properties of the individual building blocks and on the many-body exchange interactions. The presence of long-range translational order in nanoparticle superlattices can make them fundamentally different from amorphous and polycrystalline solids. The coupling among ordered quantum dots can lead to a splitting of the quantized carrier energy levels of single particles and result in the formation of three-dimensional collective states, minibands.[237,238] Although different types of long-range ordered single- and multicomponent NC superlattices had already been self-assembled from colloidal NCs, very little attention has been paid to the theoretical description of electronic structure, carrier, and phonon transport in such structures. To the best of our knowledge, no electronic structure calculations for fcc or BNSL structures have been reported. At the same time, a reasonably good description of the extended states has been developed for one-dimensional quantum well superlattices[239−243] and quantum dot crystals grown by molecular beam epitaxy.[237,244−246] In the latter case, the analysis was based on the effective mass or envelope function approach.[247] The one-electron Schrödinger equation was used in the form of an effective mass equation involving the envelope of the electron wave functions. The effect of the background atomic potential was accommodated as an effective mass for the electron moving under the influence of macroscopic potential perturbations. For simplicity, the theory was developed for simple cubic and tetragonal lattices (Figure 12). The motion of a single carrier in such a system can be described by the Schrödinger equation:

$$\left[-\frac{\hbar^2}{2}\nabla_r\frac{1}{m^*(\mathbf{r})}\nabla_r + V(\mathbf{r})\right]\varphi(\mathbf{r}) = E\varphi(\mathbf{r}) \qquad (4)$$

The atomic structure of the quantum dot crystal enters the analysis as an effective mass m^*. This parameter assumes different values in the quantum dot and the barriers. The potential $V(\mathbf{r})$ corresponds to an infinite sequence of quantum dots of size L_x, L_y, and L_z separated by the barriers of thickness H_x, H_y, and H_z (Figure 12). For simplicity, it was assumed that $V(\mathbf{r})$ can be written as a sum of three

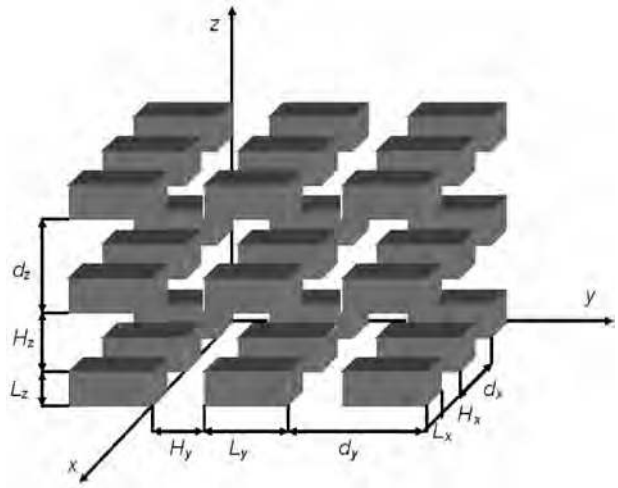

Figure 12. Schematic structure of a modeled quantum dot crystal. Reprinted with permission from ref 248. Copyright 2001 American Institute of Physics.

independent periodic functions of coordinates x, y, and z with periods of d_x, d_y, and d_z ($d_\xi = L_\xi + H_\xi$):

$$V(\mathbf{r}) = V_x(x) + V_y(y) + V_z(z) \tag{5}$$

where

$$V_\xi(\xi) = \begin{cases} 0 & \text{in the quantum dots} \\ V_0 & \text{in the barrier} \end{cases} \tag{6}$$

Here, index ξ denotes a particular coordinate axis. This choice of potential allowed one to separate the carrier motion along three coordinate axes and decouple the three-dimensional (3D) Schrödinger equation into three identical one-dimensional (1D) quantum-well superlattice equations. The 3D envelope wave function $\varphi(\mathbf{r})$ was presented as a product of three 1D eigenfunctions $\chi(\xi)$ in the following way:

$$\varphi(\mathbf{r}) \equiv \varphi_{n_x n_y n_z}(x, y, z) = \chi_{n_x}(x)\chi_{n_y}(y)\chi_{n_z}(z) \tag{7}$$

where n_ξ denoted the quantum number. The total energy spectrum for this wave function was given by

$$E_{n_x n_y n_z} = E_{n_x} + E_{n_y} + E_{n_z} \tag{8}$$

where E_n are the eigenvalues of the one-dimensional Schrödinger's equations.

Equation 4 with the potentials from eqs 5 and 6 was solved analytically.[248] Despite its simplicity, this approach captured the key features of quantum dot superlattices, at least for "type I" superlattices where the envelope function varied slowly on the scale of the atomic lattice period.[238,249,250] The validity of this model has been also confirmed by numerical solutions of the Schrödinger equation with more realistic forms of the potential barrier.[245]

The above formalism has been applied by Lazarenkova and Balandin[237,251] and by Jiang and Green[238] to Si quantum dots embedded in Ge, SiO_2, Si_3N_4, and SiC matrices and to various III−V quantum dot superlattics.[246,252] Figure 13 shows the calculated conduction band dispersion relation of a cubic silicon quantum dot superlattice in a dielectric matrix of silicon nitride (~1.9 eV barrier height for the condction band). The dot size was 2 × 2 × 2 nm^3, and the interdot distance was 1 nm in all three coordinate directions, that is,

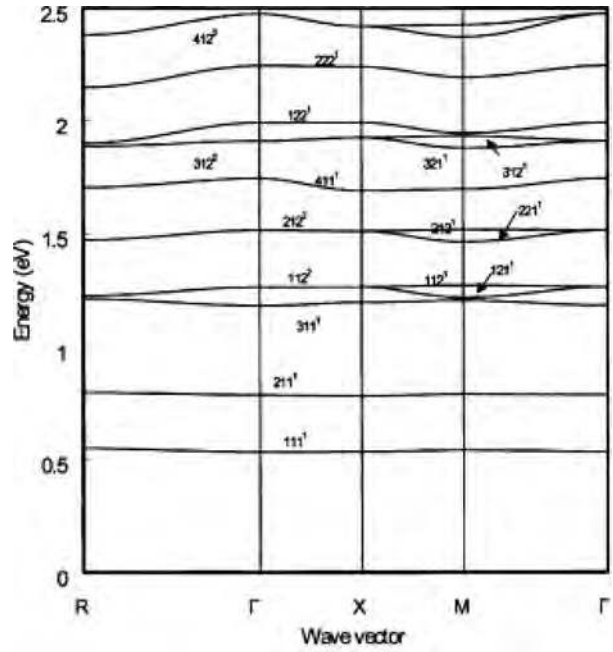

Figure 13. Conduction band dispersion relation for a cubic silicon quantum dot superlattice in a silicon nitride matrix. The dot size is 2 × 2 × 2 nm^3, and the interdot distance is 1 nm in all three coordinate directions. The dielectric effective mass is $0.4m_o$, and the barrier height is 1.9 eV relative to the conduction band edge of silicon. The energy bands are denoted by three quantum numbers $n_x n_y n_z$ with the superscript indicating the fundamental degeneracy of the band. Reprinted with permission from ref 238. Copyright 2006 American Institute of Physics.

quite similar to the parameters observed for nanoparticle superlattices. To describe the energy bands, Lazarenkova and Balandin[237] introduced three quantum numbers $n_x n_y n_z$, which corresponds to the numbering of the allowed solutions in each direction. The superscripts in Figure 13 indicate the fundamental degeneracy of the band neglecting the electron spin degeneracy. Jiang and Green showed that a matrix with lower barrier height yielded higher density of bands and higher dispersion.[238] They also demonstrated a dramatic effect of the barrier height and width on the miniband energy and the bandwidth (Figure 14). The lower height and narrower width of the dielectric barrier produce broader bands. The dot size had a greater influence on the band energy level rather than the bandwidth. At the same time, the calculated energy and width of the minibands was relatively insensitive to electron effective mass in the dielectric barrier.[238]

It is well-known that a single quantum dot has a discrete spectrum. When quantum dots are separated by a finite barrier and positioned very close to each other so that there is a significant wave function overlap, the discrete energy levels split into minibands. This can be seen in Figure 14b for the interdot distance H below 2 nm. For other material systems, such as InAs/GaAs, the splitting may occur at much larger distances.[246] As the interdot distance or barrier height increases, the wave function overlap decreases, and the minibands reduce to discrete levels.

A carrier density of states (DOS), which is a number of carrier states in an interval of energy per unit volume, and the effective mass tensor are important for virtually all electronic and optical applications of semiconductor struc-

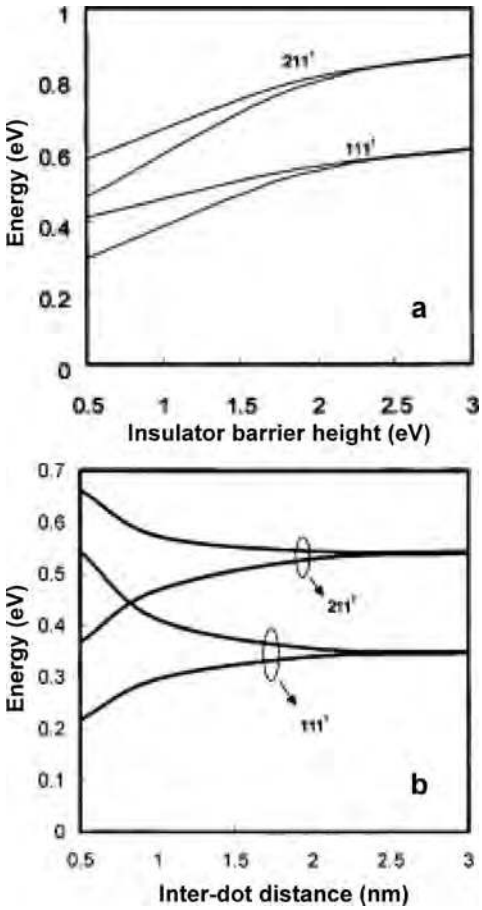

Figure 14. Minibands in a silicon quantum dot crystal. (a) The effect of dielectric barrier height on bandwidth and energy levels in modeled quantum dot crystal. The dielectric effective mass is $0.4m_o$. The reference energy is taken from the conduction band edge of silicon. The dot size, interdot distance, and anisotropic silicon effective mass are the same as in Figure 13. (b) The effect of interdot distance on bandwidth and energy levels. The calculation parameters are the same as in Figure 13 except for the barrier height, which was 0.5 eV (typical for SiC matrix). Reprinted with permission from ref 238. Copyright 2006 American Institute of Physics.

tures. Lazarenkova and Balandin calculated these parameters for heavy hole minibands in a simple cubic array of Si quantum dots in Ge matrix.[237,245] They observed that DOS and the effective mass tensor in quantum dot crystals are fundamentally different from those in bulk semiconductors and in quantum well superlattices. The calculations showed that the effective mass in quantum dot crystal is highly anisotropic and strongly dependent on the miniband index. The same authors solved elasticity equations and calculated the phonon spectrum in Si/Ge quantum dot crystals.[245] Apart from the fundamental scientific importance of the electron and phonon spectra in ordered quantum dot arrays, there is a practical interest in addressing this problem because these parameters are very important for operation of photovoltaic[253] and thermoelectric[254,255] devices.

By changing the size of quantum dots, interdot distances, barrier height, and regimentation, one can engineer the 3D minibands in quantum dot crystals and fine-tune electronic and optical properties of such nanostructures, providing exciting possibilities for optimization of electronic, photovoltaic, and thermoelectric devices. At the same time, formation of the extended states requires high materials quality in terms of (i) periodicity of the quantum dots in an array; (ii) homogeneity of the dot size and shape; (iii) strong interdot coupling; (iv) low concentrations of surface defects, etc.[238,245] In real quantum dot crystals, there is always some distribution of dot size and fluctuations in the dot position. Extended states and minibands can still be formed as long as the bandwidth due to wave function overlap exceeds the total broadening, which is mostly determined by the inhomogeneous broadening.[256] An important source of disorder, which is often overlooked, originates from the fluctuations of local interdot coupling strengths. This type of disorder should be very common for arrays of colloidally synthesized NCs separated by amorphous disordered layers of insulating organic ligands. The interplay of the interparticle coupling and disorder will be discussed in detail in section 5.

There is only limited information available on the formation of extended states in superlattices of chemically synthesized NCs. Formation of extended electron states and minibands has been reported by Artemyev et al.[257−259] for a dense quantum dot ensemble consisting of monodisperse small CdSe dots of average radius $R = 1.6-1.8$ nm; extended electronic states have been observed in arrays of metallic (Au and Ag) NCs.[260,261] On the basis of the existing theoretical framework, these are all possible reasons to expect miniband formation in NC solids and BNSLs with properly designed interparticle communications.

In chemically synthesized NC solids, surface ligands form dielectric interparticle barriers. The barrier height and width play the key roles in the evolution of the band structure and transport phenomena. Different approaches to the ligand design are discussed in the next section.

4. Design of Surface Ligands

In section 2, we discussed the important role that surface ligands play in the synthesis of colloidal nanomaterials; they control nucleation, growth, chemical, and colloidal stability. The surface ligands are also extremely important for assembling individual particles into a NC solid. They contribute to the interparticle interactions and determine the spacing between neighboring NCs in short- and long-range ordered NC assemblies. It was shown in section 3.4 that the inteparticle spacings have an extremely strong impact on the electronic structure of NC solids. The importance of surface ligands can hardly be overemphasized. Because of high surface-to-volume ratio inherent to the nanoscale objects, the surface has a strong influence on physical properties of NCs including photophysics,[156,262] charge transport,[185,263] catalysis,[264] and magnetism.[4] Proper surface chemistry is considered a key to make a good NC-based photodetector,[265] solar cell,[168] transistor,[23] or light-emitting device.[266] Table 1 summarizes the structural elements of the ligand molecules considered and employed for electronic applications of NC solids.

The most common ligand coatings described in the literature are based on organic hydrocarbon molecules with anchoring end groups. Such molecular structure offers the highest chemical flexibility; however, it has a number of serious drawbacks. Most organic ligands act as bulky insulating barriers between NCs, hindering charge transport. Numerous literature reports studied the effect of length of ligand molecules on charge transport in arrays of metallic NCs. Most common examples include Au and

Table 1. Different Types of Surface Ligands Used in Nanocrystals and Nanocrystal Solids

Ligand type	Molecular structure	Interparticle spacing	Functions, characteristics, typical examples
Molecules with single head group and a long hydrocarbon chain	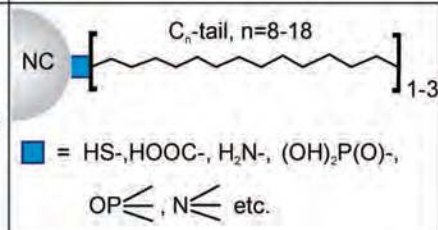	>1.5 nm	• Most common ligands used for NC synthesis • Form stable colloidal solutions • Hydrophobic surface • Form highly insulating NC solids, $\sigma \sim 10^{-12}$-10^{-9} S cm^{-1}
Short-chain molecules with single head group	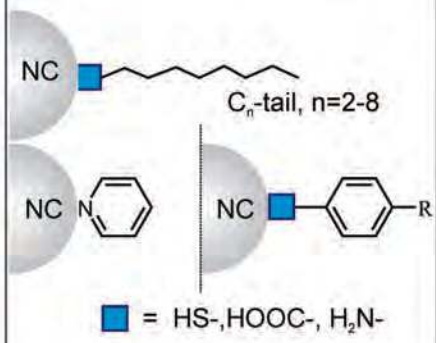	0.3-1 nm	• Treatment of NC solids or ligand-exchange in solutions • Decreased colloidal stability • Improved electronic transport compared to long-chain ligands • Reported detectivity of $\sim 10^{12}$-10^{13} Jones in photodetectors on PbS NCs caped with butylamine[270] • Conductivities of up to 10^{-1} S cm^{-1} in arrays of metallic NCs[267]
Cross-linking molecules with two end groups	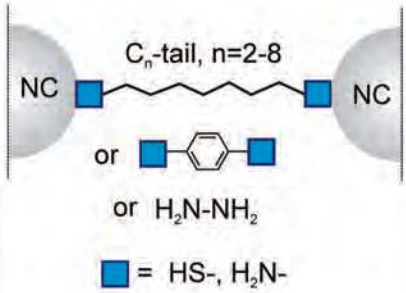	0.3-1 nm	• Mainly prepared by treating NC solids • μ up to 2 cm^2 V^{-1} s^{-1} in arrays of PbSe NCs treated with N_2H_4[23] • $\mu \sim 10^{-2}$ cm^2 V^{-1} s^{-1} in arrays of CdSe NCs treated with 1,4-phenylenediame[185] • Solar cells based on PbS and PbSe NC solids showed power conversion efficiencies of up to 2.1%[253,271,272]
Metal chalcogenide complexes	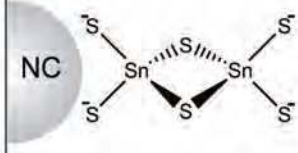	≥ 0.5 nm	• Prepared via solution phase ligand-exchange • Complete removal of original organic ligands • Hydrophilic surface • High conductivities of ~200 S cm^{-1} in Au-$Sn_2S_6^{4-}$NC solids[273]

Ag NCs capped with alkylthiol molecules. For a detailed discussion of ligand effects on transport in metallic systems, we refer the reader to a recent review article by Zabet-Khosouri and Dhirani.[267]

The complete removal of organic surface ligands has proven to be very difficult; it often generates multiple surface dangling bonds and midgap charge-trapping states.[156] Annealing of NC samples can partially remove the organic ligands, but it often leads to sintering of NCs.[268] Moreover, high temperature annealing typically leaves behind undesirable carbonaceous species due to partial ligand pyrolysis.[269] Simple exchange of original bulky ligands by smaller molecules is a widely used approach for improving charge transport (section 4.1). Mild chemical treatments with dilute hydrazine solutions,[23] phenylenediamine,[185] and other cross-linking molecules (section 4.2) enabled considerable progress in the preparation of conductive NC solids. However, these small molecules are not stable against oxidation and volatility, leading to instabilities of the electronic properties. Furthermore, conventional semiconductor technology always

preferred pure, all-inorganic, and highly crystalline materials, which stimulated the development of functional all-inorganic ligand coatings (section 4.3).

4.1. Organic Ligands with Long Hydrocarbon Chains, Their Removal, and Exchange for Smaller Molecules

The most common class of surface ligands used for synthesis and processing of NCs is represented by molecules having a head group (thio-, amino-, carboxylic, etc.) with high affinity to the NC surface and the aliphatic tail that provides sterical stabilization of a colloidal solution in nonpolar solvents. There are an extensive number of studies dedicated to NCs capped with such surface ligands, and we refer the reader to several review articles that explicitly cover the topic.[108,109,274] Oleic acid, trioctylphosphine oxide (TOPO), dodecanethiol, oleylamine, hexadecylamine, and phosphonic acids are examples of the most frequently used surfactants. We have to admit that our current understanding of the binding modes at the NC−ligand interface is rather incomplete. As an example, recent X-ray diffraction studies by Jadzinsky and co-workers revealed that "simple" binding of thiol molecules to the surface of Au NCs can indeed be very nontrivial.[275] It is usually believed that surface ligands form uniform shells around the NC core. It was recently reported that two kinds of ligand molecules can self-assemble into complex patterns driven by segregation of different tail groups at the NC surface.[276]

Bulky ligands, convenient for colloidal synthesis, create thick insulating barriers around each nanoparticle, blocking the charge transport in NC solids. In addition, simple monofunctional ligands do not have any functional end groups, which could be used for carrier transport, conjugation with other molecules and surfaces, etc. To overcome these limitations, the original surface ligands can be replaced with new ones.

The ligand exchange procedure typically involves an exposure of colloidal NCs to the large excess of competitive ligand, resulting in partial or complete exchange of surface molecules.[26,39,156] This procedure can be prolonged up to a few days or repeated multiple times to maximize the removal of original ligands, often accelerated by gentle heating. The ligand exchange is typically carried out without high temperature treatments, allowing one to introduce low boiling ligands such as pyridine[26] or 1-butylamine[265] and others incompatible with high-temperature conditions. Because of the effect of mass action, the incoming ligand may have lower affinity to NC surface than the leaving molecule. The exchange process is often facilitated by the phase-separation of the products by using, for example, two-phase mixtures of polar and nonpolar solvents.[277] The degree of ligand exchange is usually probed by NMR[156,278] and Fourier-transform infrared spectroscopy (FTIR),[279] and X-ray photoelectron spectroscopy (XPS).[278,280,281] In many cases, such studies are supplemented by elemental analysis, dynamic light scattering, and mass spectrometry. Ligand-exchange reactions can be classified into two kinds: (i) reaction involving the same functional group and different tails and (ii) competition of molecules with different anchoring functional groups.

Ligand Exchange for Molecules with the Same Head Group

Thiol-for-thiol exchange serves as a classical example. Using NMR and FTIR techniques, Hostetler and co-workers studied the mechanism and dynamics of ligand-exchange reactions using Au NCs and alkanethiols.[282] They found that, in addition to the expected concentration dependence, there is also strong impact from the size of the alkyl tail because the molecules have to penetrate through the existing ligand shell. The smaller was the tail group of the leaving molecule, the higher was the exchange rate observed. In so-called phase-transfer reactions, hydrophilic thiols can be easily replaced by alkylthiols[277] and vice versa,[283] allowing an easy switch between hydrophilic and hydrophobic NC surface.

Ligand Exchange for Molecules with Different Head Groups

Many ligand manipulations involve the use of pyridine as weakly coordinating ligand, which was first demonstrated for CdSe NCs in a seminal paper by Murray, Norris, and Bawendi.[26] Typically, NCs are refluxed in pyridine, which makes the product insoluble in nonpolar aliphatic solvents but readily dispersible in more polar solvents, aromatics, small-molecule chlorinated solvents, and mixtures thereof. Pyridine is often used as a ligand that can be replaced by other molecules or removed by vacuum and/or heat treatments. The pyridine exchange was utilized in the synthesis of core−shell NCs like CdSe/CdS[94] or to integrate CdSe NCs into hybrid structures of colloidal NC and bulk semiconductors.[284] In the latter case, easy removal of pyridine molecules allows uniform growth of ZnSe capping layer by molecular beam epitaxy (MBE). Pyridine was also used as an efficient intermediate ligand when the direct exchange between desired and original surface ligands was impossible.[285] In addition to II−VI nanomaterials, III−V (InP)[286,287] and IV−VI (PbSe)[288] semiconductor NCs can be functionalized with pyridine molecules. In case of PbSe NCs, pyridine treatment was found to significantly improve the charge transport and photoconductivity.[288]

In some cases, postpreparative surface modification is required to improve chemical and colloidal stability of NCs. Thus, Hutchison et al. demonstrated the facile phosphine-to-thiol exchange using 1.4 nm Au NCs.[289−291] Triphenylphosphine was originally used for the synthesis of very small Au NCs, which, however, were not stable in the long term. Simple addition of hydrophobic or hydrophilic thiols considerably improved stability without damaging the NC core. Using ω-functionalized thiol,[289] Hutchison and co-workers demonstrated that ligand exchange can tolerate a very broad range of functional groups. At the same time, phosphine-to-amine exchange using 1.4 nm Au clusters occurred with lower substitution rate and was accompanied by a slow increase of the NCs size.[290,292]

A typical limitation of the solution-phase exchange of larger ligands by smaller ones is the decrease of colloidal stability often leading to nanoparticle aggregation. To address this issue, the ligands exchange can be applied not to solution of NCs, but to a film or a superlattice. This approach benefits from convenient fabrication of high-quality NC films using colloidal solutions stabilized by original ligands followed by soaking the NC film in a solution containing new capping ligands. Typical examples include treatment of CdSe or PbSe NCs with various short-chain molecules such as methylamine, ethylamine, butylamine, ethanethiol, sodium hydroxide, pyridine, or hydrazine.[23,25,293−296] This approach is also very useful for NC cross-linking using molecules with two functional end groups such as diamines or dithiols (see section 4.2). Such treatments significantly decrease the interparticle spacings and improve electronic transport in NC

solids crucial for applications in electronic, photoconductive, and photovoltaic devices.

The problem of poor colloidal stability with small-molecule ligands can be also addressed by using electrostatically stabilized nanoparticle colloids in polar solvents. For example, the surface of II−VI semiconductor NCs can be capped with small molecules containing both thiol group (attached to NC surface) and a charged group (e.g., $R-COO^-$ or $R-NH_3^+$).[96] These charges create repulsive forces between NCs, preventing their aggregation. Unfortunately, relatively little attention has been paid so far to this promising approach. In a few successful examples, Gao et al. studied light-emitting devices based on CdTe NCs capped with thioglycolic acid,[297] and Kim et al. used 1-thioglycerol-capped HgTe NCs for making field-effect transistors.[298]

The inter-NC charge transport can be improved not only by introducing shorter or linking molecules, but also by using capping molecules that can support charge transport. Thus, ligand coatings based on conductive conjugated polymers and oligomers such as end-functional polythiophenes[299] or derivatives of poly(*para-n*-phenylene vinylene)[300] were applied to improve charge transport and film morphologies for solar cells and light-emitting devices.

The use of specially designed degradable ligands is another promising strategy. This direction is largely underexplored and, so far, is probably limited to a single report by Voitekhovich et al.,[301] who studied CdS NCs capped with 1-substituted 5-thiotetrazoles. Tetrazoles are the five-membered heterocyclic compounds containing four nitrogen atoms in the cycle and having the highest content of nitrogen among all organic substances (for example, 82.3 wt % for 5-aminotetrazole). Tetrazoles can thermally decompose at relatively low temperatures (400−500 K) with formation of only gaseous products. For example, CdS NCs capped with 5-aminotetrazole could be successfully sintered into a continuous film at temperatures as low as 230 °C.[302]

A different approach to remove strongly surface-bound ligands such as alkylphosphonic acids has been recently proposed by Owen et al.[278] Ligands were cleaved from the surface of CdSe NCs by using reagents with reactive silicon−chalcogenide and silicon−chloride bonds. In the latter case, the resulting NCs are terminated with chloride ions instead of long hydrocarbon chains. Still, these NCs can form stable colloidal solutions in toluene in the presence of tridecylammonium chloride.

4.2. Cross-Linking Surface Ligands

Cross-linking of NCs using bifunctional ligands provides another approach to reduce the interparticle separation, strengthen electronic coupling between NCs, or attach them to electrodes or surfaces. Guyot-Sionnest and co-workers demonstrated a considerable improvement of charge transport in CdSe NC solids by cross-linking individual particles with various aliphatic and aromatic diamines.[185] By treating highly insulating TOP/TOPO capped CdSe NCs ($\sigma \approx 10^{-14}$ S cm^{-1}) with 1,7-heptanediamine, the conductivity increased by a factor of 10, and another 1000-fold improvement was obtained using 1,4-phenylenediamine. With additional electrochemical filling of $1S_e$ states, the conductivity of $\sim 6 \times 10^{-3}$ S cm^{-1} was achieved.[185]

In 1995, Brust and co-workers showed that Au NCs can be cross-linked by short-chain dithiols, simply by adding linker into toluene solutions of alkylammonium-stabilized NCs.[303] Instantly, this leads to the precipitation of the NCs. Authors prepared pellets from dried precipitates and studied their electrical properties. Reasonable conductivity of $\sim 10^{-2}$ S cm^{-1} was shown using *p*-xylylenedithiol as the linking unit. Using essentially the same approach, Müller et al.[304] studied the conductivity of Au NCs linked with α,ω-alkanedithiol ($HS(CH_2)_nSH$ with $n = 2-15$) and found that the conductivity could be described in terms of percolation theory considering the network of varying tunneling separations between adjacent NCs. Zabet-Khosousi et al. observed a metal to insulator transition in arrays of 5 nm Au NCs linked with dithiol $HS(CH_2)_nSH$ molecules at $n = 5$.[260]

Katari and Alivisatos demonstrated that a uniformly covered and dense monolayer of CdSe NCs can be obtained by linking NCs to Au substrate by 1,6-hexanedithiol molecules.[281] Since then, hexanedithiol linking is routinely used in sample preparation for STM and STS studies of NCs.[305] Deposition of multiple, cross-linked NC layers is a powerful tool to make functional NC solids. In such process, the substrate is repeatedly dipped into NC solution to absorb NC monolayer and into linker solution to functionalize the outmost NC layer. This approach was first demonstrated by Brust and co-workers using Au NCs and $HS(CH_2)_nSH$ ($n = 6-12$) as a linker.[306] Cross-linking with short-chain dithiols has been also demonstrated to improve the photoconductive properties of PbS and PbSe NC solids.[253,271,307]

4.3. Metal Chalcogenide Complexes as Surface Ligands

The original long-chain organic ligands can be replaced by soluble molecular metal chalcogenide complexes (MCCs) such as Zintl ions (e.g., SnS_4^{4-}, $Sn_2Se_6^{4-}$, $In_2Se_4^{2-}$, $Ge_4S_{10}^{4-}$) and one-dimensional metal chalcogenide chains solvated by hydrazinium cations and/or neutral hydrazine molecules (e.g., $(N_2H_4)_2ZnTe$).[273] MCCs are known as convenient precursors for solution-processed semiconductor thin films[308] and mesoporous frameworks.[309−311] A simple general route to various MCC compounds involves dissolution of bulk metal chalcogenides along with excessive chalcogen in hydrazine.[308,312,313] MCC-capped NCs can be obtained by simple ligand exchange and dispersed in polar solvents like hydrazine, dimethylsulfoxide, ethanolamine, or water (Figure 15a and d). The nearly complete removal of the initial organic ligands has been confirmed by FTIR spectra and by elemental analysis. A very diverse range of NC-MCC combinations is accessible due to the generally strong affinity of undercoordinated surface metal atoms to strongly nucleophilic chalcogenides, as illustrated by Figures 15b and 15c. MCCs appear to be very good stabilizers as they can solubilize NCs of virtually any size and shape, from small Au clusters to micrometers-large CdSe nanowires. Solutions of MCC-capped NCs form stable colloidal solutions in polar solvents due to significant negative surface charge arising from surface-bound MCCs.[273] Good electronic passivation of surface dangling bond by MCC ligands is evidenced by good luminescence properties of colloidal NCs (Figure 15e).

Another attractive feature of MCCs is their facile thermal decomposition to metal chalcogenides, which not only further decreases the interparticle spacing, but also creates a layer of conductive "glue" between the NCs. For instance, $(N_2H_5)_4Sn_2S_6$ is decomposed at 180 °C according to the reaction:[308]

$$(N_2H_5)_4Sn_2S_6 \rightarrow 2SnS_2 + N_2H_4 + H_2S \qquad (9)$$

As a result, a high-mobility SnS_2 compound is formed around the NCs. In this case, the surface ligands act not only as a tunable spacer and potential barrier between NC, but participate in the charge transport. For example, field-effect transistors have been assembled from 5 nm CdSe NCs stabilized with 5 wt % of $(N_2H_5)_4Sn_2S_6$, annealed at 200 °C.[273] A similar approach based on MCC ligands can be used to integrate colloidal NCs into different metal chalcogenide matrices such as In_2Se_3, In_2Te_3, Ga_2Se_3, HgSe, ZnTe, Bi_2Te_3, and $CuIn_xGa_{1-x}Se_2$. Combined with the diversity of properly engineered colloidal NCs, we expect a rapid development of many novel all-inorganic nanocomposites for electronic, photovoltaic, and thermoelectric applications.

5. Transport in Nanocrystal Solids

Generally speaking, the NC solids represent a class of artificial materials composed of close-packed metal or semiconductor particles embedded into an insulating matrix. The particles should be large enough to possess distinct electronic structure, but sufficiently small to exhibit effects of quantized electronic levels of confined electrons.[314] Such systems combine properties of individual NCs and collective properties of a coupled NC array. Electronic properties of granular materials have been extensively studied both theoretically and experimentally for several decades. The important pieces of theoretical framework were put together by Mott,[315] Efros and Shklovskii,[316] Altshuler,[317] and others. However, early theories could be tested only on highly disordered systems with large spread in grain size, available to experimentalists at those times. It is relatively recently that developments in particle synthesis and assembly techniques enabled ordered 1D, 2D, and 3D arrays of uniform metal or semiconductor NCs (see section 3). Several recent reviews provided a detailed background of physical concepts related to transport phenomena in granular electronic materials and nanoparticle assemblies.[267,318] For example, Zabet-Khosousi and Dhirani[267] provided a comprehensive overview of charge transport in arrays of metal NCs; Beloborodov et al.[314] presented deep theoretical analysis of granular metals in normal and superconducting states. In this section, we briefly overview the fundamental aspects of transport phenomena in NC solids, emphasizing the topics not covered in the above-mentioned articles.

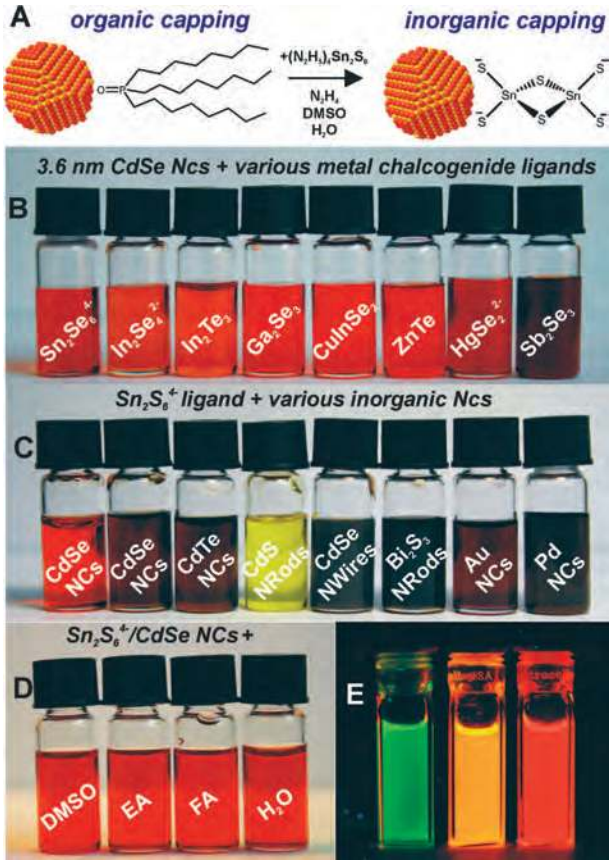

Figure 15. (A) A sketch of a generic exchange of original organic ligands by metal chalcogenide complexes: the original organic ligands (TOPO) at the surface of CdSe NC are replaced by $Sn_2S_6^{4-}$ Zintl ions. (B) Stable colloidal solutions of 3.6 nm CdSe NCs capped with various metal chalcogenide complexes in hydrazine. (C) From left to right: stable colloidal solutions obtained by combining $(N_2H_5)_4Sn_2S_6$ with 3.6 and 5.8 nm CdSe NCs, 9 nm CdTe NCs, 5 × 60 nm CdS nanorods (NRods), CdSe nanowires (NWires, ~25 nm wide, 2−5 μm long), 6 × 25 nm Bi_2S_3 NRods, 5 nm Au NCs, and 3 nm Pd NCs. (D) From left to right: CdSe/$Sn_2S_6^{4-}$ NCs dispersed in dimethylsulfoxide, ethanolamine, formamide, and water. (E) Photograph of NC photoluminescence excited by a UV lamp. From left to right: 2.9 nm CdSe/$Sn_2S_6^{4-}$ NCs in EA (green emission, quantum yield QY ≈ 2%), 3.6 nm CdSe/$Sn_2S_6^{4-}$ in DMSO (yellow emission, QY ≈ 3%), and $Sn_2S_6^{4-}$-capped CdSe/CdS core−shell NRods in hydrazine (red emission, QY = 10%). Reprinted with permission from ref 273. Copyright 2009 American Association for Advancement of Science.

5.1. Exchange Coupling Energy

In close-packed films and superlattices, the NCs are separated by surfactant molecules that play a dominant role in electrical transport. To travel between the NCs, the charge carriers should transfer through the interparticle medium. Commonly used surfactant molecules with long hydrocarbon chains behave as dielectric tunneling barriers. In the regime of weak coupling, the electronic structure of individual sub-10 nm metallic or semiconductor NC can be described by discrete quantum confined wave functions localized on individual particles[3,318] When two or more metallic or semiconducting nanoparticles find themselves in close proximity to each other, these wave functions can interact (couple), forming "molecular orbitals" delocalized over several NCs or even propagating throughout the entire array of NCs. The quantum mechanical coupling between the energy levels can be expressed in terms of the coupling energy $\beta \approx h\Gamma$, where h is Planck's constant and Γ is the tunneling rate between two orbitals of NC neighbors.[319,320] The tunneling rate can be approximated as[267,320]

$$\Gamma \approx \exp\{-2(2m^*\Delta E/\hbar^2)^{1/2}\Delta x\} \qquad (10)$$

where m^* is the electron effective mass, and ΔE and Δx are the height of tunneling barrier and the shortest edge-to-edge distance between the NCs, respectively.[38,39] As one can see, the tunneling rate drops exponentially with increasing separation between the NCs and somewhat weaker depends on the barrier height and the carrier effective mass. Reducing Δx and ΔE by proper design of the interparticle medium or introducing conjugated molecular linkers are powerful tools for increasing the strength of electronic coupling between the NCs.[23,185] For example, the conductivity (σ) of the films of 2.2 nm Au NCs cross-linked with $HS(CH_2)_nSH$ molecules scales as $\sigma \approx \exp(-\kappa n)$, where κ is the decay constant,[321,322] showing strong dependence of the transport properties on the width of the tunneling barrier (interparticle separation).

5.2. Charging Energy

In addition to the coupling energy, there are two other important contributors to electronic structure and transport properties of NC solids: Coulombic charging energy (E_c) and disorder in site energies (typically expressed as $\Delta\alpha$). Coulombic charging energy E_c is the energy cost that has to be paid to put an additional electron on the NC.[314,318,319] It is also referred to as the self-capacitance of individual NCs. In its simplest form, charging energy is inversely related to the NC radius (r) and static dielectric constant of the surrounding medium (ε_m):

$$E_c = e^2/(4\pi\varepsilon_m\varepsilon_0 r) \quad (11)$$

where ε_0 is the permittivity of vacuum and e is the fundamental unit of charge. For individual NCs, E_c can be determined by scanning tunneling spectroscopy measurements: $E_c = 0.34$ eV has been measured for 3 nm diameter silver NCs.[323] Under all circumstances, E_c acts against the facile migration of carriers from one NC to another. For example, E_c must be paid twice to move a single electron from one isolated metal NC to another in the following process:

$$NC + NC \rightarrow NC^+ + NC^- \quad (12)$$

In an array of weakly coupled NCs, the charging energy creates the Coulomb energy gap (also often called the Hubbard gap) $E \approx 2E_c$, which suppresses low-bias conduction in the effect known as the Coulomb blockade[314,318] (Figure 16). At sufficiently large applied bias voltage $V > V_t$, the Coulomb blockade is overcome, and current can flow through the NC solid (Figure 17). V_t is a global Coulomb threshold voltage that depends on E_c, the number of nanoparticles spanning the gap between the electrodes, temperature, NC packing symmetry, and several other parameters.[324]

The delocalized states can exist only if $\beta \geq k_BT$ (so-called strong coupling regime). If the coupling energy is smaller than the thermal energy ($\beta \ll k_BT$), there is only weak coupling between the NCs, and the electron transport can occur by sequential tunneling between the neighboring particles.[318,319] In an array of strongly coupled metallic NCs,

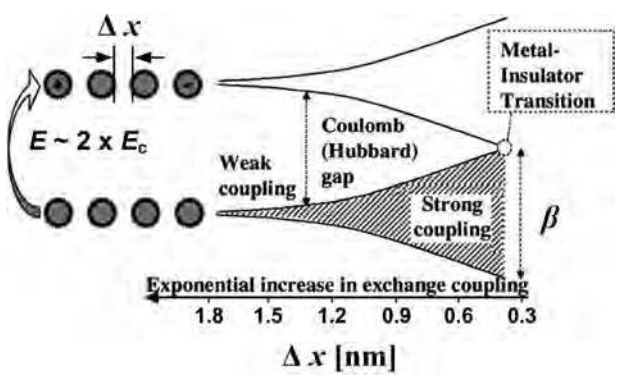

Figure 16. Electronic structure and interparticle interactions in a nanocrystal solid. At large interparticle distance Δx, the nanocrystals are electrically isolated, and the nanocrystal solid is an insulator with a Coulomb gap. As the interparticle distance decreases, exchange interactions become significant, and the electronic wave functions of the individual nanocrystals spread out over multiple particles. At the point of metal−insulator transition, the delocalized orbitals extend over the entire nanocrystal solid. Adopted with permission from ref 39. Copyright 2000 Annual Reviews.

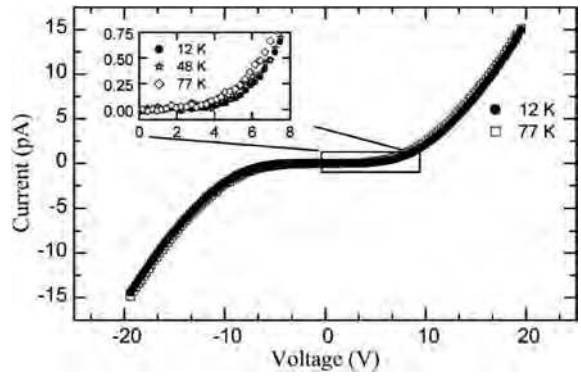

Figure 17. Charge transport through an array of metal nanocrystals in the regime of weak coupling. $I-V$ curve for a two-dimensional layer of 5.5 nm Au nanoparticles separated by ~1.7 nm of insulating dodecanethiol ligands. At low bias, conduction is suppressed by the Coulomb blockade. Reprinted with permission from ref 325. Copyright 2001 American Institute of Physics.

the discrete wave functions form a band with width proportional to the exchange coupling energy β. When the interparticle spacing decreases, the bandwidth increases as shown in Figure 16. If $\beta > E_c$, the Coulomb gap disappears, and carriers can move freely throughout the NC solid. This sudden change in behavior is known as the Mott metal–insulator transition (MIT).[315,318] Above the transition point, the coherent molecular-type orbitals extend over many NCs in analogy to an ordinary crystal. The onset of electronic delocalization is observed by dramatic changes in the optical and electronic properties of the metal NC solids.[261,326]

Heath et al. studied charge transport in monolayers of alkylthiol-capped silver NCs using a Langmuir trough to tune the coupling energy by adjusting interparticle distances. Specifically, they studied MIT in a two-dimensional array of 3 nm Ag NCs capped with propanethiol.[261] When the interparticle spacing was reduced below ~5 Å, the sharp discontinuity of the optical second-harmonic generation response, as well as the changes in the reflectance of NC film, manifested the insulator-to-metal transition. On the metallic side of this phase transition, the absorbance and reflectance of NC film resembled those of a thin continuous metal film supporting delocalization of carriers over many NCs.[261,326]

Ligand-tailored MIT in metallic NC assemblies has long been an important research subject. Zabet-Khosousi et al. studied the transport properties of disordered films of 5 nm Au NCs molecularly linked by $HS(CH_2)_nSH$ ($n = 2-10$) and observed MIT at $n = 5$.[260] At the transition point, the conductivity of the NC solid jumped by more than 2 orders of magnitude, and the temperature coefficient of resistance (TCR = dR/dT) changed its sign from positive for $n < 4$ to negative for $n > 5$ (Figure 18). Metals and insulators are known generally to exhibit positive and negative TCR, respectively. The same authors proposed a model predicting that the Mott−Habbard-type insulator-to-metal transition in Au NC arrays should be observed when the interparticle spacing approaches 1.1 nm.[260]

The capping of NC surfaces with Zintl ions and other metal chalcogenide complexes (see section 4.3) can significantly improve the electronic properties of NC solids, as compared to materials capped by organic ligands. For the case of 5 nm Au NCs (Figure 19), the replacement of original dodecanethiol molecules by $Sn_2S_6^{4-}$ molecules decreased the separation between NCs from ~2 to ~0.5 nm (Figure

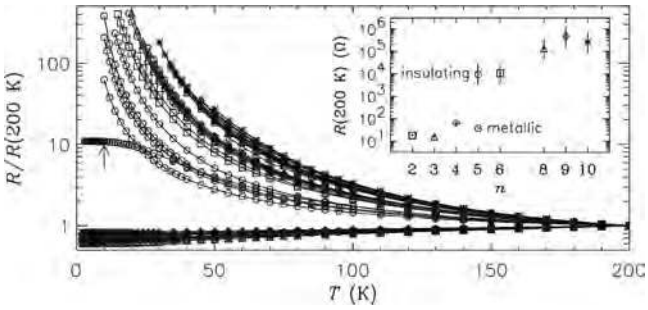

Figure 18. Low-temperature resistance (R) of a layer of 5 nm Au NCs linked by $HS(CH_2)_nSH$ molecules with various n. The resistances are normalized to their respective values at 200 K. Inset: R of the samples at 200 K as a function of n. Reprinted with permission from ref 260. Copyright 2006 American Institute of Physics.

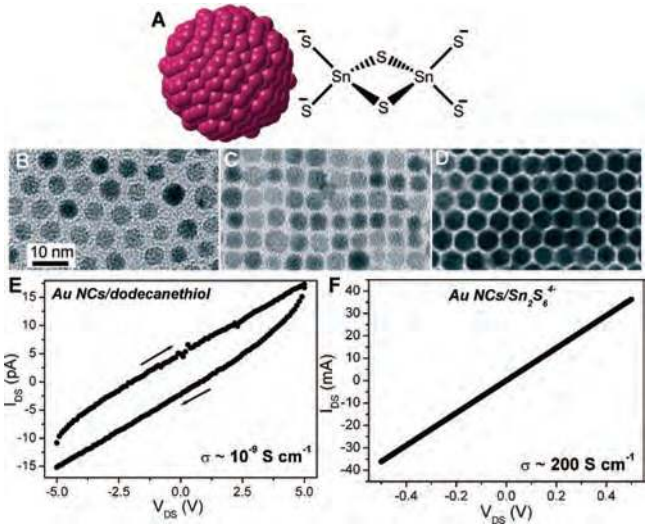

Figure 19. Conductivity of 5 nm Au nanocrystals stabilized by $Sn_2S_6^{4-}$. (A) Sketch of Au nanocrystal capped with $Sn_2S_6^{4-}$ ions. (B) TEM image of Au nanocrystals capped with dodecanethiol. (C,D) TEM images of 2D and 3D superlattices formed by Au nanocrystals capped with $Sn_2S_6^{4-}$. (E) $I-V$ scan for ~200 nm thick film of dodecanethiol-capped Au nanocrystals. (F) $I-V$ scan for ~200 nm thick films of Au nanocrystals stabilized with $Sn_2S_6^{4-}$. Adapted with permission from ref 273. Copyright 2009 American Association for Advancement of Science.

19b−d). Correspondingly, the electrical conductivity increased by ~11 orders of magnitude, and the material converted from highly insulating (Figure 19e) to metallic[273] (Figure 19f). In the case of CdSe NCs capped by $Sn_2S_6^{4-}$ ions, the delocalization of electron and hole wave functions manifested itself through the red shift of excitonic transitions in the optical absorption spectra.

5.3. Effects of Electronic and Structural Disorder

Disorder ($\Delta\alpha$) is the other key player in the electronic properties of NC solids. Because the NCs are not atomically defined objects, there is always a finite dispersion in their size and shape. Advanced synthetic techniques allow for dispersion within a single atomic layer,[30,326] which still leads to a standard deviation of several percent. Size distribution results in the finite dispersion of the orbital energies (α) of individual particles. The energies of occupied and unoccupied states in semiconductor quantum dots, scale approximately as $1/r^2$,[318,319] leading to $\Delta\alpha/\alpha \approx 2\Delta r/r$ dispersion in site energies due to quantum confinement. Electron transfer between two NCs is the most efficient when their energies

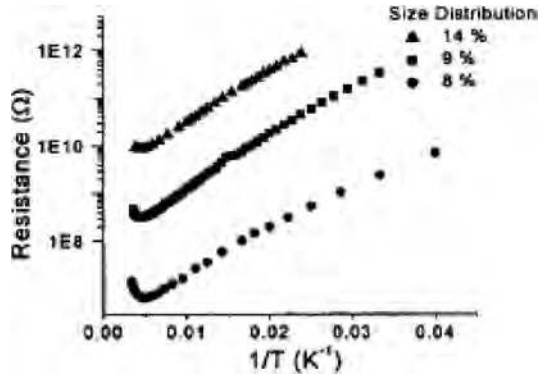

Figure 20. The temperature dependence of the experimentally determined low-bias resistance for 7 nm Ag nanoparticle monolayer films with different amount of disorder originating from the particle size distribution. Reprinted with permission from ref 328. Copyright 2002 American Association for Advancement of Science.

are equal (the conditions of resonant tunneling); otherwise, phonons have to be absorbed or emitted during the transition. The transition rate drops quickly with increasing disorder,[320,327,328] pointing to the importance of narrow size and shape distribution of individual NCs. The interplay of exchange coupling energy β and disorder $\Delta\alpha$ defines an important type of metal−insulator transition called Anderson localization.[315,319] If β is larger than $\Delta\alpha$, the coupling is sufficiently strong to overcome the dispersion in the energy levels of the individual NCs, and extended wave functions still can exist. In the opposite case, the system breaks into small isolated regions where strong coupling prevails, separated by weakly conducting regions. Heath et al. observed a dramatic effect of size distribution on charge transport in arrays of Ag NCs; the conductivity of the NC monolayers changed over several orders of magnitude upon rather small change of $\Delta\alpha$ as shown in Figure 20.

Another type of disorder very typical for NC solids is the disorder in NC packing that leads to variation of spacing between neighboring NCs. Here, long-range ordered NC assemblies can have significant advantage over disordered glassy films. Remacle and Levine[318] and Beloborodov et al.[314] presented a detailed theoretical framework for the interplay of $\Delta\alpha$, β, and E_c and their effect on the transport characteristics of NC solids; an outline of the trends is schematically shown in Figure 21.

5.4. Conduction Mechanisms: Hopping, VRH, ES-VRH, Cotunneling, Bloch Transport

Important information on the mechanism of charge transport can be obtained from the effect of temperature on conductivity (G) of NC solids. Typical temperature dependences for conductivity of monolayer thick films of metal NCs are shown in Figure 20. At high temperatures (>200 K), close-packed layers of monodisperse metal NC can exhibit an increase in resistance with increasing temperature, the behavior typical for metals.[328] At lower temperatures, the carriers are localized on individual NCs and transport occurs by sequential tunneling; the electron hops from a particle to its nearest neighbor along the current path. Arrhenius type temperature dependence of conductivity $\log(G) \sim 1/T$ is characteristic of this transport regime. At even lower temperatures, below ~60 K the conductivity of Au and Ag NC layers scales as $\log(G) \sim 1/T^{1/2}$.[328,329] Tran et al. explained such behavior by inelastic cotunneling transport mechanism dominated by cooperative, multielectron hops

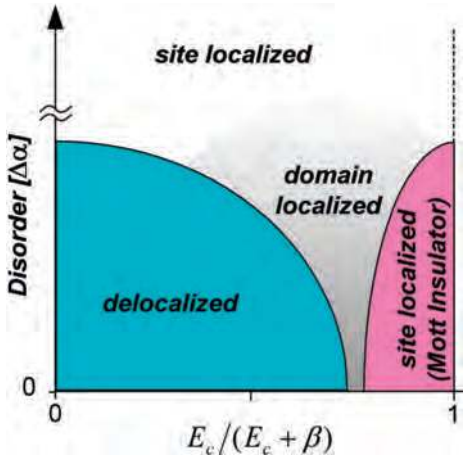

Figure 21. A phase diagram showing different coupling regimes for an array of nanocrystals with size and/or packing disorder. The x-axis is the dimensionless parameter $E_c/(E_c + \beta)$, where β and E_c are the exchange coupling energy and Coulombic charging energy, respectively. For very large disorder, the electronic states are localized on individual nanocrystals (site localized). Reducing the disorder allows for the interparticle couplings. At very small disorder, Coulombic effects dominate with a Mott-like transition from a delocalized to a site-localized state. The fully delocalized and fully localized states are separated by the regions where the nanocrystal wave functions delocalize over small domains. Adopted with permission from ref 318. Copyright 2001 Wiley.

that each go to the nearest neighbor but are synchronized to move charge over distances of several particles.[329]

The conduction mechanism in semiconductor NC solids strongly depends on the strength of interparticle coupling. Bulky capping ligands typically result in the activated nearest-neighbor hopping observed for several materials at near-room temperatures.[330] Other mechanisms, including variable range hopping (VRH) with the Coulomb energy gap (so-called Efros−Shklovskii variable range hopping, ES-VRH),[331] have been recently proposed to explain non-Arrhenius behavior observed in doped semiconductor NC solids. In VRH, the hopping probability at a given temperature depends on two parameters: the spatial separation of the sites and their energy separation. A hopping electron finds an optimal path with the lowest activation energy and the shortest hopping distance. At low temperatures, the most favorable hops may not be neighboring ones, leading to temperature dependencies of $\log(G) \sim 1/T^{\nu}$, where ν depends on dimensionality and Coulombic interactions in the NC solid.[315] Guyot-Sionnest et al. observed $\nu = 1/2$ for CdSe NCs cross-linked with 1,4-phenylenediamine molecules.[331] Such temperature dependence is typical for ES-VRH transport mechanism, which was also supported by low-temperature magnetoresistance measurements.[332] More detailed information on different charge transport mechanisms in metal NC solids can be found in ref 314.

The ultimate goal in designing functional NC solids for electronic applications is to achieve bulk type carrier transport through the minibands formed due to strong interparticle coupling. In the miniband transport regime, one can expect much higher carrier mobility than in the hopping regime.[241] Jiang and Green theoretically estimated Bloch carrier mobility in Si quantum dot crystals with simple cubic packing symmetry for three different dielectric matrices.[238] They calculated idealized Bloch mobility as

$$\mu = e\tau/m^*_{\mathrm{QDS}} \tag{13}$$

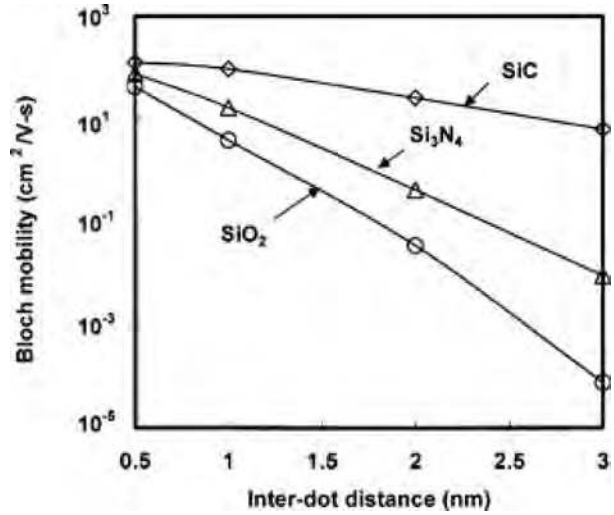

Figure 22. The effect of interparticle distance on Bloch electron mobility. The Si NC size is $2 \times 2 \times 2$ nm^3. The barrier heights for silicon dioxide, silicon nitride, and silicon carbide are 3.17, 1.9, and 0.5 eV, respectively, with the reference energy taken from the conduction band edge of silicon. Reprinted with permission from ref 238. Copyright 2006 American Institute of Physics.

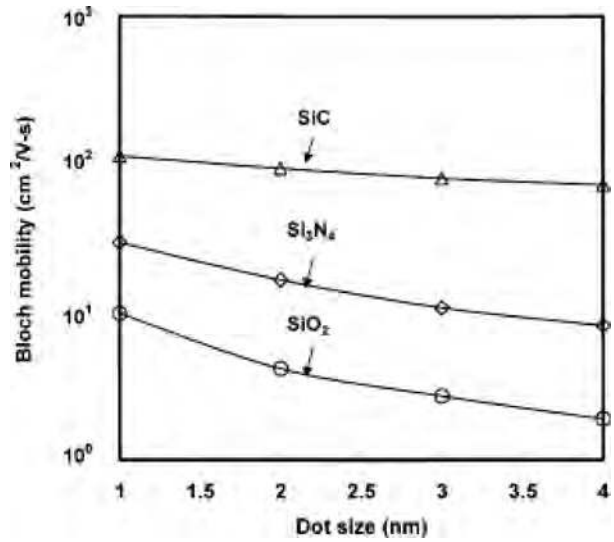

Figure 23. The effect of Si NC size on Bloch electron mobility. The dielectric parameters are the same as in Figure 22. The interparticle distance is 1 nm in all directions. Reprinted with permission from ref 238. Copyright 2006 American Institute of Physics.

where τ is the carrier scattering time and m^*_{QDS} is the electron effective mass in the quantum dot superlattice calculated from the dispersion relation (Figure 13).[238] Figures 22 and 23 illustrate calculated Bloch mobility for different interparticle distances and NC sizes, respectively. The dielectric material parameters are the same as the ones used in Figure 14. In Figure 22, the size of Si NC is $2 \times 2 \times 2$ nm^3 for all three matrices (SiC, Si_3N_4, and SiO_2). In Figure 23, the interparticle distances in all directions are 1 nm for the three dielectric matrices. From these results, it is clear that the NC size has only a minor effect on the carrier mobility, while the interdot distance changes the mobility by several orders of magnitude. For carriers to have a useful mobility, the required interparticle distance has to be in the subnanometer range.

5.5. Magnetic Nanocrystals: Spin-Dependent Transport, Magnetoresistance

Many magnetic materials including ferromagnetic Fe, Co, Ni, FePt, $CoPt_3$, γ-Fe_2O_3, ferrimagnetic Fe_3O_4, and antiferromagnetic CoO have been recently synthesized in the form of monodisperse colloidal NCs[4,29,45,99,333] (Figure 24a,b). In these materials, electron spins on different atoms align in parallel over large regions called magnetic domains. Magnetic NCs typically have single-domain structure where all spins align in one directional and flip simultaneously following external magnetic field.[4] At room temperature and in the absence of external fields, most sub-10 nm magnetic NCs show superparamagnetic behavior; thermal energy is sufficient to flip and randomize magnetization directions of different particles,[4,99] as shown in Figure 24c. This makes NCs different from bulk magnets where the magnetization direction is pinned to a certain crystallographic orientation, the easy axis of magnetization. External magnetic field aligns the NC magnetic moments as shown in Figure 24d. Such alignment is most favorable for electron transport. The tunneling rate, Γ, between two magnetic NCs separated by an insulator can be expressed as

$$\Gamma = \Gamma_0(1 + P^2 \cos \theta) \tag{14}$$

where Γ_0 is the spin-independent tunneling rate, θ is the angle between the magnetic moments of two particles, and P is the electronic spin polarization of the material.[334] More explicitly,

$$P = (D_\uparrow - D_\downarrow)/(D_\uparrow + D_\downarrow) \tag{15}$$

where $D_\uparrow$ and $D_\downarrow$ are the densities of electronic states at the Fermi energy for electrons with opposite spins. The difference in resistance between parallel ($\theta = 0$) and antiparallel ($\theta = \pi$) configurations is

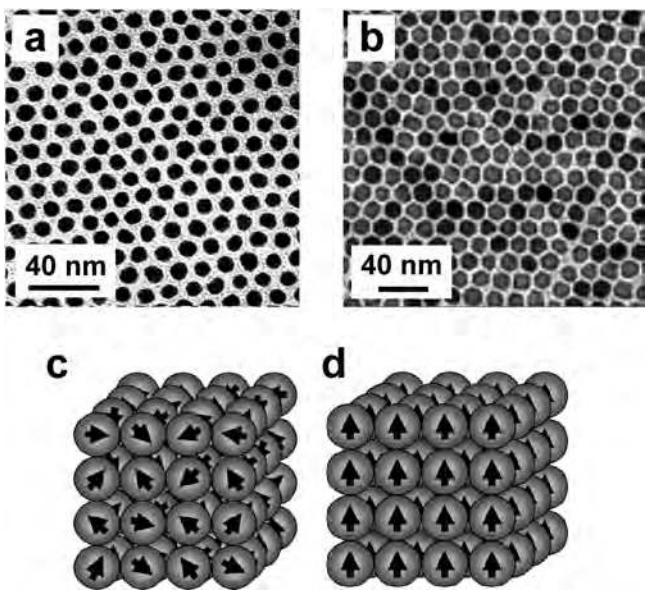

Figure 24. (a,b) Arrays of Co and Fe_3O_4 nanocrystals, respectively. (c) A superlattice of superparamagnetic nanocrystals in zero magnetic field. The magnetic moments of individual nanocrystals are randomly oriented. (d) External magnetic field aligns the magnetic moments of nanocrystals. (a) Reprinted with permission from ref 335. Copyright 2000 American Association for Advancement of Science. (b) Reprinted with permission from ref 336. Copyright 2002 American Chemical Society. (c,d) Adopted with permission from ref 337. Copyright 2007 American Institute of Physics.

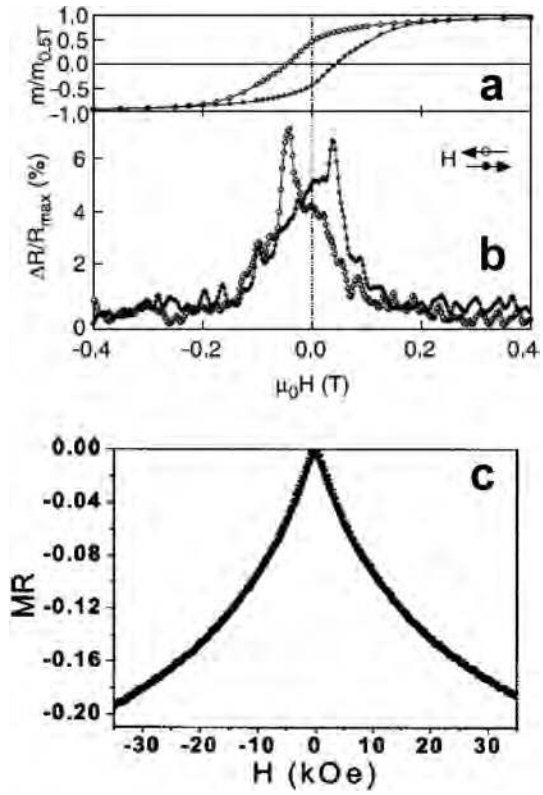

Figure 25. Spin-dependent transport in assemblies of magnetic nanoparticles. (a) Magnetization hysteresis loop for a film of 10 nm cobalt nanocrystals at 5 K. (b) Magnetoresistance of cobalt nanocrystal film at 2 K. Reprinted with permission from ref 335. Copyright 2000 American Association for Advancement of Science. (c) Magnetoresistance of self-assembled superlattice of 6 nm Fe_3O_4 nanocrystals measured at 100 K as a function of the applied magnetic field. Reprinted with permission from ref 341. Copyright 2006 American Institute of Physics.

$$\Delta R/R_{max} = 2P^2/(1 + P^2) \tag{16}$$

For a more realistic case of disordered magnetic moments, θ takes a random value between 0 and π. The maximum $\Delta R/R_{max}$ is then given by

$$\Delta R/R_{max} = P^2/(1 + P^2) \tag{17}$$

The parameter $\Delta R/R_0$ where R_0 is the resistance at zero field is called magnetoresistance (MR) and commonly used to characterize the electric response of a material to external magnetic field. For bulk elemental magnetic materials such as Ni, Co, and Fe, the measured electron spin polarizations P are 0.11, 0.34, and 0.44,[338] leading to MR values of 1.2%, 10%, and 16%, respectively. In agreement with these predictions, Black et al. found that at low temperatures ($T = 2$ K), the resistance of an array of 10 nm Co NCs separated by 1 nm thick organic surfactant layers dropped by 8−12% when 0.4 T magnetic field (H) was applied in the plane of the NC superlattice[335] (Figure 25a,b). Below the blocking temperature, magnetization of Co NCs is hysteretic,[99] resulting in the hysteresis in MR (Figure 25a,b). The device resistance increases as H is lowered from saturation through ~0.1 T, and NC magnetic moments begin to randomize. After H passes through zero, the resistance reaches a maximum near the coercive field (H_c) when the NC moments

are maximally disordered. For fields beyond H_c, the resistance again decreases to the initial value[335] (Figure 25b). With increasing temperature above 2 K, MR decreases rapidly due to spin-flip scattering, down to ~10% of its maximum value at 20 K. At very low temperatures, the cotunneling processes can result in significant enhancement of MR.[339]

Larger values of MR can be achieved with the class of materials called half-metals. A half-metal is characterized by the presence of an energy gap at the Fermi level for only one electron spin direction, while the energy band for the opposite spin direction is continuous.[340] Such band structure leads to $P = 1$ and theoretical $\Delta R/R_{max}$ values of 100% and 50% for antiparallel and random spin orientations at $H = 0$, correspondingly. Magnetite Fe_3O_4 is the example of a half-metal. Recently, Zeng et al. reported appreciable 20−35% MR values at $T = 60$ K for a superlattice of 6 nm diameter Fe_3O_4 NCs.[341](Figure 25c). At room temperature, MR of Fe_3O_4 NC solids remained as large as 12%. For comparison, room temperature MR of magnetite thin films does not exceed a few percent.[341]

The presence of a very large number of tunneling junctions in a weakly coupled NC solid has several advantageous effects on spin-dependent electronic transport. Because current through the NC array is carried by multiple parallel conduction paths containing different numbers of NCs, the device MR should be less sensitive to applied bias voltage.[342] Indeed, both Co and Fe_3O_4 NC solids demonstrated weak dependence of magnetoresistance on the applied voltage, in contrast to thin film devices that often show steep reduction in MR with increasing bias.[334,341] This advantage may help NC arrays to find use in magnetic recording heads and nonvolatile magnetoresistive random access memory (MRAM) applications.[343] However, further developments in understanding and improving spin-dependent electronic properties are necessary to successfully compete with more mature technologies based on vacuum-deposited thin films and heterostructures. The possibility of combining magnetic NCs with other materials, for example, semiconductor quantum dots in form of multicomponent nanostructures (Figure 6) or binary superlattices (Figure 11), may lead to interesting multifunctional electronic materials.

5.6. Semiconductor Nanocrystals: Electronic Structure and Shell Filling

Semiconductor NCs represent probably the most interesting and important class of inorganic solution processed electronic materials. They have a real chance to find use in the next generations of large area solar cells and light-emitting devices. Fundamental understanding of charge transport is also crucial for developments of NC-based electrically pumped lasers, low-dimensional thermoelectric materials,[254] photodetectors,[265,294] and many other technologies.

The electronic structure of semiconductor NCs is dictated by strong quantum confinement, which gives rise to discrete electron and hole states called quantum confined orbitals (Figure 26a). Their energies are directly related to the NC size and shape.[3,39] In a spherical NC, the quantum confinement leads to the series of electron and hole states with S, P, D, and F symmetries identical to the energy levels of a hydrogen atom (Figure 26b). The electron and hole states will be further labeled with "e" and "h" indexes, respectively. The symmetry of NC atomic lattice determines the degeneracy of the quantum confined states. Thus, NCs with wurtzite and zinc blend lattices

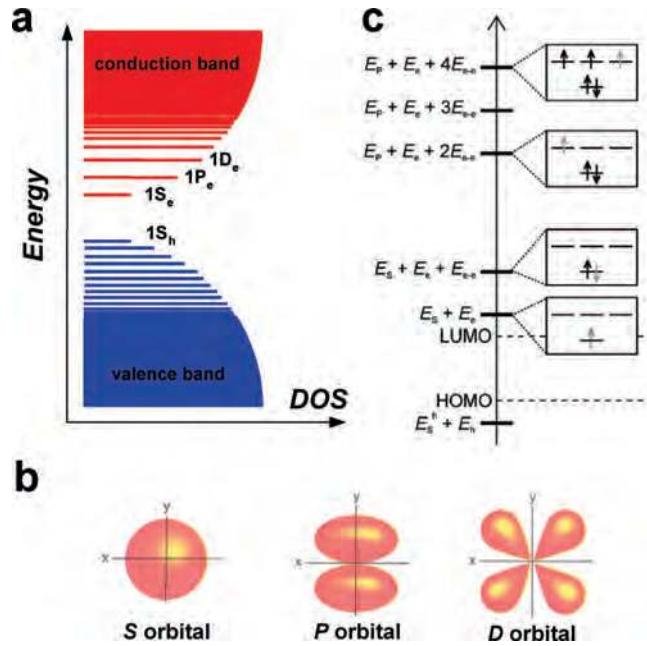

Figure 26. (a) Size-dependent electronic structure of individual semiconductor nanocrystal. Because of strong quantum confinement, the continuum of electronic states in the valence and conduction bands collapses into a set of discrete states corresponding to the atomic-like S, P, and D orbitals shown in (b). (c) The electrochemical potentials for sequential additions of electrons (indicated in gray) to a typical semiconducotor nanocrystal. The first and second electron is added to the S orbitals, the third to eighth electron to the P orbitals. The Coulombic charging energy lifts degeneracy of S and P states. Adopted with permission from ref 319. Copyright Royal Chemical Society.

typical for most II−VI and III−V semiconductors have 2-, 6-, and 10-fold degenerated $1S_e$, $1P_e$, and $1D_e$ states, respectively,[3] whereas PbS, PbSe, and PbTe NCs with rock salt lattices have 4 times higher degeneracy and can accommodate up to eight electrons on their $1S_e$ and $1S_h$ states.[344] In a neutral NC, the highest occupied ($1S_h$) and lowest unoccupied ($1S_e$) states are separated by the forbidden energy gap that is much larger than k_BT (~25 meV at 300 K), and electrons cannot be thermally excited into $1S_e$ state. Semiconductor NCs do not contain conduction electrons and holes in the neutral ground state, and additional carriers should be added or generated by, for example, photoexcitation to make the NCs solid conductive.

The conductivity of a NC solid depends on the number of conduction electrons or holes per NC and their mobility, which in turn is determined by the tunneling rate discussed above. In strongly confined NCs, the gaps between S, P, and D states exceed thermal energy, and additional carriers sequentially occupy the quantum confined states following the Pauli principle[319,320] as shown in Figure 26c. Banin et al. directly observed sequential filling of the quantum confined states in NC quantum dots using scanning tunneling spectroscopy.[345] Addition of each electron to the NC costs Coulombic charging energy (E_c) and the energy of electrostatic repulsion between the incoming electron and the additional electrons already present in the NC (E_{e-e}). These terms lift degeneracy of the S, P, and D states[320] (Figure 26c).

5.7. Doping of Semiconductor Nanoparticles and Nanoparticle Assemblies

Numerous early studies have revealed low electronic conductivity of semiconductor NC solids because of negli-

gibly small concentration of mobile carriers and the presence of traps associated with dangling bonds at NC surfaces.[263,346,347] The attempts to increase the concentration of mobile carriers in NC solids by substitutional doping, that is, by adding atomic impurities with larger or smaller number of valence electrons as compared to the atoms in the host lattice, demonstrated only limited success[348] for several reasons. First, the incorporation of atomic impurities in NCs was found to be difficult because of the lack of appropriate chemical techniques and the effect of self-purification; the impurities could easily anneal away from the NC due to its tiny size.[348,349] Moreover, the incorporation of a heterovalent impurity does not guarantee stable electronic doping of a NC. In a bulk material, the electronic dopant forms a shallow trap state that lies within a few meVs of the corresponding band edge. This alignment can be easily distorted by the quantum confinement; the depth of impurity level (δE) that determines the probability to thermally excite carrier into the conduction 1S state changes with particle size.[348] The trap depth can increase when the NC band gap becomes wider in response to the quantum confinement.[350] At the same time, when the NC size becomes comparable with $\vartheta = [\varepsilon/(m^*/m_0)]a_B$, where a_B is the hydrogen Bohr radius and m_0 is the free electron mass, the shallow trap itself starts feeling the confinement potential and shifts to higher energy.[3] For sizes smaller than ϑ, the quantum confinement blurs the distinction between shallow traps and the Fourier transform states (quantum confined orbitals); the impurities autoionize and provide carriers to the crystallite.[348] These competitive trends result in complicating the size dependence of δE.

Because substitutional doping of NCs and NC solids is somewhat complicated, other approaches have been explored. Yu et al. reported that the conductivity of CdSe NC solids increased by about 3 orders of magnitude after exposure to potassium vapor in high vacuum.[185] It was shown that deposited potassium atoms donate electrons to $1S_e$ states of CdSe NCs. The carriers can also be injected in the NC solid by electrochemical charging. Charge screening by mobile ions present in the electrolyte substantially reduced E_c, facilitating charging of a NC solid with several additional electrons per NC[3,351] (Figure 27). Electrochemical charging allowed precise tuning of the electrochemical potential and controlling the doping level of NC solid. Guyot-Sionnest et al. demonstrated sequential filling of $1S_e$ and $1P_e$ orbitals by electrochemical charging and studied carrier transport through S and P states of quantum confined CdSe NC solids[185,352,353] (Figure 27a,b). The filling of the quantum confined states was accompanied by the characteristic maxima and minima of electron differential mobility corresponding to half- and completely filled S- and P-states of the NCs (Figure 27b). The electron transfer rate from an occupied to empty state is proportional to $\xi(1-\xi)\mathbf{\Gamma}$, where ξ is the occupation fraction. It maximizes at $\xi = 0.5$, leading to the conduction maximum for the half-filled shell.[185] The complete filling of S or P shells ($\xi = 1$) creates transport bottleneck. In this situation, conduction is only possible by exciting the electron to the next unoccupied shell.[185] To confirm that injected charge carriers indeed occupy the quantum confined states rather than being trapped at the NC surface, Guyot-Sionnest et al. monitored the evolution of optical absorption spectra during electrochemical charging of the NC solid[185,352−354] (Figure 27c). The presence of electrons at the $1S_e$ or $1P_e$ quantum confined states should lead to reduction of the absorption cross section for interband (e.g., $1S_{h(3/2)}-1S_e$) excitonic transitions, so-called "optical bleaching" of the excitonic peaks (Figure 27c). In addition, new absorption bands corresponding to the intraband (e.g., $1S_e-1P_e$) optical transitions should appear in the mid-IR region.

Nanocrystals and NC solids can also be doped via charge transfer from other chemical species. The treatment of CdSe, CdS, or ZnO NCs with sodium biphenyl results in the

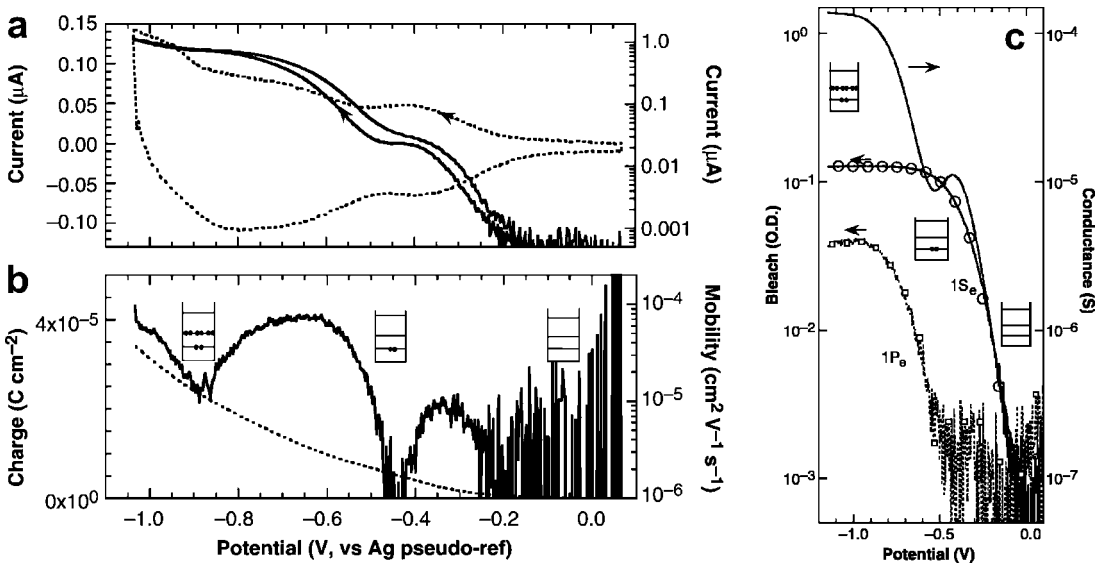

Figure 27. Electrochemical doping and charge transport in CdSe nanocrystal solids. (a) Cyclic voltammetry of a TOP/TOPO-capped 6.4 nm CdSe nanocrystal solid treated with 1,7-heptanediamine. The arrows indicate the cycle direction. The dotted line (linear scale) is the electrochemical current, and the solid line (logarithmic scale) is the current proportional to the conductivity of the nanocrystal film. (b) Additional charge injected into a film of 6.4 nm CdSe nanocrystals by electrochemical charging (dotted line, linear scale) leads to the variations in and electron differential mobility (solid line, logarithmic scale) with maxima and minima corresponding to half- and fully occupied S and P quantum confined orbitals. (c) The correlation of conductance and optical bleach of the excitonic peaks for a film of 5.4-nm CdSe nanocrystals. The solid line represents the conductance. The "○" represent the bleach magnitude at the 1S exciton peak (593 nm), and the "□" represent the bleach magnitude at the 1P exciton (520 nm). The first exciton is completely bleached at the most negative potentials. The potentials are measured against the Ag pseudoreference electrode. Reprinted with permission from ref 185. Copyright 2003 American Association for Advancement of Science.

bleaching of $1S_h-1S_e$ excitonic transition in the absorption spectrum and the appearance of a new absorption band in mid-IR corresponding to the intraband $1S_e-1P_e$ electronic transition.[355] These changes in the absorption spectrum unambiguously point to the charge transfer from biphenyl radical anion to $1S_e$ state of the NCs. N-type charge-transfer doping has been also demonstrated for PbSe NCs with hydrazine molecules adhered to the NC surface.[23]

Tuning of the NC stoichiometry could be a powerful technique for NC doping because the minor changes in surface termination can lead to significant changes of the NC stoichiometry.[356] It is well-known that vacancies and surface atoms can create donor and acceptor states in bulk semiconductors. A similar effect has been observed in PbSe NC solids; the presence of acceptor states moved the Fermi energy toward the $1S_h$ state providing p-type doping.[23,265,330] Here, it is important to emphasize the distinction between charges residing in the NC and on the surface. Depending on the depth of the surface state, surface charges can either interact with the quantum confined orbitals of the NC or be highly localized, not participating in the charge transport process.

5.8. Multicomponent Assemblies

Multicomponent nanostructures and BNSLs could be the most intriguing class of nanoparticulate electronic materials. They do not have analogues in nature and could not be synthesized even a decade ago. Such materials can deliver novel unexpected properties originating from the cross-talk between quantum confined components with different functionalities. This area of research is largely underexplored because of the novelty of multifunctional nanomaterials. At the same time, even early studies demonstrated nontrivial behavior of multicomponent NC solids. Urban et al. reported enhanced p-type conductivity in binary assemblies of PbTe and Ag_2Te NCs[357] (Figure 28a,b). Silver is known as a p-type dopant for bulk PbTe. It is somewhat surprising that similar doping principles can be extended to the NC solids. The mechanism of electronic doping in multicomponent nanoparticle assemblies requires further studies.

Multiple components can be integrated into the individual nanostructures as in the case of Au−PbS core−shells shown in Figure 28c where the metal and semiconductor form a single quantum-confined structure. The core−shell morphology maximizes the interaction between the components and provides convenient platform for studying exciton−plasmon interactions and electronic coupling between metal and semiconductor at the nanoscale. Lee et al. reported that electronic properties of Au−PbS core−shell NC solids differ significantly from the properties of PbS and Au NCs.[24] Arrays of Au−PbS core−shell particles are highly conductive and exhibit p-type conductivity, whereas PbS NC solids show n-type transport under similar conditions. The doping in Au−PbS NC solids can be explained by the intraparticle charge transfer from the highest occupied $1S_h$ state of PbS shell into Au core[24] (Figure 28d). A very high static dielectric constant of PbS ($\varepsilon \approx 170$) facilitates such charge displacement, which can also be described as the injection of a mobile hole into the PbS shell. This effect is conceptually similar to the formation of charge-transfer complex observed, for example, in tetrathiafulvalene-tetracyanoquinodimethane (TTF-TCNQ) system.[358] The electronic properties of multicomponent nanostructures combining magnetic FePt core and semiconducting PbS shell will be discussed in section 7.4.2.

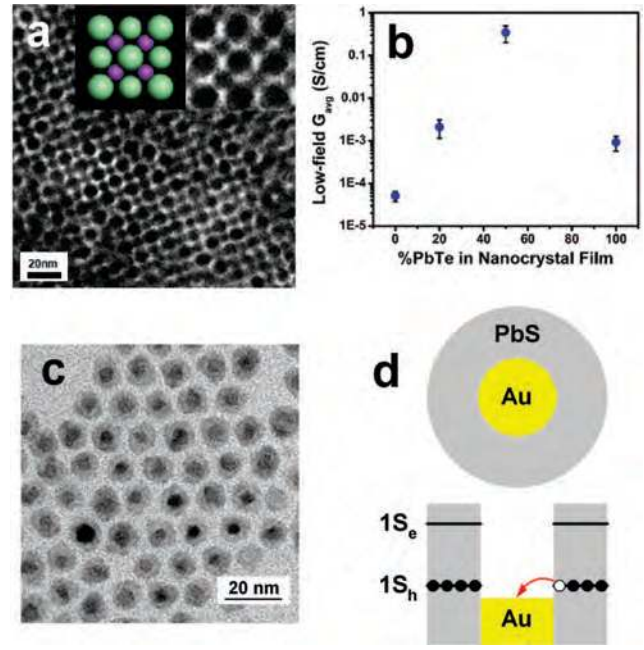

Figure 28. Charge transport in multicomponent nanocrystal solids. (a) TEM image of binary nanoparticle superlattice combining 6.5 nm PbTe and 3.2 nm Ag_2Te nanocrystals. (b) Comparison of low-field conductances for pure Ag_2Te films, pure PbTe films, binary 1:1 PbTe−Ag_2Te films, and binary 5:1 PbTe−Ag_2Te films. These data demonstrate the synergistic enhancement of conductivity manifest in the binary nanocrystal solids. Reprinted with permission from ref 357. Copyright 2007 Nature Publishing Group. (c) TEM image of Au-PbS core−shell nanostructures. (d) The energy level diagram for Au-PbS core−shell nanocrystals predicts intraparticle charge transfer that creates mobile holes in PbS shell and leads to p-type doping of Au-PbS nanocrystal solids. Reprinted with permission from ref 24. Copyright 2008 American Chemical Society.

6. Nanocrystal Solids for Device Applications: General Aspects

For many practical device applications, the detailed mechanism of charge transport is not important, and NC solids can be considered as a homogeneous medium with effective electron and hole mobility, doping density, band diagram, dielectric constant, etc. In this section, we will describe how these parameters can be measured and used for design of NC-based devices.

6.1. Contacts to Nanocrystal Solids

Contacts play a very important role for the operation of electronic and optoelectronic devices. Both charge transport measurements and device operation require establishing proper electrical contacts between the electronic materials and external circuits. In case of conductive NC solids, charge carriers have to be injected from the electrode into an unoccupied electronic level (for electron conductors) or into an occupied state (for hole conductors). The efficiency of extraction of photogenerated nonequilibrium carriers from the NC solid determines the performance of a solar cell or a photodetector. The contact resistance put limitations on the fill factor of solar cells[359] and maximum on-currents of field-effect transistors.[6]

Comparing the work function (φ) of the metal electrode with energy levels of a NC can help in determining whether efficient charge injection is possible and whether high or low contact resistance is to be expected. The efficiency of injection or extraction of carriers depends on the energy barriers that form at the electrode/NC interface due to the difference in the work functions of contact material and the lowest unoccupied (for electron conductors) or highest occupied (for hole conductors) state of the NCs. A metal−semiconductor junction forms an ohmic contact (i.e., a contact with voltage independent resistance) if the Schottky barrier height, ϕ_B, is zero or negative. In such case, the carriers are free to flow in or out of the semiconductor so that there is a minimal resistance across the contact. A good ohmic contact is expected when the work function of the injecting metal is close to the highest occupied or lowest unoccupied states of the NCs.[360] In other words, for n-type material, the work function of the metal must be close to or smaller than the electron affinity of the semiconductor. The p-type semiconductor requires that the work function of the metal must be close to or larger than the sum of the electron affinity and the band gap energy. If these conditions are not satisfied, a potential barrier is formed, leading to poor charge injection and nonohmic contacts. High nonohmic contact resistance typically manifests itself in the transport measurements through I−V curves with suppressed current at low bias followed by superlinear increase of current at large applied voltages. High potential barriers at the metal−semiconductor interface combined with low semiconductor doping levels lead to formation of blocking contacts, that is, the contacts that cannot inject charge carriers into semiconductor. This situation is demonstrated in Figure 29a, which shows the energy diagram for CdSe NCs of different size and different contact materials: indium−tin oxide (ITO), highly conductive polythiophene derivative PEDOT:PSS, and In−Ca eutectics. According to this energy diagram, electrons can easily flow from In−Ga eutectic (EGaIn) into the NCs, but not vice versa. PEDOT:PSS cannot inject either electrons or holes into the NCs, forming a blocking contact. Indeed, Weiss et al. observed strong rectification behavior for a layer of CdSe NCs sandwiched between PEDOT:PSS and EGaIn in the device ITO/PEDOT:PSS/CdSe_NCs/EGaIn (Figure 29b).[361,362]

The band gap energy of quantum confined semiconductors is strongly size dependent (Figures 3 and 29a), and size effects can play an important role because they determine absolute energies of the quantum-confined states in semiconductor NCs.[3,39] For example, Au contacts can readily inject holes into bulk lead sulfide and PbS NCs larger than ~6 nm.[24,265] At the same time, a positive potential barrier forms at the interface between Au and small, for example, 2 nm, PbS NCs.[363] Generally, both electrons and holes can flow from small into large semiconductor quantum dots, whereas the reverse flow will be an uphill process. Surface ligands can also affect the position of energy levels in semiconductor NCs. Tessler et al. demonstrated tuning of the electronic level positions with respect to the vacuum level in colloidal InAs NCs using different surface ligands.[364] Such size and ligand effects must be taken into account by designers of NC solar cells and other devices.[361,362]

In other examples, the work function of gold (φ = 5.1 eV) is well aligned with the $1S_h$ state of 7 nm PbSe NCs (~4.7 eV), which should lead to a low contact resistance. In contrast, it should be very difficult to inject electrons or holes from Au into 4 nm CdSe NCs with $1S_e$ state at ~ −4.6 eV and $1S_h$ state at ~ −6.5 eV as compared to vacuum level; the contact resistance is expected to be very high. Bawendi et al. observed that Au forms blocking contacts to ~4 nm CdSe NCs,[263,269] preventing any detectable current in the NC film. At the same time, gold electrodes could inject holes into $1S_h$ state of CdTe NC film due to lower ionization potential of CdTe as compared to the CdSe phase.[296] Ohmic contact was observed between gold electrodes and PbS,[22,24,265,365] PbSe,[23,25,366] and PbTe[87,357] NC solids. Sargent and Nozik groups reported formation of hole-injecting ohmic contacts between indium−tin oxide (ITO) electrodes and PbS,[365] PbSe[271,367] NCs.

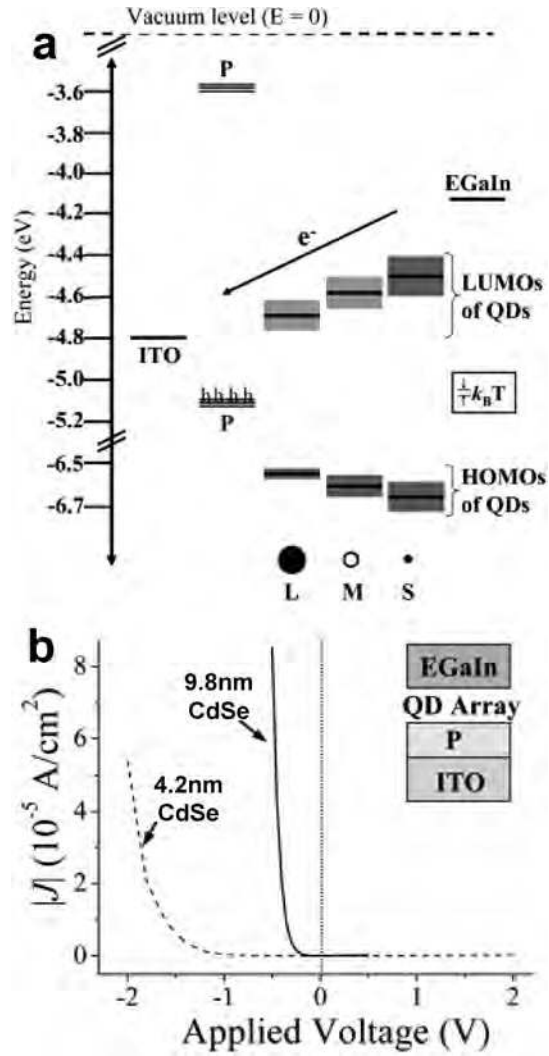

Figure 29. (a) Energy diagram for the components of the ITO/PEDOT:PSS/CdSe_NCs/EGaIn junctions: the Fermi level of ITO, the valence and conduction bands of PEDOT:PSS, the $1S_h$ (HOMO) and $1S_e$ (LUMO) levels of the 4.2 nm (S), 5.3 nm (M), and 9.8 nm (L) CdSe nanocrystals, and the Fermi level of In−Ga eutectic (EGaIn). The gray boxes indicate the uncertainty in the energies of the HOMOs and LUMOs of the nanocrystals. The arrow indicates the direction that the electrons move when $V > 0$, where the device turns on. (b) Plots of the absolute value of current J versus applied voltage V for the junctions ITO/PEDOT:PSS/CdSe NCs/EGaIn for two different nanocrystal sizes. The junctions behave as diodes: electrons flow from EGaIn to ITO, but not vice versa. Reprinted with permission from ref 361. Copyright 2008 American Chemical Society.

Doping of NC solids can play an important role in improving the contact resistance. In case of bulk semicon-

ductors, when there is no appropriate metal available to form a low-barrier contact, a tunnel contact is used. Such contacts do have a positive barrier at the metal−semiconductor interface, but also have a high enough doping in the semiconductor that there is only a thin potential barrier separating the metal from the semiconductor. If the width of the depletion region at the metal−semiconductor interface is very thin, carriers can readily tunnel across such barrier. Gyout-Sionnest demonstrated that doping of CdSe NCs by potassium evaporation or by electrochemical charging results in the formation of ohmic electron-injecting contacts with Au and even Pt ($\varphi \approx 5.6$ eV) electrodes.[185]

Often, the interface exhibits an additional dipole barrier that tends to change the metal work function[368,369] and hence the interface barrier height. Intentionally introduced dipoles at the metal surface, for example, through self-assembled monolayers (SAMs), were used to improve charge injection into organic semiconductors, as demonstrated by de Boer et al.[370] and Hamadani et al.[371] The I−V characteristic should also depend on the density of electronic states in contacts and NC solids. The electronic structure of NC solids with sharp spikes in the density of states can lead to unusual electronic properties. Thus, the Heath group reported tunnel diode behavior with pronounced negative differential resistance for Au/SAM/CdSe_NCs/SAM/Au structure.[372]

Contact resistance can be measured as the voltage drop at the electrodes with noncontact scanning probe potentiometry (e.g., Kelvin probe),[373] by four-point probe measurements,[374] or by determining the channel resistance of transitors with different channel lengths and extrapolating to zero channel length (transfer line method).[375,376] There is only limited experimental information available for the contact resistance at the metal−NC interface. At the same time, some useful analogies can be drawn between metal−NC interface discussed here and much better studied metal−bulk semiconductor and metal–organic semiconductor interfaces. We would like to address the readers to several reviews describing charge injectrion and associated effects in inorganic[377] and organic[376,378,379] semiconductors.

6.2. Schottky Barriers to Nanocrystal Solids

Sargent and Nozik groups recently reported that vacuum deposition of low work function metal electrodes (Ca, Mg, Al) on a film of lead chalcogenide (PbS or PbSe) NCs leads to the formation of a Schottky barrier at the interface between evaporated metal and NC solid[22,271,272,366,367,380] (Figure 30). The possibility of forming well-controlled Schottky contacts to NC solids, in addition to the ability to form ohmic contacts, can offer significant benefits for device applications.

In analogy with bulk semiconductors, formation of a Schottky barrier can be caused by defects formed at the interface, which pin the Fermi energy at the interface due to the large density of surface states. The Schottky barrier creates a built-in electric field, which can be used for fast separation of electrons and holes in photovoltaic devices and photodetectors.[22,271,367] Moreover, metal−semiconductor interface with a Schottky barrier forms a junction that has rectifying characteristics, suitable for use as a diode.[365] As compared to more traditional p−n junction diodes, the Schottky diode can provide very fast switching times, with essentially zero reverse recovery time, when the diode switches from nonconducting to conducting state and vice versa.[381] In

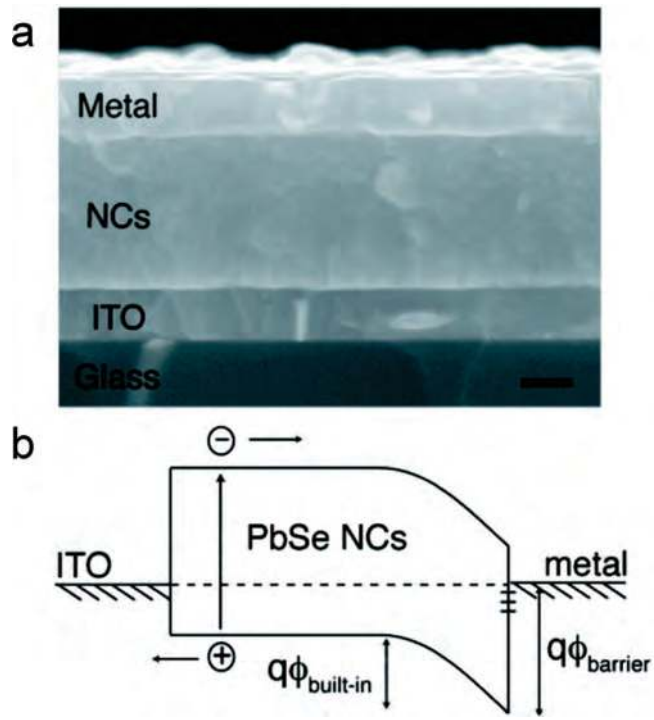

Figure 30. (a) Scanning electron microscopy cross-section of the ITO/PbSe_NCs/metal device stack. The metal is 20 nm Ca/100 nm Al. The scale bar represents 100 nm. (b) Proposed equilibrium band diagram, showing the presence of a Schottky barrier and bending in the conduction band and valence band near the matal/nanocrystal interface. The built-in electric field within the depletion region of the nanocrystal layer governs the transport of photogenerated electrons and holes. Reprinted with permission from ref 271. Copyright 2008 American Chemical Society.

addition, the Schottky barrier provides a useful tool to obtain important information about electronic characteristics of a NC solid.

Luther et al. measured the capacitance (C) of the Schottky barrier as a function of voltage (V) applied to the ITO/PbSe_NCs (5 nm, linked with ethylenediamine)/Al structure and observed linear dependence in $C^{-2}-V$ coordinates known as the Mott−Schottky coordinates[271] (Figure 31). The capacitance−voltage ($C-V$) measurements shown in Figure 31 provide direct evidence for the Schottky junction. In addition, Mott−Schottky analysis permits a determination of the built-in potential, depletion width, and carrier concentration of the NC film. The analysis assumes no free carriers in the depletion region and a carrier concentration outside the depletion region equal to the total acceptor density (section 6.3).

6.3. Effective Carrier Mobility, Lifetime, Diffusion Length, and Doping in Nanocrystal Solids: Measurement Techniques and Reported Values

The capacitance of the depletion region formed in semiconductor in proximity to metal contact (Figure 31) is expressed as:[382]

$$\frac{1}{C^2} = \frac{2}{A^2 e \varepsilon_0 \varepsilon N_a}\left(\phi_{\text{built-in}} - \frac{k_B T}{e} - V\right) \qquad (18)$$

where A is the device area, V is the applied bias, N_a is the acceptor density, $\phi_{\text{built-in}}$ is the built-in potential, and ε and

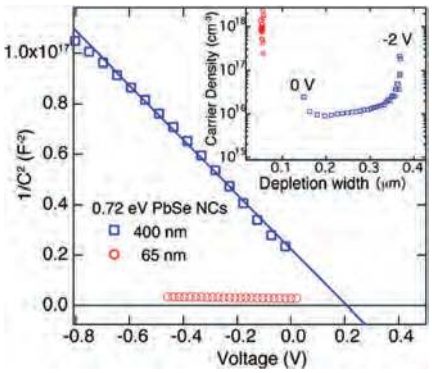

Figure 31. Analysis of the Schottky barrier formed in ~5.8 nm PbSe nanocrystal solid. Mott−Schottky plots measured at the frequency 1 kHz for devices with a thin (65 nm, red) and thick (400 nm, blue) nanocrystal layer. The capacitance of the thin device is larger and changes little with reverse bias. A linear fit shows that the built-in potential of the thick device is 0.2 V. The inset shows the carrier concentration at the edge of the depletion layer for both devices. The thick device has an equilibrium depletion width of ~150 nm, while the thin device is fully depleted. Reprinted with permission from ref 271. Copyright 2008 American Chemical Society.

ε_0 are the static permittivity of the semiconductor and vacuum, respectively.

Extraction of the acceptor density (N_a) and the built-in potential ($\phi_{\text{built-in}}$) is achieved by fitting eq 18 to the measured capacitance over a range of applied biases. The depletion width, W_{depl}, of an abrupt Schottky junction is equal to

$$W_{\text{depl}} = \sqrt{\frac{2\varepsilon\varepsilon_0(\phi_{\text{built-in}} - V)}{eN_a}} \tag{19}$$

where the carrier concentration (acceptor density) is

$$N_a = \frac{1}{A^2}\frac{2}{e\varepsilon_0 \frac{d}{dV}\left(\frac{1}{C^2}\right)} \tag{20}$$

The Mott−Schottky analysis requires knowledge of static dielectric constant of the material. Because NC solid is a dielectrically inhomogeneous medium, obtaining accurate numbers for ε can be complicated.[23,271] Luther et al. used the Bruggeman effective media theory and calculated $\varepsilon = 12$ for 6 nm PbSe NCs linked by 1,2-ethanedithiol molecules.[271] Sargent et al. used the carrier extraction by linearly increasing voltage (CELIV) technique and reported $\varepsilon = 17 \pm 2$ for butylamine-capped PbS NCs[365] and $\varepsilon = 15 \pm 1$ for 5 nm PbSe NCs cross-linked with 1,4-benzenedithiol molecules.[365] In conductive PbS and PbSe NC solids, $\phi_{\text{built-in}}$ approaches several hundreds millielectronvolts and depends on the particle size; smaller NCs demonstrated larger $\phi_{\text{built-in}}$ due to wider band gaps.[271] The depletion width depends on the carrier density and increases with the applied bias. For PbS and PbSe NC solids, the reported W_{depl} was about 100 nm in equilibrium, increasing to ~400 nm under reverse bias. Equilibrium carrier densities typically ranged from 10^{16} to 10^{17} cm^{-3}.[271,365,367] We have to admit that the classical Mott−Schottky model is not always sufficient to describe behavior of real systems where various complications can arise from structural imperfections, inhomogeneous distribution of trap states, etc.

Carrier mobility (μ) can be obtained from the conductance measurements $G = I/V$ if the concentration of mobile carriers (n) is known and electrodes form ohmic contacts to a NC solid:

$$\mu = \frac{1}{ne}G\left(\frac{L}{Wh}\right) \tag{21}$$

where L, W, and h are the length, width, and thickness of the conducting channel, respectively. The carrier density in the NC solid can be obtained from the Mott−Schottky analysis or from the measurements of the optical density for the intraband $1S_e-1P_e$ excitonic transition.[185]

Among other popular techniques used to measure the carrier mobility, we should mention Hall effect[383] and field-effect transistor (FET) techniques.[6] However, for materials with relatively low carrier mobility, such as organic semiconductors or NC solids, the Hall effect measurements often lead to experimental artifacts,[315] whereas FET measurements allow one to obtain accurate numbers for mobility of majority carriers.[6,23,376] This technique is described in detail in section 7.4.1 of this Review.

Time-resolved THz spectroscopy (TRTS) is a relatively new experimental tool that can be used to characterize materials electrical properties in a noncontact manner.[381] The THz spectroscopy can measure both time-dependent conductivity $\sigma(t)$ related to the inter-NC coupling and carrier dynamics, with subpicosecond temporal resolution without attaching any probe wires to the sample.[384] Murphy et al. reported TRTS measurements for a series of PbSe NC samples where the interparticle distance has been tuned systematically by chemical treatments.[385] The mobility of the carriers was estimated by assuming that all absorbed photons produce carriers at $t = 0$ and $\sigma(t) = en\mu(t)$. It was shown that simple chemical treatments can have major effects on both the degree of inter-NC coupling and the carrier dynamics.[385]

The Sargent group applied various techniques to measure effective characteristics of PbS and PbSe NC films with different capping ligands. CELIV was used to extract the majority carrier (hole) mobility and static relative permittivity.[365,367] A linearly increasing voltage was applied across Al/PbS_NCs/ITO devices with a 300−600 nm thick NC layer under reverse bias (i.e., Al at a higher potential than ITO), and the current signal was monitored. Figure 32a shows a CELIV transient at a ramp rate (M) of 80 000 V s^{-1}. The majority carrier mobility can be extracted from the time required for the transient current signal to reach its maximum value $t_{\max}$ according to

$$\mu_h = \frac{2d^2}{3Mt_{\max}^2\left(1 + 0.36\frac{\Delta j}{j_d}\right)} \tag{22}$$

where μ_h is the hole mobility, d is the device thickness, j_d is the displacement current, and Δj is the maximum drift current. In this manner, the hole mobility in the film of 6 nm PbS NCs capped with n-butylamine was found to be $(1.5 \pm 0.1) \times 10^{-3}$ cm^2 V^{-1} s^{-1}.[272,365]

To obtain the minority carrier (electron) mobilities, Johnston et al. used time-of-flight technique in optically thick samples.[272] Time-of-flight transients were obtained by illuminating the ITO/NCs/metal devices through the ITO contact with a 10 ns pulse at 532 nm using an yttrium aluminum garnet laser. Devices were reverse biased to isolate the electron transport dynamics. The NC film thickness was

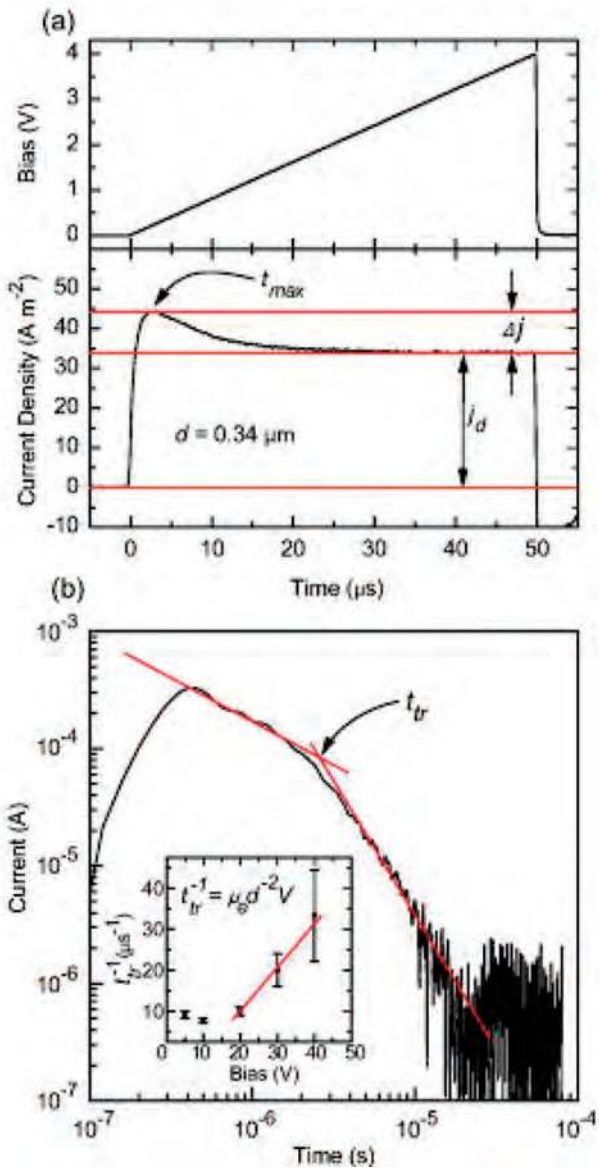

Figure 32. Current transient signals used to extract (a) the hole mobility (CELIV, 80 000 V s^{-1} ramp rate) and (b) the electron mobility (time-of-flight, under 40 V bias). The inset shows the bias dependence of the transit time (t_{tr}). The slope of the data above 15 V was used to determine the mobility. The dashed red lines represent in (a) the different current density levels and in (b) the least-squares fits to the data. Reprinted with permission from ref 272. Copyright 2008 American Institute of Physics.

much greater than the absorption depth at the laser wavelength. A typical time-of-flight transient is shown in Figure 32b. The intersection time of the transient asymptotes was used to determine the transit time.The bias dependence of the transit time is shown in the inset of Figure 32b. In the fully depleted regime, the electron mobility (μ_e) was found to be $(2 \pm 1) \times 10^{-4}$ cm^2 V^{-1} s^{-1}.[272]

Table 2 summarizes the electron and hole mobilities reported for different semiconductor NC films. One can see a large spread in the reported data. It could be explained by lack of commonly accepted measurement protocolts and sample preparation techniques. So far, we can only conclude that higher doping levels and shorter surface ligands result in larger carrier mobility. Lead chalcogenide NCs show higher carrier mobilities than do II−VI NCs. On the other hand, understanding the effects of particle size and shape on the mobility of charge carriers will require additional experimental studies.

The recombination-limited lifetime of carriers (τ_{rec}) in the NC solids was measured using the decay of the open-circuit voltage (V_{oc}) following illumination turn off, so-called transient open circuit voltage decay (OCVD). For these measurements, ITO/NCs/metal devices were illuminated with a pulse modulated 975 nm diode laser. Immediately after laser turn off, the initial slope of the decay curve (dV_{oc}/dt) is related to τ_{rec}.[272,381] Measured lifetimes for PbS and PbSe NC solids showed that the lifetime decreased steadily from 1 ms at low light intensities to ~10 μs at high light intensities.[272,367]

Carriers in the depletion region are separated via the action of the built-in field resultant from the metal−semiconductor, or Schottky, junction (Figure 30b). Their drift length (L_{drift}) is given by

$$L_{drift} = \frac{\mu \tau_{rec} \phi_{built\text{-}in}}{W_{depl}} \tag{23}$$

where μ is the carrier mobility. For PbSe NCs cross-linked with 1,4-benzenedithiol, L_{drift} was estimated as 8.5 μm for electrons and 14.5 μm for holes.[367]

In the quasi-neutral region of NC solid, charge transport occurs mainly through diffusion, and the carrier diffusion length (L_{diff}) may be obtained from

$$L_{diff} = \sqrt{\frac{\mu \tau_{rec} k_B T}{e}} \tag{24}$$

The calculated minority carrier (electrons) diffusion length for 1,4-benzenedithiol linked PbSe NCs was about 220 nm,[367] which allows a substantial fraction of the minority carriers to diffuse out of the neutral region in NC-based solar cells and photoderectors.

6.4. Sintering Metal and Semiconductor Nanoparticles into Continuous Films

Nanoparticles can be deposited onto a substrate by spin-coating or inkjet printing a colloidal solution and sintered into a continuous conductive film during subsequent annealing step. Coalescence of individual nanoparticles yields polycrystalline solids with grains considerably larger than the initial nanoparticles.[388] Sintering individual NCs is facilitated by significant reduction of the melting temperature with decreasing particle size.[389,390] Size-dependent melting-point depression is a general effect observed across a broad class of materials, including technologically important metals and semiconductors (Figure 33). The reduction of the melting point can be described by the effect of surface tension that plays an increasingly important role when particle size decreases below 10 nm.[390] Changes in the melting temperature (T_m) of the particle of size R_{sol} as compared to that of the bulk (T_b) are given by:[389,390]

$$T_m - T_b = \frac{2T_m}{L_{fusion}\rho_{sol}R_{sol}}\left[\gamma_{sol} - \gamma_{liq}\left(\frac{\rho_{sol}}{\rho_{liq}}\right)^{2/3}\right] \tag{25}$$

where L_{fusion} is the molar latent heat of fusion, and γ and ρ are the surface tension and density of solid (sol) and liquid (liq) phases, respectively. The size-dependent suppression

Table 2. Reported Electron and Hole Mobilities for Various NC Films[a]

material	ligand/sample treatment	particle size (nm)	electron mobility ($cm^2/V \cdot s$)	hole mobility ($cm^2/V \cdot s$)	measurement technique	ref
CdSe	HT		1		FET	268
	charge injection	6.4	0.8×10^{-2}		El-Chem	185
	K doping	5.4	3×10^{-6}		El-Chem	185
		2.7−5.0	10^{-4}−10^{-6}		SCLC	346
ZnO			0.1		El-Chem	351
	HT	6.0	2.4×10^{-4} (μ_{lin}) 4.6×10^{-4} (μ_{sat})		FET	386
HgTe	HT			0.82 (BG) 2.38 (TG)	FET	298
CdTe/CdHgTe	HT			0.21 (BG) 0.026 (TG)	FET	387
PbS	N_2H_4	7.1	0.08 (μ_{lin}) 0.12 (μ_{sat})		FET	24
	ethanedithiol	5		1×10^{-4}	FET	380
PbSe	N_2H_4	8.1 9.2	0.4 (μ_{lin}) 0.95 (μ_{sat})	0.12−0.18	FET	23
	N_2H_4		0.5−1.2		FET	25
	butylamine	5.7	7.4		THz spectroscopy	385
	N_2H_4		29.4			
	NaOH		35			
	ethylenediamine		47			
	HT			4×10^{-5}	FET	330
PbTe	N_2H_4		0.95	0.15	FET	357

[a] Abbreviations: HT, heat treatment; N_2H_4, hydrazine treatement; BG, back gate; TG, top gate; FET, field-effect transistor measurements; El-Chem, electrochemical measurements; THz, terahertz spectroscopy measurements; SCLC, space-charge limited current model.

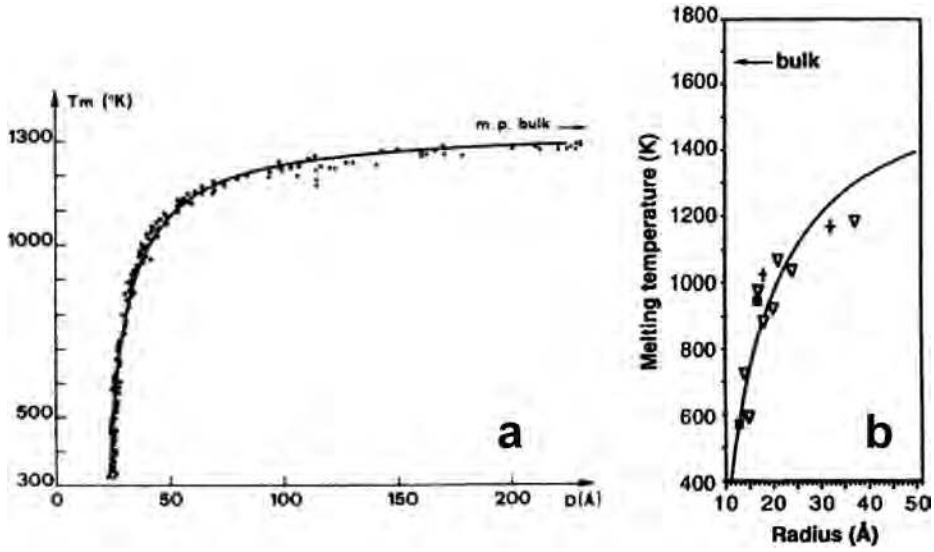

Figure 33. Size-dependence of the melting temperature for (a) Au and (b) CdS nanoparticles. (a) Reprinted with permission from ref 389. Copyright 1976 American Institute of Physics. (b) Reprinted with permission from ref 390. Copyright 1992 American Association for Advancement of Science.

of the melting temperature of metals and semiconductors can exceed 1000 °C, allowing one to sinter very small (~2 nm) NCs at temperatures below 300 °C (Figure 33).

The ability of NCs to fuse at relatively modest temperatures provides a low-temperature route to thin-film growth. This approach has been successfully utilized for formation of metallic (Au,[391] Ag[392]) and semiconducting (CdS,[389] CdSe,[268] HgTe[298]) thin films with good electrical conductivity. However, a serious limitation of this approach is associated with the presence of organic ligands at the nanoparticle surface, necessary to stabilize particles in solution. These ligand molecules often partially destroy and carbonize during the sintering process, contaminating semiconducting materials and reducing size of crystalline grains. As a result, carrier mobility in semiconducting films obtained by sintering of corresponding nanoparticles is much lower than the mobility of CVD-grown thin films. For example, the reported electron mobility in CdSe thin films derived from 2 nm nanoparticles sintered at 350 °C was 1 $cm^2/(V\ s)$, more than 2 orders of magnitude lower than the mobilities in vapor-deposited CdSe films.[268] The further improvement should be possible by designing special surface ligands, which can be reliably removed from the nanoparticle surface without leaving any solid residue behind.

7. Nanocrystal Devices

Examples of NC devices include photoresistors, diodes with rectifying I−V characteristic, field-effect transistors, memory elements, light-emitting and photovoltaic devices, etc. All of these have been recently assembled from chemically synthesized metal and semiconductor NCs.

Among the benefits provided by this class of electronic materials, there are properties inherent to nanoscale materials such as size-dependent electronic structure, charging energy, melting temperature, and other parameters that can be fine-tuned by varying NC size. For example, superior luminescent properties of semiconductor NCs (size-tunable color, narrow emission band, almost 100% luminescence quantum efficiency, high stability, etc.) have been utilized in light-emitting devices (LEDs).

In addition, colloidal NCs offer opportunities for inexpensive device fabrication by solution-based techniques like spin-coating, dip-coating, inkjet printing, etc., and can be used in roll-to-roll processing. As a result, colloidal NCs are condidered as a very promising class of materials for large area applications, such as thin film solar cells and for the applications where low fabrication cost is very important. Along these lines, solution-cast NC field-effect transistors (FETs) show respectable carrier mobilities, which compare favorably to the best devices made from organic electronic materials.[23,24,87,386,393] Several interesting concepts have been proposed for NC-based solar cells.[271,394−397] The progress in developments of commercially successful NC devices requires collaborative efforts of chemists synthesizing new materials, scientists studying materials properties, engineers working on device architecture, and technologists involved in the process of device fabrication. In this section, we provide an overview of state-of-the-art for several classes of applications utilizing colloidal NCs.

7.1. Light-Emitting Devices (LEDs)

Colloidal NCs have been explored as the emitters for thin film light-emitting diodes (LEDs).[398−407] In a typical LED, a thin layer of light-emitting NCs, for example, CdSe/ZnS core−shells or $Cd_{1-x}Zn_xSe$ (recombination layer), is sandwiched between the hole transport layer (HTL) and electron transport layer (ETL), which provide injection of carriers into the NCs (Figure 34). The performance of NCs-based LEDs has remarkably improved over the past decade.[404,408,409] Among the strong points of NC-based LEDs are their high color purity (i.e., narrow emission band) and tunability of the emission color from UV to near-IR by simply varying the NC size.[410] Because size-dependent emission of semiconductor NCs is well described by the quantum dot (QD) formalism, the NC-based LEDs are often named "QD-LEDs". To be fully competitive with other emerging technologies such as organic LEDs, both brightness and especially lifetime of QD-LEDs have to be considerably improved.[411] The room for such improvements is associated with the higher stability of core−shell NCs and electron- and hole-transport layers, better understanding and controlling chemical and physical phenomena at the NC−organics interfaces, optimization of the energy transfer, and carrier injection from organic molecules into the NCs. In this section, we introduce the basic principles of QD-LED operation and review recent progress in NC-based LEDs.

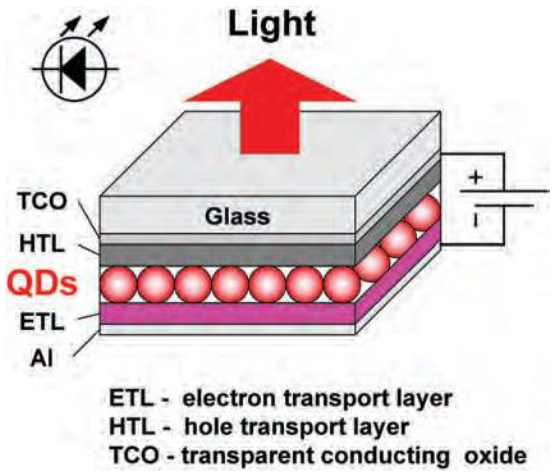

Figure 34. Schematic diagram and a typical structure of a thin film LED utilizing semiconductor NCs.

7.1.1. LED Performance Characteristics

Internal Quantum Efficiency (η_{int}). Not every electron–hole pair injected into LED recombines radiatively. Nonequilibrium carriers can recombine radiatively or nonradiatively depending on the available local recombination pathways. The internal quantum efficiency (η_{int}) can be expressed as

$$\eta_{int} = \frac{\text{(number of photons generated per second)}}{\text{(number of electrons injected into LED per second)}} = \frac{(P_{int}/h\nu)}{(I/e)} \quad (26)$$

where P_{int} is the optical power emitted from the active region, and I is the injection current.

Light Extraction Efficiency ($\eta_{extraction}$). Photons emitted by the active region should escape from the LED. In an ideal LED, all photons emitted by the active region are emitted into free space. However, in a real device, not all emitted photons can escape due to reabsorption or internal reflections. The light extraction efficiency is defined as

$$\eta_{extraction} = \frac{\text{(number of photons emitted into free space per second)}}{\text{(number of photons generated per second)}} = \frac{(P/h\nu)}{(P_{int}/h\nu)} \quad (27)$$

where P is the optical power emitted into free space.

External Quantum Efficiency (η_{ext}). A very important metric of an LED is the external quantum efficiency, which is the ratio of the number of photons emitted into free space to the number of injected carriers. η_{ext} can be defined as

$$\eta_{ext} = \frac{\text{(number of emitted photons per second)}}{\text{(number of electrons injected into LED per second)}} = \frac{(P/h\nu)}{(I/e)} = \eta_{int} \times \eta_{extraction} \quad (28)$$

The power efficiency is defined as

$$\eta_{power} = \frac{P}{IV} = \frac{\text{number of photons emitted externally} \times h\nu}{IV} \quad (29)$$

where I is the current flowing through the LED and V is the applied voltage. The power efficiency is comparable with $\eta_{external}$ only if the device operational voltage is approximately equal to the energy gap of semiconductor.[411]

Eye Sensitivity and Brightness. The physical properties such as the number of photons, photon energy, and optical

Table 3. Typical Values for Luminance of Displays, Organic LEDs, and Inorganic LEDs[411]

device	luminance (cd/m^2)
display	100 (operation)
display	250−750 (max. value)
III−V LED	10^6−10^7
organic LED	100−10 000

power of electromagnetic radiation are characterized by radiometric units. However, response of human eye (luminous efficiency) is limited to the wavelengths between 400 and 700 nm. Because eye sensitivity varies significantly within this spectral range, practical LED applications (e.g., displays) should take into account relative response of the eye at the wavelength of interest. For human brightness and color perception, different types of units are required. These units are called photometric units. The luminous flux (lumen, lm) is the light power of a source as sensed by human eye. One lumen (lm) is defined as a monochromatic light source emitting an optical power of (1/683) watt at 555 nm. For all other wavelengths, the luminous flux can be calculated by multiplying optical power by the luminosity function $V(\lambda)$, which describes the average sensitivity of the human eye to light of different wavelengths. The luminous intensity unit, candela (cd), is defined as a monochromatic light source emitting an optical power of (1/683) watt at 555 nm into the solid angle of 1 sr.

The brightness of an LED output is measured by the luminous flux (F) as

$$F = L_o \int V(\lambda) P_{op}(\lambda)\, d\lambda \tag{30}$$

where L_o is a constant (683 lm/W), and $P_{op}(\lambda)$ is the light power (watts per unit wavelength). $V(\lambda)$ is normalized to unity for the peak at $\lambda = 555$ nm where the human eye has its maximum sensitivity. The difference between lm and cd reveals one candela equals one lumen per steradian (sr), cd = lm/sr.

The luminance of an LED (L_v) is measured in units of cd/m^2 as

$$L_v = \frac{d^2F}{dA\, d\Omega \cos\theta} \tag{31}$$

where θ is the angle between the surface normal and the specified direction, A is the area of device surface (m^2), and Ω is the solid angle (sr).

Table 3 compares typical luminance of displays, organic LEDs, and inorganic LEDs based on III−V semiconductors.

7.1.2. Nanocrystal-Based QD-LEDs

First LEDs utilizing CdSe colloidal NCs have been reported by Colvin et al. in 1994.[398] Since then, significant progress has been achieved in optimization of all components of the QD-LEDs. Using core−shell NCs as the emitters allowed one to significantly increase the efficiency of radiative recombination and device internal quantum efficiency.[399] To achieve higher injection currents, heavily doped electron transporting layers were introduced, whereas the thickness of the emitting layer was reduced down to one or two monolayers of highly luminescent semiconductor NC.[408] The important breakthrough in understanding operation of efficient QD-LEDs is associated with the works of the Bulovic and Bawendi groups, who realized that excitons

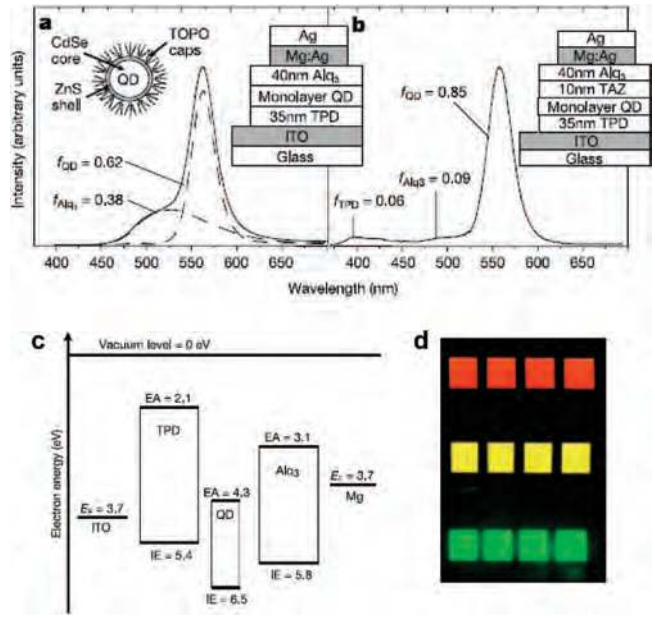

Figure 35. Electroluminescence spectra and structures of QD-LEDs (a) without and (b) with a hole-blocking (TAZ) layer. Alq_3 is tris (8-hydroxyquinoline) aluminum; TPD is *N*,*N*′-bis(4-butylphenyl)-*N*,*N*′-bis(phenyl)-benzidine; TAZ is 3-(4-biphenylyl)-4-phenyl-5-*t*-butylphenyl-1,2,4-triazole. (c) Proposed energy level diagram of the device. Reprinted with permission from ref 408. Copyright 2002 Nature Publishing Group. (d) Optical photographs of green, yellow, and red light emitting devices using CdSe/ZnS core−shell nanocrystals with different sizes of CdSe cores. Reprinted with permission from ref 405. Copyright 2007 Nature Publishing Group.

formed in the polymer can be nonradiatively transferred to and recombine in the semiconductor NCs.[408]

Nowadays, the most widely accepted structure of QD-LED is outlined in Figures 34 and 35. Typically, a thin layer of luminescent NCs is sandwiched between the electron- and hole-transporting layers. When forward bias is applied, the electrons and holes are injected into the NC layers from ETL and HTL layers, respectively. The recombination of electron–hole pairs in the NCs generates photons with the energy corresponding to the gap between highest occupied ($1S_h$) and lowest unoccupied ($1S_e$) states in the NC. Optimization of ETL and HTL layers, development of highly luminescent, stable, and, ideally, environmentally benign semiconductor NCs are the active areas of ongoing research. Generally speaking, core−shell NCs have an advantage for solid-state QD-LEDs due to their enhanced photoluminescence and electroluminescence (EL) quantum efficiencies and their greater tolerance to the processing conditions during device fabrication. Table 4 provides a summary of reported QD LEDs structures, L_v, emission colors and η_{ext}.

In the first QD LEDs, the Alivisatos group used TOPO-TOP capped CdSe NCs as the emitting and electron transporting layer and poly(*p*-phenylenevinylene) (PPV) as HTL.[398] The spectrum of electroluminescence (EL) was dominated by the NC emission, and the emission color of the QD-LED could be changed from red to yellow by tuning the NC size. The luminance of ∼100 cd m^{-2} was obtained for a device with the structure glass/ITO/PPV/CdSe QDs/Mg.[398] However, η_{ext} of those first QD-LEDs was fairly low (0.001−0.01%) due to imbalanced carrier injection into the NCs. Moreover, the EL spectra often combined light emission from the QDs and organic layers, negatively affecting the color purity. Mattoussi et al. also reported LED devices

Table 4. Device Structure, Luminance (L_v) and External Quantum Efficiency (η_{ext}) of Reported Quantum Dot LEDs[a]

QD material	device structure	L_v (cd/m^2)	EL color	η_{ext} (%)	year ref
CdSe	ITO/QDs/PPV/Mg		green to red	0.001−0.01	1994[398]
CdSe/CdS	ITO/PPV/QDs/Mg/Ag	600	green to red	~0.22	1997[399]
CdSe/ZnS	ITO/TPD/QDs/Alq_3/Mg:Ag/Ag	2000		~0.52	2002[408]
CdSe/ZnS	ITO/TPD/QD(monolayer)/Alq_3/Mg:Ag/Ag	7000	red	>2	2005[402]
$Cd_xZn_{1-x}Se/Cd_yZn_{1-y}S$	ITO/CBP/QD(monolayer)/TAZ//Alq_3/Mg:Ag/Ag		green	<0.5	2006[403]
CdSe/CdS	ITO/PS-TPD-PFCB/m-QD/TPBI/Ac/Ag	100	red	~0.8	2006[409]
		1000 (max)			
		9064	red		
CdSe/CdS	ITO/PEDOT/poly-TPD/QD/Alq_3/Ca/Al	3200	orange		2007[405]
CdSe/CdS/ZnS		4470	yellow		
		3700	green		
ZnCdSe	ITO/NiO/QDs/ZnO:SnO_2/Ag	1950	red	~0.1	2008[266]
CdSe/ZnS	ITO/NiO/QDs/Alq_3/Ag/Mg/Ag	3000	red	~0.18	2006[404]
CdSe/ZnS	ITO/PEDOT/PFH-MEH/QDs/Alq_3/Ca/Al		white	~0.24	2005[413]
CdSe/ZnS	ITO/PEDOT:PSS/TPD/QD(monolayer)/TAZ/Alq_3/Mg/Ag	100	white	~0.36	2007[93]
CdSe/ZnS	Sapphire/p-GaN/QDs/n-GaN/In		red	0.001−0.01	2005[406]
ZnCdS	ITO/PEDOT:PSS/spiroTPD/TPBi/Mg:Ag/Ag	15	blue	0.4	2009[414]
ZnSe/CdSe/ZnS		28	green	2.6	
ZnCdSe		7	red	1.0	
CdSe/ZnS		13	orange	2.7	
CdSe/CdS/ZnS	ITO/PEDOT:PSS/TFB/QD/TiO_2/Al	12 380	red		2009[415]

[a] Abbreviations: PPV (poly(*p*-phenylenevinylene)), TPD (*N*,*N*′-bis(4-butylphenyl)-*N*,*N*′-bis(phenyl)benzidine), TAZ (3-(4-biphenylyl)-4-phenyl-5-*t*-butylphenyl-1,2,4-triazole), Alq_3 (tris(8-hydroxyquinoline) aluminum), TPBI (1,3,5-tri(*N*-phenylbenzimidazol-2-yl)benzene), HTL (hole transport layer), ETL (electron transport layer), HBL (hole blocking layer), TPBi (2,2′,2″-(1,3,5-benzenetriyl)-tris(L-phenyl-1*H*-benzimidazole), spiroTPD (spiro-*N*,*N*′-diphenyl-*N*,*N*′-bis(3-methylphenyl)-(1,1′-biphenyl)-4,4′-diamine), TFB (poly[(9,9-dioctylfluorenyl-2,7-diyl)-*co*-(4,4′-(*N*-(4-*sec*-butylphenyl)) diphenylamine)], CBP (4,4′-*N*,*N*′-dicarbazolyl-biphenyl).

composed of PPV as the HTL and TOPO capped CdSe or CdSe/ZnS core−shell NCs as the ETL.[400] The device emission was almost exclusively generated within the inorganic layer, although a very weak EL signal from the PPV appeared at high applied voltages. The devices showed $\eta_{ext} \approx 0.1\%$ and operation lifetimes above 50−100 h. Schlamp et al. reported devices combining PPV HTL layer and a film of CdSe/CdS core/shell NCs as emitting and ETL layer.[399] The emission color of the device was tunable from red to green; η_{ext} improved to 0.22% at luminance of 600 cd/m^2 and current density of 1 A/cm^2. The devices operated at voltages as low as 4 V and showed lifetimes under constant current flow of hundreds of hours. However, even in those improved QD-LEDs, poor electron transport through the QD multilayers led to imbalanced charge injection, and, consequently, the luminescence efficiency of the QD-LED was still low (~0.1 cd/A) as compared to single-crystal and organic LEDs.

The breakthrough in performance of QD-LEDs was achieved when a single monolayer of CdSe/ZnS core/shell NCs was sandwiched between hole- and electron-transport organic layers.[408] The devices were fabricated by the phase separation of the QDs (TOPO capped CdSe/ZnS core−shell NCs) and hole-transporting *N*,*N*′-bis(4-butylphenyl)-*N*,*N*′-bis(phenyl)benzidine (TPD) organic molecules. The QD concentration in TPD/QD solutions was optimized to form a complete single monolayer on top of continuous TPD film during spin-coating. To form ETL, a layer of tris(8-hydroxyquinoline) aluminum (Alq_3) was thermally deposited on top of the QD layer followed by evaporation of the top electrode with a low work function, typically Al or its alloys (Figure 35a). The holes are injected from the indium tin oxide (ITO) contact into the TPD host matrix and are transported toward the single QD monolayer. Similarly, electrons are injected from the Mg:Ag cathode into the Alq_3 and are transported to the QDs. Well-optimized HTL and ETL allowed for balanced injection of carriers into the QD recombination layer. Exciton generation on QDs occurred via two parallel processes: direct charge injection and exciton energy transfer from organic molecules. For direct charge injection, electrons may be trapped at the QDs due to the relative energy alignment of the lowest unoccupied molecular orbital (LUMO) levels of TPD, Alq_3, and the QDs (see the energy diagram in Figure 35c). For these charged QDs, the barrier to hole injection from the TPD is reduced. Upon acceptance of holes from TPD, excitons form on the QDs and can subsequently recombine radiatively. Alternatively, excitons can be formed on organic molecules that are near grain boundaries, interstitial spaces, and voids in the single QD monolayer. These excitons can then undergo Förster energy transfer to the lower-energy QD sites, where they recombined radiatively. The emission of TDP and Alq_3 significantly overlapped with the absorption spectra of CdSe/ZnS NCs, allowing efficient exciton energy transfer from these molecules to the NCs. Here, the NCs with large absorption cross sections are desirable to maximize the efficiency of Förster energy transfer from electroluminescing organic molecules to NCs. Nonradiative transfer of excitons from organic layers into the NCs solves the problem of imbalanced carrier injection and helps in preventing NC charging.[412]

The external quantum efficiency of devices with the layer sequence of glass/ITO/TPD/CdSe_NCs/Alq_3/Mg exceeded $\eta_{ext} = 0.4\%$ for a broad range of luminances (from 5 to 2000 cd m^{-2}), peaking at $\eta = 0.52\%$ at 10 mA cm^{-2}. The luminance of 100 cd m^{-2} was achieved at a current density 5.3 mA cm^{-2} and voltage 6.1 V (i.e., 1.9 cd/A^{-1}). At 125 mA cm^{-2}, the brightness of device was 2000 cd m^{-2} (1.6 cd A^{-1}), which was a dramatic improvement over previously reported QD-LEDs. To further improve the color purity, a thin hole blocking layer (HBL) of 3-(4-biphenylyl)-4-phenyl-5-t-butylphenyl-1,2,4-triazole (TAZ) was evaporated between the layer of QDs and Alq_3 (Figure 35b). TAZ suppressed Alq_3 emission by blocking transport of both holes and excitons into the Alq_3 and allowed one to obtain devices with pure emission from CdSe/ZnS NCs.

For similar device structures, the EL peak was spectrally tuned from green to red by varying the diameter of CdSe

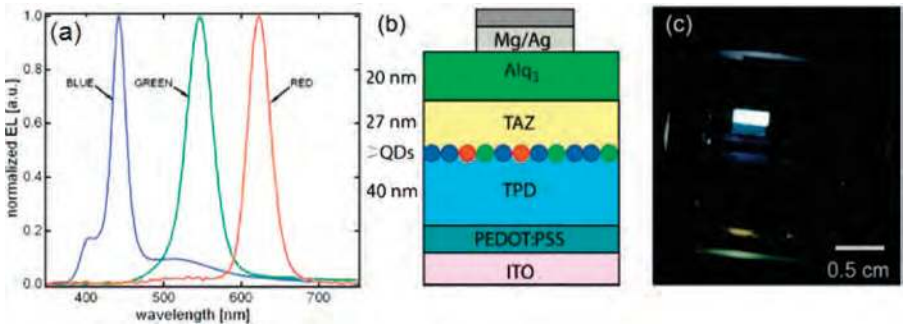

Figure 36. White light emitting LED utilizing a mixture of red, green, and blue emitting semiconductor nanocrystals. (a) Normalized EL spectra of devices containing only blue-, green-, and red-emitting nanocrystals. (b) Device cross section, and (c) photograph of white QD-LED. Reprinted with permission from ref 93. Copyright 2007 American Chemical Society.

core in emitting CdSe/ZnS core−shell NCs from 3.2 to 5.8 nm; η_{ext} was improved to ~1.1% by optimizing the thickness of ZnS shell.[407] Optimization of packing and ordering of NCs allowed enhancing η_{ext} to over 2% (>1 lm W^{-1}) with a maximum brightness of over 7000 cd m^{-2}.[402] The electroluminescence spectrum was dominated by the NC emission with excellent color purity.[402] Steckel et al. reported LEDs utilizing $Cd_xZn_{1-x}Se/Cd_yZn_{1-y}S$ core−shell NCs integrated into a four-layered HTL/QDs/HBL/ETL structure.[403] The color saturated green emission was achieved with a peak η_{ext} of 0.5% at low operating voltages (<10 V). For blue QD-LEDs, the same authors used CdS/ZnS NCs as the emitting materials.[416] Zhao et al. deposited a thin layer of CdSe/CdS QDs on top of thermally cross-linked solvent-resistant HTL (polystyrene(PS)-*N*,*N*′-diphenyl-*N*,*N*′-bis(4-*n*-butylphenyl)-(1,1′-biphenyl)-4,4′-diamine(TPD)-perfluorocyclobutane-(PFCB)) and reported efficient LEDs with a narrow (30 nm, fwhm) EL bandwidth, an external quantum efficiency of 0.8% at 100 cd m^{-2}, and a maximum luminance greater than 1000 cd m^{-2}.[409]

In 2007, Sun et al. reported high-performance QD-LEDs with saturated red, orange, yellow, and green emissions, all utilizing CdSe/ZnS core−shell NCs (Figure 35d).[405] As compared to the Bulovic−Bawendi design, they introduced a layer of PEDOT:PSS between ITO electrode and HTL to improve the hole injection and used poly-TPD spin coated from chlorobenzene solution as the HTL. Even more important, they found that the thickness of the NC layer determines the efficiency and luminance of QD-LED and should be carefully optimized for each color, depending on the size and structure of NCs. The optimized thickness of NC layers for red, orange, yellow, and green QD-LEDs was 2.0 (17.0 nm), 2.5 (18.75 nm), 4.0 (22.0 nm), and 7.0 (21.0 nm) NC layers, respectively. The maximum luminance reached 9064, 3200, 4470, and 3700 cd m^{-2}, respectively, and these are probably the highest values reported to date for correspondingly colored QD-LEDs. Moreover, these QD-LEDs had low turn-on voltages of 3−4 V, improved injection efficiency (1.1−2.8 cd A^{-1}), saturated color with narrow EL bandwidth, and longer operation times at high luminance ($t_{50\%}$ = 300 h at >1100 cd m^{-2}).[405] Uniform and defect-free EL emission from the QDs over a large surface area (1.5 cm × 2.5 cm) was displayed, promising for the application of QD-LEDs in large-area displays.

Other potential areas of application for thin film LEDs are large area lighting systems and backlighting for liquid crystal displays. Such applications require LEDs emitting white light. Here, colloidal NCs with their tunable emission colors and the possibility of inexpensive solution-based device fabrication have a potential to successfully compete with other technologies such as OLEDs. Li et al. fabricated white organic/NCs LEDs by combining blue emitting poly[(9,9-dihexyloxyfluoren-2,7-diyl)-*alt*-*co*-(2-methoxy-5-phenylen-1,4-diyl)] (PFH-MEH) polymer doped with red-emitting QDs and green-emitting Alq_3.[413] The key for balanced white emission in the hybrid ternary systems PFH-MEH/QDs/Alq_3 was the charge-transfer processes from PFH-MEH and Alq_3 to the QDs. Maximum external quantum efficiency of 0.24% at 1 mA cm^{-2} and 11 V during operation in air was reported.

Anikeeva et al. reported white QD-LEDs with the emitting layer assembled of a balanced mixture of red, green, and blue emitting NCs integrated into ITO/PEDOT:PSS/TPD/QDs/TAZ/Alq_3 device (Figure 36).[93] The mixed-monolayer QD-LED revealed uniformly white luminescence with the international commission on illumination (CIE) coordinates (0.35, 0.41) at an applied voltage of 9 V. At 5 V applied bias (1.51 mA/cm^2), the peak η_{ext} of white QD-LED was 0.36%, corresponding to 0.9 cd A^{-1}. The independent processing of HTL and emitting layer of NCs provided precise tuning of the emission spectrum by simply changing the color ratio of QDs without altering the device structure.

In contrast to significant efficiency improvements of QD-LEDs, the lifetime of hybrid organic/NC devices is limited by the instability of the metal contacts and degradation of organic components under high current operation conditions. In an attempt to overcome these limitations, the organic hole transport and electron transport layers have been replaced with much more robust inorganic materials. Caurge et al. reported QD-LEDs with p-type inorganic NiO films as HTL.[266] Inorganic NiO films demonstrated higher chemical, thermal, and electrical stability as compared to TPD and other tested organic materials. A maximum $\eta_{ext} \approx 0.18\%$ and brightness ~3000 cd m^{-2} were achieved by optimizing resistivity of the NiO layer. In the next step toward all-inorganic QD LEDs, same authors fabricated inorganic ETL by replacing TAZ and Alq_3 layers with sputtered amorphous ZnO:SnO_2 semiconductor.[266] The all-inorganic QD-LED combined HTL of p-type NiO, luminescent $Cd_{1-x}Zn_xSe$ NCs as the emitting layer, and n-type ZnO:SnO_2 ETL as shown in Figure 37. These devices demonstrated pure QD emission with the peak luminance of 1950 cd m^{-2} and enabled very high injection currents of 3.5A cm^{-2}. The maximum η_{ext} was about 0.1%. The ability of inorganic HTL and ETL to drive high currents into QD layers may one day open up bright perspectives for electrically pumped lasers on colloidal NCs.

Highly luminescent spectrally tunable core−shell NCs can also be coupled to bright and efficient single-crystal LEDs. This approach utilizes NCs as the down-converting medium, which efficiently absorbs blue light emitted by, for example,

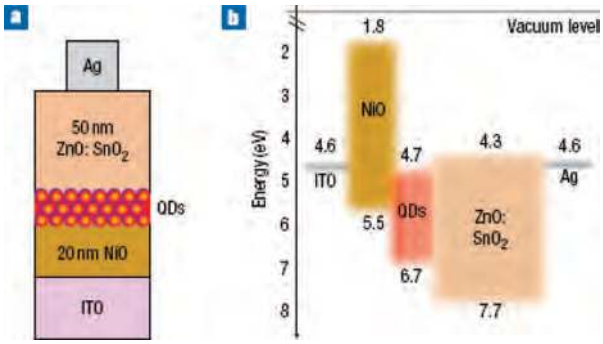

Figure 37. Structure of an all-inorganic QD-LED. (a) Schematics of the device structure showing the ITO anode, NiO hole transport layer, QDs active luminescent layer composed of $Cd_{1-x}Zn_xSe$ nanocrystals, $ZnO:SnO_2$ electron transport layer, and silver cathode. (b) A band diagram determined from UV photoemission spectroscopy and optical absorption measurements, giving the approximate electron affinities and ionization energies of the QD-LED materials. Reprinted with permission from ref 266. Copyright 2007 Nature Publishing Group.

highly efficient GaN LED and converts it to another wavelength of choice. Taking into account the outstanding characteristics of III−V LEDs, the overall performance of such tandem device can be superior to an LED based on direct injection of carrier into the NCs. Lee et al. combined GaN LED with CdSe/ZnS NC−polymer composites.[417] Roither et al. recently reported colloidal CdSe/ZnS NCs operating as color converters for InGaN LEDs with high color stability. The color conversion was further enhanced using dielectric mirrors with high reflectivity at the emission band of NCs.[418] In 2008, Evident Technologies, Inc. released Christmas lights using III−V LEDs and luminescent NCs as the down converters. These Christmas lights were probably the first commercial optoelectronic devices utilizing colloidal quantum dot technology.

Klimov et al. studied an optically pumped device with a monolayer of CdSe/ZnS NCs on top of the InGaN quantum well.[419] Direct nonradiative Förster-type energy transfer from InGaN quantum wells to the NCs resulted in an impressive ~55% light conversion efficiency; the energy transfer rate was sufficiently high to provide noncontact pumping into NCs from the quantum wells. The LEDs with a single monolayer of CdSe NCs deposited on top of the electrically driven InGaN/GaN quantum well structure demonstrated nonradiative energy transfer from quantum wells into the QDs.[420] The color conversion efficiency was 13%, and the overall efficiency of QD-based hybrid LED was higher than that of III−V LEDs with conventional down-converting phosphor or stand-alone QD-LEDs. Mueller et al. also reported LEDs with semiconductor NCs directly integrated into the p−n junction formed by GaN injection layers.[406] The NCs/GaN hybrid structure was fabricated by encapsulation of CdSe/ZnS NCs within the GaN matrix. The electrical pumping led to emission exclusively from the NCs with a turn-on voltage of 3.5 V. Also, the EL spectra could be tuned by varying the NC diameter. Along the same lines, Chen et al. reported white light generation from red emitting CdSe-ZnS QDs deposited on top of a blue/green InGaN/GaN quantum well LED.[421] Nizamoglu et al. recently reported white light generation controlled by multicolor-emitting CdS/ZnS/CdS NCs combined with InGaN/GaN quantum well LEDs.[418]

After about 15 years of research and development, NC LEDs are approaching commercialization stage; they can now compete with organic-LEDs and other emerging display and solid-state lighting technologies. Commercial perspectives of QD-LEDs will depend on their ability to compete with OLEDs in performance, cost, lifetime, manufacturability, etc. One of the serious obstacles for using QD LEDs in consumer products is the toxicity of Cd-based NCs. Serious attempts are made to address this issue by developing highly luminescent NCs not containing toxic elements, for example, InP/ZnS core−shells[422,423] or $CuInSe_2$.[397,424] Another promising avenue for QD LEDs is the near-infrared (near-IR) emitting devices based on narrow gap semiconductor NCs, such as InAs,[425,426] PbSe,[31,427] and HgTe.[428] Development of inexpensive large area near-IR LEDs addresses the needs of optical communications, chemical spectroscopy, and chemical sensing; such devices are considered for on-chip integration for optoelectronic circuits, etc. Several research groups recently reported solution-processed LED with the emission picked at telecommunication wavelengths of 1.3 and 1.55 μm.[425,429] There are several recent review articles covering this interesting topic.[425,430,431]

7.2. Photodetectors

There is a large variety of sensitive photon detection systems operating in the visible spectral range: photomultiplier tubes, single crystal silicon detectors, and CCD cameras. Unfortunately, in the infrared the situation is not nearly as good; available detection systems, especially array-based, are either insensitive or very expensive. The reason is simple; silicon, which is a main workhorse for CCD and APD technologies, cannot operate beyond 1.1 μm, whereas other materials show higher noise levels or are difficult to process using standard single-crystal-based microfabrication techniques. At the same time, markets for near-IR and mid-IR detectors span from telecommunication to night-vision systems, bioimaging, environmental sensing, spectroscopy, and chemical analysis. For all of those areas, it is highly desirable to find new materials that enable high detectivity at a reasonable cost. Recent developments provide good expectations for photodetectors based on NC solids.[270]

Application of NCs for photon detection is receiving steadily growing attention. The progress in this direction is driven by the unique opportunities given by the size-tunable NC electronic structure, NC surface chemistry, and surface trap engineering, compositional flexibility, and the possibility to manufacture devices using inexpensive solution processing. Relatively wide band gaps of conductive organic polymers and small molecules limit their absorption to visible spectral range. For applications requiring light absorption/emission in the near-IR region, inorganic NCs, especially those made of narrow-gap PbS, PbSe, PbTe, HgTe, InAs, and InSb semiconductors, are in strong position to compete with other technologies, because their band gap can be precisely tuned from the visible spectral region upto the wavelengths of 3500 nm. For more detail on the synthesis and optical properties of IR-active NCs, we refer the readers to a recent review by Rogach et al.[425]

7.2.1. Figures of Merit for Photoconductive Detectors

Photoconductive detectors change their electrical conductivity under illumination due to the generation of additional mobile charge carriers. Other types of IR photodetectors (bolometers and pyrometers) exploit thermal effects and will not be discussed here. The photoconductivity can be observed

in virtually any semiconductor; however, development of a photoconductor with characteristics suitable for a particular application is a big scientific and technological challenge. There are several figures of merits used to characterize photoconductive photodetectors.[432,433] These are responsivity, spectral response, noise-equivalent power (NEP), detectivity, response time, and frequency response.

Responsivity (R_i). This parameter is also often called sensitivity. The responsivity provides a quantitative measure for the output signal such as photocurrent i_{ph} per watt of the input optical power P_{in}. R_i is the function of both modulation frequency (f) and photon wavelength (λ):

$$R_i(f,\lambda) = \frac{i_{ph}}{P_{in}} \tag{32}$$

Spectral response describes the spectral dependence of R_i, that is, the dependence of R_i versus λ. Typically, responsivity of IR detectors rises monotonically with increasing wavelength, then peaks and drops to zero upon reaching semiconductor band gap energy (so-called cutoff wavelength of intrinsic photodetector). In NC photodetectors, the spectral response generally follows the shape of the NC absorption spectrum.

Noise-Equivalent-Power. The internal noise current i_n is the main factor limiting the ability to detect small optical signals because the signal produced by the input power must be above the noise level. The noise-equivalent-power (NEP) is determined as a light power that yields a signal-to-noise ratio equal to 1 and can be expressed as:

$$\mathrm{NEP} = \frac{i_n}{R_i} \tag{33}$$

Detectivity. For comparison of different devices, it is important to provide an area independent figure of merit D^* (detectivity):

$$D^*(\lambda,f) = \frac{R_i\sqrt{A\Delta f}}{i_n} \tag{34}$$

where A is the detector area. The detectivity D^* is the root-mean-square signal-to-noise output when 1 W of monochromatic radiant flux modulated at frequency f is incident on 1 cm^2 detector area, with a noise-equivalent bandwidth of 1 Hz. D^* is typically reported in Jones (1 Jones = 1 cm $Hz^{1/2}$ W^{-1}).

Response time (t). Response time, also known as the time constant, is calculated as follows:

$$t = \frac{1}{2\pi f_{3db}} \tag{35}$$

where f_{3db} is the frequency at which the signal power is 3 dB lower than the value at zero frequency; that is, the photocurrent is $1/\sqrt{2} \approx 0.707$ of that at zero frequency.

Frequency Response. At low modulation frequencies, the photocurrent can follow the rise/decay of the illumination intensity. However, at higher frequencies, responsivity becomes a strong function of the response time:

$$R(f) = \frac{R_0}{\sqrt{1 + (2\pi f t)^2}} \tag{36}$$

where R_0 is the responsivity at zero frequency, and t is the response time.

Other important characteristics of photodetectors are the linear dynamic range (the range over which detector responds linearly to the incident optical power) and the noise spectrum (i.e., the dependence of i_n vs f).

7.2.2. Photoconductivity in Nanocrystal Solids

A basic structure of the photoconductive detector is depicted in Figure 38. Ohmic contacts are attached to a slab or a thin film of a semiconductor.[434] For the latter case, smaller electrode spacings are accessible, favorable for efficient collection of photogenerated charges. For NC-based photodetectors, thin film geometry is preferred because homogeneous submicrometer-thick NC films can be readily prepared from colloidal solutions. Furthermore, it is a common practice to use a substrate with lithographically defined electrodes and deposit a layer of NCs on top of the electrodes (Figure 38b).

The photocurrent in a semiconductor can be generally described as:

$$i_{ph} = \eta e N_\lambda G_i \tag{37}$$

where η is the quantum efficiency (i.e., the number of excess carriers produced per absorbed photon), e is the elemental charge, N_λ is the number of photons of wavelength λ absorbed in the sample per unit time, and G_i is the internal (photoconductive) gain.

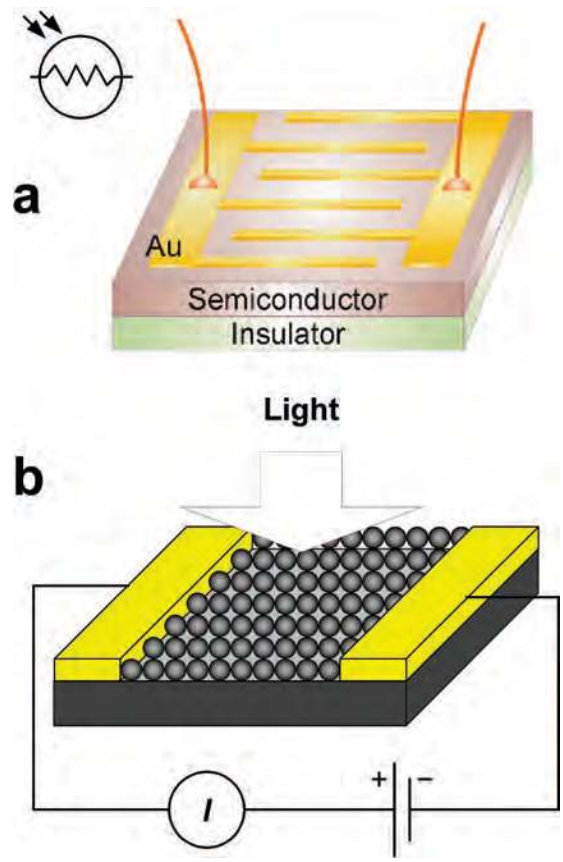

Figure 38. (a) A sketch of typical thin film photoconductive photodetector. Interdigitate electrode structure is deposited onto the surface of active semiconductor. (b) A photodetector geometry that is typically used for NC-based devices: thin NC layer is deposited on top of the prepatterned electrode structure. Au is shown as an example of metal contact material.

Photoconductive gain is determined by the ratio between the free carrier lifetime (τ) and transit time (T_t):

$$G_i = \frac{\tau}{T_t} \tag{38}$$

G_i is a very important parameter, which is determined by the number of electrons flowing through the external circuit per each absorbed photon or, in other words, the number of cycles the majority carriers can make before recombining. $G_i \leq 1$ represents the case of a primary photoconductor. $G_i > 1$ indicates the presence of the secondary photoconductivity, when more carries flow through the circuit than the number of photons absorbed per unit time. Photoconductive gain can be efficiently controlled by adjusting both τ and T_t. The former is mainly controlled by engineering trapping states, whereas the latter is determined by device design and electronic properties of material. In the presence of long-living traps, the carrier lifetime is effectively prolonged, and the majority carriers can cycle in the circuit until they recombine with trapped carriers. The secondary photocurrent, induced by traps, can in principle last for hours and days; its duration is determined by the release rate of minority carriers from the trap states. This situation typically results in a slow decay of the photocurrent after illumination turn off.

Equation 38 demonstrates the main trade-off for photoconductive detectors. If the fast response is the goal, the carrier lifetime must be short. This leads to a low gain and lower sensitivity. On the other hand, very sensitive photoconductors are slow and have a long response time. With respect to the NC photodetectors, this situation will be illustrated in the following sections. G_i can generally take values from much less than unity to the upper limit of $\sim 10^6$ given by the restrictions imposed by the charge-limited current flow, impact ionization, and dielectric breakdown.[434] Lifetime τ can range from 10^{-13} s to many seconds depending on the particular material. For example, in highly sensitive photodetectors based on PbS NC solids, τ was reported to lie in the millisecond-to-second time scale, and G_i was estimated to be about 10^2-10^4.[265,435] Transit time T_t depends on the device length of conducting channel L, electric field E, and carrier mobility μ:

$$T_t = \frac{L}{\mu E} \tag{39}$$

Taking into account eq 37, $E = V/L$ (where V is applied voltage), and $N_\lambda = P_{in}/h\nu$, we can express the photocurrent as:

$$i_{ph} = \eta e\left(\frac{P_{in}}{h\nu}\right)\left(\frac{\mu\tau V}{L^2}\right) \tag{40}$$

Noise. The main noise sources in photoconductors are Johnson noise, generation-recombination, and $1/f$ noise. The Johnson noise i_j originates from the fluctuations induced by the thermal motion of the charge carriers, which causes the fluctuating charge gradients. It is expressed through the noise-equivalent bandwidth Δf and detector resistance R as shown by eq 41:

$$i_j = \sqrt{\frac{4kT\Delta f}{R}} \tag{41}$$

Johnson noise is independent of the applied bias; all other kinds of noise are bias dependent. Generation-recombination noise i_{gr} originates from the statistical fluctuations in the generation and recombination rates of nonequilibrium charge carriers. $1/f$ noise is given by:

$$i_{1/f} = \sqrt{\frac{i^2\Delta f}{f}} \tag{42}$$

where f is the electrical frequency, Δf is the electrical bandwidth, and i is the dc current. The $1/f$ noise is affected by the nonohmic contancts and surface traps. Therefore, reduction of $1/f$ noise is rather an experimental art. Usually, $1/f$ noise is significant at low modulation frequencies, while at higher frequencies its amplitude drops below that of Johnson noise or generation-recombination noise.

7.2.3. Photoconductivity Measurements

Figure 39 shows a typical setup for photoconductivity measurements. Very similar designs were used for measuring NC-based samples.[265,436−438] This setup allows one to obtain spectral responsivity and all other figures of merits described in section 7.2.1. A very similar setup is used for characterization of solar cells (see section 7.3), and we will describe it here in more detail.

A suitable light source (typically quartz, tungsten, xenon lamp) is used depending on the spectral region of interest. The light is dispersed by a monochromator and focused onto the sample. The optical flux at the wavelength of interest can be measured by placing a power meter or calibrated detector in the place of sample. The input optical power is then calculated taking into account the actual area of tested photodetector. The sample has to be biased using low-noise source, and its $I-V$ characteristics are recorded under illumination and in the dark. To obtain a high signal-to-noise ratio, the photocurrent response is usually measured using a lock-in amplification; the incident light is modulated by a mechanical chopper, and the modulation frequency and phase are used as a reference for lock-in amplifier of chopping. The use of lock-in technique allows for the measuring of very weak photocurrents in the presence of a noise signal.

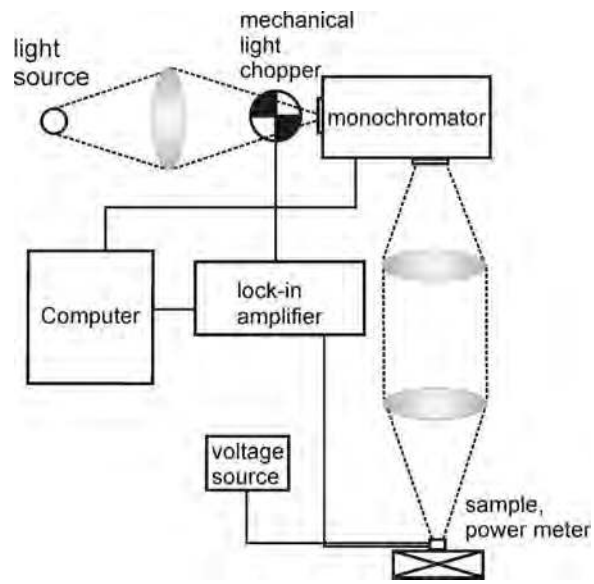

Figure 39. Typical experimental setup for photoconductivity measurements.

An attenuator (a neutral density filter) is placed between the light source and chopper to study the dependence of photocurrent on the intensity of incident light. Noise currents can be measured using a low-noise preamplifier and oscilloscope. Ideally, noise and leakage currents associated with the experimental setup should be eliminated wherever possible by using triaxial cables.

7.2.4. Photodetectors Based on Treated Nanocrystal Solids

The first detailed photoconductivity studies on TOPO−TOP capped CdSe NC solids by Leatherdale et al.[439] revealed that: (i) free carriers in CdSe NC solid originate from electron−hole pairs (excitons) photogenerated within individual NCs; (ii) charge separation was much slower as compared to the interband relaxation; and (iii) charge transport was dominated by tunneling of carriers through the interparticle medium. When studied at low temperatures, TOPO−TOP capped CdSe solids showed very low dark currents i_d (sub-pA range, often limited my measurement resolution), $i_{ph}/i_d \approx 10^2$, low G_i of 10^{-4}, temperature-independent nonlinear $I-V$ characteristics, and strong field-dependence of photocurrent. Large interparticle spacing, insulating nature of surface ligands, and high exciton binding energy (~200 meV for 2 nm CdSe NCs) resulted in negligible thermally assisted separation of photoexcited carriers (i.e., exciton ionization). These results were explained by the interplay of tunneling rate, charging energy, and the rates of carrier generation and recombination.

To improve the interparticle charge transport, CdSe NC solids were treated with small molecular linkers: alkylamines or strong bases.[293,295] The highest photocurrents on CdSe NC solids were achieved after soaking films of TOPO−TOP capped CdSe NCs in butylamine or sodium hydroxide followed by drying at 70 °C.[293] The improvement of photocurrent in this case was attributed to an increase of the exciton ionization efficiency due to an decrease in interparticle spacing and better surface passivation. With Au electrodes, G_i was limited to 1, because of the blocking nature of Au contacts to CdSe NCs (see section 6.1). Using butylamine-treated CdSe NC solids, Oertel et al.[294] fabricated photodetectors by sandwiching NC layer between ITO/PEDOT:PSS and Ag electrodes. Under illumination of 110 mW/cm^2 (514 nm), devices exhibited $i_{ph}/i_d \approx 10^3$ at zero applied bias (photovoltaic operation), and 3 dB bandwidth of 50 Hz. However, no detectivity values were reported. G_i of about 10 was achieved for CdTe NC solids prepared and treated in a similar manner.[440] In that case, high photoconductive gains were possible due to hole injection from Au contacts into CdTe NCs (injecting contacts). In CdTe NC solids, holes were found to be the majority carriers. Porter et al. fabricated primary photoconductors (i.e., no or little trap-induced photocurrents) with decreased nonradiative decay rate of the excitons using annealed and chemically treated films of core−shell CdSe/ZnS NCs.[296] They observed (i) the unity internal quantum efficiency at room temperature, (ii) the increase in the magnitude of photocurrent upon increase of temperature, and (iii) low dark currents and a 3 dB bandwidth of 14 kHz.

The further progress in NC-based photoconductors led to the near-IR detectors with device characteristics comparable to commercial devices.[270] In 2006, Konstantatos et al. reported simple but highly sensitive IR detectors based on PbS NCs.[265] This was also one of the first works presenting thorough characterization of device characteristics, setting high standards for subsequent studies. Devices were fabricated by spin-coating butylamine-treated PbS NCs to form submicrometer thick films on the prepatterned electrode structure (Figure 38). The performance of fabricated devices was found to be sensitive to the postdeposition treatment. The best characteristics were obtained after treating the films with methanol under inert atmosphere followed by controllable surface oxidation. Unprecedented high detectivity of ~2 × 10^{13} Jones at the modulation frequency of 30 Hz, higher than that of commercial InGaAs photodiodes, and more than 60 dB linear dynamic range were reported (Figure 40). High gain of $G_i \approx 10^2-10^4$ was attributed to the presence of long-living traps electron traps generated by chemical treatment of the NC surface. In 2007, the same authors reported detectors based on very small (~2 nm) PbS NCs with cutoff wavelengths of 850−900 nm, suitable for sensing in the visible spectral region.[435]

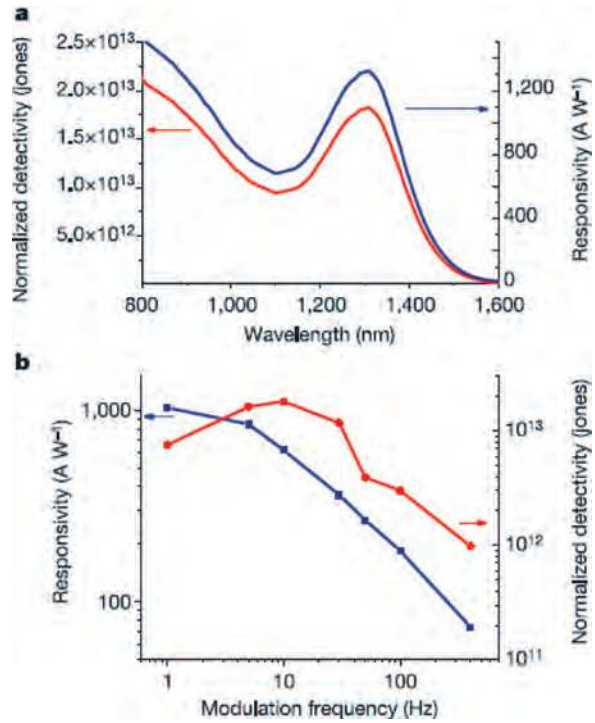

Figure 40. Characteristics of highly sensitive near-IR photodetectors based on PbS NC solids.[265] (a) Spectral response and detectivity spectrum. (b) Electrical frequency response for the same device under applied bias of 40 V. Devices consisted of 0.5 μm thick NC films deposited on prepatterned electrodes with the channel length of 5 μm and width of 3 mm. Reprinted with permission from ref 265. Copyright 2006 Nature Publishing Group.

In general, commercially competitive IR photodetectors must have the highest possible D^* (typically $10^{12}-10^{13}$ Jones) and the response time as short as possible, on the order of tens milliseconds to achieve the imaging rate of 10−60 frames per second. Combining high detectivity with fast response can be nontrivial problem for the detectors where traps play an important role in the photocurrent generation. Trapping effectively increases the photoconductive gain (eq 38) by increasing carrier lifetime. On the other hand, short response time requires fast decay of the photocurrent (i.e., short carrier lifetime). The Sargent group invested considerable effort to learn about the nature of long-living trap states in PbS NCs and to improve the response time of PbS-based detectors.[441−443] It was found that by

treating NC films with different molecules (butylamine, formic acid, small thiols, etc.), it is possible to control the chemistry of surface sites acting as the trap states and, consequently, the detector response time. For example, the shortest time constant of ~33 ms and $D^* > 10^{12}$ were obtained by treating films with ethanethiol in acetonitrile,[442] which led to the formation of $PbSO_3$ species at the NC surface upon exposure to air.

HgTe is another narrow gap semiconductor suitable for detector applications. Efficient photocurrent generation and spectral response up to the wavelength of 1.8 μm was demonstrated in the films of thioglycerol-capped HgTe NCs.[444,445] In 2007, Böberl and co-workers reported inkjet printed photodetectors with $D^* \approx 10^{10}$ Jones using inks composed of concentrated solutions of dodecanethiol-capped HgTe NCs in chlorobenzene.[436] Glass slides with gold electrodes were used as substrates. By tuning NC size between 3 and 10 nm, spectral response was pushed to the mid-infrared up to 3 μm. The high flexibility in terms of the choice of substrates has been shown by infiltrating HgTe NCs into a porous alumina membrane.[437]

In the light of the general trend toward "greener" materials and methods, lead-, cadmium-, and mercury-free devices are highly desirable, especially for consumer applications. Konstantatos and co-workers recently showed efficient photodetectors utilizing arrays of Bi_2S_3 nanorods.[438] Devices were prepared and chemically treated similarly to the above-described PbS detectors and showed $D^* \approx 10^{11}$ Jones.[438]

A photodiode can potentially offer significantly higher response speed than the photoconductor. Clifford et al. demonstrated the fast and sensitive IR photodiodes based on PbS NC solids.[22] In these devices, the layer of PbS NCs was sandwiched between ITO and Al contacts. The device performance was determined by the Schottky barrier at the NC−metal interface (Schottky barrier in a NC solid was discussed in section 6.2). The built-in potential opens exciting opportunities for fast separation of photogenerated carriers. Because the carrier velocity is much higher in the depletion region than in the diffusion layer, the optimal device performance was obtained when the thickness of NC layer was adjusted so that there was no diffusion layer. The sensitivity-bandwidth product of the photodiodes was >1000-fold improved as compared to similar NC solids in the configuration of photoconductive phtodetectors.[270] This improvement originated mainly from much faster operation with 3 dB bandwidth of up to 35 kHz, while the detectivities of $\sim 10^{12}$ Jones were similar to previously reported values for photoconductive detectors.

7.2.5. Hybrid Photodetectors Using Nanocrystals and Semiconducting Organic Materials

In this section, we present several examples of photodetectors using blends of NCs with organic materials. In these systems, the use of NCs allowed one to obtain higher responsivity or extend spectral response to the infrared spectral region.

Small molecules such as fullerene derivatives or π-conjugated polymers are known as light-sensitive materials suitable for fabrication of solar cells and photodetectors. However, their spectral response is limited to the visible spectral region. Narrow gap NCs can be an excellent sensitizer when blended with semiconducting organic materials. The concept of hybrid organic−NC devices was used to examine synergistic light harvesting and charge transport. For example, 3 orders of magnitude enhancement of photocurrent was achieved by sensitizing crystalline arrays of C_{60} with CdSe NCs.[446] This enhancement was explained by efficient light absorption of CdSe NCs, fast electron transfer from NCs to C_{60}, and high carrier mobilities within the array of C_{60} molecules. A similar idea, but for the IR range, was demonstrated by combining PbS NCs and soluble C_{60} derivative, [6,6]-phenyl-C61-butyric acid methyl ester (PCBM).[447] Interestingly, the films of untreated, oleic acid capped PbS NCs are highly insulating and show very poor photoresponse. However, composite solids made of PbS/PCBM in a 1:1 weight ratio exhibited $D^* \approx 2.5 \times 10^{10}$ Jones and $i_{ph}/i_d \approx 10^4$. Importantly, spectral response follows the absorption spectrum of PbS NCs with cutoff wavelength in the near-IR. Reference samples of pure PCBM exhibited 2−3 orders of magnitude lower responsivity. These results combined with time-resolved luminescence and transient absorption measurements were explained by the efficient electron transfer from PbS NCs to PCBM.

The blends of oleic-acid capped PbSe NCs and poly-*N*-vinylcarbazole (PVK) exhibited 3% quantum efficiency in the near-IR.[448] Similarly, IR photoresponse with internal efficiency of $\sim 10^{-5}$ charges/photon was reported for hybrid detector based on PbS NCs and poly[2-methoxy-5-(2′-ethoxyloxy)-1,4-phenylenevinylene] (MEH-PPV).[449] For devices based on PbSe NCs and MEH-PPV, a 2−3-fold increase of the external quantum efficiency in the visible spectral region was observed, as compared to pure MEH-PPV.[450]

Recently, solution processed infrared photodiodes were integrated with amorphous Si active matrix (a-Si AM) backplanes.[451] PbS NCs were employed as infrared-sensitive inorganic component. Near-infrared photosensitivity of the imagers is provided by a nonstructured inorganic/organic bulk heterojunction operating in contrast to organic visible imagers[452] on the concept of charge separation between an infrared sensitizer (PbS NCs), and separate electron (PCBM) or hole (P3HT) accepting and transporting materials. Figure 41 illustrates an operation of such camera by recording the image of a monarch butterfly under the infrared illumination. The authors also demonstrated a real time infrared imaging at a frame rate of 5 Hz.

7.3. Nanocrystals in Solar Cells

The growing demand for renewable energy requires significant efforts to be invested in the development of efficient and inexpensive photovoltaic materials. Semiconductor NCs are considered promising candidates for photovoltaic applications due to the combination of superior optical and electronic properties of inorganic semiconductors with the opportunities for inexpensive, solution-based device fabrication. NC-based photovoltaics are probably the most desired kind of NC devices that can make a really significant technological impact. In this section, we discuss different approaches used to employ colloidally synthesized nanomaterials in photovoltaics, state-of-the-art developments in the field, and future perspective directions for NC-based solar cells.

7.3.1. Performance Metrics and Basic Operation Principles of Solar Cells

Photovoltaic cell contains materials that absorb light and separate photogenerated electron and holes. There are several

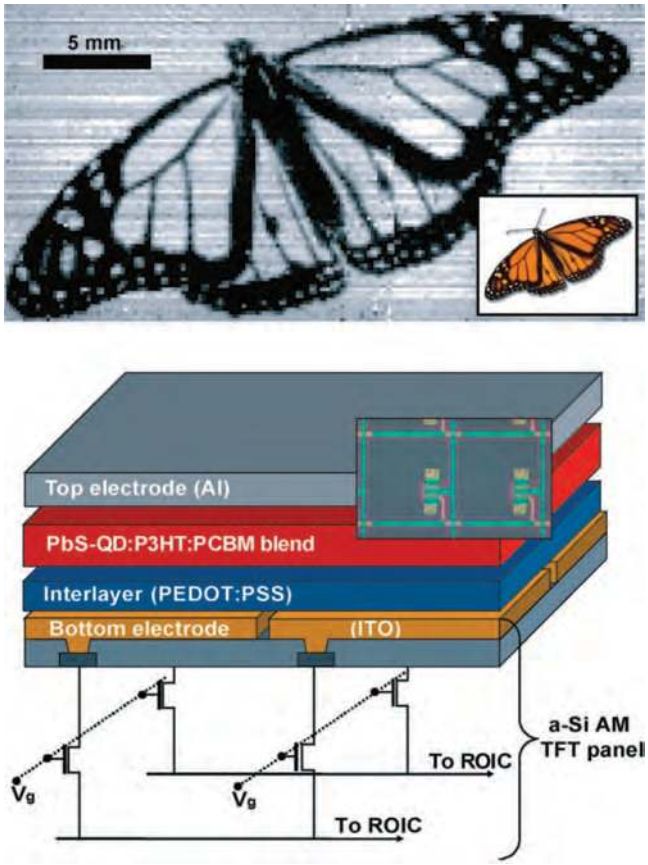

Figure 41. Infrared camera based on hybrid PbS:P3HT:PCBM blend as infrared-active layer. (Upper panel) Infrared shadow cast at 1310 nm (1.6 mW/cm^2) of a slide showing a monarch butterfly (cf., original slide in the inset). Butterfly is placed directly onto camera (256 × 256 pixels). (Bottom panel) Schematic illustration of the imager with an a-Si AM backplane and an unstructured inorganic/organic hybrid frontplane. The inset shows an optical micrograph of two active matrix pixels with a pixel pitch of 154 μm. Courtesy of Siemens Erlangen.[451] Reprinted with permission from ref 451. Copyright 2009 Nature Publishing Group.

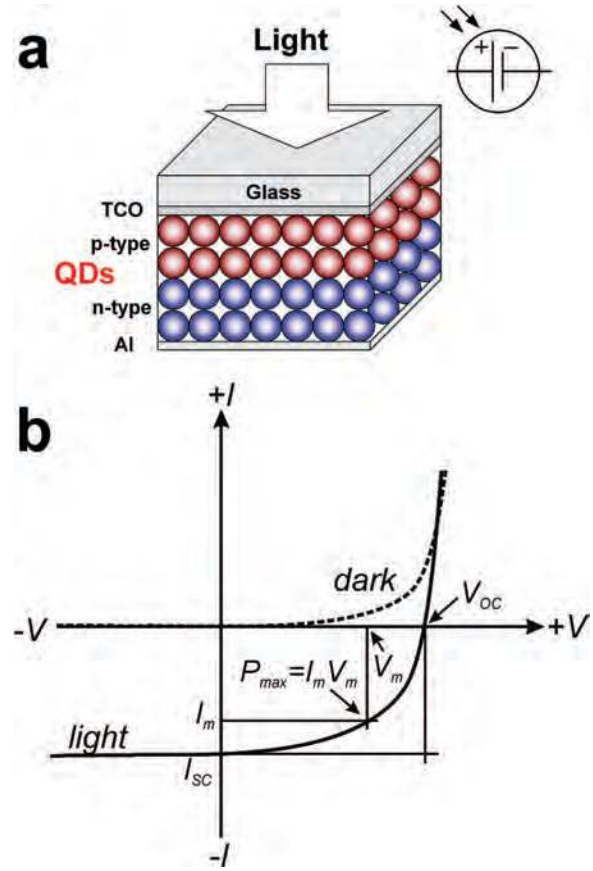

Figure 42. (a) A sketch of a solar cell with the layers of nanocrystals with n- and p-type conductivity. TCO is the transparent conductive oxide. (b) Current−voltage ($I-V$) characteristics of a solar cell. V_{oc} is the open-circuit voltage, and I_{sc} is the short-circuit current. The generated electrical power is characterized by its maximum value P_{max}.

kinds of solar cells, differing in the used materials and the approaches to separate positive and negative charge carriers. The common examples include a planar p−n junction, a network of donor−acceptor pairs, Schottky barrier, or semiconductor–liquid interface. Most of these have been considered for NC-based devices. For example, Figure 42a shows a device built of the layers of p- and n-type conducting NC solids sandwiched between transparent conductive oxide (anode) and a metal electrode (cathode).

Operation of a solar cell can be illustrated by its $I-V$ characteristics as shown in Figure 42b. In the dark, the $I-V$ curve is strongly asymmetric and shows a diode behavior, typical for a p−n or Schottky junction. There is very little dark current flowing under reverse bias, and there is an abrupt current increase when the device is biased in the forward direction. Under illumination, the $I-V$ curve of a solar cell exhibits a vertical shift caused by light-induced current generation (Figure 42b). Device produces power only when operating in the forth quadrant, that is, when biased in the forward direction and applied voltage is between zero and open circuit voltage V_{oc}. Many performance parameters for the cell can be determined from a simple $I-V$ scan, as described below. For more details on the operation principles of thin film solar cells, we refer the reader to several review articles.[453−456]

Open-circuit voltage (V_{oc}) is the difference of electrical potential between two terminals of device when there is no external load connected; that is, the circuit is broken or open. Under these conditions, there is no electric current flowing through the external circuit. The open-circuit voltage is the maximum possible voltage that can be generated by a solar cell. This parameter is directly related to the structure and energy diagram of the device. Because the mechanism of the photoconversion is different in different types of solar cells, different effects can contribute to V_{oc}. Thus, the built-in potential associated with p−n junction determines V_{oc} of conventional (e.g., Si or III−V) solar cells with a planar junction. In bulk heterojunction solar cells (e.g., organic P3HT/PCBM solar cells), a gradient of chemical potential of electrons and holes is created by the difference in the HOMO and LUMO levels of the donor and acceptor components. V_{oc} can be also created by the difference in the work functions of two metal contacts in a simple metal−semiconductor−metal structure or by the difference between the work function of the metal contact and the semiconductor quasi-Fermi levels in Schottky solar cells. Morphological features, chemical processes, and trap states formed at interfaces can greatly affect the value of V_{oc}. Some particular examples will be discussed later.

Short-circuit current (i.e., current under zero bias) is the parameter determined by the product of the charge carrier density n under illumination, carrier mobility μ, and the electric field E acting on the carriers:

$$I_{SC} = en\mu E \quad (43)$$

I_{SC} shows the maximum number of the photogenerated carriers that can be extracted from the solar cell. Hence, the external quantum efficiency, also known as incident photon to current efficiency (IPCE), can be calculated as:

$$\mathrm{IPCE}(\lambda) = \frac{1240}{\lambda}\frac{I_{SC}}{P_{in}} \quad (44)$$

where P_{in} is an incident power at wavelength λ. If one electron−hole pair is created and separated per every absorbed photon, the ultimate ICPE is 100%. Generally speaking, the fate of photogenerated carriers is determined by the product of $\mu\tau$ (μ is the mobility of charges, and τ is the carrier lifetime), which has to be large enough to enable carrier separation before their recombination. ICPE can exceed 100% for devices generating more than one electron and hole per absorbed photon, for example, via impact ionization or carrier multiplication processes.

Fill Factor (FF). The fill factor determines the quality of voltage−current characteristics. It is defined as the ratio of the maximum power P_{max} under matched load conditions to the product of the open circuit voltage V_{oc} and the short-circuit current I_{SC}:

$$\mathrm{FF} = \frac{I_m V_m}{I_{SC} V_{oc}} \quad (45)$$

FF depends on the ability of charges to reach the electrodes when the driving force for carrier separation is lowered by the external bias. Typically, shunt resistances inside a solar cell account for a decrease in the fill factor.

Power conversion efficiency (η) by definition is the maximum fraction of the input optical power converted into the electrical power:

$$\eta = \frac{P_{max}}{P_{in}} = \mathrm{FF}\frac{I_{OC}V_{SC}}{P_{in}} \quad (46)$$

To compare different solar cells, special optical source simulating the sun spectrum is used as an input optical power. This source called AM1.5 (air mass of 1.5) was characterized by the power density of ~1000 W/m^2 with the spectral intensity distribution matching that of sunlight at the earth's surface at an incident angle of 48.2°. A full description of the AM1.5 standard spectrum can be found at http://rredc.nrel.gov/solar/spectra/am1.5/. A typical experimental setup used to measure IPCE and other characteristics of a photovoltaic cell is shown in Figure 39. Table 5 provides a summary of NC-based photovoltaic devices reported in recent years. Different nanocrystalline materials and cell designs have been studied, but this work is currently far from completion. Below, we discuss several most promising directions in NC photovoltaics.

7.3.2. Nanocrystals in Hybrid Bulk Heterojunction Solar Cells

Polymer solar cells based on conjugated organic polymers or polymer/fullerene blends are promising alternatives to conventional silicon-based technology. They comprise low cost fabrication by means of different printing techniques[470] with the flexible choice of various substrates.[471,472] These days, cells with single active layer can achieve power conversion efficiency of about 5%.[473,474] Recently, efficiency of ~7% was demonstrated for a tandem solar cell with different band gaps.[475] The outdoor lifetime of such solar cell was found to be more than 1 year.[476]

The main factors limiting the performance of polymer solar cells are chemical and photochemical stability of polymers and contacts as well as relatively poor electronic properties of organic materials. Typically used polymers show reasonable hole mobility of ~0.1 cm^2 V^{-1} s^{-1}, while the electron mobilities are much lower (<10^{-4} cm^2 V^{-1} s^{-1}). Another limitation of plastic solar cells comes from

Table 5. Survey of Nanocrystal-Based Photovoltaic Devices[a]

NC materials	active layer design, electrodes	I_{SC} (mA/cm^2)	V_{OC} (V)	*FF*	η%, illumination	IPCE (%)/ wavelength	year, ref
CdSe NCs/P3HT	Al/**BH**/PEDOT:PSS/ITO	5.7	0.7	0.4	1.7% (AM1.5)	55%/485 nm	2002[457−459]
CdSe NCs/PPV	Al/**BH**/PEDOT:PSS/ITO	7.3	0.65	0.35	1.8% (AM1.5)	45%/485 nm	2003[460]
CdSe NCs, CdTe NCs	Ca/**CdTe-CdSe**/ITO	13.2	0.45	0.49	2.9% (AM1.5)		2005[168]
HgTe NCs/P3HT	Au/**BH**/TiO_2/ITO	2	0.4	0.5	0.4% (AM1.5)	10%/500 nm 2%/1100 nm	2006[461]
PbS NCs	Au/P3HT/**PbS**/ITO	0.13	0.4	0.38	0.02% (AM1.5)		2008[462]
CdSe hyperbranched NCs/P3HT	Al/**BH**/ITO	3.5	0.6	0.55	2.2% (AM1.5)	23%/500 nm	2007[396]
CdSe NCs	**NSSC**, Co(II)/Co(III) redox	3.15	0.61	0.6	1% (AM1.5)	36%/500 nm	2008[463]
Cu_2S NCs, CdS NCs	Al/**CdS/Cu_2S**/PEDOT:PSS/ITO	5.63	0.6	0.47	1.6% (AM1.5)	40%/600 nm	2008[464]
$CuInSe_2$ NCs	Glass/Mo/ **$CuInSe_2$**/CdS/ZnO/ITO	25.8	0.28	0.39	2.82% (AM1.5)		2008[465]
PbSe NCs	Mg/**PbSe**/ITO	17	0.23		1.1% (AM1.5) 3.6% (975 nm)	70%/600 nm 25%/1250 nm	2008[253]
PbSe NCs	Al/Ca/**PbSe**/ITO	24.5	0.24	0.41	2.1% (AM1.5)	62%/600 nm 25%/1400 nm	2008[271]
PbS NCs	Al/**PbS**/ITO	12.3	0.33	0.49	1.8% (AM1.5) 4.2% (975 nm)	60%/600 nm 37%/975 nm	2008[272]
Si NCs/P3HT	Al/**BH**/PEDOT:PSS/ITO	3.3	0.75	0.46	1.15% (AM1.5)	26%/500 nm	2009[466]
PbS NCs/Si	Al/a-Si/**PbS**/ITO	9	0.2	0.39	0.7% (AM1.5)	50%/500 nm 7%/1100 nm	2009[467]
$PbSe_xS_{1-x}$ NCs	Al/**$PbSe_xS_{1-x}$**/ITO	14.8	0.45	0.5	3.3% (AM1.5)		2009[468]
Cu_2ZnSnS_4 NCs	Glass/Au/**Cu_2ZnSnS_4**/CdS/ZnO/ITO	1.95	0.321	0.37	0.23% (AM1.5)		2009[469]

[a] Abbreviations: BH (bulk heterojunction), NSSC (nanocrystal-sensitized solar cells of Gratzel type), I_{SC} (short-circuit current), V_{OC} (open-circuit voltage), η% (power conversion efficiency), *FF* (fill factor). I_{SC}, V_{OC}, and fill factor are reported for AM1.5 illumination. The values of ICPE are chosen to represent its peak wavelength and/or its extend to the infrared.

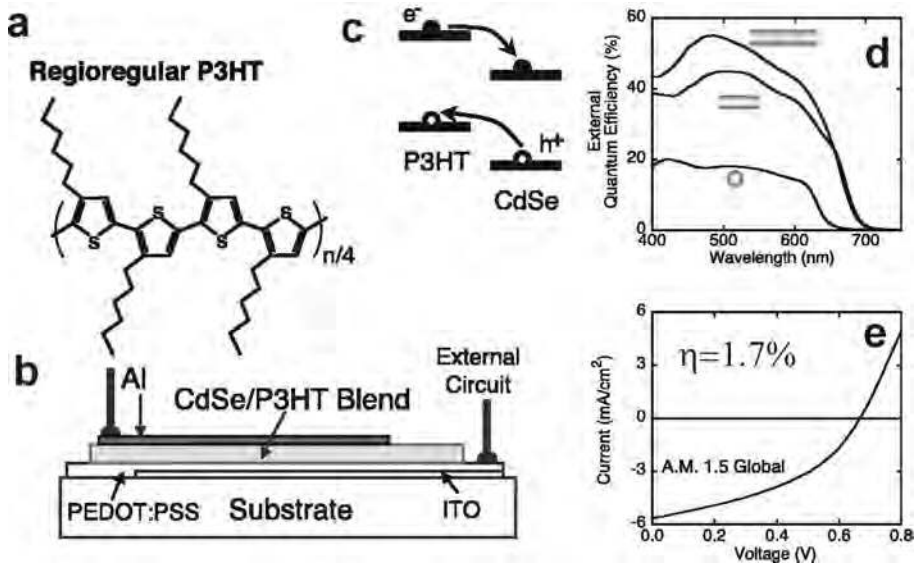

Figure 43. Hybrid nanorod−polymer solar cells based on the distributed network of heterojunction formed by poly(3-hexylthiophene) (P3HT) and CdSe NCs of various shapes (dots and rods). (a) Structure of regioregular P3HT. (b) The device structure including PEDOT:PSS coated ITO and Al electrodes. (c) Energy level diagram and charge separation in the P3HT/CdSe system. (d) IPCE spectra for photovoltaic cells containing CdSe dots (7 nm) and rods (7 × 30 and 7 × 60 nm). (e) $I-V$ curve under AM1.5 illumination for a device containing 7 × 60 nm nanorods. Reprinted with permission from ref 457. Copyright 2002 American Association for Advancement of Science.

the wide energy gap of the most semiconductor polymers. In this respect, semiconductor NCs are considered promising sensitizers, which allow one to extend the absorption into the red and near-IR range. The combination of NCs and conductive polymers was realized in so-called bulk heterojunction donor−acceptor solar cells, often called "hybrid solar cells". The concept of bulk heterojunction implies blending of p- and n-type components to achieve efficient charge separation at interfaces, followed by charge transport through the percolation pathways. All electron−hole pairs are generated in close vicinity of a heterointerface and are promptly separated by transfer of one type of carrier (electron or hole) through the heterointerface. This approach is especially useful because of the short diffusion length of excitons in organic semiconductors. A typical example is a donor−acceptor combination of poly(3-hexylthiophene) (P3HT)[477] and soluble fullerene derivative [6,6]-phenyl-C61-butyric acid methyl ester (PCBM), respectively.[455,472,478,479] Control over the nanoscale morphology of the blend is very critical for the device performance: interpenetrating networks and column-like structures were found in efficient P3HT/PCBM devices by AFM, TEM, and small-angle X-ray studies.[473,480] Strong light absorption, excellent solution processability of colloidal NCs, and the possibility of fine-tuning the electronic structure motivate the integration of NCs into bulk heterojunction devices. In hybrid solar cells, NCs can be introduced as either p- or n-type components.[481] Various compositions containing Si,[466] CdSe,[457−460,482] $CuInSe_2$,[483] ZnO,[484,485] CdS,[486] PbS,[462,487−490] PbSe,[491] and HgTe[461] NCs were tested in prototype solar cell structures. Below, we briefly discuss several characteristic examples.

In 2002, Alivisatos and co-workers reported hybrid solar cell based on blends of P3HT and shape-engineered CdSe NCs (dots and rods),[457] forming donor−acceptor heterojunctions (Figure 43). To improve efficiency of carrier separation at the P3HT−CdSe interface, original hydrocarbon ligands were partially stripped off the CdSe NC surface and replaced by labile pyridine molecules. It was shown that CdSe nanorods allow one to achieve higher light conversion efficiencies as compared to spherical CdSe NCs due to the smaller number of interparticle hopping events necessary for electron to reach the collecting electrode. The maximum load of CdSe nanocomponent in its blend with P3HT could approach 90% by weight. The IPCE spectrum of the photovoltaic cell was determined by the absorption spectrum of CdSe component covering the entire visible spectrum from UV to ∼720 nm. Under simulated AM1.5 illumination, devices based on 7 × 60 nm CdSe rods exhibited promising power conversion efficiencies of ∼1.7%. Unfortunately, the tendency of nanorods to align parallel to substrate (i.e., ITO electrode) was unfavorable for efficient collection of the photogenerated electrons. CdSe tetrapods blended with poly(2-methoxy-5-(3′,7′-dimethyl-octyloxy)-*p*-phenylenevinylene), also known as OC_1C_{10}-PPV, demonstrated improved electron transport across the films.[460] The power conversion efficiency, however, was very similar (η = 1.8% under AM1.5 illumination). The use of hyperbranched CdSe and CdTe NCs[396] allowed one to prevent the formation of phase-separated domains and aggregates, a well-known problem for hybrid solar cells. Furthermore, large hyperbranched NCs can span throught the distance between anode and cathode electrodes, eliminating the need for rigorous control of the blend morphology (Figure 44). The resulting power conversion efficiencies of ∼2.2% were still lower than expected, presumably due to the limited penetration of polymer chains between densely packed branches of CdSe component. The light conversion efficiencies comparable to the CdSe/P3HT cells were obtained using ZnO NCs as electron acceptor and P3HT ($\eta \approx 0.9\%$)[484,485] or poly[2-methoxy-5-(3′,7′-dimethyloctyloxy)-1,4-phenylenevinylene] (MDMO-PPV, $\eta \approx 1.4\%$).[485]

Narrow gap semiconductor NCs have been used in hybrid photovoltaic cells to harvest infrared part of solar spectrum. So far, reported hybrid solar cell devices using HgTe,[461] PbS,[462,488,490] and PbSe[492] NCs showed power conversion efficiencies below 1%, presumably due to inappropriate surface chemistry (traps, insulating nature of surface ligands) and partial phase separation of the blend components. The crucial role of surfaces in NC solar cells had to

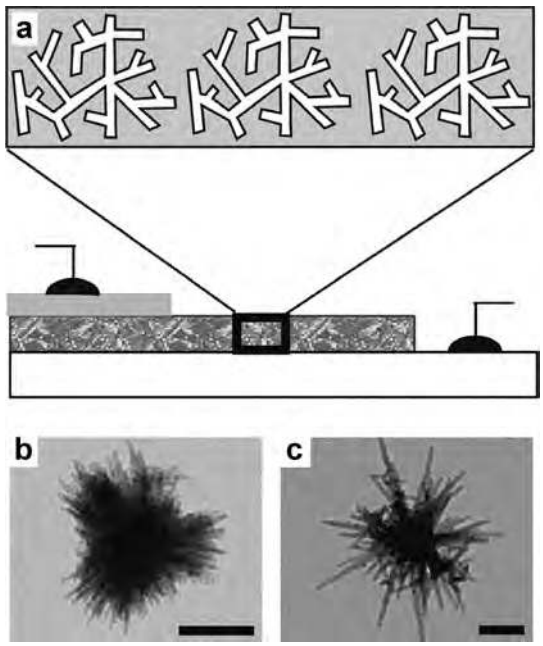

Figure 44. (a) Solar cells based on hyperbranched nanocrystals blended with conductive polymer (P3HT). The blend morphology is determined by the 3D structure of the nanocrystals, eliminating macroscopic phase separation. The electron transport is enhanced due to efficient bridging of electrodes by large hyperbranched nanocrystals. (b,c) TEM images showing the morphology of CdSe and CdTe hyperbranched nanocrystals, respectively. Scale bars are 100 nm. Reprinted with permission from ref 396. Copyright 2007 American Chemical Society.

be properly addressed in future research. Also, the nanoscale morphology of NC−polymer blends and the ways to tailor it have to be studied in great detail. Furthermore, the optimization of device performance will require accurate determination of the absolute positions of NC energy levels. The effects of surface ligands and dielectric environment on the absolute energies of quantum confined states in semiconductor NC have to be taken into account.[364]

7.3.3. Colloidal Nanocrystals for All-Inorganic Solar Cells

The weakest link of polymer-based solar cells is rather low stability of conductive polymers against oxidation and photodegradation, which should also affect the solar cells utilizing NC−polymer blends. All-inorganic solar cells made of colloidal NCs could avoid unstable organic components while keeping the benefits of solution-based device fabrication. For example, CdSe and CdTe NCs can create the donor−acceptor pairs with a staggered band alignment, similar to that at CdSe/P3HT interface (Figure 45a). Gur et al. fabricated a photovoltaic cell with spin-coated layers of pyridine-treated CdTe and CdSe nanorods (Figure 45b,c).[168] Under illumination, photogenerated electrons transferred to the CdSe phase, while holes found lower energy states in CdTe phase. The difference in work functions of ITO and Al electrodes provided additional driving force for charge separation. Sintering of the nanorods significantly improved carrier mobility and the device performance. With I_{SC} =13.2 mA/cm^2, V_{oc} = 0.45 V, and FF = 0.49, solution-processed solar cells demonstrated power conversion efficiency approaching 3% and impressive stability in air (Figure 45d,e). In similar device configuration with Cu_2S NCs and CdS nanorods, Wu et al. demonstrated a solar conversion efficiency of 1.6%.[464] Unlike hybrid solar cells, blending of

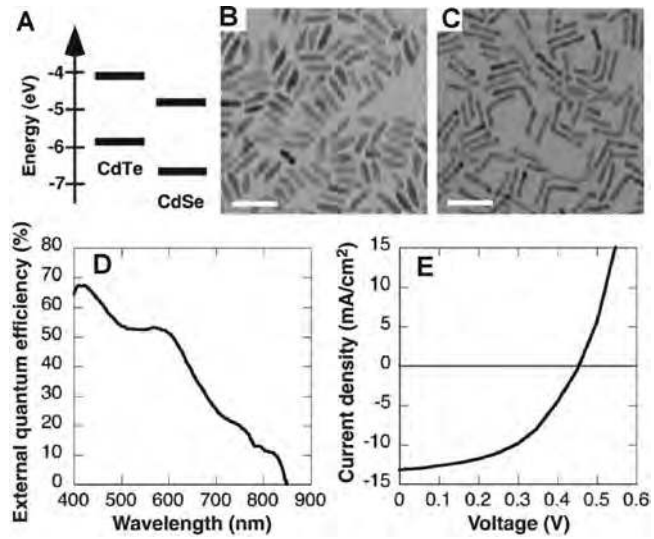

Figure 45. (A) An energy diagram of the conduction and valence band levels in the CdTe/CdSe system. (B,C) TEM images of CdSe and CdTe nanorods, respectively, used for fabrication of all-inorganic nanocrystal solar cell. Scale bars are 40 nm. (D) Incident photon to current efficiency spectrum for a sintered device composed of the layers of CdSe and CdTe nanorods. (E) Photocurrent density−voltage characteristic for the device exhibiting 2.9% power conversion efficiency under AM1.5 illumination. Reprinted with permission from ref 168. Copyright 2005 American Association for Advancement of Science.

CdTe and CdSe rods into a single active layer showed much poorer performance, presumably because of shortcuts and insufficient driving force for carrier separation.

Bulk I−III−VI_2 chalcopyrite compounds are known as efficient photovoltaic materials.[493] Particularly, solar cells based on copper indium-gallium selenide (CIGS) routinely demonstrate >15% solar conversion efficiency and are used for a wide range of commercial applications.[494,495] Importantly, CIGS has good environmental prospects because it is free of highly toxic elements. However, conventional fabrication of CIGS modules involves costly and elaborated techniques for controlling the stoichiometry of quaternary CIGS phase. High-quality CIGS films are typically prepared by evaporation of In, Cu, Ga, followed by selenization process by Se vapors or toxic H_2Se gas. Solution processed solar cells using hydrazine-based CIGS precursor demonstrated promising solar conversion efficiencies of 10.3% under AM1.5 illumination.[496] Inspired by the reports on bulk I−III−VI_2 compounds, several research groups dedicate significant efforts to explore colloidal synthesis of $CuInS_2$,[497−502] $CuInSe_2$,[465,498,500,502] and CIGS[502−504] NCs. In several recent reports, these NCs were tested in prototype solar cells, typically in a standard device configuration of glass/Mo/(p-type I−III−VI_2 semiconductor)/CdS/ZnO/ITO. Efficiencies of ∼3% were achieved using sintered $CuInSe_2$ NCs (Figure 46).[465]

Sargent and Nozik groups recently reported a number of encouraging papers describing the fabrication and operational principles of Schottky photovoltaic devices using PbS[253,270,272,505,506] and PbSe[253,271,507] NC solids. The Schottky cells reported by these groups had a simple and essentially similar configuration: NC solids were solution-deposited on ITO-coated glass followed by evaporation of top metal contact (Mg, Al, Ca/Al). The NC films were deposited using either layer-by-layer process in which NC monolayers were cross-linked by short-chain dithiol molecules or by spin-

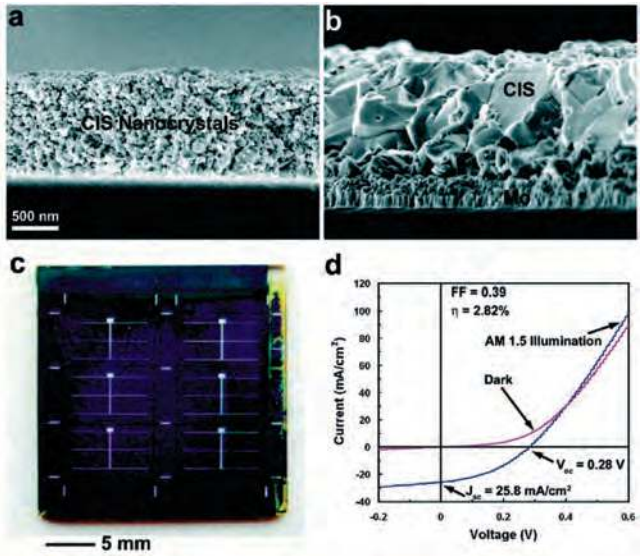

Figure 46. Solar cells using sintered $CoInSe_2$ NCs. (a) Cross-sectional SEM image of ~1.5 μm thick active layer spin-coated from $CoInSe_2$ NC ink. (b) Same film after annealing under Se vapors forms large CIS crystallites. (c) A photograph and (d) solar cell characteristics for the complete device. Reprinted with permission from ref 465. Copyright 2008 American Chemical Society.

casting followed by dipping into a surfactant solution (butylamine, ethanedithiol, benzenedithiol, etc.) to exchange original bulky surface ligands with smaller molecules. Figure 47 illustrates the basics of Schottky solar cell. As described in section 6.2, pinning of the Fermi level at the NC−metal interface creates a built-in field that separates photogenetared charge carriers. Electrons are collected at the metal contact, while holes escape into ITO. The performance of the Schottky cell is affected by the built-in potential, the width of the depletion region, and the transport of electron and holes through the NC solid. Most of these parameters were demonstrated to be tailorable by adjusting the morphology, thickness, and chemical treatments of NC solids. Presently, reported power conversion efficiencies for PbSe-based device are 3.6% (monochromatic 975 nm illumination, 12 mW/cm^2),[253] 1.1% (AM1.5 illumination),[253] and 2.1% (AM1.5 illumination).[271] Devices based on PbS NCs showed efficiencies of 4.2% (monochromatic 975 nm illumination, 12 mW/cm^2) and 1.8% (AM1.5 illumination).[272]

7.3.4. Nanocrystals in Dye-Sensitized Solar Cells

The dye-sensitized solar cells (DSSC), also known as Grätzel cells, include the nanostructured TiO_2 electrode covered with molecular sensitizer such as ruthenium(II) bipyridine compexes, the electrolyte redox couple, typically I^-/I_3^-, dissolved in an organic solvent, and the metal counter electrode (Figure 48).[508] The role of synthesizer is to absorb visible light and inject photogenerated electrons into the conduction band of TiO_2. Next, positively charged synthesizer molecules electrochemically oxidize I^- ions to I_3^- in solution. The latter is reduced to I^- at the counter electrode, closing the circle. As a result, the cell does not undergo any permanent chemical changes but photoelectrochemically converts the light energy into electrical power. To increase the area of the TiO_2−electrolyte interface, the nanoporous TiO_2 electrodes obtained by sintering anataze nanoparticles are used. The highest reported power conversion efficiencies of DSSC are in the impressive range of 10−11%.[509] However, this technology has several limitations. Ruthenium used in sensitizer is a precious metal, and its supply is limited. The use of liquid electrolyte is another serious drawback of DSSC due to the need for elaborate encapsulation techniques, thermal stability problems, electrolyte freezing at low temperatures, thermal expansion and evaporation at higher temperatures, etc. As a possible solution, nonvolatile ionic liquids as electrolytes were tested demonstrating power conversion efficiency of 7%.[510,511] Recently, the higher solar conversion efficiency of 8.2% was obtained using eutectic imidazolium salt melts as the electrolyte.[512] Another approach to solid-state DSSC includes the use of various solid-state hole conducting materials such as CuI (reported 4.5% solar conversion efficiency)[513] or small organic molecules[514] in place of electrolyte.

Semiconductor NCs are considered as a possible replacement for ruthenium complexes in DSSC. Low cost, solution processing, and size-tunable energy levels make semiconduc-

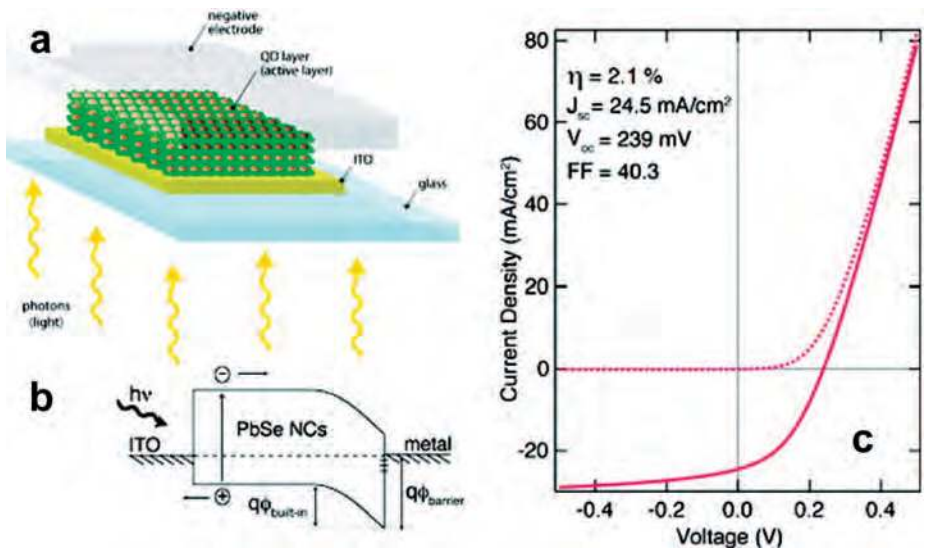

Figure 47. (a) Sketch of a Schottky solar cell using a close-packed film of PbSe nanocrystals and (b) the energy diagram showing the Schottky barrier formed at the metal/semiconductor interface. The majority carriers are separated in the depletion region and diffuse through the quasi-neutral region to the negative electrode. (c) Device characteristics under AM1.5 illumination. Reprinted with permission from ref 253. Copyright 2008 American Chemical Society.

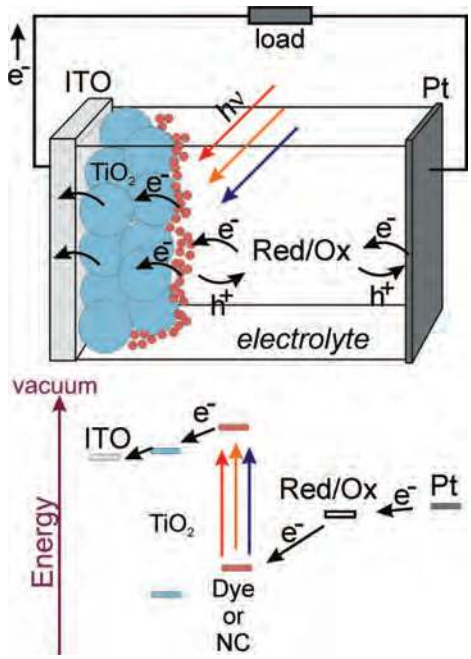

Figure 48. Schematics of the structure (top) and energy diagram (bottom) of a dye(nanocrystal)-sensitized solar cell (Grätzel cell). Following the absorption of photons by sensitizer, the photogenerated electrons are injected into nanostructured TiO_2 and collected into external circuit. Subsequently, positively charged dye molecules or nanocrystals are electrochemically reduced by I^- or Co^{2+} ions in solution converted into I^{3-} or Co^{3+}, respectively. These diffuse to the counter electrode (Pt) and were being electrochemically reduced to I^- or Co^{2+}, closing the photoelectrochemical circle.

tor NCs very attractive in this regard. Other advantages include sharp absorption onset, large absorption coefficients, and robustness of inorganic materials. In NC-sensitized solar cells (NSSC), the role of NCs is to absorb light and to inject photogenerated electrons into nanostructured TiO_2, while the holes are scavenged and transported to the opposite electrode by the redox couple. Such electron transfer is quite efficient and fast at the TiO_2/CdSe interface.[395,515,394] Various semiconductor NCs including CdS,[516−518] InP,[519] InAs,[520] PbS,[521,522] and Bi_2S_3[523,524] were examined as sensitizing components. All of these NCs, with few exceptions, were grown directly at the surface TiO_2 electrode with rather poor control over the materials properties and surface chemistry. NSSC demonstrated so far relatively low efficiencies: some of the best recently reported cells sensitized by CdSe NCs combined with Co(II)/Co(III) redox system demonstrated ~1% power conversion efficiency.[463] It is anticipated that the use of well engineered near-infrared-active colloidal NCs (CdTe, $CuInSe_2$, PbS, PbSe, InAs, etc.) could substantially improve the performance and commercial perspectives for NSSC.

7.3.5. Can Nanocrystal Solar Cell Beat the Shockley−Queisser Limit?

The efficiency of a solar cell can be improved by increasing three parameters: open-circuit voltage, short-circuit current, and the fill factor. In 1961, Shockley and Queisser determined the maximum theoretical light conversion efficiency for conventional solar cells. Their analysis led to the conclusions that maximum η for a single junction solar cell under one sun (AM 1.5) illumination requires a semiconductor band gap of 1.4 eV and cannot exceed ~31%, known as the Shockley−Queisser (S−Q) limit.[525] This limitation is also mostly applicable to hybrid solar cells with distributed heterojunctions and DSSCs. The most straightforward way to obtain higher power conversion efficiencies is to build a stack of several solar cells with different band gaps (so-called multijunction or tandem cell), which can harvest solar radiation more efficiently.[526] The stack of layers is arranged in such a way that the higher energy photons are absorbed by the first layer, while low energy infrared photons are harvested in the last layer. Theoretically, tandem solar cell with an infinite number of layers and with absorption profile perfectly matching the solar spectrum can reach 66% power conversion efficiency. Fabrication of multijunction cells requires multiple deposition steps and is very demanding to materials purity and structural perfection. It is hard to envision this technology to be used for mass production. Instead, multijunction cells made of III−V semiconductors are used for satellite, military, and other applications where efficiency per weight is more important than cost.

To beat the S−Q limit in a single-junction device, some new ways to utilize the excessive energy of short-wavelength photons have to be introduced. These days, several interesting ideas for harvesting the energy of hot carriers before they thermalize are widely discussed in literature. We should emphasize that physical phenomena described below are known and well-documented; however, their applicability for boosting up efficiency of real solar cells, as of 2009, has not been experimentally demonstrated.

Hot Carrier Solar Cell. Theoretically, a very high light-to-electricity conversion efficiency can be achieved by using a material with suppressed electron−phonon scattering. In 1982, Ross and Nozik proposed the model of a solar cell where generation of electron−hole pairs is not followed by thermalization of electrons to the bottom of the conduction band and holes to the top of the valence band.[527] In this model, electron−electron scattering within the conduction band creates Fermi distribution of the electrons, which have a higher temperature than the lattice temperature (same idea applies to holes in the valence band). If the extraction of carriers would occur without heat loss, the thermodynamically attainable power conversion efficiency can ultimately reach 66%.[527] Despite obvious attractiveness, this approach would be very difficult to implement using bulk semiconductors where the intraband cooling process is extremely fast, on the order of subpicoseconds to picoseconds (Figure 49a). At the same time, cooling of the hot carriers is expected to be much slower in semiconductor NCs. In semiconductor NCs, three-dimensional quantum confinement gives rise to discrete electronic density of states, which was predicted to significantly slow the intraband relaxation because of reduced availability of pairs of electronic states that satisfy energy conservation in phonon-assisted processes (the phonon-bottleneck effect) (Figure 49b).[528] The phonon bottleneck is expected to particularly affect relaxation dynamics in strongly confined NCs where the separation between energy levels can exceed several longitudinal-optical phonon energies, and, therefore, phonon-assisted carrier relaxation can occur only via multiphonon processes.

The efficiency of phonon bottleneck in real NC systems has been debated for a long time because, in the case of colloidally grown CdSe NCs,[529] surprisingly fast cooling rates (hundreds of femtoseconds) were demonstrated for the 1P-to-1S intraband relaxation. This fast relaxation has been attributed to confinement-enhanced, electron-to-hole energy transfer.[530] In this mechanism, the excess energy of the

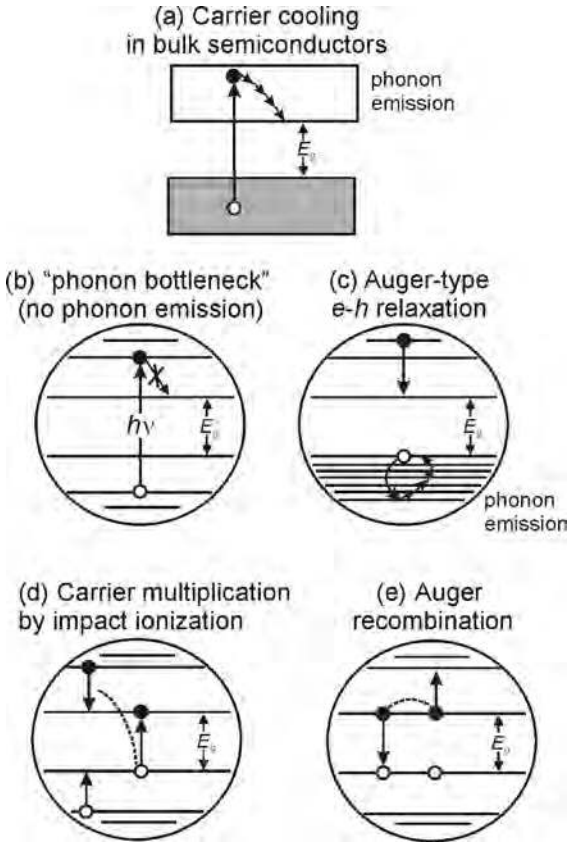

Figure 49. Dynamics of hot carriers in semiconductor nanocrystals. (a) Photogeneration of hot carrier in bulk semiconductors is followed by the fast cooling (thermalization) due to transfer of excessive kinetic energy to lattice vibrations (phonons). (b) In nanocrystals, the phonon emission is considered to be strongly suppressed due to the large spacing between electronic energy levels (i.e., mismatch between the frequency of electronic transitions and phonon frequencies). (c) However, because of typically smaller electron effective mass and larger hole density of states (CdSe nanocrystals is an example), the fast Auger-like relaxation is possible. The excessive kinetic energy of holes is subsequently scattered on phonons. (d) Because of increased carrier−carrier interactions in nanocrystals, carrier multiplication is a highly probable mechanism of the hot carrier relaxation. (e) Auger recombination essentially is an opposite process to carrier multiplication. This process is responsible for a fast decay of multiple excitons generated by impact ionization.

electron is transferred to a hole, which subsequently loses its energy via phonon emission because in contrast to a sparse spectrum of the electron states, the hole states form a dense, quasicontinuous spectrum even in very small CdSe NCs[531] (Figure 49c). In agreement with this mechanism, the cooling rate increases with decreasing the NC size due to stronger electron−hole Coulomb interactions in smaller dots, as shown for InP NCs.[532] It was observed that electron cooling can be slowed by surface trapping of the holes leading to partial decoupling of carriers.[533] Harbold et al. showed that relaxation is slower in PbSe NCs,[534] where Auger-like relaxation is improbable due to nearly equal effective masses and densities of states of holes and electrons. Still, the relaxation in the picoseconds range was observed, much shorter than that expected from the effect of "phonon bottleneck". Fast cooling in lead chalcogenide NCs could occur through the intermediate trap states or through the resonant energy transfer to molecular vibrations.[533] Slowing the cooling rate is a complex problem that requires removal or suppression of multiple competing relaxation mechanisms.

Very encouraging results were recently reported by Pandey and Guyot-Sionnest.[262] They demonstrated a remarkable increase of intraband relaxation time to >1 ns in CdSe NCs with specially designed epitaxial shells including a thin (1/2 of lattice constant) layer of ZnS, thick (up to 10 monolayers) layer of of ZnSe, followed by 1 monolayer of CdSe. Such shell structure allowed separation of electron and hole: electrons are confined within the CdSe core, while holes are localized in the outer CdSe monolayer capped with hole-trapping alkanethiol ligands. The presence of CdSe outer layer and thiol surface ligands also prevents surface trapping of electrons.

Not only the NC design but also the device fabrication is a highly challenging task for hot carrier solar cells. The separation and collection of carriers has to be faster than their thermalization. One suggested design of hot carrier cell implies the use of selective energy contacts, which collect and transmit carriers only with energies within the narrow range.[535]

Carrier-Multiplication (Multiple Exciton Generation) is another phenomenon that has been proposed to boost the efficiency of NC-based photovoltaics. The effect of carrier multiplication (CM) implies utilization of the excessive energy of the photogenerated carriers via creation of more than one electron−hole pair per one absorbed high energy photon (Figure 49d). This phenomenon is well-known in bulk semiconductors as impact ionization. However, the efficiency of impact ionization in solar cells made of bulk semiconductors is very low and does not provide any considerable contribution to overall light conversion efficiency. The possibility of much more efficient carrier multiplication (CM) in semiconductor NCs has attracted significant attention after it was reported in 2004 by Schaller and Klimov for PbSe NCs.[536] In the following years, highly efficient CM has been reported by several groups for PbSe,[537] PbS,[538] CdSe,[539] InAs,[426,540] and Si NCs.[541] Impressive CM efficiencies have been reported both for colloidal solutions and for NC films.[541] At the same time, other researchers subject the efficiency of CM in semiconductor NCs to intense debate. For example, Nair and Bawendi studied CM using time-resolved photoluminescence and found no evidence of CM in CdSe and CdTe NCs,[542] while PbS and PbSe NCs showed low CM efficiencies of at most 25%.[543] To date, all reports published on CM in semiconductor NCs have been based on spectroscopic measurements, where CM efficiency was determined by analyzing the effects of the formation of multiple excitons on light. All of these spectroscopic measurements are nevertheless indirect methods of measuring CM. The most direct method for determining how many electron−hole pairs are created per absorbed photon is to count the electrons in the photocurrent measured in an external circuit. The most convincing confirmation of efficient CM would be a measurement of the external quantum efficiency above 100% with respect to the incident photon flux, which has not been observed so far.[507] Another serious difficulty for utilization of CM in photovoltaic devices is a very fast (∼100 ps) decay of the multiexciton state via Auger recombination (Figure 49e). To make use of the CM process, the multiexcitonic state should be separated by rapid extraction of individual carriers or excitons from the photoexcited NC. At this moment, strong disagreement within the research community on the efficiency of CM processes in NCs and NC solids does not allow us to evaluate its potential utility for photovoltaic applications.

7.4. Field-Effect Transistors (FETs)

Colloidal semiconductor NCs with precisely controlled size, morphology, and chemical composition have been explored as the building blocks for thin film transistors.[11,23,24,49,87,298,351,387,393,544−546] Potential benefits of employing colloidal NCs in FET devices include possibility of inkjet printing of active electronic circuits on flexible plastic substrates, low temperature solution processing for large area applications such as flat panel displays, etc.

Among natural competitors for NCs in this area, we should mention organic electronic materials. Organic FETs have been extensively studied during the past decade and demonstrated impressive improvements of their performance.[376,547−549] The major limitations of FETs based on organic polymers and small molecules are rather low carrier mobilities, on the order of a few $cm^2\ V^{-1}\ s^{-1}$ or less even for well-optimized devices.[376,547] Organic FETs typically operate in p-type regime. Despite significant research efforts invested in the developments of n-type and ambipolar organic FETs, only limited progress has been achieved in terms of carrier mobility and operational stability.[376] Availability of materials for stable n-type FETs is highly desired for fabrication of CMOS (complementary metal oxide semiconductor) circuits using solution-processed organic or inorganic components. In general, CMOS allows easier circuit design, greater speed, and lower power consumption than n-MOS or p-MOS circuitry alone.[550] Other classes of materials for solution-fabricated FETs include molecular precursors for inorganic semiconductors,[551,552] networks of carbon nanotubes[553−555] and nanowires,[31,556] and hybrid organic−inorganic films.[557] However, none of these approaches can yet enable devices with performance comparable to that of conventional inorganic semiconductors.

Conventional crystalline inorganic semiconductors offer superior charge carrier mobilities; however, they are difficult to form by low cost processes. In this regard, semiconductor NCs can be logical building blocks for solution-processed electronic and optoelectronic devices because they are preformed solution proccesable fragments of inorganic semiconductors. However, there are several problems that have to be solved to enable the application of NC solids for electronic circuits. Performance of NC FETs crucially depends on the strength of the electronic coupling between individual NCs; this parameter has to be maximized by proper NC and ligands design. As we discussed in section 5, colloidal NCs capped with bulky organic ligands show very poor charge transport properties due to weak exchange coupling.[263,346] To improve conductivity of the NC solids, original capping ligands are typically exchanged with small molecules and/or removed by thermal or chemical treatments.[23,25,298,366] In addition, special care should be taken to minimize the effects of nonzero charging energies and carrier traps at the NC surface, both negatively affecting carrier transport in NC solids (see sections 5 and 6). Finally, the type and concentration of carriers must be controlled and tuned to optimize the device performance.[25] In this section, we will briefly describe the basic principles of FET operation and present recent development in the NC-based FETs.

7.4.1. Structure, Operation, and Performance Metrics of FETs

Typical FET is a three terminal device: the terminals are called gate, drain, and source. The names of the terminals refer to their functions. The gate terminal may be thought of as controlling the opening and closing of a physical gate. This gate permits electrons to flow through or blocks their passage by creating or eliminating a conductive channel between the source and drain. Figure 50 shows the schematics of typical FETs with conductive channel assembled from solution-cast NCs.[23,386] The device structure includes source (S) and drain (D) electrodes directly connected to the transistor channel (array of semiconductor NCs). The source and drain electrodes are usually lithographically patterned on the SiO_2 dielectric layer prior to NC deposition. The gate (G) electrode is electrically insulated from the transistor channel through a thin (from ~1 nm up to 300 nm) layer of a dielectric material called a "gate dielectric". Wide band gap oxides such as SiO_2, Al_2O_3, and HfO_2 and polymers such as PMMA are usually used as the dielectric layers. For simple testing purposes, a heavily doped silicon wafer (substrate) with a layer of thermally grown SiO_2 can be used as the gate and the dielectric, respectively (Figure 50a). The dielectric layer and gate electrode can be also deposited on top of the NC layer (Figure 50b) using electron beam or atomic layer (ALD) deposition techniques. Top-gated FETs can tolerate thinner dielectric layers and operate at lower voltages. For some demanding applications, both bottom and top gates can be electrically biased to better control the transistor channel.[298] The gate electrode is capacitively coupled to the transistor channel; a bias applied to the gate electrode creates an electric field in the channel. This field attracts and accumulates electric charges of opposite sign in a thin layer of semiconductor near the gate dielectric interface. Depending on the initial type and concentration of carriers in the channel, the additional charges can either deplete the transistor channel, increasing its resistance, or provide an effective doping boosting up the current flowing between source and drain electrodes.[376] By controlling the gate voltage, the current through the semiconductor channel can be easily flipped on and off enabling signal amplification and logic operations. In electronic circuits, voltage is usually applied to the gate electrode (V_G) and the drain (V_D) electrode. The source electrode is usually grounded ($V_S = 0$).

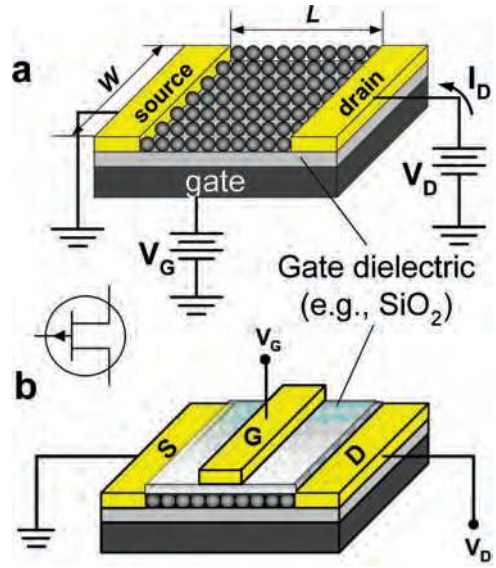

Figure 50. Basic configurations of nanocrystal based field-effect transistor (FET). (a) Bottom-gated FET, (b) top-gated FET. *L* and *W* show transistor channel length and width, respectively. S, D, and G are the source, drain, and gate electrodes (terminals).

For device applications, it is essential to be able to pass high currents through the transistor channel. This puts two important general requirements for design of practical NC FETs. First, the coupling energy between individual NCs should be high enough to allow easy passage of charge carriers through the NC solid. Second, the electrodes should form low resistance, ideally ohmic contacts to the NC solid (see section 6.1). Otherwise, a potential barrier (contact resistance) formed at the electrode−channel interface will block charge injection. Contact resistance becomes even more important when the length of the channel of the transistor is small and when FET operates at low bias.

The additional charge in the transistor channel (Q_i) induced by the voltage applied to gate electrode (V_G) is proportional to the capacitance (C_i) created by the dielectric layer:

$$Q_i = C_i V_g \tag{47}$$

For a flat capacitor, $C_i = A\varepsilon\varepsilon_0/d$, where A is the area of the capacitor, and d is the thickness of the dielectric layer. The gate dielectrics are characterized by their relative dielectric constant (ε), and ε_o is the permittivity of vacuum. The engineering community broadly uses k rather than ε for description of relative dielectric constant; it created broadly accepted terms of "high-k" and "low-k" dielectric materials. Thermally grown silicon dioxide with a dielectric constant of $\varepsilon = 3.9$ is the most commonly used dielectric material for NC FETs. To increase the amount of additional charge injected into the FET channel for a given V_G, the thickness of dielectric layer is pushed to be as thin as possible. Another approach to lower operation voltage is to use gate dielectrics with high ε, such as Al_2O_3, HfO_2.[298,558]

The response of current flowing through the FET to applied gate voltage depends on the type of majority carriers in the transistor channel. If the NCs are n-type conductive, a negative gate bias depletes electrons in the channel switching off the device. FET switches from conducting to insulating state when the bias applied to the gate approaches the value called threshold voltage (V_T) as shown in Figure 51a. V_T depends both on the parameters of semiconductor channel (initial doping level, presence of deep trap states that have to be filled before gate induced charges can flow, etc.) and on the properties of the gate dielectric (presence of donor or acceptor states, trapped charges, interfacial dipoles, etc). For n-FETs, if $V_T > 0$ the device operates in the enhancement mode; a positive V_G is necessary to create a conductive channel, because one does not exist naturally within the transistor. The positive voltage attracts free-floating electrons within the channel body toward the gate, forming a conductive channel. If $V_T < 0$, the FET operates in the depletion mode; the transistor channel is naturally conductive, and negative V_G has to be applied to deplete carriers in the channel. If the depletion region is large enough to completely close the channel, the FET is turned off (Figure 51a). If the majority of carriers in the FET channel are holes, the effect of the gate voltage is reversed. In p-FET, the channel current increases when negative bias is applied to the gate electrode (Figure 51b); $V_T > 0$ and $V_T < 0$ correspond to the depletion and enhancement operation modes, respectively. In the case of ambipolar FET, negative gate voltage leads to accumulation of mobile holes at the interface with the gate dielectric and holes becoming major charge carriers in the conductive channel, while positive gate voltage switches the type of conductivity to n-type by accumulating electrons in the conductive channel (Figure 51c).

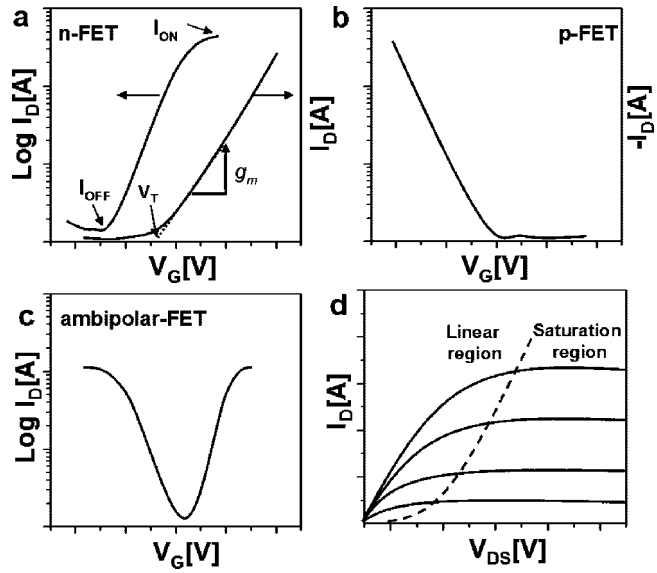

Figure 51. Typical $I-V$ characteristics of thin-film FETs (shown curves were measured for PbSe nanocrystal devices). (a) Plots of drain current I_D versus gate voltage V_G at a constant source-drain bias V_{DS} for n-type FET plotted on linear (right) and logarithmic (left) scales. (b,c) I_D versus V_G plots at constant V_{DS} for p-type and ambipolar FETs, respectively. (d) Plot of drain current I_D versus drain-source voltage V_{DS} measured for different gate voltages V_G (for n-type device, V_G decreases stepwise from top to bottom curves). Dashed line shows switching from linear to saturation regimes (see text for details).

The key performance metrics of an FET are the carrier mobility (so-called field-effect mobility); current modulation, that is, I_{on}/I_{off}, where I_{on} and I_{off} are the currents between source and drain electrodes when the device is in the "on" and "off" states, respectively; threshold voltage discussed above; and the subthreshold slope defined as $S = dV_G/d(\log I_D)$.

Figure 51d shows the current between source and drain electrodes (I_D) versus drain-source voltage (V_{DS}) measured for n-channel FET at different applied gate voltages. At low V_{DS}, the current I_D increases linearly with V_{DS}. In this mode, the FET operates like a variable resistor, and the FET is said to be operating in a linear regime (Figure 51d). I_D can be obtained from the following equation:

$$I_D = \frac{WC_i\mu_{lin}}{L}\left(V_G - V_T - \frac{V_D}{2}\right)V_D \tag{48}$$

where L is the channel length, W is the channel width, C_i is the capacitance per unit area of the dielectric layer, V_T is the threshold voltage, and μ_{lin} is the linear regime field-effect mobility. μ_{lin} is usually calculated from the transconductance (g_m) by plotting I_D versus V_G at a constant low V_D. The slope of this plot is equal to g_m:

$$g_m = \left.\frac{\partial I_D}{\partial V_G}\right|_{V_D=\text{const}} = \frac{WC_iV_D}{L}\mu_{lin} \tag{49}$$

At high V_{DS} the current saturates as the channel "pinches off" near the drain electrode.[6] If V_{DS} voltage is increased further, the pinch-off point of the channel begins to move away from the drain toward the source. The FET is said to be in the saturation regime. For $V_{DS} \geq (V_{GS} - V_T)$, I_D can be expressed as:

$$I_D = \frac{WC_i\mu_{sat}}{2L}(V_G - V_T)^2 \quad (50)$$

where μ_{sat} is the saturation regime field-effect mobility. This important parameter is typically calculated from the slope of $[I_D]^{1/2}$ versus V_G.

The charge mobilities extracted from I_D-V_G curves are often higher in the saturated regime than those measured in the linear regime. This difference in measured carrier mobility can occur due to contact resistance when a large part of the source-drain voltage drops at the contacts and not across the channel, due to the presence of carrier trapping centers, etc.[6,557]

7.4.2. State-of-the-Art for Nanocrystal Transistors

The first inorganic FETs fabricated using colloidal semiconductor nanoparticles were reported in 1999 by Jacobson et al.[268] These devices were assembled from pyridine-capped CdSe NCs. Pyridine is a rather labile and volatile surface ligand, and annealing of the nanoparticle layer above 250 °C allowed sintering of CdSe NCs into a polycrystalline CdSe film. Strictly speaking, the device reported by Jacobson et al. cannot be assigned to NC FETs because no NCs were present in the FET channel after annealing above 250 °C. The device annealed at 350 °C for 1 h showed a linear regime mobility (μ_{lin}) of 1 cm^2/V·s, I_{ON}/I_{OFF} ratio of 3.1×10^4, and a threshold voltage of 6.7 V. The carrier mobility in those inorganic FETs was significantly greater than typical mobilities achieved for printed organic FETs. The conductance of the NC films was significantly increased by sintering,; however, the large concentration of structural defects limited the device switching speeds and induced large hysteresis of the I_D-V_G scans.

NC-FETs with the conductive channels assembled of close-packed quantum confined semiconductor NCs have been first reported by our team in 2005.[23] As starting material, we used PbSe NCs capped with oleic acid. Thin NC films fabricated by spin-coating or drop-casting were very insulating ($\sigma \approx 10^{-10}$ S cm^{-1}) and did not show any gate effect. However, replacement of bulky oleic acid with small hydrazine molecules by simply soaking NC films in 1 M solution of N_2H_4 in acetonitrile reduced the interparticle spacing from ~1.2 to ~0.4 nm and increases conductivity of PbSe NC films by ~10 orders of magnitude.[23] As shown in Figure 52a, the size and shape, as well as the morphology of NC films, did not change after the threatment with hydrazine solution. Figure 52b shows a current modulation I_{on}/I_{off} of $\sim 2.5 \times 10^3$ for a PbSe NC n-FET. In the "on" state, the low-field specific conductance of PbSe NC film was ~0.82 S cm^{-2}, and the current density in saturation regime approached 2.7×10^4 A cm^{-2}. Field-effect electron mobilities extracted from a series of devices yielded $\mu_{lin} \approx$ 0.4 cm^2 V^{-1} s^{-1} and $\mu_{sat} \approx 0.7$ cm^2 V^{-1} s^{-1} in the saturation regime. Since then, technical improvements is sample preparation allowed one to achieve respectable electron mobility approaching $\mu_{sat} \approx 2.5$ cm^2 V^{-1} s^{-1} for 8 nm PbSe NC FETs, keeping the I_{on}/I_{off} ratio above 10^3.[559] All of these numbers were reported for devices prepared at room temperature, without any heat treatment. Under these conditions, individual PbSe NCs preserved their QD-type electronic structure, confirmed by the observation of excitonic features

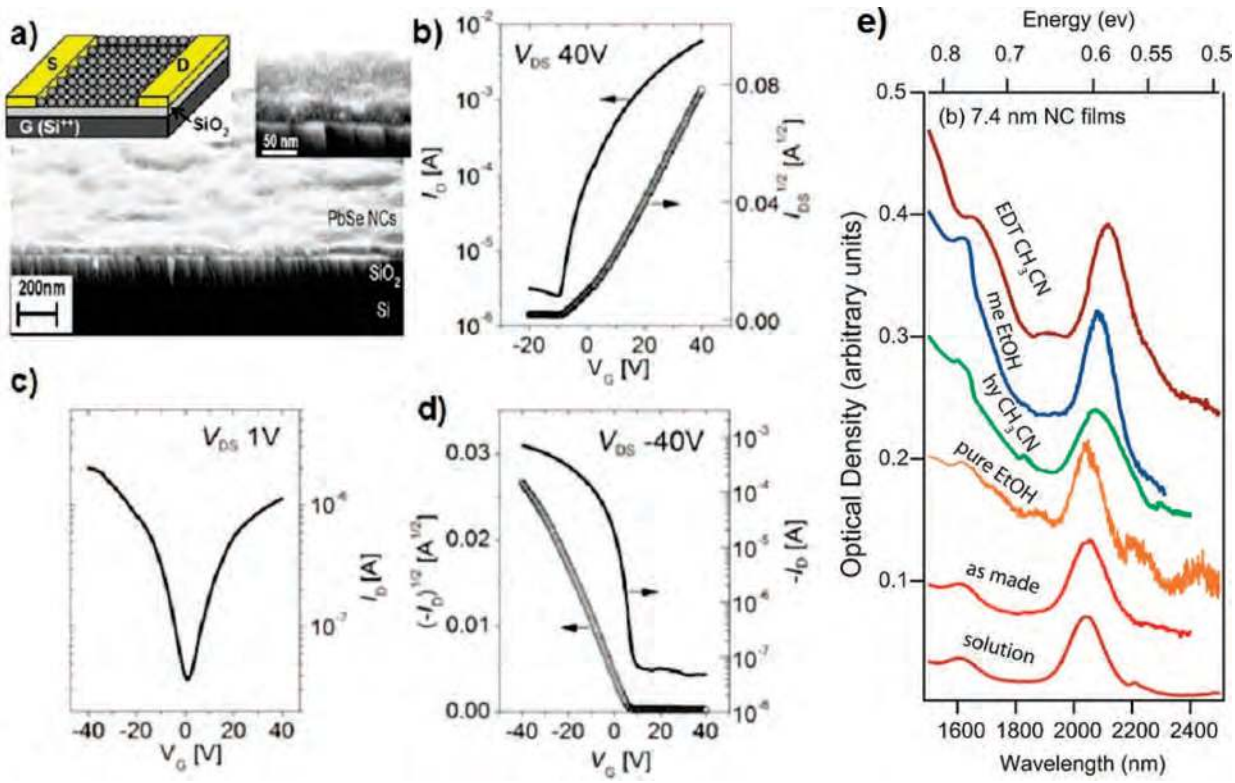

Figure 52. Device characteristis of FETs made from ~8 nm PbSe nanocrystals treated with 1 M N_2H_4 in acetonitrile. (a) SEM images of the FET channel assembled from PbSe nanocrystals. (b) I_D and $I_D^{1/2}$ versus V_G curves measured at a constant $V_{DS} = 40$ V for a n-channel FET, (c) I_D versus V_G plot at a constant $V_{DS} = 1$ V for an ambipolar FET. (d) I_D-V_{DS} plot at $V_{DS} = -40$ V for a p-channel FET. Reprinted with permission from ref 23. Copyright 2005 American Association for Advancement of Science. (e) Extinction spectra of PbSe NC films, made from 7.4 nm nanocrystals, after various chemical treatments. Spectra are vertically offset for clarity. Reprinted with permission from ref 560. Copyright 2009 American Chemical Society.

Table 6. Structural and Electrical Data for Chemically Treated PbSe NC Film[25]

treatment/solvent	Δ NC spacing, Å	σ, S cm^{-1}	type
N_2H_4/acetonitrile	8	5×10^{-3}	n
N_2H_4/ethanol	10	5×10^{-2}	n
methylamine/ethanol	9	1×10^{-4}	p
pyridine/ethanol	n/a	5×10^{-3}	p
ethanol	5.5	1×10^{-2}	p
1,2-ethaneditiol/acetonitrile	16	5×10^{-5}	n,p

in the films treated with hydrazine and other small molecular ligands by Beard et al. (Figure 52e).[560]

After the treatment with N_2H_4, PbSe NC solids exhibit n-type conductivity; however, removal of hydrazine in a vacuum switched the conductivity from n-type (Figure 52b) to ambipolar (Figure 52c) and finally to the p-type (Figure 52d) as the hydrazine fully desorbed. The resulting p-type FETs showed stable operation with room temperature hole mobilities μ_{sat} of 0.12−0.18 cm^2 V^{-1} s^{-1} and current modulations of $\sim 10^2$. At low temperatures (120 K), the current modulation increases to $\sim 1.6 \times 10^4$, while the hole mobility decreases to μ_{sat} 0.09 cm^2 V^{-1} s^{-1} and was independent of the gate voltage (Figure 52d). Switching between electron and hole transport was fully reversible upon re-exposure to hydrazine. Annealing the hydrazine-treated PbSe NC films at ∼200 °C and re-exposing them to hydrazine solution allowed one to achieve degenerate doping and metallic conductivity ($\sigma \approx 8.5$ S cm^{-1}). The semiconductor−metal transition was reversible, as the partial removing of the hydrazine yielded n-type semiconducting films with rather high electron mobility ($\mu_{lin} \approx 2.5$ cm^2 V^{-1} s^{-1}), thus demonstrating that tailoring the electron coupling and the doping density allows for the controllable switching between insulating, semiconducting, and metallic states in films made of N_2H_4-treated PbSe NCs.

The Nozik group recently reported a systematic study of FETs made of PbSe NC films chemically treated with different amine and thiol ligands (hydrazine, methylamine, pyridine, and ethanedithiol).[25,366] Table 6 summarizes the structural and electrical characteristics of chemically treated PbSe NC films. Electron microscopy studies (SEM and TEM) showed that these treatments did not cause changes of NC shape and size, but markedly reduced the interparticle spacing ("Δ NC spacing" column in Table 6).[25] PbSe NC films treated with 1 M N_2H_4 in ethanol instead of acetonitrile resulted in n-type FETs with high conductivity but poor current modulation. Treatment of the NC film with methylamine or pyridine solutions in ethanol also resulted in significant increase of the conductivity of the NC solid, while the I_D versus V_G scans revealed the p-type conductivity. PbSe NC films treated with 1,2-ethanedithiol showed ambipolar behavior in the dark, but the devices converted to p-FETs with 30−60 times higher conductance after exposure to 300 mW/cm^2 broadband illumination.[366] These observations point to the complexity of the processes involved in the chemical treatments of PbSe NC films and the important role of surface ligands. Simple removal of the surface ligands and their replacement with small molecules is the only one of several processes necessary to achieve good performance of NC FETs. Proper surface treatment should simultaneously affect the exchange coupling energy (β), charging energy (E_c), trap density, and the doping of a NC solid. Following the previous example, hydrazine is a strong Lewis base, which enables it to saturate dangling bonds at the NC surface by donating a lone pair of electrons. Hydrazine also acts as a reducing agent, both preventing oxidation of the bare NC surface and "repairing" PbSe NCs with oxidized surface sites. This function is important because oxidation of surface atoms can introduce carrier trapping midgap states. Replacement of oleic acid ($\varepsilon \approx 2$) with polarizable N_2H_4 molecules ($\varepsilon \approx 52$) reduces E_c. The increase of β and decrease of E_c help to close the Hubbard gap in the NC solid.[314,318] Finally, hydrazine behaves as a charge-transfer n-type dopant, providing mobile charge carriers to the NCs.[23,348] The ease of switching between n- and p-transport in PbSe NC arrays provides interesting opportunities for CMOS FET circuits. The large surface-to-volume ratio of NC FETs might be exploited in chemical sensors (e.g., for hydrazine, alkyl hydrazines, ammonia and amines, hydroxylamine, which behave as charge-transfer dopands for PbSe NC solids).

Our team as well as other groups successfully applied the above-described hydrazine treatment to other NC solids including PbSe,[23,25,330,366] PbS,[24] PbTe,[87,357] and SnTe NCs.[393] Thus, PbTe NC films after treatment with a 1.0 M solution of hydrazine in acetonitrile also showed ∼10 orders of magnitude improvement in conductivity and n-channel behavior.[87] The mobility of electron and hole in the linear region was ∼0.95 and 0.15 cm^2 V^{-1} s^{-1}, respectively.[87] The field-effect mobility of n-FET with 8.5 nm PbS NCs treated with a hydrazine solution was ∼0.08 cm^2 V^{-1} s^{-1} in the linear region and 0.12 cm^2 V^{-1} s^{-1} in the saturation regime.[24] PbS NC FETs showed more stable n-FET behavior as compared to PbSe and PbTe NC films.

Further optimization of NC exchange coupling, doping, and improvements in film morphology could significantly increase carrier mobility. The use of thinner gate oxides or replacing SiO_2 with a high-*k* dielectric material, for example, HfO_2, should decrease the operating voltage of NC devices. Kim et al. reported bottom and top gated FETs with p-channels of sintered HgTe NCs.[298] They demonstrated the possibility to achieve high field-effect mobility at low gate voltages for solution-processed inorganic FETs by employing high-*k* dielectric materials as the gate insulators. Figure 53a and b shows I_D-V_{DS} and I_D-V_G output characteristics for HgTe-based bottom-gated FETs with a 300 nm thick layer of SiO_2 ($\varepsilon \approx 3.9$) gate dielectric on heavily doped Si substrate. The device operated as a p-channel transistor, and high gate voltages had to be applied to modulate the current through drain electrode. The saturation regime field-effect mobility, I_{on}/I_{off}, and V_T of the bottom-gated FET were $\mu_{sat} = 0.82$ cm^2 V^{-1} s^{-1}, 10^3, and 7.7 V, respectively. However, the same semiconductor layer made of sintered HgTe NCs, but integrated in a top-gated FET with 60 nm thick dielectric layer of Al_2O_3 with $\varepsilon \approx 8.6$, enabled device operation at much lower gate voltages, as shown in Figure 53c. The top-gated transistors demonstrated an I_{on}/I_{off} ratio and V_T of 2×10^2 and −2.2 V, respectively, and the field-effect mobility of ∼2.38 cm^2 V^{-1} s^{-1} (Figure 53d). Somewhat counterintuitive, the material of gate insulator can have a huge influence on carrier mobility in semiconductor channel due to the formation of surface states at the semiconductor–dielectric interface.[376] The advantage of top-gated FETs is the possibility to print electronic circuits on virtually any substrate. Kim et al. demonstrated p-type HgTe NC-FETs fabricated on glass and plastic substrates.[546] On glass, the hole mobility was $\mu_{sat} = 1.06$ cm^2 V^{-1} s^{-1} and $\mu_{lin} = 0.55$ cm^2 V^{-1} s^{-1}. The I_{on}/I_{off} ratio and threshold voltage were $\sim 10^3$ and 0.2 V, respectively. The hole mobility in HgTe NC FETs fabricated on flexible polyethersulfone substrates

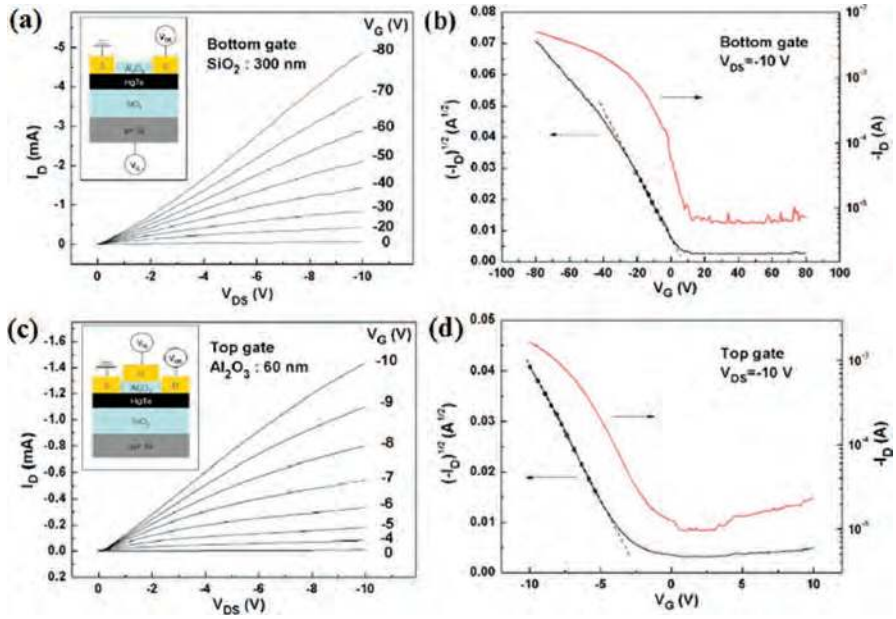

Figure 53. Comparison of the output characteristics of bottom- and top-gated HgTe nanocrystal-based FETs. I_D-V_{DS} and $(I_D)^{1/2}-V_G$ scans measured for the (a,b) bottom-gated and (c,d) top-gated FETs made from HgTe nanocrystals. Reprinted with permission from ref 298. Copyright 2006 American Institute of Physics.

was $\mu_{lin} = 1.20$ cm^2 V^{-1} s^{-1} in the linear regime, greater than that of most flexible organic transistors. The on/off ratio of the device was about 10^3, and the threshold voltage was about -3.0 V.

Colloidal ZnO nanomaterials represent another very interesting class of materials for solution processed FET devices.[351,386,561,562] Among the advantages of ZnO, we should mention its nontoxicity, low cost, chemical stability, transparency in the visible, etc. It can be a very promising candidate for thin-film transistors operating individual pixels in liquid-crystal flat-panel displays.[561−563] ZnO FETs reported by Sun and Sirringhaus were prepared from 6 nm ZnO NCs with butylamine ligands.[386,563] ZnO NCs were spin-cast on Si wafers with a 300 nm layer of SiO_2 gate dielectric and prepatterned Cr/Au (3 nm/12 nm) electrodes. The annealing at 230 °C under N_2/H_2 atmosphere for 30 min significantly increased the carrier concentration and mobility. All devices showed n-type transistor behavior with low turn-on voltage and good operating stability. The mobilities of ZnO NC TFTs were $\mu_{lin} = 2.4 \times 10^{-4}$ cm^2 V^{-1} s^{-1} and $\mu_{sat} = 4.6 \times 10^{-4}$ cm^2 V^{-1} s^{-1}, and the I_{on}/I_{off} ratio was 5×10^3.[386] The FET device performance could be significantly improved by using ZnO nanorods instead of spherical NCs. Thus, FETs made of 65 nm-long 10 nm-diameter nanorods showed almost 2 orders of magnitude higher mobility as compared to the devices made from 6 nm spherical NCs. Nanorod-based devices exhibited an I_{on}/I_{off} ratio of 1.1×10^5 and higher mobility of $\mu_{sat} = 0.023$ cm^2 V^{-1} s^{-1} and $\mu_{lin} = 0.013$ cm^2 V^{-1} s^{-1}. The approximately 10-fold larger size of the nanorod particles as compared to the nanospheres reduced the number of interparticle hopping events that an electron has to undergo when moving from source to drain electrode. By using octylamine surface ligands for ZnO, Sun and Sirringhaus achieved partial assembly of monodisperse ZnO nanorods in the transistor channel into superstructures with nematic liquid crystalline ordering (Figure 54a,b).[563] Unidirectional alignment of nanorods resulted in improved FET performance; the devices with octylamine-capped ZnO nanorods as active layer after annealing exhibited $\mu_{sat} = 0.1-0.12$ cm^2 V^{-1} s^{-1} and an I_{on}/I_{off} ratio of 10^5-10^6 (Figure 54c,d). The

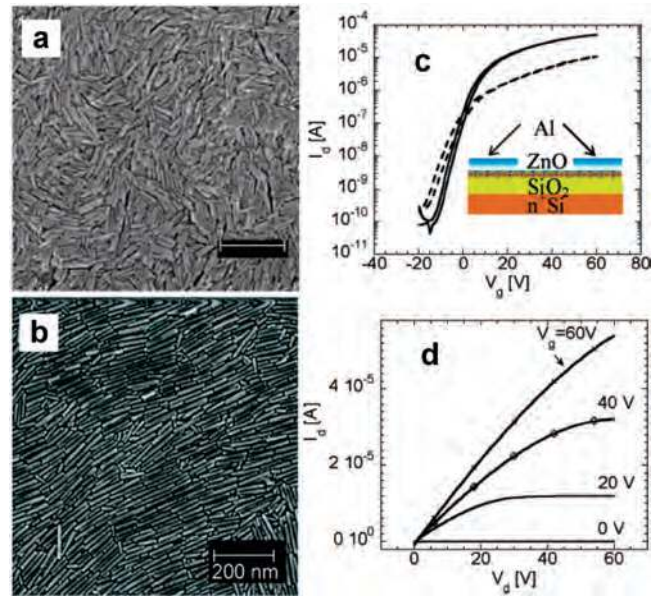

Figure 54. (a) SEM image of randomly oriented ZnO nanorods coated with octylamine. Scale bar, 200 nm. (b) Uniform nanorod film fabricated by spin-coating of ZnO nanorods. The nanorods self-assembled into domains with nematic ordering. (c) Saturated transfer characteristics (I_D-V_G scan) for a thin-film transistor fabricated by spin-coating of ZnO nanorods with different ligands: octylamine (solid line), butylamine (dashed line). $V_D = 60$ V. (d) Output characteristics of a spin-coated device made from octylamine capped ZnO nanorods. The device structure is shown in the inset in (c). Adopted from ref 563. Copyright 2006 American Chemical Society.

mobility extracted from the linear region ($V_d = 5$) had lmost the same values as μ_{sat}, suggesting a low contact resistance. The mobility value was 5−6 times higher than that of butylamine-capped ZnO FETs. This improvement of mobility with ligand length was fully consistent with the changes in film morphology and showed that a high degree of in-plane nanorod alignment is beneficial for transport in the nanorod films.

The performance of FET devices assembled of ZnO nanorods was further enhanced by the postdeposition hydrothermal growth step when a thin layer of ZnO was chemically deposited into the voids between ZnO nanorods.[563] After such treatment was followed by the annealing step in hydrogen atmosphere, the devices achieved mobility values of 1.2−1.4 $cm^2 V^{-1} s^{-1}$ and an I_{on}/I_{off} ratio of 10^6-10^7. These mobility values, combined with optical transparency and solution-based fabrication, have a good chance to pave the way for ZnO NC FETs into commercial applications.

The next interesting step in development of NC-based FETs was to combine multiple functionalities using engineered multicomponent NCs as the building blocks for transistor channel. Recent developments in the colloidal synthesis of inorganic nanostructures allowed exciting opportunities for cointegration of materials with different functionalities in form of core−shell, dumbbell, and other nanostructures (see section 2). In 2008, Lee et al. demonstrated FETs employing multifunctional NCs, core−shell particles with plasmonic Au core and semiconducting PbS shell (Figure 28c,d).[24] The intraparticle charge transfer between Au core and PbS shell formed the charge-transfer complex resulting in p-type doping of the FET channel. Later, Lee et al. demonstrated FETs combining semiconductor and magnetic functionalities. Specifically, they used core−shell and dumbbell nanostructures combining FePt and PbS or PbSe as magnetic and semiconducting components.[564] Figure 55a shows the TEM image of FePt/PbS core−shell NCs used as active elements of the bottom-gated FET. The devices demonstrated good electronic performance, with n-type operation and $\mu_{sat} = 0.01$ $cm^2 V^{-1} s^{-1}$ and an I_{on}/I_{off} ratio of $\sim 10^2$ (Figure 55c,d). The FET behavior was complemented by superparamagnetic response of FePt core (Figure 55b) directly integrated in the transistor channel. The examples of FETs assembled from Au/PbS ad FePt/PbS multicomponent nanostructures show an intriguing direction in the NC electronics. The progress in synthetic chemistry will further expand the list of material combinations; developments in the ligand design should enable strong electronic coupling between the components, and development in electronic structure calculations of nanostructures will provide deeper understanding of interactions between the components both on intra- and interparticle levels. With all of these expected contributions, we envision good prospects for multicomponent nanostructures in various electronic applications.

7.5. Memory Elements

Memory elements are the integral part of personal computers, ID cards, and various consumer electronics from DVD players to coffee makers and toys. Depending on the application, different types of memory technology can be employed. Three leading technologies used today are the dynamic random access memory (DRAM), hard-disk drives (HDDs), and flash memory. In addition, many other memory devices are currently in stage of active development.[565] Among new promising concepts, we should mention magnetic random-access memory (MRAM) and ferroelectric random access memory,[566,567] phase-change memory,[568,569] and other resistance-change memory concepts based on switching behavior in inorganic and organic materials.[570]

The performance metrics of memory elements include data density, writing and erasing speeds, retention time, the number of erase-rewrite cycles, power consumption, and cost per bit of stored information. There is no "ideal memory"; different approaches have their strong and weak points and

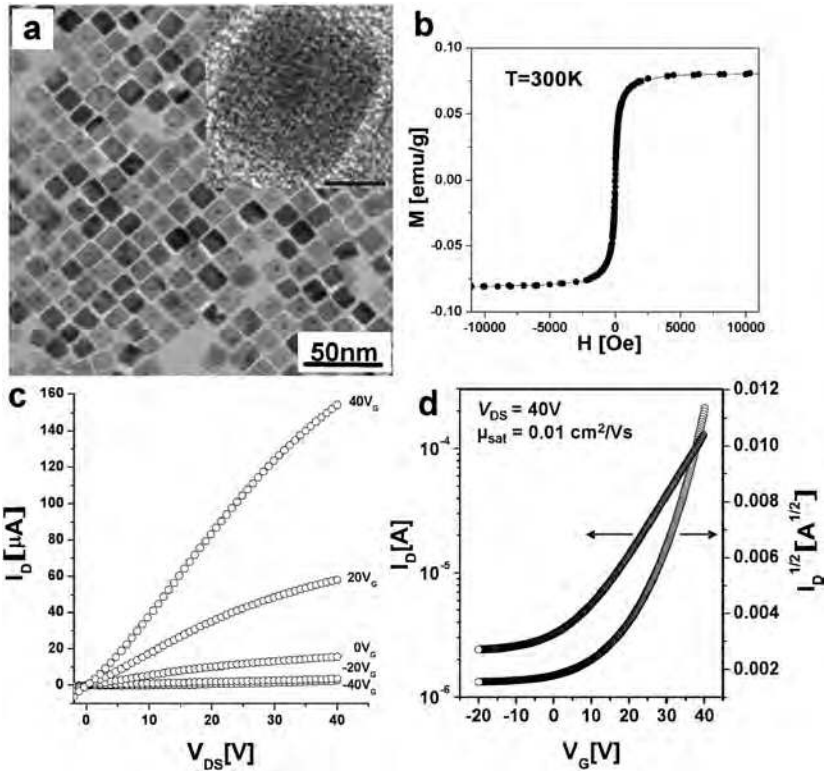

Figure 55. (a) TEM image of cubic FePt/PbS core−shell nanocrystals. (b) Magnetization loop for cubic FePt/PbS core−shells measured at 300 K. (c) Plot of I_D versus V_{DS}, measured at different values of V_G for n-FET assembled from cubic FePt/PbS core−shell nanocrystals treated with 1 M hydrazine solution in acetonitrile for 24 h. (d) Plots of I_D and $I_D^{1/2}$ versus V_G at constant $V_{DS} = 40$ V used to calculate current modulation and field-effect mobility in the saturation regime. Channel length is $L = 4.5$ μm, and channel width is $W = 7800$ μm.

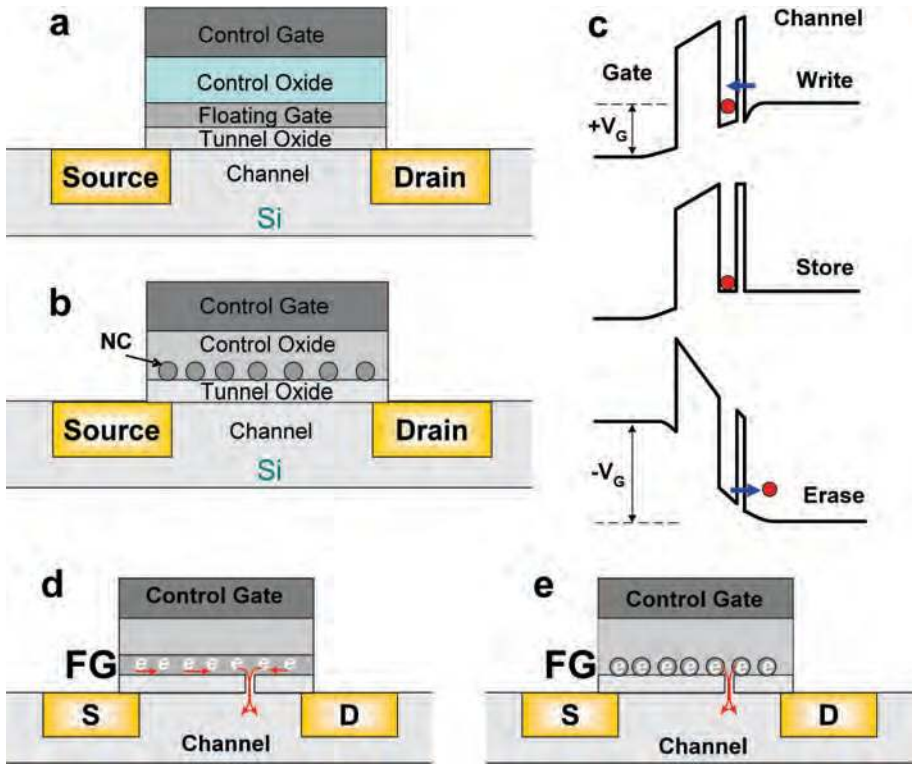

Figure 56. The structures of floating gate memory devices. (a) Conventional nonvolatile flash memory. (b) Nanocrysal nonvolatile flash memory. (c) Operation mechanism of flash memory: write, shore, and erase conditions. (d) A single discharge path from a weak spot in the tunneling oxide ruins conventional flash memory, and (e) discharge path in the tunneling oxide of nanocrystal nonvolatile flash memory.

target different market niches. For example, DRAM has very high switching speed and large number of write-erase cycles. At the same time, DRAM is relatively expensive, has to be refreshed every few milliseconds, and consumes power during its refresh cycles. HDDs can achieve very high data density at rather low cost and allow many write-erase cycles, but are slow to access, consume power to keep the disks rotating in readiness, and are prone to crashes of the head, which flies just tens of nanometers above the disk surface. The major advantage of flash memory is its nonvolatility, that is, the ability to store information for a long time without any power consumption, which, however, comes at the expense of low write-erase speed and limited number of rewrite cycles.

Memory devices utilizing NCs have been extensively explored during the past decade as possible solutions to overcome the scaling issues and improve endurance of nonvolatile memory devices[370,571−579] and HDDs.[580,581] Same as with other application, NCs provide an opportunity to precisely control electronic and magnetic properties of materials by tuning NC size and shape. The possibility of device fabrication using colloidal solutions allows significant cost reductions, especially important for the products such as wireless identification tags and smart cards where the prime criterion is cost rather than outstanding performance.

7.5.1. Flash Memory Devices

The structure of conventional flash memory is shown in Figure 56a. Each memory cell is represented by the metal–oxide−semiconductor−field-effect-transistor (MOSFET) with a modified gate stack structure, which has a floating gate (an island of polycrystalline silicon) embedded in the dielectric layer. The floating gate (FG) is electrically insulated from the FET channel by a thin (∼2−5 nm) layer of a dielectric material called tunnel oxide. Thermally grown SiO_2 is typically used as tunnel oxide; however, high-*k* dielectric materials such as HfO_2 can provide higher device performance and are now actively studies for this purpose. FG is also insulated from the FET gate (in flash memory devices called "control gate") by a thick layer of dielectric called "control oxide". When a positive bias is applied to the control gate, electrons from the channel can tunnel through the layer of tunnel oxide into the FG as shown in Figure 56c. The writing cycle of memory operation is based on the charging of FG. Charge carriers injected into FG remain trapped there for many years, storing a bit of information. To erase information, negative voltage is applied to the control gate, pushing the electrons to tunnel from FG to the FET channel and restoring the initial state of memory device (Figure 56c). The charges stored in the FG create an electric field, which either depletes or accumulates majority carriers in the FET channel, and the presence of charge stored in the FG can be easily sensed because it is directly proportional to the threshold voltage of the MOSFET.

The voltage applied to the control gate and the writing speed of flash memory device strongly depend on the thickness of tunnel oxide. To enable operation at standard CMOS voltage, the thickness of tunnel oxide should not exceed a few nanometers. The thickness of the tunnel oxide layer also significantly affects the operation (write/erase) speed,[582] with thin tunnel oxide layers promoting high write/erase speeds. However, thinner tunnel oxide can also result in a low breakdown voltage, leakage of current through defects in tunnel oxide layer, and a limited number of erase−rewrite cycles. Trap sites such as defects in the gate oxide can also affect the electron tunnel behavior.[583] The

conventional flash memory is extremely prone to failure of insulation; one weak spot in the tunneling oxide is sufficient to create a fatal discharge path (Figure 56d). A promising way to alleviate this problem, while still preserving the fundamental operation principles of the flash memory, is to store charge not on the continuous poly silicon FG, but on a layer of discrete, mutually isolated NCs (Figure 56b). Each NC will store only few electrons; collectively, the charges stored on NCs can control the threshold voltage of the FET. The concept of distributed charge storage is more fault-tolerant because minor damages in the tunnel oxide layer are not detrimental for memory operation (Figure 56e). Thinner tunneling oxide can be used to achieve lower operating voltages and/or increase the operating speed.

The properties of a thin SiO_2 dielectric layer can be seriously degraded under continuous memory programming (write/erase), and this severely decreases the data retention time of conventional and NC-based flash memory devices. Stability increases with increasing oxide thickness; however, thicker oxide layer reduces the tunneling current through dielectric layer, requires higher operating voltages for write/erase, and puts restrictions on down-scaling dimensions of the nodes. For most flash memories, the retention time and operating speed are in inverse proportion to each other. Several approaches have been studied to achieve the fast programming speed (write/erase) and the long retention time of memory simultaneously.[583−585] Recently, researchers have focused on improving data retention time without decreasing the programing speed at low voltages.[586−588] For this purpose, it was proposed to replace the conventional SiO_2 dielectric layer with a high-*k* gate dielectric for the control and tunnel oxide layers. High-*k* dielectric materials with lower conduction band offsets with Si provide lower tunneling barriers at the dielectric channel.

The idea of NC-based flash memory has been proposed in 1996 by IBM.[571,582] Since then, different metal and semiconductor NCs have been tested as FGs.[589−592] The integration of 5 nm Si NCs into the gate oxide strongly affects the transfer characteristics of the MOSFET as shown in Figure 57.[593] In the control device where no FG is embedded into gate insulator, the drain current (I_D) versus gate voltage (V_G) scans show no hysteretic behavior; I_D has same magnitude when V_G is scanned from −4 to 4 V and when V_G is scanned from 4 to −4 V (Figure 57, dashed curve). However, huge hysteresis of transistor transfer characteristics is observed when small Si NCs are integrated into the gate oxide. For example, the difference in I_D measured during forward and backward gate scans exceeds 10^6 at $V_G = 0$ V (Figure 57, solid curve).[593] Such behavior is fully consistent with flash memory operation principles described above; charging of NCs shifts the FET threshold voltage. The performance of NC flash memories depends strongly on the accurate control of NC size, density, and their uniform distribution in a thin layer of oxide.[590,592,594,595]

Si and Ge Nanocrystal-Based Flash Memory Devices. Si NCs-based FG memory is seriously considered among the candidates for the next generation of nonvolatile memory devices.[370,571−573,584,596−604] Tiwari et al. reported the first Si NC-based FG memory device embedded in a SiO_2 layer.[571] The device operation is based on direct tunneling and storage of electrons in the NCs (also called nodes). Capacitance and size of the NCs limit the number of stored charges per node. Electron-injection occurs through direct tunneling from an inversion layer when positive (with respect to the source and drain electrodes) gate voltage is applied ($+V_G$). Such devices demonstrate high speed operation (less than 100s of nanosecond per write−erase cycle), small dimensions, and long operation times (excess of 10^9 cycles).[571] The performance of Si-based memories depends on the accurate control of NC size, density, and arrangement in the thin oxide.

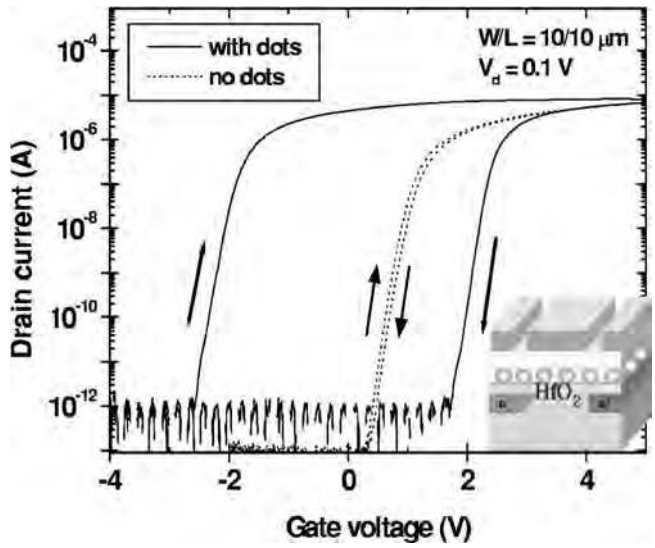

Figure 57. Transfer characteristics (I_D vs V_G scan) of a nanocrystal-based flash memory device consisting of FET and the floating gate made of ∼5 nm Si nanocrystals separated from the transistor channel by a thin 9 nm layer of HfO_2 tunnel oxide and from the control gate by a thicker layer (20 nm) of SiO_2 control oxide. The presence of Si nanocrystals introduces hysteretic behavior of FET transter characteristics (solid line). The control experiment with same thicknesses of HfO_2 and SiO_2 layers but without Si nanocrystals shows nearly ideal transistor behavior with no hysteresis (dashed line). Reprinted with permission from ref 593. Copyright 2006 American Institute of Physics.

Punchaipetch et al. studied the effect of tunnel layer thickness on the memory performance (write/erase) and data retention of Si NC-based floating gate devices.[605] The 10 nm SiO_2 tunnel oxide showed the most stable performance as compared to the 3 and 5 nm oxide layer. Degradation of threshold voltage was not observed even after 10^8 operating cycles. Lu et al. reported the effect of NC density on the operation of the floating gate memory.[606] It was shown that the operating speed can be further increased by increasing the density of NCs in the FG layer. As mentioned above, the retention time is inversely correlated to the thickness of the tunnel oxide layer.

King et al. reported the gemanium NC memory devices that could operate at low voltages and high speeds superior to Si-based memory devices.[579] The device consisted of MOSFET with Ge NC FGs embedded within the gate dielectric. Lu et al. also reported the memory devices with Ge NCs embedded in $LaAlO_3$ (LAO) high-*k* dielectric.[607] This device showed a significant memory effect with a very high density of stored charge up to $2 \times 10^{13}/cm^2$. A maximum shift in the threshold voltage of 3.2 V was achieved for the trilayer structure of LAO(8 nm)/Ge_NCs/LAO(3 nm)/Si. Ge NC FGs showed excellent charge retention time, whereas the decay in memory capacitance after 10^4 s of stress under a flat band voltage was only 8%. Kim et al. compared memory characteristics of SiGe NCs embedded in HfO_2 or SiO_2 dielectric layers.[558] Reported results indicated that the HfO_2 tunneling oxide with SiGe NCs shows a faster charge carrier trapping and detrapping

at low voltages even when the oxide thickness was slightly thicker than that for SiO_2 tunneling oxide memory.

Metal Nanocrystal-Based Flash Memory Devices. Recently, it was realized that flash memory devices using metal NCs as floating gates can be superior to the devices utilizing semiconductor NCs.[576−578,586−589,591,608−611] The advantages of metal NCs for memory applications are higher density of states near the Fermi level, stronger electrostatic coupling to the conducting channel, tunable work function, and small energy perturbations due to carrier confinement. The work function can be tuned by using different metals and metal alloys offering an opportunity to optimize the trade-off between write/erase speed and charge retention because the work function of NC FGs controls not only the depth of the potential well at the storage node but also the density of states available for carrier tunneling. Numerous attempts have been made to develop nonvolatile memory devices using for FG metal NCs such as Au, Pt, Ni, Co, Ag, etc.[589,591,592] So far, Au is one of the most promising materials because it is chemically stable and has a large work function. Isolated Au NCs form a deep quantum well between the control oxide and tunnel oxide, desirable for the FG application.

For example, Chan et al. reported the memory characteristics of Au NCs embedded in the amorphous HfAlO tunnel layer.[587] A significant threshold voltage shift was obtained due to charge trapping on Au NCs. The memory window and stored charge density were ~10 V and ~$1 \times 10^{14}/cm^2$, respectively. A smaller size of Au NCs showed a higher tunneling coefficient and a larger memory window. Lo et al. reported charge storage characteristics of Au NCs on the multistacked layer of $Al_2O_3/HfO_2/SiO_2$.[588] The device showed high efficiencies of charge injection and detrapping with long retention times. There are several good review articles on metal NCs-based memory devices.[589,591,592,612,613]

All above-described devices employed metal and semiconductor NCs deposited from the gas phase using CVD or high-vacuum deposition techniques. Such processes typically have difficulties with controlling NC size and packing density. In addition, high temperature processes for making NCs can provide a source of metallic contamination due to diffusion of metal atoms into FET channel. Colloidal synthesis of NCs provides a convenient opportunity to overcome many problems of gas-phase NC growth. It can easily provide monodisperse NCs of different materials with precisely tunable size. The NCs can be integrated into the memory device using low temperature solution processing. Recently, memory devices using colloidal NCs as charge-trapping elements have been reported.[614−622] Park et al. reported the memory effects for colloidal gold NCs embedded between thermally grown SiO_2 tunnel oxide and Al_2O_3 control oxide deposited by atomic layer deposition (ALD).[622,623] To characterize the memory behavior, they measured the dependence of capacitance versus DC bias applied to Al/Al_2O_3(60 nm)/Au_NCs /SiO_2(6.3 nm)/p-Si metal−oxide−semiconductor (MOS) capacitor. Because MOS capacitor represents the gate stack of a flash memory device, such capacitance measurements allow modeling the memory behavior using a simple device structure with only passive elements, without building an active MOSFET-based memory cell. The write and erase cycles are represented by shifts in the flat-band voltage of MOS capacitor, directly related to the threshold voltage of flash memory FET.[622] The $C-V$ curves of MOS capacitor with embedded Au NCs showed a flat-band voltage shift of about 4.3 V depending on the bias

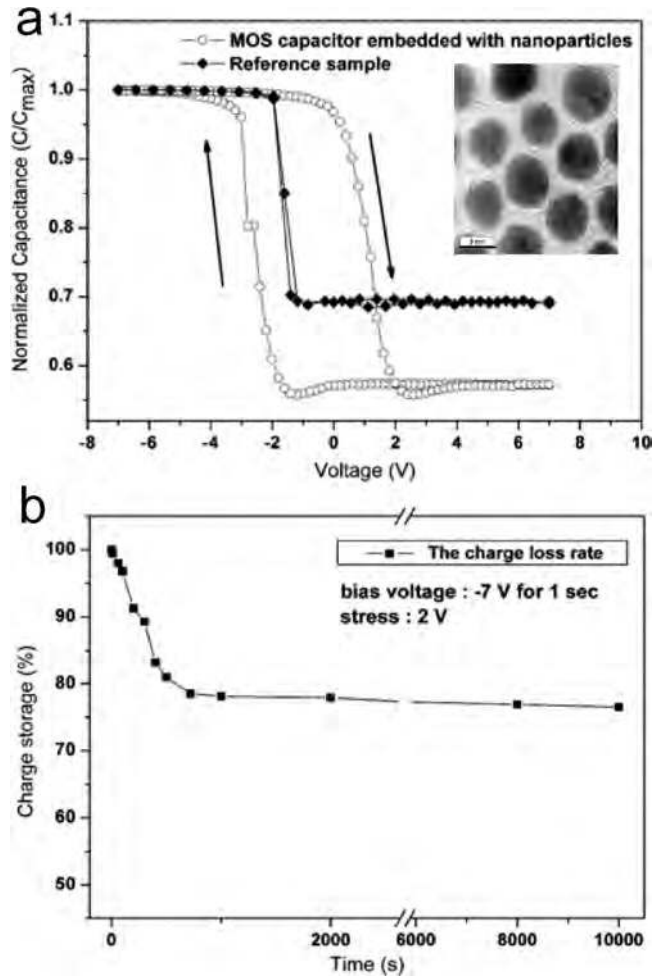

Figure 58. (a) Capacitance versus applied bias curves for MOS capacitors with or without embedded chemically synthesized Au nanoparticles. (b) Storage of charges trapped in Au nanoparticles embedded between tunnel and control oxide layers. Reprinted with permission from ref 622. Copyright 2006 Institute of Physics.

history (Figure 58a). This shift originated from the trapping of charge carriers on Au NCs. The estimated number of charge carriers stored in the Au NCs was about 3×10^{11} cm^{-2} when the voltage was swept in the range of ±7 V. The device also showed relatively good retention time, after losing ~18% of initial charge during the first 500 s, remaining charge stabilized with ~2% additional decay after 10^4 s (Figure 58b).

Choi et al. reported the FG memory device using colloidally synthesized 4 nm Pt NCs.[624] The monolayer of Pt NCs was immobilized on a SiO_2 substrate using poly(4-vinylpyridine) as a surface modifier. A MOS-type memory device with Pt NCs exhibited a relatively large memory window of 5.8 V under ±7 V for write/erase voltage. Lee et al. demonstrated the possibility to tune the properties of charge-trapping layer by utilizing binary mixtures of NCs with different electron affinities (Co and Au).[625] All of these results indicate that chemically synthesized metal NCs can be successfully integrated in nonvolatile flash memory devices.

The concept of charge-trapping memory can also be realized by integrating colloidal NCs into a matrix of organic insulator. Thus, Lee et al. demonstrated hysteresis in $C-V$ curves measured for a metal−insulator−semiconductor (MIS) capacitor with the insulating layer composed of polyelectrolyte/Au NCs multilayer films.[619] These charge-trapping insulating films were prepared by the layer-by-layer

deposition process. The optimum performance (memory window of ~1.8 V) was observed for a device with three polyelectrolyte/Au_NC bilayers and a 1.4 nm thick HfO_2 tunneling oxide layer. Li et al. reported charge trapping leading to hysteretic $C-V$ curves and electrical bistability for CdSe/ZnS core−shell NCs embedded in MEH-PPV[617] or C_{60} fullerene[618] matrices.[615,616] The authors explained observed shifts in flat-band voltage by charge trapping in CdSe/ZnS NCs.

Current literature demonstrates encouraging proof-of-principle demonstrations of NC-based memory devices. The further progress in this field might be accelerated by synthetic engineering of NCs. For example, a thin uniform layer of insulating oxide (SiO_2, TiO_2, etc.) can be grown on top of Au NCs.[626,627] Such Au/SiO_2 core−shell NCs look like perfect candidates for FG memory applications because they include both FG and tunnel oxide cointegrated together in the form of solution processed units with precisely tunable size of Au core and thickness of SiO_2 shell.

7.5.2. Resistance-Change Memory Devices

Devices incorporating switchable resistive materials are generically classified as resistive random access memory, or RRAM. The appeal of RRAM is that each element is a two-terminal device: switching between high and low resistance is achieved by means of an appropriate electrical pulse, and the read-out process consists of applying a lower voltage to probe the state of the resistance. This type of element can be incorporated into cross-point arrays (Figure 59a), provided that it exhibits sufficient rectification or other nonlinear response.[570]

Many inorganic and organic materials exhibit electrical switching behavior and, potentially, can be considered for resistive memory applications. As will be discussed at the end of this section, numerous additional requirements put very stringent limitations on materials for application in RRAM devices. In the recent years, hybrid inorganic−organic composites containing metal or semiconductor NCs are considered among the most promising materials for this type of memory. Below, we discuss several examples of hybrid memory devices; more detailed information can be found in recent reviews by Scott and Bozano[570] and by Yang et al.[629]

Many reported hybrid memory devices combined inorganic NCs blended into an organic host. For example, Yang et al. demonstrated resistive switching behavior in a system containing 2.8 nm Au NCs capped by dodecanethiol ligands, an inert polymer such as polystyrene (PS) or poly(methyl methacrylate), and conjugated organic compound such as Alq_3, 8-hydroxyquinoline (8HQ), or 9,10-dimethylanthracence (DMA).[629] Figure 59b shows $I-V$ characteristics for the device Al/(PS+Au-DT+DMA)/Al tested in air. Initially, the device was in the off state, and the current was approximately 10^{-10} A at 1 V. The electrical transition from the off state to the on state took place at 6.1 V with an abrupt current increase from 10^{-10} to 10^{-6} A (curve 1). The device exhibited good stability in this high conductivity state during the subsequent voltage scan (curve 2). The high conductivity state was able to return to the low conductivity state by applying negative bias as indicated in curve 3, where the current suddenly dropped to 10^{-10} A at −2.9 V. This switching behavior can be repeated numerous times and can be driven by short voltage pulses as well. The transition time from the off state to the on state was less than 25 ns. The electrical behavior of the device was strongly dependent on

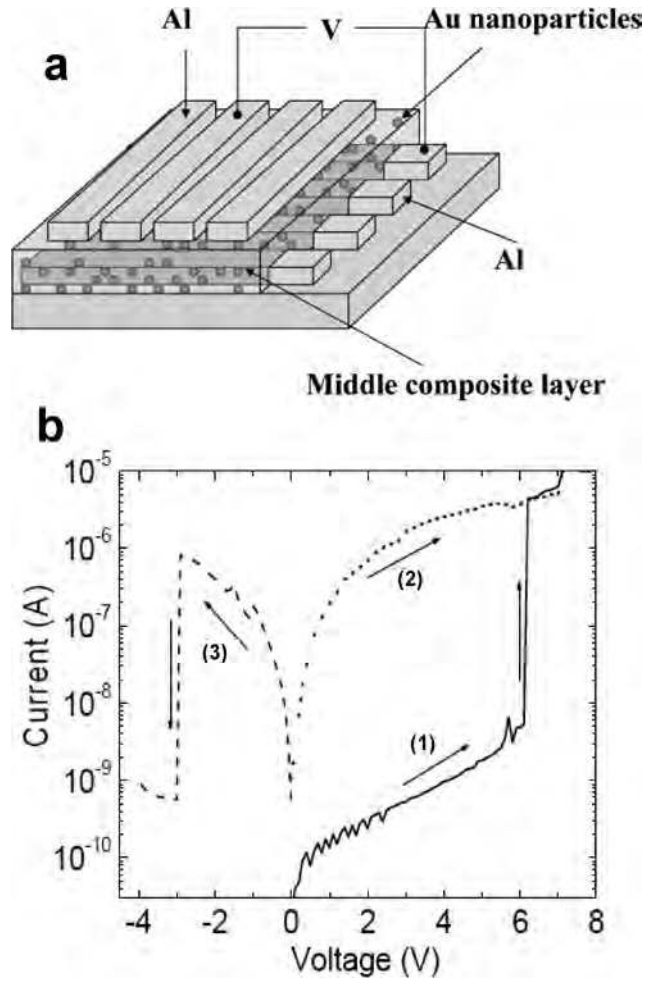

Figure 59. (a) Device structure for resistive memory array. (b) $I-V$ curves for a device Al/(composite layer)/Al with the composite layer containing 2.8 nm dodecanethiol-capped Au nanocrystals mixed with polystyrene and 9,10-dimethylanthracence. (1), (2), and (3) represent the first, second, and third bias scans, respectively. The arrows indicate the voltage-scanning directions. Reprinted with permission from ref 628. Copyright 2005 Springer.

the nature of the metal nanoparticles and the conjugated small organic compound. The polymer in the composite layer served as a matrix for dodecanethiol-capped Au NCs and DMA molecules. An electric-field-induced charge transfer between the Au nanoparticle and DMA of 8HQ through the layer of dodecanethiol ligands was proposed for the switching mechanism.[629] When the electric field reaches a threshold, the electrons on the HOMO of 8HQ gain enough energy and tunnel through the insulator coating on the Au-DT nanoparticle into the metal core. This results in the generation of the charge carriers on 8HQ. The conductance of the films increased. The recombination of the positive charge on the 8HQ and Au nanoparticle is prevented by the insulator coating on the Au nanoparticle. The use of metal NCs with specially designed surface ligands, such as Au NCs capped with naphthalenethiol,[630] and blending them with inert polymer allowed one to obtain write-once-read-many times (WORM) electronic memory elements.[570] WORM devices are characterized by a rapid increase in conductivity if applied voltage exceeds threshold voltage. Once switched to the high-conductivity state, neither a low nor high voltage bias of either polarity is able to cause the device to revert to the low-conductivity state.

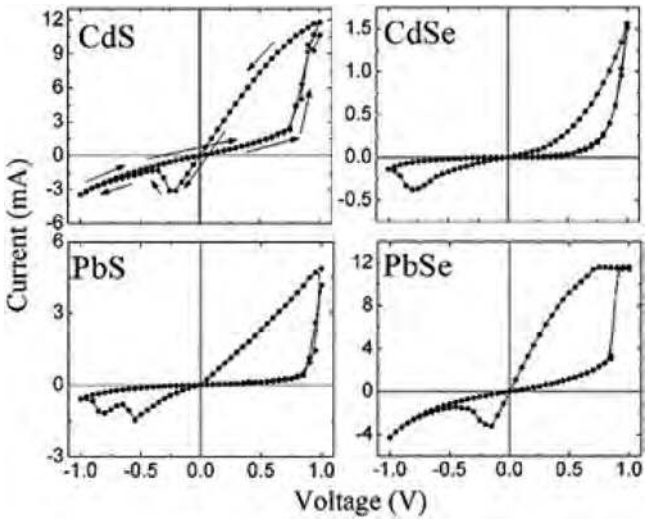

Figure 60. Conductivity switching observed in $I-V$ characteristics measured for monolayers of CdS, CdSe, PbS, and PbSe nanocrystals. Voltage scans originated at 0 V in all cases. The monolayers show electrical bistability with a jump in current in the positive voltage direction; higher-conductivity state retracts at a negative bias. Reprinted with permission from ref 631. Copyright 2008 Wiley.

There are numerous examples of bistable switching behaviors observed in NC−organic hybrid systems.[614,617,618,620,631,632] Lai et al. reported Au NCs/poly-(*N*-vinylcarbazole) memory devices.[632] Electrical bistability was demonstrated for a broad range of NC-to-poly-(*N*-vinylcarbazole) weight ratios. Another recent example of resistive memory included Pt NPs deposited onto the surface of tobacco mosaic viruses and blended as nanowires into poly(vinylalcohol).[633] Semiconducting particles have also been blended into organics, including wide band gap inorganic oxides (ZnO) in polystyrene,[634] and copper−phthalocyanine in Alq_3.[635] The most common explanation of the switching from insulating to conducting states in hybrid devices containing metal or semiconductor NCs and conductive organic polymer or small molecules suggests electric-field-induced transfer of electrons from organic molecules to nanoparticles. Formation of the charge-transfer complex increases the number of mobile charge carriers (holes) in the organic component. The shell of insulating ligands at the surface of NCs is assumed to act as a barrier to recombination.[629,630,636,637]

Electrical bistability and resistive switching was also observed for semiconductor NCs.[614,616−618,620,638] Pal et al. showed the existence of low- and high-conductivity states and switching behavior in the films containing different semiconductor NCs separated by poly(allylaminohydrochloride) PAH or poly(methylmetacrylate) PMMA molecules. Different semiconductor NCs demonstrated similar switching behavior (Figure 60) pointing to general character of electrical bistability in these semiconductor NCs.[620] To date, switching and memory effects were observed in systems containing CdSe/ZnS,[614,616,617,639] CdSe/PbS,[640] CdSe/Ag_2S,[640] CdS,[631] CdSe,[620,621] PbS,[631] and PbSe[631] NCs blended with different organic matrices. Design of the NC structure can be used to tailor switching behavior. Recently reported CdS/PbS core−shell NCs showed significantly enhanced on/off ratio as compared to individual CdS or PbS NCs.[640] The memory characteristics can be controlled by tuning the shell thickness. Similarly, CdS/Ag_2S core−shell NCs showed reproducible electrical bistability with the on/off ratios approaching 10^4.[640] Fischbein and Drndic reported memory effects in electronic transport through close-packed arrays of CdSe NCs capped with trioctylphosphine oxide ligands.[638] Several reports demonstrated that switching of the conductivity in semiconductor NCs can be controlled by voltage pulses and is quite stable over many on/off cycles.[631,640,641] To the best of our knowledge, there is no agreement about the mechanism of electrical switching in semiconductor NCs. We can speculate that redox processes involving oxidation or reduction of chalcogen atoms at the NC surface may lead to conductivity switching. It is known that shallow midgap states often form in II−VI and IV−VI semiconductor upon oxidation or reduction of surface sites and can behave as dopands for semiconductor NCs.[255,330]

Many materials including organic polymers and small molecules, inorganic solids, nanoparticle films, and hybrid organic−inorganic blends can exhibit electrical bistability behavior necessary for RRAM operation. We have to admit, however, that electrical switching is a necessary but not sufficient requirement for memory applications. Scott and Bozano from the IBM Research Division discussed the performance requirements for a memory element that have to be satisfied to consider it for commercial memory devices.[570] They selected nine different metrics, the on−off resistance ratio, read time, write/erase time, cycling endurance, retention time, power consumption, rectification, ruggedness, and cost, and estimated acceptable limits for each of these parameters to approach the level of commercial viability. They also pointed to several common misconceptions, for example, the on−off resistance ratio does not have to be very large (in many cases, a factor of 10 is more than sufficient), whereas the reproducibility of switching characteristics for many devices, sharp switching threshold, on-state resistance, and rectifying $I-V$ characteristic do really matter. To evaluate prospects for a given material for memory applications, multiple metrics have to be measured and reported. Unfortunately, most of the literature reports lack this depth of characterization.

7.5.3. Nanocrystals for Magnetic Data Storage (HDDs) Applications

In 2000, Sun and Murray proposed to use colloidal NCs for magnetic data storage applications.[27] The electron spins inside magnetic NC are all aligned parallel to each other, and their orientations can be manipulated by applying external magnetic field. A ferromagnetic NC can store a bit of information encoded in its magnetic moment. In the most optimistic scenario where magnetic NCs are assembled in a long-range ordered array and each NC is used for storing information, such advanced magnetic media can reach enormous magnetic recording densities up to 1 Tb/in^2. However, technical realization of this great idea requires addressing several very difficult problems. A detailed discussion of magnetic phenomena at the nanoscale falls outside the scope of this Review, and we only briefly describe achievements and challenges on the way to employing magnetic NCs for data storage. The reader can find detailed information on this topic in several reviews and book chapters.[45,642,643]

To be applicable for magnetic storage medium, the magnetization direction in a material should be very stable and not reverse due to thermal fluctuations. In other words, the NCs should have high magnetic coercivity (H_c). It was found that the coercivity of a magnetic particle strongly depends on its size. If NC contains only one magnetic domain

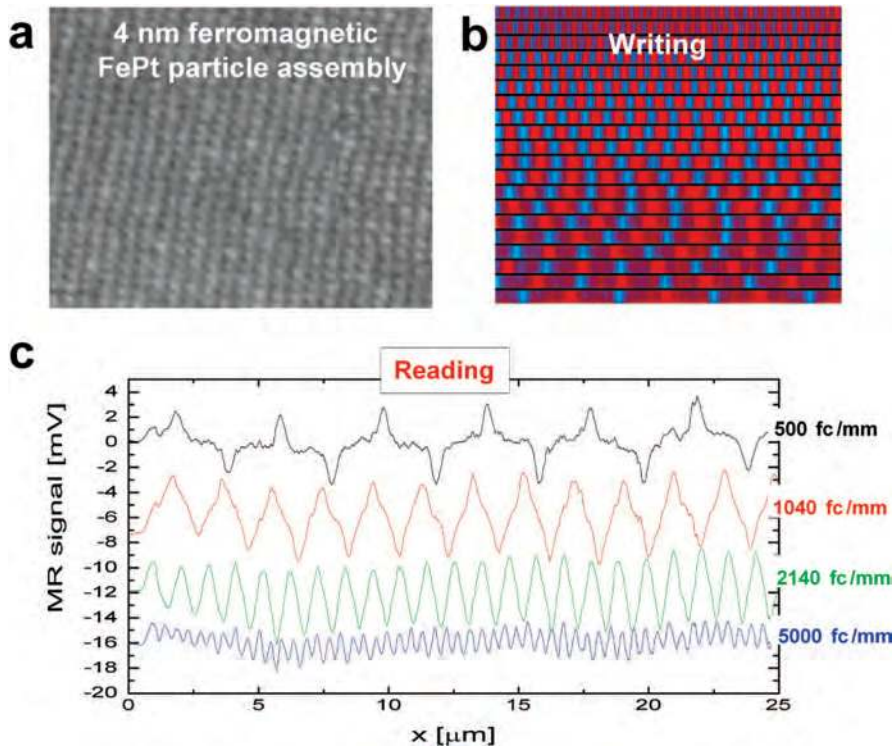

Figure 61. (a) An array of 4 nm FePt nanocrystals used for magnetic data recording. (b, c) Magnetoresistive (MR) read-back signals from written bit transitions in a 120 nm thick assembly of 4 nm diameter $Fe_{48}Pt_{52}$ nanocrystals. The individual line scans reveal magnetization reversal transitions at linear densities of 500, 1040, 2140, and 5000 flux changes per millimeter (fc/mm).[27] Courtesy C. B. Murray.

(very typical for colloidal magnetic NCs), reducing particle size decreases the number of exchange coupled spins.[4,644] As a result, the coercivity falls due to the progressively increasing role of the thermal fluctuations leading to superparamagnetism. The coercivity of a superparamagnetic particle is zero ($H_c = 0$) because thermal fluctuations prevent the existence of a stable magnetization. Superparamagnetic NCs cannot be used for data storage. To beat the superparamagnetic limit, magnetic materials with very large magnetocrystalline anisotropy have to be used.

One of the most studied magnetic nanoparticles are the iron−platinum alloys.[27] As-synthesized FePt nanoparticles usually exhibit the chemically disordered fcc structure with relatively poor magnetic properties. Thus, fcc FePt nanoparticles are superparamagnetic at room temperature and can be handled in form of colloidal solution for casting films, making self-assembled arrays, etc. Further, the FePt nanoparticles can be annealed under inert atmosphere. This annealing induces the iron and platinum atoms to rearrange and convert the particles to the chemically ordered face-centered tetragonal (fct) phase and transforms them into nanoscale ferromagnets with the room temperature with coercivity high enough to use the arrays of fct FePt NCs in a data storage device.[45,645,646] The annealed FePt NCs array (Figure 61a) can support stable magnetization reversal transitions (bits) at room temperature.[27]

Depending on Fe_xPt_{1-x} stoichiometry and NC size, the transition temperature has to be in the range of 500−700 °C,[45] while for the bulk material the reported value was 1300 °C.[647] To further reduce the phase transition temperature, it was proposed to introduce silver atoms into the lattice of FePt NCs during their synthesis.[648] It was suggested that Ag atoms leave the FePt lattice at temperature less than 400 °C and the formed vacancies increase the mobility of the Fe and Pt atoms, accelerating the phase transformation.

Figure 61 shows a standard write/read test acquired for an annealed film of 4 nm FePt NCs.[27] The read-back sensor voltage signals (Figure 61c) from written data tracks (Figure 61b) correspond to linear densities of 500, 1040, 2140, and 5000 flux changes per millimeter (fc/mm). These write/read experiments demonstrated that 4 nm FePt ferromagnetic NC assembly supports magnetization reversal transitions at moderate linear densities that can be read back nondestructively. To achieve much higher recording densities, not only size and magnetic properties of individual NCs have to be controlled, but also orientations of individual NCs in the array have to be pinned to provide unidirectional alignment of easy axes of magnetization (i.e., the preferable magnetization direction, typically linked to a certain crystallographic axis) for individual NCs. This is a challenging problem, especially if we take into account that such alignment has to be achieved throughout the entire hard disk area by using high-throughput fabrication techniques. Deposition of magnetic NCs in the presence of magnetic field or designing NCs with anisotropic shape has been proposed to facilitate orientation of individual particles.[649] Future perspectives of colloidal NCs for magnetic data storage will strongly depend on the development of novel syntheses for materials with very high magnetic anisotropy (e.g., Co_5Sm) and methods for fast and reliable assembly of chemically synthesized NCs into uniform, ideally, long-range ordered two-dimensional arrays.

7.6. Nanocrystal Solids for Thermoelectric Applications: Expectations and Challenges

Solid-state cooling and power generation based on thermoelectric (TE) effects have potential applications in waste-heat recovery, air conditioning, and refrigeration. A simple thermoelectric energy conversion device contains two semiconductors, one p-type and one n-type, connected in series

as shown in Figure 62. The heat applied to one side of TE module will force majority carriers to flow from the hot side to the cold side (Seebeck effect),[650] generating DC current through TE module. Alternatively, forcing DC current through TE element will create a temperature gradient (Peltier effect, Figure 62), which can be used for refrigeration. Developing low-cost and efficient thermoelectric materials is a field of growing academic and technological interests.[651] During the past decade, it was both theoretically predicted and experimentally confirmed that nanostructuring of semiconducting materials can improve their TE performance. The performance of a TE material can be evaluated by its dimensionless thermoelectric figure of merit (ZT):[652]

$$\mathrm{ZT} = S^2\sigma T/\kappa \tag{51}$$

where S is the Seebeck coefficient (also known as thermopower), σ is the electrical conductivity, κ is the thermal conductivity, and T is the absolute temperature. The efficiency of TE energy generator producing electricity from a temperature difference between cold and hot sides with temperatures T_c and T_h, respectively, can be expressed through the ZT value:[653]

$$\eta = \eta_C \frac{\sqrt{1+\mathrm{ZT}} - 1}{\sqrt{1+\mathrm{ZT}} + {}^{T_c}/_{T_h}} \tag{52}$$

The maximum power-generation efficiency of TE generator is thermodynamically limited by the Carnot efficiency $\eta_C = 1 - T_c/T_h$, and eq 52 shows what fraction of the Carnot efficiency can be achieved at a given ZT value. The larger is the ZT, the more efficient a thermoelectric material becomes. The Carnot efficiency corresponds to infinitely large ZT. Another important metric of TE performance is the power factor $P = S^2\sigma$, which is related to the amount of electric power that can be generated by given TE module.[654] For more detailed information on thermoelectric phenomena, we can recommend several books[655,656] and review articles[650,653,657] on the fundamental aspects of thermoelectrics.

For the past 50 years, a number of thermoelectric materials have been developed for different temperature regions, from cryogenic to above 1000 °C.[656] A recent review by Snyder and Toberer compares state-of-the-art p-type and n-type high ZT materials based on bulk semiconductors.[653] TE generators found applications in various locations, including deep space Voager missions;[656] TE coolers can be found in many optoelectonic devices and consumer products including cooled car seats.[657] When speaking about potential applications, TE devices have to be compared to other heat engines in power generation efficiency and other characteristics. Generally, steam turbines and combustion engines are more efficient, but only when operated under optimized conditions (large scale, large temperature gradients, stable heat flow, etc.).[658] At the same time, there are numerous niches where TE does not have obvious competitors. These are all kinds of medium- and small-scale applications; in subkilowatt applications, TE generator can easily beat heat engine in efficiency.[658] Because TE heat converters do not have movable parts, they can work reliably for many years without maintenance, can switch on and off many times, and do not generate any noise. Generally speaking, TE devices and heat engines are two very complementary parts of the energy portfolio; TE can cover many areas where turbines and other heat engines cannot be used. In cooling applications, the prospects of TE technology are strongly dependent on the availability of materials with high ZTs at low temperatures; development of inexpensive material with ZT ≈ 3 at room temperature would lead to massive switching of the consumer refrigerators market to TE technology.

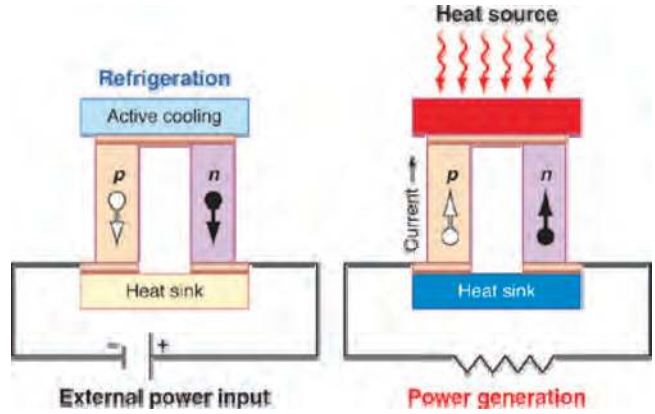

Figure 62. Thermoelectric refrigeration and power generation. A single thermoelectric couple is shown, configured for refrigeration (left) or power generation (right). The labels "p" and "n" refer to the sign of the majority charge carriers in each leg; "○" correspond to holes, and "●" correspond to electrons. The copper-colored regions depict electrical connections. Reproduced with permission from ref 650. Copyright 2002 American Association for Advancement of Science.

So far, widespread use of TE technology beyond selected niche applications is limited by relatively low efficiency of available TE materials. From the late 1950s until the early 2000s, the field of TE research was stagnant with ZT ≈ 1, and efficiencies of about 10% of the Carnot limit were achieved in commercial devices using bismuth telluride based alloys.[659] The complications in development of more efficient TE materials were associated with complex relations between S, σ, and κ in bulk solids. Very often improvement of one parameter in eq 51 negatively affected two others, leading to very small, if any, gain in ZT. This pessimistic situation changed in the early 1990s when Hicks and Dresselhaus[660,661] pointed out that reducing the dimensionality of a semiconducting material can enhance the electronic density of states near the Fermi level, which is predicted to enhance the power factor. As an additional benefit, the interfaces in nanostructured materials can successfully scatter phonons reducing thermal conductance κ, which further enhances ZT. Generally, κ has two additive terms, electronic thermal conductivity (κ_e) associated with heat carried by electrons, and lattice thermal conductivity (κ_{ph}) associated with heat carried by phonons. The former is proportional to electrical conductivity via the Wiedemann−Franz law,[662] whereas κ_{ph} can be lowered by proper material engineering.

The physics of and design ideas for low-dimensional TE materials have been developed in numerous theoretical studies. Mahan and Sofo derived that a narrow distribution of the energy of electrons participating in the transport process is needed for maximum thermoelectric efficiency.[663] Such delta-functional features in the density of electronic states can be formed in semiconductor nanostructures due to two- or three-dimensional quantum confinement. Sun et al. predicted that quantum-confined Bi nanowires reach a ZT of 1.5 at a wire diameter of 10 nm.[664] Lin et al. predicted ZT values of about 4 and 6 for 5 nm-diameter PbSe/PbS and PbTe/PbSe superlattice wires at 77 K.[665] Balandin and Lazarenkova predicted enhanced ZTs for a superlattice of

Si NCs embedded into Ge matrix.[666] Humphrey and Linke derived conditions under which reversible diffusive electron transport could be achieved in nanostructured thermoelectric materials.[667] Their work further supported the idea that delta-functional density of states is optimal for thermoelectric materials and predicted that optimized nanostructured materials with a delta-like DOS may have ZT approaching 10 at room temperature. This exciting prediction originated from the fundamental difference between thermodynamics and transport in nanostructured materials as compared to bulk semiconductors.[667] In 2008, Mueller reported an encouraging theoretical study of TE behavior in an array of molecular junctions.[659]

The experimental studies of low-dimensional TE materials supported optimistic theoretical predictions. Harman et al. observed ZT ≈ 1.6 in a PbSeTe-based quantum dot superlattice grown by molecular beam epitaxy (MBE),[12] Venkatasubramanian et al. achieved ZT ≈ 2.4 in a p-type Bi_2Te_3/Sb_2Te_3 superlattice,[668] and Hsu et al. reported ZT ≈ 2.2 in alloys containing nanometer-sized metallic grains embedded in a semiconducting matrix.[669] In 2008, Heath et al.[670] and Yang et al.[671] reported very high ZT values measured for individual Si nanowires. Most of these ZT enhancements were attributed to lowering the thermal conductance due to phonon scattering at the heterointerfaces and grain boundaries. However, until very recently, practical use of these materials was hampered by complicated and expensive synthesis techniques, such as molecular beam epitaxy.[12] In the last several years, important steps toward cost-effective nanostructured TE materials were reported. The Kanatzidis group synthesized several families of complex chalcogenide phases, such as n-type $AgPb_{18+x}SbTe_{20}$ (LAST)[669] and p-type $Na_{0.95}Pb_{20}SbTe_{22}$ (SALT)[672] showing ZT values of ~1.7 and 1.6, respectively. These high ZT values originated from low thermal conductivity caused by the presence of nanoscale inclusions in the host material spontaneously formed due to phase separation during crystallization of melted phase. In 2008, Poudel et al. reported a very intriguing discovery; simple grinding of bulk $(Bi,Sb)_2Te_3$ indots into a nanopowder (Figure 63a) followed by hot-pressing nanoscale grains back into a bulk solid (Figure 63b) produced a material with ZT ≈ 1.4 at 100 °C.[673] This number was a record for the $(Bi,Sb)_2Te_3$ phase whose TE properties have been studied and optimized for more than 50 years. Electrical and thermal transport measurements (Figure 63c−f) showed that the ZT improvement is a result of low thermal conductivity caused by increased phonon scattering by grain boundaries and structural defects.[673] The same group later extended this approach based on ball-milling and hot-pressing of bulk materials to p-SiGe, reporting a ZT of 0.95 at 800 °C, which was about 50% higher than the previous reported record in p-type SiGe alloys. These studies showed that bulk nanocomposite materials prepared at low-cost can deliver record TE characteristics. Further ZT improvements may be associated with more precise design of the nanoscale elements.

Colloidal synthesis of monodisperse NCs could offer a convenient route to low-cost and production-scalable low-dimensional thermoelectric materials. Moreover, chemical synthesis allows precise tuning of the NC size in the sub-10 nm range typically inaccessible for molecular beam epitaxy grown quantum dots[674] or ball-milled powders. This opens up the possibility to explore thermoelectric properties of strongly quantum-confined materials. In this regime, the valence and conduction bands of a semiconductor collapse

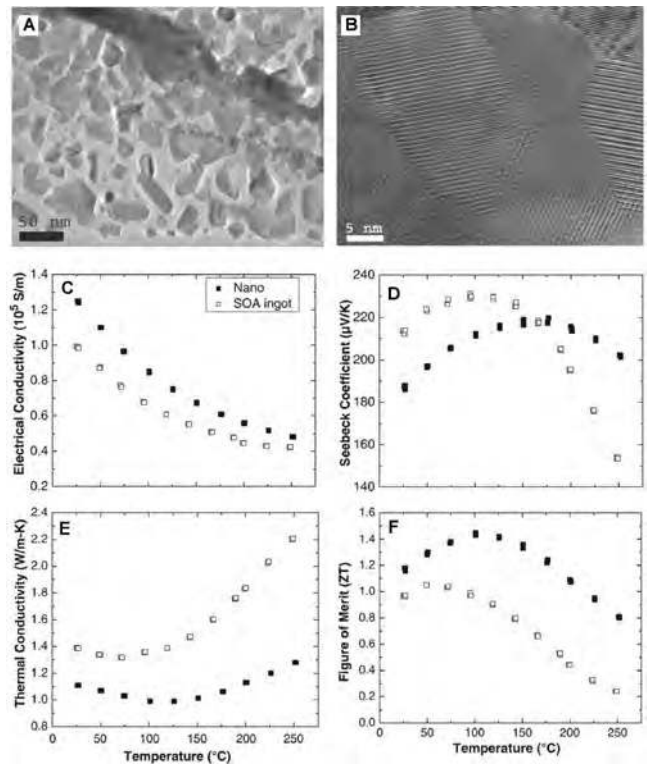

Figure 63. TEM images of a nanopowder obtained by ball-milling of bulk $Bi_{2-x}Sb_xTe_3$ indots (A) before and (B) after hot-pressing. Temperature dependence of (C) electrical conductivity, (D) Siebeck coefficient, (E) thermal conductivity, and (F) ZT of a hot-pressed nanocrystalline bulk sample (■) as compared to that of a state-of-the-art $Bi_{2-x}Sb_xTe_3$ ingot (□). Reprinted with permission from ref 673. Copyright 2008 American Association for Advancement of Science.

into well-separated discrete energy states,[39,254,675] which alter fundamental properties of a semiconductor such as the electronic density of states (DOS) and band gap energy.[39,254,675] Quantum confinement leads to sharp delta-function-like peaks in the DOS, which is predicted to be the best possible electronic structure for a thermoelectric material.[663] It is also anticipated that these materials will have advantageous thermal properties because the NC diameters are much smaller than the phonon mean free path (~10^{-7} to 10^{-8} m for crystalline materials at room temperature),[676,677] causing a strong suppression of thermal conductivity due to phonon scattering at the NC boundaries.[678,679]

The major challenge for employing colloidal NCs in TE applications is very high electrical conductivities necessary to achieve reasonable power factors and ZT values. The conductivity of a NC solid should be comparable to that of bulk degeneratively doped semiconductor. For example, Figure 63c shows that state-of-the-art $(Bi,Sb)_2Te_3$ TE materials exhibit $\sigma > 1000$ S cm^{-1}. It is unlikely to achieve these levels of conductivity in arrays of colloidal NCs with organic ligands. However, recent developments in surface ligands utilizing conductive inorganic molecules show promising improvements in charge transport through arrays of metal and semiconductor NCs. Thus, our team reported $\sigma \approx 200$ S/cm in a film of 5 nm Au NCs capped with $Sn_2S_6^{4-}$ Zintl ions and $\sigma \approx 250$ S/cm[273] in solution-processed $(Bi,Sb)_2Te_3$ nanocomposite films formed from colloidal NC solutions.[680] The developments of electronically transparent surface ligands may lead to high-mobility Bloch transport through three-dimensional minibands.[237] In addition, temperature dependences of σ for a heavily doped conventional semi-

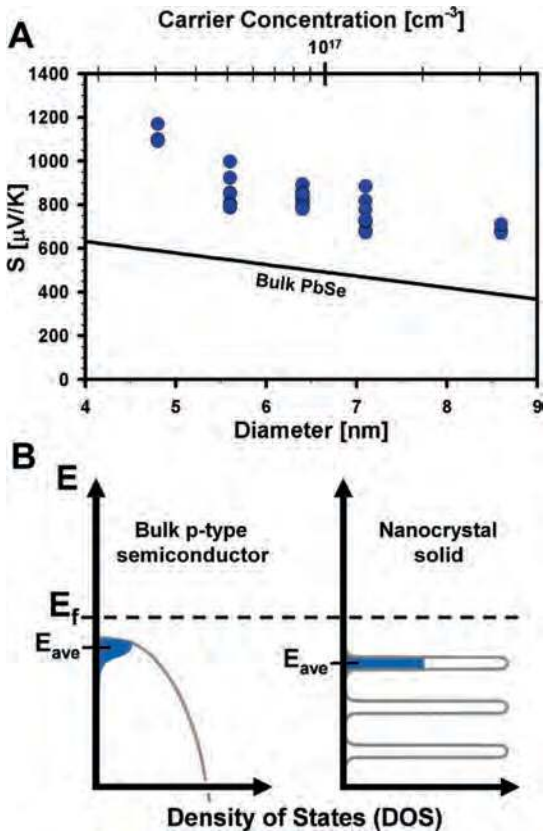

Figure 64. (A) Size-dependent Siebeck coefficient (also known as thermopower) observed in superlattices of PbSe nanocrystals. Solid line shows the dependence of Siebeck coefficient on carrier concentration in bulk p-type PbSe. (B) A mechanism that can qualitatively explain enhancement and size-dependence of Siebeck coefficient in the nanocrystal solids. The electronic density of states is represented by the gray lines. The carrier concentration is represented by the area of the blue region, and the thermopower is approximately proportional to $E_f - E_{ave}$, where E_f and E_{ave} are the Fermi energy and average energy of conducting holes, respectively. See text for more detail. Reprinted with permission from ref 255. Copyright 2008 American Chemical Society.

conductor and for a NC solid have opposite trends: for bulk phases, σ decreases with temperature due to increased role of electron−phonon interactions, whereas σ of NC solids typically increases, following the law $\sigma \approx \exp(-T^{-1/\alpha})$, where $\alpha = 1$, 2, or 4 depends on the conduction mechanism (section 5.4).[267,314] Conductivity of NC solids increases with temperature due to facilitated interparticle coupling, typical for granular electronic systems.[314]

While improvements in ZT for nanostructured materials have generally been attributed to reductions in thermal conductivity,[254,651] the unique electronic structure of low dimensional semiconductors can also have a strong impact on thermopower and charge transport.[661] The impact of strong quantum confinement on thermopower of NC solids was recently studied by Wang et al.[255] When a temperature gradient was created across the NC film, an open circuit voltage V_{oc} proportional to the temperature gradient was observed. The Seebeck coefficient was calculated as $-dV_{oc}/dT$ (e.g., a positive Seebeck coefficient implies that the cold region develops a higher potential than does the hot region). The dependence on NC size for thermopower is shown in Figure 64a. As the NC size decreases from 8.6 to 4.8 nm, the thermopower increases from 700 to 1150 μV/K. The positive sign of thermopower indicates that transport in these films was p-type. For comparable carrier concentrations, the PbSe NC solid exhibited a significant thermopower enhancement of several hundred μV/K relative to bulk PbSe.[255] This enhancement in thermopower was attributed to the presence of the sharp peaks in the NC solid DOS relative to the bulk DOS. The thermopower is approximately proportional to the difference between the Fermi energy (E_f) and average mobile carrier energy (E_{ave}). In a bulk material with parabolic bands, the Fermi−Dirac occupation function gives a wide distribution of carrier energies (schematically shown in Figure 64b, left). The DOS of zero-dimensional quantum dots differs from the DOS of a bulk semiconductor (Figure 64b, middle and right).[237,254,675] It has been predicted the thermoelectric power factor ($S^2\sigma$) can be greatly enhanced when the chemical potential is within a few kT's of the deltalike function of the ground state and/or one of the excited states.[663] Aside from enhanced thermopower, nanomaterials should also benefit from a relaxation in the Wiedemann−Franz law because it loses validity in materials with a delta-like DOS. Relative to bulk materials, nanostructured materials can have an increased ratio of electrical conductivity to electronic thermal conductivity, yielding overall greater values of ZT.[667] Another plausible mechanism leading to enhanced thermopower in nanostructured solids is the alteration of scattering mechanisms, which can lead to carrier energy filtering.[681]

Besides obvious interest in thermoelectric applications of NC solids, thermopower measurements are proven to be a very powerful technique in fundamental studies of electronic structure and doping of conventional semiconductors. In particular, it can unambiguously point to the type of carriers responsible for charge transport and provide valuable information on the Fermi energy under particular experimental conditions. Because thermopower is measured under open-circuit conditions, it is not affected by contact resistance. In contrast, the data obtained by current measurements in the field-effect transistor configuration can be strongly affected by nature of the contacts formed between the channel and electrodes.

If the electrical conductivity of NC solids can be improved, these materials will represent an emerging class of inexpensive and scalable TE materials. To compete with commercial thermoelectric materials, the conductivity of NC solids should be increased by at least 2−3 orders of magnitude. This can be done by either increasing the carrier concentration or improving mobility. Increasing carrier concentration generally results in a decrease of thermopower, but could enhance ZT up until a maximum $S^2\sigma$ is reached. A more promising route to improve ZT is to improve mobility (e.g., reduce carrier scattering). Colloidal NCs embedded in a host material would be an interesting system that may exhibit a reduction in carrier scattering. Furthermore, if the reduction in carrier scattering has a favorable energy dependence, thermopower could be enhanced due to energy filtering as proposed in ref 681. In this ideal case, electrical conductivity and thermopower could be enhanced simultaneously.

8. Outlook and Future Directions

Colloidal "bottom-up" synthesis and self-assembly offer the precision of size/shape engineering and placement of semiconductor, plasmonic, and magnetic components going far beyond the capabilities of current top-down lithographic techniques. The modular design of electronic materials by assembling these solution-processed functional building blocks can make a significant impact on the development of

novel materials and devices. We are not sure if NC devices will ever compete in performance with silicon chips. At the same time, when the cost arguments or large dimensions do not allow using single crystal wafers, the NC solids should step into play, successfully competing with polycrystalline and amorphous semiconductors and organic electronic materials.

The commercialization of NC devices is a slow process. Such a situation is not surprising; it took a couple of decades for many revolutionary technologies to bridge the gap between laboratory discovery and the real world applications. As a good sign, in recent years, numerous startup companies joined the race for NC LEDs and solar cells. It means that the pragmatic venture community was convinced by scientific arguments and considered NC devices as potentially profitable. Having these focused players aboard will accelerate the process of finding suitable market niches and filling them. In the meantime, many scientific problems need to be solved. Below, we provide our vision of the major challenges and missing pieces that have to be addressed to employ colloidal NCs in commercial electronics and optoelectronics.

Nanocrystal synthesis has now developed into an active branch of synthetic chemistry. An impressive progress has been achieved, which enabled different single- and multicomponent nanostructures to be created in cost-effective ways. At the same time, it is important to understand that numerous factors such as chemical composition, size, shape, and surface states can contribute to the NC properties. The inability to control all of these parameters can lead to irreproducible characteristics of NCs-based devices. Future developments of synthetic methodology should not only pursue the goal of making more and more sophisticated nanostructures, but also perfect run-to-run reproducibility of "routine" nanoparticle syntheses. Automation of nanoparticle synthesis should substantially improve our ability to control various reaction conditions, especially for nanomaterials with complex shapes and compositions. The use of nontoxic materials will be necessary for many consumer products and special attention should be paid to developments of nonheavy metal-based semiconductor nanomaterials such as InP, $CuInS_2$, etc.

The other extremely important problem, relevant to nanoscience in general, is standardization of nanomaterials. The properties of nanomaterials synthesized by different research groups often vary because of the lack of commonly accepted synthetic protocols. Minor variations of the reaction parameters have led to the situation in which samples prepared by different research groups are (slightly) different from one another, even though they considered nominally same materials. Our research community has to agree upon the list of experimental conditions and characterization techniques, sufficient for quantitative reproducibility of properties for every important type of nanomaterials. Only in that case can results from different researchers be directly compared to each other. The problem of standardization is not unique. Other fields, including semiconductors and polymers, have faced very similar challenges in their early days. Introduction of standards, widely accepted by research and industrial communities, would also greatly facilitate optimization and scaling of NC synthesis. Until now, synthetic developments were driven mostly by the excitement of scientists with novel nanoscale phenomena, while only limited efforts were dedicated to materials optimization. We have all reasons to believe that optimization of synthetic protocols by introducing less expensive and greener chemicals should bring the manufacturing costs for high-quality semiconductor NCs down to about $1/g or less. The "self-purification" effect,[348] long viewed only as a problem to make doped NCs, should allow making electronically pure materials from technical grade chemicals without costly purification procedures.

Moving from synthesis to electronic applications, we want to emphasize that the electronic properties of NC solids depend equally strongly on the NCs themselves and on the surface ligands, which determine the properties of the medium separating individual NCs. Past research focused almost exclusively on the design of NCs, whereas little attention has been paid to the electronic properties of the surface ligands. To improve conductivity, either removal of original surface ligands or their replacement by small molecules was typically used. Although quite successful, this approach is far from being perfect. Removal of surface ligands often introduces dangling bonds and trap states, whereas volatility or oxidation of small ligand molecules imparts instabilities of the long-term electronic properties of NC solids. A significant effort should be dedicated to the development of ligand molecules, enabling facile carrier transport between individual NCs. We should also look beyond the organic molecules as surface ligands; inorganic and hybrid ligands for colloidal NCs could provide the interparticle medium more transparency for charge carriers.

On the fundamental level, little is known about collective phenomena in the nanoparticle assemblies. Simple semi-qualitative analysis predicts the possibility of formation of the collective electronic states (minibands) in properly engineered superlattices of semiconductor NCs. However, detailed electronic structure, carrier dynamics, phonon spectra, and other characteristics of single and multicomponent nanoparticle assemblies have never been a subject of thorough theoretical analysis. Because of the absence of theoretical background, the superlattice approaches to materials design are still in the early stages of development. The generation of truly high-performance materials, requiring the optimization of many competing parameters, is still some way off. At the same time, first results represent the important steps in the rational design of NC solids for targeted applications.

Nanocrystal light-emitting devices are on a good track. It is now clear that they can provide brightness sufficient for displays and other applications. In terms of color purity, NC LEDs easily outperform their immediate competitors, organic LEDs (OLEDs). As of 2009, in other characteristics, such as quantum efficiency, peak brightness, and long-term stability, the more mature OLEDs are still ahead of the NC devices. The major challenge is to interface luminescent NCs with organic or inorganic electron- and hole-injecting layers. Future hopes are also associated with the development of LEDs using noncadmium-based NCs. High luminescence efficiency, precisely tunable narrow emission band, and broad absorption spectrum make NCs excellent materials for tandem devises using high-efficiency GaN-based blue LED and the down-conversion layer with NCs absorbing blue light and emitting at any desired wavelength.[682] These simple structures will be the first commercial application of NCs in optoelectronics. The most-wanted fundamental development in the field would be electrically pumped lasers on NCs. However, to make this dream real, the conductivity of NC layers has to be improved by about 2 orders of magnitude.

Photodetectors is another promising area for NCs. According to published data, performance metrics for resistive photodetectors on PbS NCs are impressively good. In the near-IR, NCs can compete with other technologies, thanks to a large photoconductive gain achieved by proper design of trap states at the NC surface. At the same time, more detailed studies involving operational stability should be carried out to fully evaluate the potential of NCs, for example, in night vision systems. Future developments will probably expand the spectral range of NC detectors, going beyond visible and near-IR into mid-IR region. In parallel, we can envision developments of X-ray and γ-detectors on lead or bismuth chalcogenide NCs. These are desirable for the applications in medical imaging and security.

The nanocrystal solar cells may offer an exciting opportunity for low-cost solar energy conversion. The power conversion efficiencies of NC solar cell are currently at the level of about 3%, which appears low as compared to other technologies represented by organic photovoltaics (~6%), Graetzel cells (11%), CdTe (~16%), CIGS (~19%), and Si (~24%) photovoltaics. However, only two types of solar cells from this list, organic and NC ones, would be naturally compatible with solution-based roll-to-roll manufacturing on flexible plastic substrates. Potential advantages of NCs compared to organic photovoltaics are the low exciton binding energy, superior thermal and photostability, and precisely adjustable band gap. Moreover, NCs can efficiently capture the near-infrared part of the solar spectrum, a challenging task for organic materials. Finally, several research groups demonstrated that colloidal NCs can be used as soluble precursors for polycrystalline CdTe or CIGS films. After the engineering aspects related to solar cell performance are properly addressed, the quantum efficiencies comparable with conventional CdTe and CIGS cells should be attainable. The major challenge, however, for using NCs as the precursors for bulk semiconductors is the presence of surface ligands that partly decompose during sintering and contaminate semiconducting phase. To prevent this scenario, development of novel ligands, which can either undergo controllable decomposition into volatile species or be converted into a good semiconducting matrix, would be highly desirable. Finally, there are several ideas related to using NCs for high-efficiency photovoltaics going beyond the limits imposed on conventional semiconductors (so-called Shockley−Queisser limit). The question if the NC solar cell can beat the Shockley−Queisser limit is discussed in section 7.3.5. We intentionally left this question unanswered because all existing proposals rely on complex carrier dynamics in quantum confined semiconductors, which is currently far from being fully understood.

It is unlikely that NC solids will ever be used in high-end electronics, which is the territory of crystalline semiconductors. On the other hand, there is a list of applications that require relatively simple circuitry operating at modest speeds. For example, each pixel in a flat-panel display is operated by an individual field-effect transistor, switching it at the video frequency. The ability to fabricate such simple circuits by inkjet printing is considered a very attractive alternative to currently used lithography and vacuum deposition techniques. Another important market niche is ultra low-cost, disposable circuits for radio frequency identification tags, labels, toys, etc. There NC devices will have to compete with organic electronics and amorphous silicon. Both of these competitors exhibit carrier mobilities on the order of 1 cm^2/(V s). We can project that achieving the carrier mobility of 5 cm^2/(V s) or higher, combined with good operational stability and nontoxic materials, would convert colloidal NCs into widely used electronic materials. Achieving these carrier mobilities will require extensive work on designing novel surface ligands enabling facile carrier transport between the NCs. As an alternative, the connections between NCs can be made by depositing an inorganic solid into the interparticle voids using atomic layer deposition (ALD).[683]

It is somewhat early to conclusively evaluate the perspectives of colloidal nanomaterials for thermoelectric cooling and power generation. There is a solid theoretical basis predicting that properly designed nanostructured materials can outperform bulk thermoelectric devices. Record thermoelectric figures of merit have been reported using molecular beam epitaxy (MBE)-grown quantum dot arrays and hot-pressed nanopowders. Chemical synthesis allows precise tuning of the NC size in sub-10 nm range, typically inaccessible for MBE grown quantum dots or ball-milled powders, providing an opportunity to further boost thermoelectric performance. In addition, NC solids may be the only option for solution-based fabrication of thermoelectric devices. At the same time, the conductivity of state-of-the art thermoelectric materials is significantly higher than the conductivities so far observed in arrays of colloidally synthesized NCs. We strongly believe that the challenging requirement for competitive thermoelectric modules could be met only by using NCs with a properly designed inorganic interparticle medium.[273]

In summary, inorganic NCs have seen a tremendous development in the past decade, with novel synthesis strategies discovered for metallic, semiconducting, and magnetic materials. The ability to establish facile electronic communication between individual nanostructures and form collective electronic states (minibands) will open the door to a new generation of electronic materials and device applications.

9. Acknowledgments

We are deeply indebted to all of our colleagues and collaborators; their names appear in the cited literature. Particularly, we thank P. Guyot-Sionnest, H. Jaeger (University of Chicago), I. Beloborodov (Argonne National Laboratory), W. Heiss (University of Linz), and C. B. Murray (University of Pennsylvania) for stimulating discussions. We thank M. Bodnarchuk for providing unpublished TEM images. D.V.T. acknowledges support from the NSF MRSEC Program under Award Number DMR-0213745, NSF CAREER under Award Number DMR-0847535, and ACS Petroleum Research Fund under Award Number 48636-G10. The work at the Center for Nanoscale Materials at Argonne National Laboratory was supported by the U.S. Department of Energy under Contract No. DE-AC02-06CH11357.

10. References

(1) Link, S.; El-Sayed, M. A. *J. Phys. Chem. B* **1999**, 8410.
(2) Efros, A. L. *Sov. Phys. Semicond.* **1982**, *16*, 772.
(3) Brus, L. *J. Phys. Chem.* **1986**, *90*, 2555.
(4) Murray, C. B.; Sun, S. H.; Doyle, H.; Betley, T. *MRS Bull.* **2001**, *26*, 985.
(5) International Technology Roadmap for Semiconductors, 2005; available online at http://public.itrs.net/.
(6) *Thin Film Transistors*; Kagan, C. R., Andry, P., Eds.; Marcel Dekker: New York, 2003.
(7) Friend, R. H.; et al. *Nature* **1999**, *397*, 121.

(8) Avouris, P.; Chen, Z.; Perebeinos, V. *Nat. Nanotechnol.* **2007**, *2*, 605.
(9) Duan, X.; Niu, C.; Sahi, V.; Chen, J.; Parce, J. W.; Empedocles, S.; Goldman, J. L. *Nature* **2003**, *425*, 274.
(10) Mitzi, D. B.; Chondroudis, K.; Kagan, C. R. *IBM J. Res. Dev.* **2001**, *45*, 29.
(11) Talapin, D. V.; Mekis, I.; Götzinger, S.; Kornowski, A.; Benson, O.; Weller, H. *J. Phys. Chem. B* **2004**, *108*, 18826.
(12) Harman, T. C.; Taylor, P. J.; Walsh, M. P.; LaForge, B. E. *Science* **2002**, *297*, 2229.
(13) Bruchez, J. M.; Moronne, M.; Gin, P.; Weiss, S.; Alivisatos, A. P. *Science* **1998**, *281*, 2013.
(14) Klimov, V. I.; Mikhailovsky, A. A.; Xu, S.; Malko, A.; Hollingsworth, J. A.; Leatherdale, C. A.; Eisler, H. J.; Bawendi, M. G. *Science* **2000**, *290*, 314.
(15) Klimov, V. I. *J. Phys. Chem. B* **2006**, *110*, 16827.
(16) Klimov, V. I.; Ivanov, S. A.; Nanda, J.; Achermann, M.; Bezel, I.; McGuire, J. A.; Piryatinski, A. *Nature* **2007**, *447*, 441.
(17) Jain, P. K.; Huang, X.; El-Sayed, I. H.; El-Sayad, M. A. *Plasmonics* **2007**, *2*, 107.
(18) Alivisatos, A. P.; Gu, W. W.; Larabell, C. *Annu. Rev. Biomed. Eng.* **2005**, *7*, 55.
(19) Hergt, R.; Dutz, S.; Muller, R.; Zeisberger, M. *J. Phys.: Condens. Matter* **2006**, *18*, S2919.
(20) Jun, Y. W.; Seo, J. W.; Cheon, A. *Acc. Chem. Res.* **2008**, *41*, 179.
(21) Laurent, S.; Forge, D.; Port, M.; Roch, A.; Robic, C.; Elst, L. V.; Muller, R. N. *Chem. Rev.* **2008**, *108*, 2064.
(22) Clifford, J. P.; Konstantatos, G.; Johnston, K. W.; Hoogland, S.; Levina, L.; Sargent, E. H. *Nat. Nanotechnol.* **2009**, *4*, 40.
(23) Talapin, D. V.; Murray, C. B. *Science* **2005**, *310*, 86.
(24) Lee, J. S.; Shevchenko, E. V.; Talapin, D. V. *J. Am. Chem. Soc.* **2008**, *130*, 9673.
(25) Law, M.; Luther, J. M.; Song, Q.; Hughes, B. K.; Perkins, C. L.; Nozik, A. J. *J. Am. Chem. Soc.* **2008**, *130*, 5974.
(26) Murray, C. B.; Norris, D. J.; Bawendi, M. G. *J. Am. Chem. Soc.* **1993**, *115*, 8706.
(27) Sun, S.; Murray, C. B.; Weller, D.; Folks, L.; Moser, A. *Science* **2000**, *287*, 1989.
(28) Park, J.; Joo, J.; Kwon, C. G.; Jang, Y.; Hyeon, T. *Angew. Chem., Int. Ed.* **2007**, *46*, 4630.
(29) Park, J.; An, K.; Hwang, Y.; Park, J.-G.; Noh, H.-J.; Kim, H.-J.; Park, J.-H.; Hwang, N.-M.; Hyeon, T. *Nat. Mater.* **2004**, *3*, 891.
(30) Yin, Y.; Alivisatos, A. P. *Nature* **2005**, *437*, 664.
(31) Cho, K. S.; Talapin, D. V.; Gaschler, W.; Murray, C. B. *J. Am. Chem. Soc.* **2005**, *127*, 7140.
(32) Shevchenko, E. V.; Bodnarchuk, M. I.; Kovalenko, M. V.; Talapin, D. V.; Smith, R. K.; Aloni, S.; Heiss, W.; Alivisatos, A. P. *Adv. Mater.* **2008**, *20*, 4323.
(33) Talapin, D. V.; Nelson, J. H.; Shevchenko, E. V.; Aloni, S.; Sadtler, B.; Alivisatos, A. P. *Nano Lett.* **2007**, *7*, 2951.
(34) Carbone, L.; Nobile, C.; De Giorgi, M.; Sala, F. D.; Morello, G.; Pompa, P.; Hytch, M.; Snoeck, E.; Fiore, A.; Franchini, I. R.; Nadasan, M.; Silvestre, A. F.; Chiodo, L.; Kudera, S.; Cingolani, R.; Krahne, R.; Manna, L. *Nano Lett.* **2007**, *7*, 2942.
(35) Milliron, D. J.; Hughes, S. M.; Cui, Y.; Manna, L.; Li, J.; Wang, L.-W.; Alivisatos, A. P. *Nature* **2004**, *430*, 190.
(36) Zeng, H.; Sun, S. *Adv. Funct. Mater.* **2008**, *18*, 391.
(37) Cozzoli, P. D.; Pellegrino, T.; Manna, L. *Chem. Soc. Rev.* **2006**, *35*, 1195.
(38) Mokari, T.; Rothenberg, E.; Popov, I.; Costi, R.; Banin, U. *Science* **2004**, *304*, 1787.
(39) Murray, C. B.; Kagan, C. R.; Bawendi, M. G. *Annu. Rev. Mater. Sci.* **2000**, *30*, 545.
(40) Chen, J.; Lim, B. K.; Lee, E. P.; Xia, Y. *Nano Today* **2009**, *4*, 81.
(41) Xia, Y.; Xiong, Y.; Lim, B.; Skrabalak, S. E. *Angew. Chem., Int. Ed.* **2009**, *48*, 60.
(42) Xia, Y.; Yang, P.; Sun, Y.; Wu, Y.; Mayers, B.; Gates, B.; Yin, Y.; Kim, F.; Yan, H. *Adv. Mater.* **2003**, *15*, 353.
(43) *Semiconductor Nanocrystal Quantum Dots: Synthesis, Assembly, Spectroscopy and Applications*; Rogach, A., Ed.; Springer Verlag: Wien, 2008.
(44) Lu, X.; Rycenga, M.; Skrabalak, S. E.; Wiley, B.; Xia, Y. *Annu. Rev. Phys. Chem.* **2009**, *60*, 167.
(45) Sun, S. *Adv. Mater.* **2006**, *18*, 393.
(46) Kwon, S. G.; Piao, Y.; Park, J.; Angappane, S.; Jo, Y.; Hwang, N. M.; Park, J. G.; Hyeon, T. *J. Am. Chem. Soc.* **2007**, *129*, 12571.
(47) Shevchenko, E. V.; Talapin, D. V.; Schnablegger, H.; Kornowski, A.; Festin, O.; Svedlindh, P.; Haase, M.; Weller, H. *J. Am. Chem. Soc.* **2003**, *125*, 9090.
(48) de Mello Donega, C.; Liljeroth, P.; Vanmaekelbergh, D. *Small* **2005**, *1*, 1152.
(49) Talapin, D. V.; Rogach, A. L.; Kornowski, A.; Haase, M.; Weller, H. *Nano Lett.* **2001**, *1*, 207.
(50) Sau, T. K.; M, C. J. *J. Am. Chem. Soc.* **2004**, *126*, 8648.
(51) Lu, X.; Yavuz, M.; Tuan, H.-Y.; Korgel, B.; Xia, Y. *J. Am. Chem. Soc.* **2008**, *130*, 8900.
(52) Jana, N. R.; Peng, X. *J. Am. Chem. Soc.* **2003**, *125*, 14280.
(53) Brust, M.; Walker, M.; Bethell, D.; Schiffrin, D. J.; Whyman, R. J. *Chem. Commun.* **1994**, *7*, 801.
(54) Skrabalak, S. E.; Wiley, B. J.; Kim, M. H.; Formo, E.; Xia, Y. *Nano Lett.* **2008**, *8*, 2077.
(55) Wiley, B.; Im, S.-H.; Li, Z.-Y.; McLellan, J. M.; Siekkinen, A.; Xia, Y. *J. Phys. Chem. B* **2006**, *110*, 15666.
(56) Tao, A. R.; Sinsermsuksakul, P.; Yang, P. *Angew Chem., Int. Ed.* **2006**, *45*, 4597.
(57) Borodko, Y.; Humphrey, S. M.; Don Tilley, T.; Frei, H.; Somorjai, G. A. *J. Phys. Chem. C* **2007**, *111*, 6288.
(58) Wang, C.; Daimon, H.; Onodera, T.; Koda, T.; Sun, S. *Angew. Chem., Int. Ed.* **2008**, *47*, 3588.
(59) Narayanan, R.; El-Sayed, M. A. *Nano Lett.* **2004**, *4*, 1343.
(60) Son, S. U.; Jang, Y.; Yoon, K. Y.; Kang, E.; Hyeon, T. *Nano Lett.* **2004**, *4*, 1147.
(61) Sun, Y.; Wiley, B.; Li, Z.-Y.; Xia, Y. *J. Am. Chem. Soc.* **2004**, *126*, 9399.
(62) Tao, A.; S. Habas, S.; Yang, P. *Small* **2008**, *4*, 310.
(63) Pastoriza-Santos, I.; Liz-Marzán, L. M. *Adv. Funct. Mater.* **2009**, *19*, 679.
(64) Puntes, V. F.; Zanchet, D.; Erdonmez, C. K.; Alivisatos, A. P. *J. Am. Chem. Soc.* **2002**, *124*, 12874.
(65) Dumestre, F.; Chaudret, B.; Amiens, C.; Renaud, A.; Fejes, P. *Science* **2004**, *303*, 821.
(66) Park, S.-J.; Kim, S.; Lee, S.; Khim, Z. G.; Char, K.; Hyeon, T. *J. Am. Chem. Soc.* **2000**, *122*, 8581.
(67) Peng, S.; Wang, C.; Xie, J.; Sun, S. *J. Am. Chem. Soc.* **2006**, *128*, 10676.
(68) Son, S. U.; Jang, Y.; Yoon, K. Y.; An, C.; Hwang, Y.; Park, J.-G.; Noh, H.-J.; Kim, J.-Y.; Park, J.-H.; Hyeon, T. *Chem. Commun.* **2005**, 86.
(69) Wang, F.; Buhro, W. E. *J. Am. Chem. Soc.* **2007**, *129*, 14381.
(70) Weitz, I. S.; Sample, J. L.; Ries, R.; Spain, E. M.; Heath, J. R. *J. Phys. Chem. B* **2000**, *104*, 4288.
(71) Wang, C.; Hou, Y.; Kim, Y.; Sun, S. *Angew. Chem., Int. Ed.* **2007**, *46*, 6333.
(72) *Monodispersed Nanoparticles*; Sugimoto, T., Ed.; Elsevier: New York, 2001.
(73) Blackman, B.; Battaglia, D. M.; Mishima, T. D.; Johnson, M. B.; Peng, X. *Chem. Mater.* **2007**, *19*, 3815.
(74) Peng, Z. A.; Peng, X. *J. Am. Chem. Soc.* **2002**, *124*, 3343.
(75) Steigerwald, M. L.; Alivisatos, A. P.; Gibson, J. M.; Harris, T. D.; Kortan, R.; Muller, A. J.; Thayer, A. M.; Duncan, T. M.; Douglass, D. C.; Brus, L. E. *J. Am. Chem. Soc.* **1988**, *110*, 3046.
(76) Morello, G.; De Giorgi, M.; Kudera, S.; Manna, L.; Cingolani, R.; Anni, M. *J. Phys. Chem. C* **2007**, *111*, 5846.
(77) Yong, K.-T.; Sahoo, Y.; Swihart, M. T.; Prasad, P. N. *J. Phys. Chem. C* **2007**, *111*, 2447.
(78) Micic, O. I.; Curtis, C. J.; Jones, K. M.; Sprague, J. R.; Nozik, A. J. *J. Phys. Chem.* **1994**, *98*, 4966.
(79) Dimitrijević, N. M.; Rajh, T.; Ahrenkiel, P.; Nedeljković, J. M.; Mićić, O. I.; Nozik, A. J. *J. Phys. Chem. B* **2005**, *109*, 18243.
(80) Talapin, D. V.; Rogach, A. L.; Shevchenko, E. V.; Kornowski, A.; Haase, M.; Weller, H. *J. Am. Chem. Soc.* **2002**, *124*, 5782.
(81) Battaglia, D.; Peng, X. *Nano Lett.* **2002**, *2*, 1027.
(82) Hines, M. A.; Scholes, G. D. *Adv. Mater.* **2003**, *15*, 1844.
(83) Lin, W.; Fritz, K.; Guerin, G.; Bardajee, G. R.; Hinds, S.; Sukhovatkin, V.; Sargent, E. H.; Scholes, G. D.; Winnik, M. A. *Langmuir* **2008**, *24*, 8215.
(84) Lee, S.-M.; Jun, Y.-W.; Cho, S.-N.; Cheon, J. *J. Am. Chem. Soc.* **2002**, *124*, 11244.
(85) Cademartiri, L.; Bertolotti, J.; Sapienza, R.; Wiersma, D. S.; von Freymann, G.; Ozin, J. *J. Phys. Chem. B* **2006**, *110*, 671.
(86) Abel, K. A.; Shan, J. N.; Boyer, J. C.; Harris, F.; van Veggel, F. *Chem. Mater.* **2008**, *20*, 3794.
(87) Urban, J. J.; Talapin, D. V.; Shevchenko, E. V.; Murray, C. B. *J. Am. Chem. Soc.* **2006**, *128*, 3248.
(88) Peng, X.; Wickham, J.; Alivisatos, A. P. *J. Am. Chem. Soc.* **1998**, *120*, 5343.
(89) Chen, Y.; Johnson, E.; Peng, X. *J. Am. Chem. Soc.* **2007**, *129*, 10937.
(90) Talapin, D. V.; Rogach, A. L.; Haase, M.; Weller, H. *J. Phys. Chem. B* **2001**, *105*, 12278.
(91) Reiss, P.; Bleuse, J.; Pron, A. *Nano Lett.* **2002**, *2*, 781.
(92) Qu, L.; P., X. *J. Am. Chem. Soc.* **2002**, *124*, 2049.
(93) Anikeeva, P. O.; Halpert, J. E.; Bawendi, A. G.; Bulović, V. *Nano Lett.* **2007**, *7*, 2196.
(94) Peng, X.; Schlamp, M. C.; Kadavanich, A. V.; Alivisatos, A. P. *J. Am. Chem. Soc.* **1997**, *119*, 7019.

(95) Rogach, A. L.; Talapin, D. V.; Shevchenko, E. V.; Kornowski, A.; Haase, M.; Weller, H. *Adv. Funct. Mater.* **2002**, *12*, 653.
(96) Gaponik, N.; Talapin, D. V.; Rogach, A. L.; Hoppe, K.; Shevchenko, E. V.; Kornowski, A.; Eychmüller, A.; Weller, H. *J. Phys. Chem. B* **2002**, *106*, 7177.
(97) Shavel, A.; Gaponik, N.; Eychmüller, A. *J. Phys. Chem. B* **2006**, *110*, 19280.
(98) Rogach, A. L.; Franzl, F.; Klar, T. A.; Feldmann, J.; Gaponik, N.; Lesnyak, V.; Shavel, A.; Eychmüller, A.; Rakovich, Y. P.; Donegan, J. F. *J. Phys. Chem. C* **2007**, *111*, 14628.
(99) Schmid, G. *Nanoparticles - from Theory to Applications*; Wiley VCH: New York, 2003.
(100) Vossmeyer, T.; Katsikas, L.; Giersig, M.; Popovic, I. G.; Diesner, K.; Chemseddine, A.; Eychmuller, A.; Weller, H. *J. Phys. Chem.* **1994**, *98*, 7665.
(101) Rogach, A. L.; Kornowski, A.; Gao, M. Y.; Eychmuller, A.; Weller, H. *J. Phys. Chem. B* **1999**, *103*, 3065.
(102) Rogach, A. L.; Franzl, F.; Klar, T. A.; Feldmann, J.; Gaponik, N.; Lesnyak, V.; Shavel, A.; Eychmüller, A.; Rakovich, Y. P.; Donegan, J. F. *J. Phys. Chem. C* **2007**, *111*, 14628.
(103) Rogach, A.; Kershaw, S.; Burt, M.; Harrison, M.; Kornowski, A.; Eychmuller, A.; Weller, H. *Adv. Mater.* **1999**, *11*, 552.
(104) Boettcher, S. W.; Fan, J.; Tsung, C.-K.; Shi, Q.; Stucky, G. D. *Acc. Chem. Res.* **2007**, *40*, 784.
(105) Niederberger, M. *Acc. Chem. Res.* **2007**, *40*, 793.
(106) Arachchige, I. U.; Brock, S. L. *Acc. Chem. Res.* **2007**, *40*, 801.
(107) Hench, L. L.; West, J. K. *Chem. Rev.* **2002**, *90*, 33.
(108) Cushing, B. L.; Kolesnichenko, V. L.; O'Connor, C. J. *Chem. Rev.* **2004**, *104*, 3893.
(109) Burda, C.; Chen, X.; Narayanan, R.; El-Sayed, M. A. *Chem. Rev.* **2005**, *105*, 1025.
(110) Mackenzie, J. D.; Bescher, E. P. *Acc. Chem. Res.* **2007**, *40*, 810.
(111) Schubert, U. *Acc. Chem. Res.* **2007**, *40*, 730.
(112) Arachchige, I. U.; Mohanan, J. L.; Brock, S. L. *Chem. Mater.* **2005**, *17*, 6644.
(113) Arachchige, I. U.; Brock, S. L. *J. Am. Chem. Soc.* **2007**, *129*, 1840.
(114) Nishio, K.; Isshiki, T.; Kitano, M.; Shiojiri, M. *Philos. Mag. A* **1997**, *76*, 998.
(115) Cozzoli, P. D.; Snoeck, E.; Garcia, M. A.; Giannini, C.; Guagliardi, A.; Cervellino, A.; Gozzo, F.; Hernando, A.; Achterhold, K.; Ciobanu, N.; Parak, F. G.; Cingolani, R.; Manna, L. *Nano Lett.* **2006**, *6*, 1966.
(116) Teng, X.; Yang, H. *Nano Lett.* **2005**, *5*, 885.
(117) Pang, Q.; Zhao, L.; Cai, Y.; Nguyen, D. P.; Regnault, N.; Wang, N.; Yang, S.; Ge, W.; Ferreira, R.; Bastard, G.; Wang, J. *Chem. Mater.* **2005**, *17*, 5263.
(118) Asokan, S.; Krueger, K. M.; Colvin, V. L.; Wong, M. S. *Small* **2007**, *3*, 1164.
(119) Manna, L.; Milliron, D. J.; Meisel, A.; Scher, E. C.; Alivisatos, A. P. *Nat. Mater.* **2003**, *2*, 382.
(120) Cozzoli, P. D.; Manna, L.; Curri, M. L.; Kudera, S.; Giannini, C.; Striccoli, M.; Agostiano, A. *Chem. Mater.* **2005**, *17*, 1296.
(121) Hu, J.; Bando, Y.; Goldberg, D. *Small* **2005**, *1*, 95.
(122) Zhang, J. W.; Yu, W. W. *Appl. Phys. Lett.* **2006**, *89*, 123108.
(123) Takeuchi, S.; Iwanaga, H.; Fujii, M. *Philos. Mag. A* **1995**, *69*, 1125.
(124) Iwanaga, H.; Fujii, M.; Takeuchi, S. *J. Cryst. Growth* **1998**, *183*, 190.
(125) Carbone, L.; Kudera, S.; Carlino, E.; Parak, W. J.; Giannini, C.; Cingolani, R.; Manna, L. *J. Am. Chem. Soc.* **2006**, *128*, 748.
(126) Lofton, C.; Sigmund, W. *Adv. Funct. Mater.* **2005**, *15*, 1197.
(127) Chemseddine, A.; Moritz, T. *Eur. J. Inorg. Chem.* **1999**, 235.
(128) Penn, R. L. *J. Phys. Chem. B* **2004**, *108*, 12707.
(129) Banfield, J. F.; Welch, S. A.; Zhang, H.; Ebert, T. T.; Penn, R. L. *Science* **2000**, *289*, 751.
(130) Penn, R. L.; B, J. F. *Science* **1998**, *281*, 969.
(131) Trentler, T. J.; Hickman, K. M.; Goel, S. C.; Viano, A. M.; Gibbons, P. C.; Buhro, W. E. *Science* **1995**, *270*, 1791.
(132) Korgel, B. A.; Fitzmaurice, D. *Adv. Mater.* **1998**, *10*, 661.
(133) Tang, Z.; Kotov, N. A.; Giersig, M. *Science* **2002**, *297*, 237.
(134) Pradhan, N.; Xu, H.; Peng, X. *Nano Lett.* **2006**, *6*, 720.
(135) Pacholski, C.; Kornowski, A.; Weller, H. *Angew. Chem., Int. Ed.* **2002**, *41*, 1188.
(136) Yu, J. h.; Joo, J.; Park, H. M.; Baik, S.-II.; Kim, Y. W.; Kim, S. C.; Hyeon, T. *J. Am. Chem. Soc.* **2005**, *127*, 5662.
(137) Yong, K.-T.; Sahoo, Y.; Zeng, H.; Swihart, M. T.; Minter, J. R.; Prasad, P. N. *Chem. Mater.* **2007**, *19*, 4108.
(138) Narayanaswamy, A.; Xu, H.; Pradhan, N.; Kim, M.; Peng, X. *J. Am. Chem. Soc.* **2006**, *128*, 10310.
(139) Yu, H.; Buhro, W. E. *Adv. Mater.* **2003**, *15*, 416.
(140) Gudiksen, M. S.; Lieber, C. M. *J. Am. Chem. Soc.* **2000**, *122*, 8801.
(141) Wu, Y.; Yang, P. *J. Am. Chem. Soc.* **2001**, *123*, 3165.
(142) Wagner, R. S.; Ellis, W. C. *Appl. Phys. Lett.* **1964**, *4*, 89.
(143) Heitsch, A. T.; Fanfair, D. D.; Tuan, H.-Y.; Korgel, B. A. *J. Am. Chem. Soc.* **2008**, *130*, 5436.
(144) Hsu, Y.-J.; Lu, S.-Y. *J. Phys. Chem. B* **2005**, *109*, 4398.
(145) Lu, X.; Fanfair, D. D.; Johnston, K. P.; Korgel, B. A. *J. Am. Chem. Soc.* **2005**, *127*, 15718.
(146) Fanfair, D. D.; Korgel, B. A. *Cryst. Growth Des.* **2005**, *5*, 1971.
(147) Smigelskas, A. D.; Kirkendall, E. O. *Trans. AIME* **1947**, *171*, 130.
(148) Yin, Y. D.; Rioux, R. M.; Erdonmez, C. K.; Hughes, S.; Somorjai, G. A.; Alivisatos, A. P. *Science* **2004**, *304*, 711.
(149) Cabot, A.; Puntes, V. F.; Shevchenko, E.; Yin, Y.; Balcells, L.; Marcus, M. A.; Hughes, S. M.; Alivisatos, A. P. *J. Am. Chem. Soc.* **2007**, *129*, 10358.
(150) Yin, Y.; Erdonmez, C.; Aloni, S.; Alivisatos, A. P. *J. Am. Chem. Soc.* **2006**, *128*, 12671.
(151) Sun, Y.; Mayers, B. T.; Xia, Y. *Nano Lett.* **2002**, *2*, 481.
(152) Sun, Y.; Xia, Y. *Science* **2002**, *298*, 2176.
(153) Haes, A. J.; Haynes, C. L.; McFarland, A. D.; Schatz, G. C.; Van Duyne, R. P.; Zou, S. *MRS Bull.* **2005**, *30*, 368.
(154) Liu, N.; Prall, B. S.; Klimov, V. I. *J. Am. Chem. Soc.* **2006**, *128*, 15362.
(155) Hines, M. A.; Guyot-Sionnest, P. *J. Phys. Chem.* **1996**, *100*, 468.
(156) Kuno, M.; Lee, J. K.; Dabbousi, B. O.; Mikulec, F. V.; Bawendi, M. G. *J. Chem. Phys.* **1997**, *106*, 9869.
(157) Dabbousi, B. O.; Rodriguez-Viejo, J.; Mikulec, F. V.; Heine, J. R.; Mattoussi, H.; Ober, R.; Jensen, K. F.; Bawendi, M. *J. Phys. Chem. B* **1997**, *101*, 9463.
(158) Liu, M.; Guyot-Sionnest, P. *J. Phys. Chem. B* **2004**, *108*, 5882.
(159) Son, S. U.; Jang, Y.; Park, J.; Na, H. B.; Park, H. M.; Yun, H. J.; Lee, J.; Hyeon, T. *J. Am. Chem. Soc.* **2004**, *126*, 5026.
(160) Kim, H.; Achermann, M.; Balet, L. P.; Hollingsworth, J. A.; Klimov, V. I. *J. Am. Chem. Soc.* **2005**, *127*, 544.
(161) Zimmer, J. P.; Kim, S.-W.; Ohnishi, S.; Tanaka, E.; Frangioni, J. V.; Bawendi, M. G. *J. Am. Chem. Soc.* **2006**, *128*, 2526.
(162) Cao, Y. W.; Banin, U. *J. Am. Chem. Soc.* **2000**, *122*, 9692.
(163) Xie, R.; Battaglia, D.; Peng, X. *J. Am. Chem. Soc.* **2007**, *129*, 15432.
(164) Talapin, D. V.; Koeppe, R.; Götzinger, S.; Kornowski, A.; Lupton, J. M.; Rogach, A. L.; Benson, O.; Feldmann, J.; Weller, H. *Nano Lett.* **2003**, *3*, 1677.
(165) Piryatinski, A.; Ivanov, S. A.; Tretiak, S.; Klimov, V. I. *Nano Lett.* **2007**, *7*, 108.
(166) He, J.; Lo, S. S.; Kim, J.; Scholes, J. D. *Nano Lett.* **2008**, *8*, 4007.
(167) Kim, S.; Fisher, B.; Eisler, H.-J.; Bawendi, M. *J. Am. Chem. Soc.* **2003**, *125*, 11466.
(168) Gur, I.; Fromer, N. A.; Geier, M. L.; Alivisatos, A. P. *Science* **2005**, *310*, 462.
(169) Ivanov, S. A.; Nanda, J.; Piryatinski, A.; Achermann, M.; Balet, L. P.; Bezel, I. V.; Anikeeva, P. O.; Tretiak, S.; Klimov, V. I. *J. Phys. Chem. B* **2004**, *108*, 10625.
(170) Manna, L.; Scher, E. C.; Li, L.-S.; Alivisatos, A. P. *J. Am. Chem. Soc.* **2002**, *124*, 7136.
(171) Xie, R.; Kolb, U.; Li, J.; Basché, T.; Mews, A. *J. Am. Chem. Soc.* **2005**, *127*, 7480.
(172) Gao, J.; Zhang, B.; Gao, Y.; Pan, Y.; Zhang, X.; Xu, B. *J. Am. Chem. Soc.* **2007**, *129*, 11928.
(173) Kudera, S.; Carbone, L.; Casula, M. F.; Cingolani, R.; Falqui, A.; Snoeck, E.; Parak, W. J.; Manna, L. *Nano Lett.* **2005**, *5*, 445.
(174) Pellegrino, T.; et al. *J. Am. Chem. Soc.* **2006**, *128*, 6690.
(175) Robinson, R. D.; Sadtler, B.; Demchenko, D. O.; Erdonmez, C. K.; Wang, L.-W.; Alivisatos, A. P. *Science* **2007**, *317*, 355.
(176) Yang, J.; Elim, H. I.; Zhang, Q.; Lee, J. Y.; Ji, W. *J. Am. Chem. Soc.* **2006**, *128*, 11921.
(177) Yu, H.; Chen, M.; Rice, P. M.; Wang, S. X.; White, R. L.; Sun, S. *Nano Lett.* **2005**, *5*, 379.
(178) Shi, W. L.; Zeng, H.; Sahoo, Y.; Ohulchanskyy, T. Y.; Ding, Y.; Wang, Z. L.; Swihart, M.; Prasad, P. N. *Nano Lett.* **2006**, *6*, 875.
(179) Buonsanti, R.; Grillo, V.; Carlino, E.; Giannini, C.; Curri, M. L.; Innocenti, C.; Sangregorio, C.; Achterhold, C.; Parak, F. G.; Agostiano, A.; Cozzoli, P. D. *J. Am. Chem. Soc.* **2006**, *128*, 16953.
(180) Figuerola, A.; Fiore, A.; Corato, R. D.; Falqui, A.; Giannini, C.; Micotti, E.; Lascialfari, A.; Corti, A.; Cingolani, R.; Pellegrino, T.; Cozzoli, P. D.; Manna, L. *J. Am. Chem. Soc.* **2008**, *130*, 4.
(181) Pacholski, C.; Kornowski, A.; Weller, H. *Angew. Chem., Int. Ed.* **2004**, *43*, 4774.
(182) Shevchenko, E. V.; Talapin, D. V.; Kotov, N. A.; O'Brien, S.; Murray, C. B. *Nature* **2006**, *439*, 55.
(183) Murray, C. B.; Kagan, C. R.; Bawendi, M. G. *Science* **1995**, *270*, 1335.
(184) Mattoussi, H.; Radzilowski, H.; Dabbousi, B. O.; Fogg, D. E.; Schrock, R. R.; Thomas, E. L.; Rubner, M. F. *J. Appl. Phys.* **1999**, *86*, 4390.
(185) Yu, D.; Wang, C.; Guyot-Sionnest, P. *Science* **2003**, *300*, 1277.
(186) Heath, J. R.; Knobler, C. M.; Leff, D. V. *J. Phys. Chem. B* **1997**, *101*, 189.
(187) Dabbousi, B. O.; Murray, C. B.; Rubner, M. F.; Bawend, M. G. *Chem. Mater.* **1994**, *6*, 216.

(188) Song, H.; Kim, F.; Connor, S.; Somorjai, G. A.; Yang, P. *J. Phys. Chem. B* **2005**, *109*, 188.
(189) Guo, Q.; Teng, X.; Rahman, S.; Yang, H. *J. Am. Chem. Soc.* **2003**, *125*, 630.
(190) Mayya, K. S.; Patil, V.; Sastry, M. *Langmuir* **1997**, *13*, 2575.
(191) Decher, G. *Science* **1997**, *277*, 1232.
(192) Sun, S.; Anders, S.; Hamann, H. F.; Thiele, J.-U.; Baglin, J. E. E.; Thomson, T.; Fullerton, E. E.; Murray, C. B.; Terris, B. D. *J. Am. Chem. Soc.* **2002**, *124*, 2884.
(193) Aliev, F. G.; Correa-Duarte, M. A.; Mamedov, A.; Ostrander, J. W.; Giersig, M.; Liz-Marzán, L. M.; Kotov, N. A. *Adv. Mater.* **1999**, *11*, 1006.
(194) Podsiadlo, P.; Kaushik, A. K.; Arruda, E. M.; Waas, A. M.; Shim, B. S.; Xu, J.; Nandivada, H.; Pumplin, B. G.; Lahann, J.; Ramamoorthy, A.; Kotov, N. A. *Science* **2007**, *318*, 80.
(195) Tekin, E.; Smith, P. J.; Hoeppener, S.; van den Berg, A. M. J.; Susha, A. S.; Rogach, A. L.; Feldmann, J.; Schubert, U. S. *Adv. Funct. Mater.* **2007**, *17*, 23.
(196) Paquet, C.; Kumacheva, E. *Adv. Funct. Mater.* **2007**, *17*, 3105.
(197) Hamann, H. F.; Woods, S. I.; Sun, S. *Nano Lett.* **2003**, *3*, 1643.
(198) Min, Y.; Akbulut, M.; Kristiansen, K.; Golan, Y.; Israelachvili, J. *Nat. Mater.* **2008**, *7*, 527.
(199) Shenhar, R.; Norsten, T. B.; Rotello, V. M. *Adv. Mater.* **2005**, *17*, 657.
(200) Wang, Z. L. *Adv. Mater.* **1998**, 13.
(201) Shevchenko, E.; Talapin, D.; Kornowski, A.; Wiekhorst, F.; Kötzler, J.; Haase, M.; Rogach, A.; Weller, H. *Adv. Mater.* **2002**, *14*, 287.
(202) Talapin, D. V.; Shevchenko, E. V.; Kornowski, A.; Gaponik, N.; Haase, M.; Rogach, A. L.; Weller, H. *Adv. Mater.* **2001**, *13*, 1868.
(203) Nagel, M.; Hickey, S. G.; Fromsdorf, A.; Kornowski, A.; Weller, H. *Z. Phys. Chem.* **2007**, *221*, 427.
(204) Talapin, D. V.; Shevchenko, E. V.; Murray, C. B.; Titov, A. V.; Kral, P. *Nano Lett.* **2007**, *7*, 1213.
(205) Alder, B. j.; Hoover, W. G.; Young, D. A. *J. Chem. Phys.* **1968**, *49*, 3688.
(206) Bolhuis, P. G.; Frenkel, D.; Mau, S.-C.; Huse, D. A. *Nature* **1997**, *388*, 235.
(207) Alder, B. J.; Carter, B. P.; Young, D. A. *Phys. Rev.* **1969**, *183*, 831.
(208) Norris, D. J.; Arlinghaus, E. J.; Meng, L.; Heiny, R.; Scriven, L. E. *Adv. Mater.* **2004**, *16*, 1393.
(209) Shim, M.; Guyot-Sionnest, P. *J. Phys. Chem.* **1999**, *111*, 6955.
(210) Li, L.-S.; Alivisatos, A. P. *Phys. Rev. Lett.* **2003**, *90*, 097402.
(211) Rabani, E.; Heternyi, B.; Berne, D. J.; Brus, L. E. *J. Chem. Phys.* **1999**, *110*, 5355.
(212) Islam, M. A.; Xia, Y.; Steigerwald, M. L.; Yin, M.; Liu, Z.; O'Brien, S.; Levicky, R.; Herman, I. P. *Nano Lett.* **2003**, *3*, 1603.
(213) Ohara, P. C.; Leff, D. V.; Jeath, J. R.; Gelbart, W. M. *Phys. Rev. Lett.* **1995**, *75*, 3466.
(214) Korgel, B. A.; Fullam, S.; Connolly, S.; Fitzmaurice, D. *J. Phys. Chem. B* **1998**, *102*, 8379.
(215) Chen, Z.; Moore, J.; Radtke, G.; Sirringhaus, H.; O'Brien, S. *J. Am. Chem. Soc.* **2007**, *129*, 15702.
(216) Tripp, S. L.; Pusztay, S. V.; Ribbe, A. E.; Wei, A. *J. Am. Chem. Soc.* **2002**, *124*, 7914.
(217) Talapin, D. V. *ACS Nano* **2008**, *2*, 1097.
(218) Talapin, D. V.; Shevchenko, E. V.; Murray, C. B.; Kornowski, A.; Förster, S.; Weller, H. *J. Am. Chem. Soc.* **2004**, *126*, 12984.
(219) Zhang, J.; Kumbhar, A.; He, J.; Das, N. C.; Yang, K.; Wang, J.-Q.; Wang, H.; Stokes, K. L.; Fang, J. *J. Am. Chem. Soc.* **2008**, *130*, 15203.
(220) Shevchenko, E. V.; Talapin, D. V.; Murray, C. B.; O'Brien, S. *J. Am. Chem. Soc.* **2006**, *128*, 3620.
(221) Kiely, C. J.; Fink, J.; Brust, M.; Bethel, D.; Schiffrin, D. J. *Nature* **1998**, *396*, 444.
(222) Saunders, A. E.; Korgel, B. A. *ChemPhysChem* **2005**, *6*, 61.
(223) Redl, F. X.; Cho, K. S.; Murray, C. B.; O'Brien, S. *Nature* **2003**, *423*, 968.
(224) Overgaag, K.; Evers, W.; de Nijs, B.; Koole, R.; Meeldijk, J.; Vanmaekelbergh, D. *J. Am. Chem. Soc.* **2008**, *130*, 7833.
(225) Hunt, N.; Jardine, R.; Bartlett, P. *Phys. Rev. E* **2000**, *62*, 900.
(226) Schofield, A. B. *Phys. Rev. E* **2001**, *64*, 051403.
(227) Eldridge, M. D.; Madden, P. A.; Frenkel, D. *Mol. Phys.* **1993**, *79*, 105.
(228) Cottin, X.; Monson, P. A. *J. Chem. Phys.* **1995**, *102*, 3354.
(229) Trizac, E.,; Eldridge, M. D.; Madden, P. A. *Mol. Phys.* **1997**, *90*, 675.
(230) Eldridge, M. D.; Madden, P. A.; Frenkel, D. *Nature* **1993**, *365*, 35.
(231) Sanders, J. V. *Philos. Mag. A* **1980**, *42*, 705.
(232) Murray, M. J.; Sanders, J. V. *Philos. Mag. A.* **1980**, *42*, 721.
(233) Sanders, J. V.; Murray, M. J. *Nature* **1978**, *275*, 201.
(234) Hachisu, S.; Yoshimura, S. *Nature* **1980**, *283*, 188.
(235) Bartlett, P.; Ottewill, R. H.; Pusey, P. N. *Phys. Rev. Lett.* **1992**, *68*, 3801.
(236) Shevchenko, E. V.; Kortright, J. B.; Talapin, D. V.; Aloni, S.; Alivisatos, A. P. *Adv. Mater.* **2007**, *19*, 4183.
(237) Lazarenkova, O. L.; Balandin, A. A. *J. Appl. Phys.* **2001**, *89*, 5509.
(238) Jiang, C. W.; Green, M. A. *J. Appl. Phys.* **2006**, *99*, 114902.
(239) Esaki, L.; Tsu, R. *IBM J. Res. Dev.* **1970**, *14*, 61.
(240) Lei, X. L.; Horing, N. J. M.; Cui, H. L. *Phys. Rev. Lett.* **1991**, *66*, 3277.
(241) Deveaud, B.; Shah, J.; Damen, T. C.; Lambert, B.; Regreny, A. *Phys. Rev. Lett.* **1987**, *58*, 2582.
(242) Faist, J.; Capasso, F.; Sivco, D. L.; Sirtori, C.; Hutchinson, A. L.; Cho, A. Y. *Science* **1994**, *264*, 553.
(243) Lei, X. L. *J. Phys.: Condens. Matter* **1992**, *4*, 9367.
(244) Brum, J. A. *Phys. Rev. B* **1991**, *43*, 12082.
(245) Lazarenkova, O. L.; Balandin, A. A. *Phys. Rev. B* **2002**, *66*, 245319.
(246) Nika, D. L.; Pokatilov, E. P.; Shao, Q.; Balandin, A. A. *Phys. Rev. B* **2007**, *76*, 125417.
(247) Luttinger, J. M.; Kohn, W. *Phys. Rev.* **1955**, *97*, 869.
(248) Lazarenkova, O. L.; Balandin, A. A. *J. Appl. Phys.* **2001**, *89*, 5509.
(249) Burt, M. G. *Appl. Phys. Lett.* **1994**, *65*, 717.
(250) Burt, M. G. *J. Phys.: Condens. Matter* **1992**, *4*, 6651.
(251) Balandin, A. A.; Lazarenkova, O. L. *Appl. Phys. Lett.* **2003**, *82*, 415.
(252) Shao, Q.; Balandin, A. A.; Fedoseyev, A. I.; Turowski, M. *Appl. Phys. Lett.* **2007**, *91*, 163503.
(253) Koleilat, G. I.; Levina, L.; Shukla, H.; Myrskog, S. H.; Hinds, S.; Pattantyus-Abraham, A. G.; Sargent, E. H. *ACS Nano* **2008**, *2*, 833.
(254) Dresselhaus, M. S.; Chen, G.; Tang, M. Y.; Yang, R. G.; Lee, H.; Wang, D. Z.; Ren, Z. F.; Fleurial, J. P.; Gogna, P. *Adv. Mater.* **2007**, *19*, 1043.
(255) Wang, R. Y.; Feser, J. P.; Lee, J.-S.; Talapin, D. V.; Segalman, R.; Majumdar, A. *Nano Lett.* **2008**, *8*, 2283.
(256) Gomez, I.; Dominguez-Adame, F.; Diez, E.; Orellana, P. *J. Appl. Phys.* **2002**, *92*, 4486.
(257) Artemyev, M. V.; Bibik, A. I.; Gurinovich, L. I.; Gaponenko, S. V.; Woggon, U. *Phys. Rev. B* **1999**, *60*, 1504.
(258) Artemyev, M. V.; Woggon, U.; Jaschinski, H.; Gurinovich, L. I.; Gaponenko, S. V. *J. Phys. Chem. B* **2000**, *104*, 11617.
(259) Artemyev, M. V.; Bibik, A. I.; Gurinovich, L. I.; Gaponenko, S. V.; Jaschinski, H.; Woggon, U. *Phys. Status Solidi B* **2001**, *224*, 393.
(260) Zabet-Khosousi, A.; Trudeau, P. E.; Suganuma, Y.; Dhirani, A. A.; Statt, B. *Phys. Rev. Lett.* **2006**, *96*, 156403.
(261) Collier, C. P.; Saykally, R. J.; Shiang, J. J.; Henrichs, S. E.; Heath, J. R. *Science* **1997**, *277*, 1978.
(262) Pandey, A.; Guyot-Sionnest, P. *Science* **2008**, *322*, 929.
(263) Morgan, N. Y.; Leatherdale, C. A.; Drndic, M.; Jarosz, M. V.; Kastner, M. A.; Bawendi, M. *Phys. Rev. B* **2002**, *66*, 075339.
(264) Lee, H.; Habas, S. E.; Kweskin, S.; Butcher, D.; Somorjai, G. A.; Yang, P. D. *Angew. Chem., Int. Ed.* **2006**, *45*, 7824.
(265) Konstantatos, G.; Howard, I.; Fischer, A.; Hoogland, S.; Clifford, J.; Klem, E.; Levina, L.; Sargent, E. H. *Nature* **2006**, *442*, 180.
(266) Caruge, J. M.; Halpert, J. E.; Wood, V.; Bulovic, V.; Bawendi, M. G. *Nat. Photon.* **2008**, *2*, 247.
(267) Zabet-Khosousi, A.; Dhirani, A. A. *Chem. Rev.* **2008**, *108*, 4072.
(268) Ridley, B. A.; Nivi, B.; Jacobson, J. M. *Science* **1999**, *286*, 746.
(269) Drndic, M.; Jarosz, M. V.; Morgan, N. Y.; Kastner, M. A.; Bawendi, M. G. *J. Appl. Phys.* **2002**, *92*, 7498.
(270) Sargent, E. H. *Adv. Mater.* **2008**, *20*, 3958.
(271) Luther, J. M.; Law, M.; Beard, M. C.; Song, Q.; Reese, M. O.; Ellingson, R. J.; Nozik, A. J. *Nano Lett.* **2008**, *8*, 3488.
(272) Johnston, K. W.; Pattantyus-Abraham, A. G.; Clifford, J. P.; Myrskog, S. H.; Hoogland, S.; Shukla, H.; Klem, J. D.; Levina, L.; Sargent, E. H. *Appl. Phys. Lett.* **2008**, *92*, 122111.
(273) Kovalenko, M. V.; Scheele, M.; Talapin, D. V. *Science* **2009**, *324*, 1417.
(274) Dahl, J. A.; Maddux, B. L. S.; Hutchison, J. E. *Chem. Rev.* **2007**, *107*, 2228.
(275) Jadzinsky, P. D.; Calero, G.; Ackerson, C. J.; Bushnell, D. A.; Kornberg, R. D. *Science* **2007**, *318*, 430.
(276) DeVries, G. A.; Brunnbauer, M.; Hu, Y.; Jackson, A. M.; Long, B.; Neltner, B. T.; Uzun, O.; Wunsch, B. H.; Stellacci, F. *Science* **2007**, *315*, 358.
(277) Gaponik, N.; Talapin, D. V.; Rogach, A. L.; Eychmuller, A.; Weller, H. *Nano Lett.* **2002**, *2*, 803.
(278) Owen, J. S.; Park, J.; Trudeau, P.-E.; Alivisatos, A. P. *J. Am. Chem. Soc.* **2008**, *130*, 12279.
(279) Hostetler, M. J.; Green, S. J.; Stokes, J. J.; Murray, R. W. *J. Am. Chem. Soc.* **1996**, *118*, 4212.
(280) Liu, I. S.; Lo, H. H.; Chien, C. T.; Lin, Y. Y.; Chen, C. W.; Chen, Y. F.; Su, W. F.; Liou, S. C. *J. Mater. Chem.* **2008**, *18*, 675.
(281) Katari, J. E. B.; Colvin, V. L.; Alivisatos, A. P. *J. Phys. Chem.* **1994**, *98*, 4109.
(282) Hostetler, M. J.; Templeton, A. C.; Murray, R. W. *Langmuir* **1999**, *15*, 3782.

(283) Foos, E. E.; Snow, A. W.; Twigg, M. E.; Ancona, M. G. *Chem. Mater.* **2002**, *14*, 2401.
(284) Woggon, U.; Herz, E.; Schops, O.; Artemyev, M. V.; Arens, C.; Rousseau, N.; Schikora, D.; Lischka, K.; Litvinov, D.; Gerthsen, D. *Nano Lett.* **2005**, *5*, 483.
(285) Zhang, C.; O'Brien, S.; Balogh, L. *J. Phys. Chem. B* **2002**, *106*, 10316.
(286) Moreels, I.; Martins, J. C.; Hens, Z. *ChemPhysChem* **2006**, *7*, 1028.
(287) Lucey, D. W.; MacRae, D. J.; Furis, M.; Sahoo, Y.; Cartwright, A. N.; Prasad, P. N. *Chem. Mater.* **2005**, *17*, 3754.
(288) Kovalenko, M. V.; Talapin, D. V.; Loi, M. A.; Cordella, F.; Hesser, G.; Bodnarchuk, M. I.; Heiss, W. *Angew. Chem., Int. Ed.* **2008**, *47*, 3029.
(289) Woehrle, G. H.; Brown, L. O.; Hutchison, J. E. *J. Am. Chem. Soc.* **2005**, *127*, 2172.
(290) Brown, L. O.; Hutchison, J. E. *J. Phys. Chem. B* **2001**, *105*, 8911.
(291) Brown, L. O.; Hutchison, J. E. *J. Am. Chem. Soc.* **1997**, *119*, 12384.
(292) Brown, L. O.; Hutchison, J. E. *J. Am. Chem. Soc.* **1999**, *121*, 882.
(293) Jarosz, M. V.; Porter, V. J.; Fisher, B. R.; Kastner, M. A.; Bawendi, M. G. *Phys. Rev. B* **2004**, *70*, 195327.
(294) Oertel, D. C.; Bawendi, M. G.; Arango, A. C.; Bulovic, V. *Appl. Phys. Lett.* **2005**, *87*, 213505.
(295) Yu, D.; Wehrenberg, B. L.; Jha, P.; Ma, J.; Guyot-Sionnest, P. *J. Appl. Phys.* **2006**, *99*, 104315.
(296) Porter, V. J.; Geyer, S.; Halpert, J. E.; Kastner, M. A.; Bawendi, M. G. *J. Phys. Chem. C* **2008**, *112*, 2308.
(297) Gao, M. Y.; Lesser, C.; Kirstein, S.; Mohwald, H.; Rogach, A. L.; Weller, H. *J. Appl. Phys.* **2000**, *87*, 2297.
(298) Kim, H.; Cho, K.; Kim, D. W.; Lee, H. R.; Kim, S. *Appl. Phys. Lett.* **2006**, *89*, 173107.
(299) Liu, J. S.; Tanaka, T.; Sivula, K.; Alivisatos, A. P.; Frechet, J. M. J. *J. Am. Chem. Soc.* **2004**, *126*, 6550.
(300) Skaff, H.; Sill, K.; Emrick, T. *J. Am. Chem. Soc.* **2004**, *126*, 11322.
(301) Voitekhovich, S. V.; Talapin, D. V.; Klinke, C.; Kornowski, A.; Weller, H. *Chem. Mater.* **2008**, *20*, 4545.
(302) Murray, C. B.; Shevchenko, E. V.; Talapin, D. V. U.S. patent US20070057255, 2007.
(303) Brust, M.; Bethell, D.; Schiffrin, D. J.; Kiely, C. J. *Adv. Mater.* **1995**, *7*, 795.
(304) Muller, K. H.; Wei, G.; Raguse, B.; Myers, J. *Phys. Rev. B* **2003**, *68*, 155407.
(305) Overgaag, K.; Liljeroth, P.; Grandidier, B.; Vanmaekelbergh, D. l. *ACS Nano* **2008**, *2*, 600.
(306) Brust, M.; Bethell, D.; Kiely, C. J.; Schiffrin, D. J. *Langmuir* **1998**, *14*, 5425.
(307) Klem, E. J. D.; MacNeil, D. D.; Cyr, P. W.; Levina, L.; Sargenta, E. H. *Appl. Phys. Lett.* **2007**, *90*, 151115.
(308) Mitzi, D. B.; Kosbar, L. L.; Murray, C. E.; Copel, M.; Afzali, A. *Nature* **2004**, *428*, 299.
(309) Bag, S.; Trikalitis, P. N.; Chupas, P. J.; Armatas, G. S.; Kanatzidis, M. G. *Science* **2007**, *317*, 490.
(310) MacLachlan, M. J.; Coombs, N.; Ozin, G. A. *Nature* **1999**, *397*, 681.
(311) Riley, A. E.; Korlann, S. D.; Richman, E. K.; Tolbert, S. H. *Angew. Chem., Int. Ed.* **2006**, *45*, 235.
(312) Mitzi, D. B.; Copel, M.; Chey, S. J. *Adv. Mater.* **2005**, *17*, 1285.
(313) Milliron, D. J.; Raoux, S.; Shelby, R.; Jordan-Sweet, J. *Nat. Mater.* **2007**, *6*, 352.
(314) Beloborodov, I. S.; Lopatin, A. V.; Vinokur, V. M.; Efetov, K. B. *Rev. Mod. Phys.* **2007**, *79*, 469.
(315) Mott, N. *Conduction in Non-Crystalline Materials*, 2nd ed.; Clarendon Press: Oxford, 1993.
(316) Shklovskii, B. I.; Efros, A. L. *Electronic Properties of Doped Semiconductors*; Springer-Verlag: Berlin, 1984.
(317) Altshuler, B.; Aronov, A. *Electron−Electron Interactions in Disordered Conductors*; North-Holland: Amsterdam, 1985.
(318) Remacle, F.; Levine, R. D. *ChemPhysChem* **2001**, *2*, 20.
(319) Vanmaekelbergh, D.; Liljeroth, P. *Chem. Soc. Rev.* **2005**, *34*, 299.
(320) Chandler, R. E.; Houtepen, A. J.; Nelson, J.; Vanmaekelbergh, D. *Phys. Rev. B* **2007**, *75*, 085325.
(321) Terrill, R. H.; Postlethwaite, T. A.; Chen, C. H.; Poon, C. D.; Terzis, A.; Chen, A. D.; Hutchison, J. E.; Clark, M. R.; Wignall, G.; Londono, J. D.; Superfine, R.; Falvo, M.; Johnson, C. S.; Samulski, E. T.; Murray, R. W. *J. Am. Chem. Soc.* **1995**, *117*, 12537.
(322) Wuelfing, W. P.; Green, S. J.; Pietron, J. J.; Cliffel, D. E.; Murray, R. W. *J. Am. Chem. Soc.* **2000**, *122*, 11465.
(323) Kim, S. H.; Medeiros-Ribeiro, G.; Ohlberg, D. A. A.; Williams, R. S.; Heath, J. R. *J. Phys. Chem. B* **1999**, *103*, 10341.
(324) Elteto, K.; Antonyan, E. G.; Nguyen, T. T.; Jaeger, H. M. *Phys. Rev. B* **2005**, *71*, 064206.
(325) Parthasarathy, R.; Lin, X. M.; Jaeger, H. M. *Phys. Rev. Lett.* **2001**, *87*, 186807.
(326) Markovich, G.; Collier, C. P.; Henrichs, S. E.; Remacle, F.; Levine, R. D.; Heath, J. R. *Acc. Chem. Res.* **1999**, *32*, 415.
(327) Beverly, K. C.; Sampaio, J. F.; Heath, J. R. *J. Phys. Chem. B* **2002**, *106*, 2131.
(328) Beverly, K. C.; Sample, J. L.; Sampaio, J. F.; Remacle, F.; Heath, J. R.; Levine, R. D. *Proc. Natl. Acad. Sci. U.S.A.* **2002**, *99*, 6456.
(329) Tran, T. B.; Beloborodov, I. S.; Lin, X. M.; Bigioni, T. P.; Vinokur, V. M.; Jaeger, H. M. *Phys. Rev. Lett.* **2005**, *95*, 076806.
(330) Mentzel, T. S.; Porter, V. J.; Geyer, S.; MacLean, K.; Bawendi, M. G.; Kastner, M. A. *Phys. Rev. B* **2008**, *77*, 075316.
(331) Yu, D.; Wang, C. J.; Wehrenberg, B. L.; Guyot-Sionnest, P. *Phys. Rev. Lett.* **2004**, *92*, 216802.
(332) Guyot-Sionnest, P.; Yu, D.; Jiang, P. H.; Kang, W. *J. Chem. Phys.* **2007**, *127*, 014702.
(333) Shevchenko, E. V.; Talapin, D. V.; Rogach, A. L.; Kornowski, A.; Haase, M.; Weller, H. *J. Am. Chem. Soc.* **2002**, *124*, 11480.
(334) Inoue, J.; Maekawa, S. *Phys. Rev. B* **1996**, *53*, 11927.
(335) Black, C. T.; Murray, C. B.; Sandstrom, R. L.; Sun, S. *Science* **2000**, *290*, 1131.
(336) Sun, S. H.; Zeng, H. *J. Am. Chem. Soc.* **2002**, *124*, 8204.
(337) Beloborodov, I. S.; Glatz, A.; Vinokur, V. M. *Phys. Rev. Lett.* **2007**, *99*, 066602.
(338) Tedrow, P. M.; Meservey, R. *Phys. Rev. B* **1973**, *7*, 318.
(339) Takahashi, S.; Maekawa, S. *J. Mag. Mag. Mat.* **1999**, *199*, 143.
(340) Degroot, R. A.; Mueller, F. M.; Vanengen, P. G.; Buschow, K. H. J. *Phys. Rev. Lett.* **1983**, *50*, 2024.
(341) Zeng, H.; Black, C. T.; Sandstrom, R. L.; Rice, P. M.; Murray, C. B.; Sun, S. H. *Phys. Rev. B* **2006**, *73*, 020402.
(342) Vedyayev, A.; Ryzhanova, N.; Vlutters, R.; Dieny, B.; Strelkov, N. *J. Phys.: Condens. Matter* **2000**, *12*, 1797.
(343) Akerman, J. *Science* **2005**, *308*, 508.
(344) Wehrenberg, B. L.; Wang, C. J.; Guyot-Sionnest, P. *J. Phys. Chem. B* **2002**, *106*, 10634.
(345) Banin, U.; Cao, Y. W.; Katz, D.; Millo, O. *Nature* **1999**, *400*, 542.
(346) Ginger, D. S.; Greenham, N. C. *J. Appl. Phys.* **2000**, *87*, 1361.
(347) Drndic, M.; Markov, R.; Jarosz, M. V.; Bawendi, M. G.; Kastner, M. A.; Markovic, N.; Tinkham, M. *Appl. Phys. Lett.* **2003**, *83*, 4008.
(348) Norris, D. J.; Efros, A. L.; Erwin, S. C. *Science* **2008**, *319*, 1776.
(349) Dalpian, G. M.; Chelikowsky, J. R. *Phys. Rev. Lett.* **2006**, *96*, 226802.
(350) Li, J. B.; Wei, S. H.; Li, S. S.; Xia, J. B. *Phys. Rev. B* **2008**, *77*, 113304.
(351) Roest, A. L.; Kelly, J. J.; Vanmaekelbergh, D.; Meulenkamp, E. A. *Phys. Rev. Lett.* **2002**, *89*, 036801.
(352) Guyot-Sionnest, P.; Wang, C. *J. Phys. Chem. B* **2003**, *107*, 7355.
(353) Wang, C. J.; Shim, M.; Guyot-Sionnest, P. *Science* **2001**, *291*, 2390.
(354) Wehrenberg, B. L.; Guyot-Sionnest, P. *J. Am. Chem. Soc.* **2003**, *125*, 7806.
(355) Shim, M.; Guyot-Sionnest, P. *Nature* **2000**, *407*, 981.
(356) Jasieniak, J.; Mulvaney, P. *J. Am. Chem. Soc.* **2007**, *129*, 2841.
(357) Urban, J. J.; Talapin, D. V.; Shevchenko, E. V.; Kagan, C. R.; Murray, C. B. *Nat. Mater.* **2007**, *6*, 115.
(358) Anderson, P. W.; Lee, P. A.; Saitoh, M. *Solid State Commun.* **1973**, *13*, 595.
(359) Brabec, C. J.; Sariciftci, N. S.; Hummelen, J. C. *Adv. Funct. Mater.* **2001**, *11*, 15.
(360) Ishii, H.; Sugiyama, K.; Ito, E.; Seki, K. *Adv. Mater.* **1999**, *11*, 605.
(361) Weiss, E. A.; Chiechi, R. C.; Geyer, S. M.; Porter, V. J.; Bell, D. C.; Bawendi, M. G.; Whitesides, G. M. *J. Am. Chem. Soc.* **2008**, *130*, 74.
(362) Weiss, E. A.; Porter, V. J.; Chiechi, R. C.; Geyer, S. M.; Bell, D. C.; Bawendi, M. G.; Whitesides, G. M. *J. Am. Chem. Soc.* **2008**, *130*, 83.
(363) Lee, J.-S.; Talapin, D. V., unpublished.
(364) Soreni-Harari, M.; Yaacobi-Gross, N.; Steiner, D.; Aharoni, A.; Banin, U.; Millo, O.; Tessler, N. *Nano Lett.* **2008**, *8*, 678.
(365) Clifford, J. P.; Johnston, K. W.; Levina, L.; Sargent, E. H. *Appl. Phys. Lett.* **2007**, *91*, 253117.
(366) Luther, J. M.; Law, M.; Song, Q.; Perkins, C. L.; Beard, M. C.; Nozik, A. J. *ACS Nano* **2008**, *2*, 271.
(367) Barkhouse, D. A. R.; Pattantyus-Abraham, A. G.; Levina, L.; Sargent, E. H. *ACS Nano* **2008**, *2*, 2356.
(368) Vazquez, H.; Oszwaldowski, R.; Pou, P.; Ortega, J.; Perez, R.; Flores, F.; Kahn, A. *Europhys. Lett.* **2004**, *65*, 802.
(369) de Boer, B.; Hadipour, A.; Mandoc, M. M.; van Woudenbergh, T.; Blom, P. W. M. *Adv. Mater.* **2005**, *17*, 621.
(370) de Boer, E. A.; Bell, L. D.; Brongersma, M. L.; Atwater, H. A.; Ostraat, M. L.; Flagan, R. C. *Appl. Phys. Lett.* **2001**, *78*, 3133.
(371) Hamadani, B. H.; Corley, D. A.; Ciszek, J. W.; Tour, J. M.; Natelson, D. *Nano Lett.* **2006**, *6*, 1303.
(372) Kim, S. H.; Markovich, G.; Rezvani, S.; Choi, S. H.; Wang, K. L.; Heath, J. R. *Appl. Phys. Lett.* **1999**, *74*, 317.
(373) Burgi, L.; Richards, T. J.; Friend, R. H.; Sirringhaus, H. *J. Appl. Phys.* **2003**, *94*, 6129.
(374) Paul, V. P.; Reid, J. C.; Christopher, R. N.; Frisbie, C. D. *J. Appl. Phys.* **2004**, *96*, 7312.

(375) Kanicki, J.; Libsch, F. R.; Griffith, J.; Polastre, R. *J. Appl. Phys.* **1991**, *69*, 2339.
(376) Zaumseil, J.; Sirringhaus, H. *Chem. Rev.* **2007**, *107*, 1296.
(377) Kuo, Y. *Thin Film Transistors: Materials and Processes*; Kluwer Academic Press: New York, 2004.
(378) Yulong Shen, D.; Hosseini, A. R.; Wong, M. H.; Malliaras, G. G. *ChemPhysChem* **2004**, *5*, 16.
(379) Kahn, A.; Koch, N.; Gao, W. Y. *J. Polym. Sci., Part B: Polym. Phys.* **2003**, *41*, 2529.
(380) Klem, E. J. D.; Shukla, H.; Hinds, S.; MacNeil, D. D.; Levina, L.; Sargent, E. H. *Appl. Phys. Lett.* **2008**, *92*, 212105.
(381) Zaban, A.; Greenshtein, M.; Bisquert, J. *ChemPhysChem* **2003**, *4*, 859.
(382) Rhoderick, E. H.; Williams, R. H. *Metal−Semiconductor Contacts*; Clarendon: Oxford, 1988.
(383) Debye, T. K. *Phys. Rev.* **1954**, *94*, 724.
(384) Beard, M. C.; Turner, G. M.; Schmuttenmaer, C. A. *Phys. Rev. B* **2000**, *62*, 15764.
(385) Murphy, J. E.; Beard, M. C.; Nozik, A. J. *J. Phys. Chem. B* **2006**, *110*, 25455.
(386) Sun, B.; Sirringhaus, H. *Nano Lett.* **2005**, *5*, 2408.
(387) Kim, D. W.; Cho, K.; Kim, H.; Moon, B. M.; Kim, S. *Microelectron. Eng.* **2007**, *84*, 1643.
(388) Klajn, R.; Bishop, K. J. M.; Fialkowski, M.; Paszewski, M.; Campbell, C. J.; Gray, T. P.; Grzybowski, B. A. *Science* **2007**, *316*, 261.
(389) Buffat, P.; Borel, J. P. *Phys. Rev. A* **1976**, *13*, 2287.
(390) Goldstein, A. N.; Echer, C. M.; Alivisatos, A. P. *Science* **1992**, *256*, 1425.
(391) Wu, Y. L.; Li, Y. N.; Ong, B. S.; Liu, P.; Gardner, S.; Chiang, B. *Adv. Mater.* **2005**, *17*, 184.
(392) Wu, Y. L.; Li, Y. N.; Ong, B. S. *J. Am. Chem. Soc.* **2006**, *128*, 4202.
(393) Kovalenko, M. V.; Heiss, W.; Shevchenko, E. V.; Lee, J. S.; Schwinghammer, H.; Alivisatos, A. P.; Talapin, D. V. *J. Am. Chem. Soc.* **2007**, *129*, 11354.
(394) Kamat, P. V. *J. Phys. Chem. C.* **2008**, *112*, 18737.
(395) Brown, P.; Kamat, P. V. *J. Am. Chem. Soc.* **2008**, *130*, 8890.
(396) Gur, I.; Fromer, N. A.; Chen, C.-P.; Kanaras, A. G.; Alivisatos, A. P. *Nano Lett.* **2007**, *7*, 409.
(397) Raffaelle, R. P.; Castro, S. L.; Hepp, A. F.; Bailey, S. G. *Prog. Photovoltaics* **2002**, *10*, 433.
(398) Colvin, V. L.; Schlamp, M. C.; Alivisatos, A. P. *Nature* **1994**, *370*, 354.
(399) Schlamp, M. C.; Peng, X. G.; Alivisatos, A. P. *J. Appl. Phys.* **1997**, *82*, 5837.
(400) Mattoussi, H.; Radzilowski, L. H.; Dabbousi, B. O.; Thomas, E. L.; Bawendi, M. G.; Rubner, M. F. *J. Appl. Phys.* **1998**, *83*, 7965.
(401) Chaudhary, S.; Ozkan, M.; Chan, W. C. W. *Appl. Phys. Lett.* **2004**, *84*, 2925.
(402) Coe-Sullivan, S.; Steckel, J. S.; Woo, W. K.; Bawendi, M. G.; Bulovic, V. *Adv. Funct. Mater.* **2005**, *15*, 1117.
(403) Steckel, J. S.; Snee, P.; Coe-Sullivan, S.; Zimmer, J. R.; Halpert, J. E.; Anikeeva, P.; Kim, L. A.; Bulovic, V.; Bawendi, M. G. *Angew. Chem., Int. Ed.* **2006**, *45*, 5796.
(404) Caruge, J. M.; Halpert, J. E.; Bulovic, V.; Bawendi, M. G. *Nano Lett.* **2006**, *6*, 2991.
(405) Sun, Q.; et al. *Nat. Photon.* **2007**, *1*, 717.
(406) Mueller, A. H.; Petruska, M. A.; Achermann, M.; Werder, D. J.; Akhadov, E. A.; Koleske, D. D.; Hoffbauer, M. A.; Klimov, V. I. *Nano Lett.* **2005**, *5*, 1039.
(407) Coe-Sullivan, S.; Woo, W.-K.; Steckel, J. S.; Bawendi, M.; Bulovic, V. *Org. Electron.* **2003**, *4*, 123.
(408) Coe, S.; Woo, W.-K.; Bawendi, M.; Bulovic, V. *Nature* **2002**, *420*, 800.
(409) Zhao, J.; Bardecker, J. A.; Munro, A. M.; Liu, M. S.; Niu, Y.; Ding, I. K.; Luo, J.; Chen, B.; Jen, A. K. Y.; Ginger, D. S. *Nano Lett.* **2006**, *6*, 463.
(410) Rogach, A. L.; Gaponik, N.; Lupton, J. M.; Bertoni, C.; Gallardo, D. E.; Dunn, S.; Pira, N. L.; Paderi, M.; Repetto, P.; Romanov, S. G.; O'Dwyer, C.; Torres, C. M. S.; Eychmuller, A. *Angew. Chem., Int. Ed.* **2008**, *47*, 6538.
(411) Schubert, E. F. *Light-Emitting Diodes*; Cambridge University Press: San Jose, 2006.
(412) Anikeeva, P. O.; Madigan, C. F.; Halpert, J. E.; Bawendi, M. G.; Bulovic, V. *Phys. Rev. B* **2008**, *78*, 085434.
(413) Yanqin, L.; Aurora, R.; Marco, M.; Luigi, C.; Liberato, M.; Roberto, C.; Giuseppe, G. *J. Appl. Phys.* **2005**, *97*, 113501.
(414) Anikeeva, P. O.; Halpert, J. E.; Bawendi, M. G.; Bulovic, V. *Nano Lett.* **2009**, *9*, 2532.
(415) Cho, K. S.; Lee, E. K.; Joo, W. J.; Jang, E.; Kim, T. H.; Lee, S. J.; Kwon, S. J.; Han, J. Y.; Kim, B. K.; Choi, B. L.; Kim, J. M. *Nat. Photon.* **2009**, *3*, 341.
(416) Steckel, J. S.; Zimmer, J. P.; Coe-Sullivan, S.; Stott, N. E.; Bulovi, V.; Bawendi, M. G. *Angew. Chem., Int. Ed.* **2004**, *43*, 2154.
(417) Lee, J.; Sundar, V. C.; Heine, J. R.; Bawendi, M. G.; Jensen, K. F. *Adv. Mater.* **2000**, *12*, 1102.
(418) Nizamoglu, S.; Ozel, T.; Sari, E.; Demir, H. V. *Nanotechnology* **2007**, 18.
(419) Achermann, M.; Petruska, M. A.; Kos, S.; Smith, D. L.; Koleske, D. D.; Klimov, V. I. *Nature* **2004**, *429*, 642.
(420) Achermann, M.; Petruska, M. A.; Koleske, D. D.; Crawford, M. H.; Klimov, V. I. *Nano Lett.* **2006**, *6*, 1396.
(421) Chen, H. S.; Yeh, D. M.; Lu, C. F.; Huang, C. F.; Shiao, W. Y.; Huang, J. J.; Yang, C. C.; Liu, I. S.; Su, W. F. *IEEE Photon. Technol. Lett.* **2006**, *18*, 1430.
(422) Li, L.; Reiss, P. *J. Am. Chem. Soc.* **2008**, *130*, 11588.
(423) Ziegler, J.; Xu, S.; Kucur, E.; Meister, F.; Batentschuk, M.; Gindele, F.; Nann, T. *Adv. Mater.* **2008**, *20*, 4068.
(424) Malik, M. A.; O'Brien, P.; Revaprasadu, N. *Adv. Mater.* **1999**, *11*, 1441.
(425) Rogach, A. L.; Eychmuller, A.; Hickey, S. G.; Kershaw, S. V. *Small* **2007**, *3*, 536.
(426) Schaller, R. D.; Pietryga, J. M.; Klimov, V. I. *Nano Lett.* **2007**, *7*, 3469.
(427) Sashchiuk, A.; Amirav, L.; Bashouti, M.; Krueger, M.; Sivan, U.; Lifshitz, E. *Nano Lett.* **2004**, *4*, 159.
(428) Rogach, A. L.; Koktysh, D. S.; Harrison, M.; Kotov, N. A. *Chem. Mater.* **2000**, *12*, 1526.
(429) Tessler, N.; Medvedev, V.; Kazes, M.; Kan, S.; Banin, U. *Science* **2002**, *295*, 1506.
(430) Li, Y. Q.; Rizzo, A.; Cingolani, R.; Gigli, G. *Microchim. Acta* **2007**, *159*, 207.
(431) Andrey, L.; Rogach, N. G.; Lupton, J. M.; Bertoni, C.; Gallardo, D. E.; Dunn, S.; Li Pira, N.; Paderi, M.; Repetto, P.; Romanov, S. G.; O'Dwyer, C.; Sotomayor Torres, C. M.; Eychmüller, A. *Angew. Chem., Int. Ed.* **2008**, *47*, 6538.
(432) Sze, S. M. *Semiconductor Devices: Physics and Technology*; John Wiley and Sons, Inc.: New York, 2002.
(433) *Optical and Infrared Detectors*; Keyes, R. J., Ed.; Springer-Verlag: New York, 1980.
(434) Saleh, B. E. A.; Teich, M. C. *Fundametals of Photonics*; John Wiley and Sons, Inc.: New York, 1991.
(435) Konstantatos, G.; Clifford, J.; Levina, L.; Sargent, E. H. *Nat. Photon.* **2007**, *1*, 531.
(436) Boberl, M.; Kovalenko, M. V.; Gamerith, S.; List, E. J. W.; Heiss, W. *Adv. Mater.* **2007**, *19*, 3574.
(437) Boberl, M.; Kovalenko, M. V.; Pillwein, G.; Brunthaler, G.; Heiss, W. *Appl. Phys. Lett.* **2008**, *92*, 261113.
(438) Konstantatos, G.; Levina, L.; Tang, J.; Sargent, E. H. *Nano Lett.* **2008**, *8*, 4002.
(439) Leatherdale, C. A.; Kagan, C. R.; Morgan, N. Y.; Empedocles, S. A.; Kastner, M. A.; Bawendi, M. G. *Phys. Rev. B* **2000**, *62*, 2669.
(440) Porter, V. J.; Mentzel, T.; Charpentier, S.; Kastner, M. A.; Bawendi, M. G. *Phys. Rev. B* **2006**, *73*, 155303.
(441) Konstantatos, G.; Sargent, E. H. *Appl. Phys. Lett.* **2007**, *91*, 173505.
(442) Konstantatos, G.; Levina, L.; Fischer, A.; Sargent, E. H. *Nano Lett.* **2008**, *8*, 1446.
(443) Ethan, J. D. K.; Harnik, S.; Sean, H.; Dean, D. M.; Larissa, L.; Edward, H. S. *Appl. Phys. Lett.* **2008**, *92*, 212105.
(444) Kim, H.; Cho, K.; Song, H.; Min, B.; Lee, J.-S.; Kim, G.-T.; Kim, S.; Kim, S. H.; Noh, T. *Appl. Phys. Lett.* **2003**, *83*, 4619.
(445) Kim, H.; Cho, K.; Park, B.; Kim, J.-H.; Lee, J. W.; Kim, S.; Noh, T.; Jang, E. *Solid State Commun.* **2006**, *137*, 315.
(446) Biebersdorf, A.; Dietmuller, R.; Susha, A. S.; Rogach, A. L.; Poznyak, S. K.; Talapin, D. V.; Weller, H.; Klar, T. A.; Feldmann, J. *Nano Lett.* **2006**, *6*, 1559.
(447) Szendrei, K.; Cordella, F.; Kovalenko, M. V.; Boberl, M.; Hesser, G.; Yorema, M.; Jarzab, D.; Mikhnenko, O. V.; Gocalinska, A.; Saba, M.; Quochi, F.; Mura, A.; Bongiovanni, G.; Blom, P. W. M.; Heiss, W. G.; Loi, M. A. *Adv. Mater.* **2009**, *21*, 683.
(448) Choudhury, K. R.; Sahoo, Y.; Ohulchanskyy, T. Y.; Prasad, P. N. *Appl. Phys. Lett.* **2005**, *87*, 073110.
(449) McDonald, S. A.; Cyr, P. W.; Levina, L.; Sargent, E. H. *Appl. Phys. Lett.* **2004**, *85*, 2089.
(450) Qi, D.; Fischbein, M.; Drndic, M.; Selmic, S. *Appl. Phys. Lett.* **2005**, *86*, 093103.
(451) Rauch, T.; Böberl, M.; Tedde, S. F.; Fürst, J.; Kovalenko, M. V.; Hesser, G.; Lemmer, U.; Heiss, W.; Hayden, O. *Nat. Photon.* **2009**, *3*, 332.
(452) Yu, G.; Cao, Y.; Wang, J.; McElvain, J.; Heeger, A. J. *Synth. Met.* **1999**, *102*, 904.
(453) Brabec, C. J.; Cravino, A.; Meissner, D.; Sariciftci, N. S.; Fromherz, T.; Rispens, M. T.; Sanchez, L.; Hummelen, J. C. *Adv. Funct. Mater.* **2001**, *11*, 374.
(454) Gunes, S.; Neugebauer, H.; Sariciftci, N. S. *Chem. Rev.* **2007**, *107*, 1324.

(455) Thompson, B. C.; Jean, M. J. F. *Angew. Chem., Int. Ed.* **2008**, *47*, 58.
(456) Brabec, C. J.; Sariciftci, N. S.; Hummelen, J. C. *Adv. Funct. Mater.* **2001**, *11*, 15.
(457) Huynh, W. U.; Dittmer, J. J.; Alivisatos, A. P. *Science* **2002**, *295*, 2425.
(458) Huynh, W. U.; Dittmer, J. J.; Teclemariam, N.; Milliron, D. J.; Alivisatos, A. P.; Barnham, K. W. J. *Phys. Rev. B* **2003**, *67*, 115326.
(459) Huynh, W. U.; Dittmer, J. J.; Libby, W. C.; Whiting, G. L.; Alivisatos, A. P. *Adv. Funct. Mater.* **2003**, *13*, 73.
(460) Sun, B. Q.; Marx, E.; Greenham, N. C. *Nano Lett.* **2003**, *3*, 961.
(461) Gunes, S.; Neugebauer, H.; Sariciftci, N. S.; Roither, H.; Kovalenko, M.; Pillwein, G.; Heiss, W. *Adv. Funct. Mater.* **2006**, *16*, 1095.
(462) Fritz, K. P.; Guenes, S.; Luther, J.; Kumar, S.; Sariciftci, N. S.; Scholes, G. D. *J. Photochem. Photobiol., A: Chem.* **2008**, *195*, 39.
(463) Lee, H. J.; Yum, J.-H.; Leventis, H. C.; Zakeeruddin, S. M.; Haque, S. A.; Chen, P.; Seok, S. I.; GraM€tzel, M.; Nazeeruddin, M. K. *J. Phys. Chem. C* **2008**, *112*, 11600.
(464) Wu, Y.; Wadia, C.; Ma, W.; Sadtler, B.; Alivisatos, A. P. *Nano Lett.* **2008**, *8*, 2551.
(465) Guo, Q.; Kim, S. J.; Kar, M.; Shafarman, W. N.; Birkmire, R. W.; Stach, E. A.; Agrawal, R.; Hillhouse, H. W. *Nano Lett.* **2008**, *8*, 2982.
(466) Liu, C.-Y.; Holman, Z. C.; Kortshagen, U. R. *Nano Lett.* **2009**, *9*, 449.
(467) Sun, B.; Findikoglu, A. T.; Sykora, M.; Werder, D. J.; Klimov, V. I. *Nano Lett.* **2009**, *9*, 1235.
(468) Ma, W.; Luther, J. M.; Zheng, H.; Wu, Y.; Alivisatos, A. P. *Nano Lett.* **2009**, *9*, 1699.
(469) Steinhagen, C.; Panthani, M. G.; Akhavan, V.; Goodfellow, B.; Koo, B.; Korgel, B. A. *J. Am. Chem. Soc.* **2009**, *131*, 12554.
(470) Hoth, C. N.; Choulis, S. A.; Schilinsky, P.; Brabec, C. J. *Adv. Mater.* **2007**, *19*, 3973.
(471) Brabec, C. J. *Sol. Energy Mater. Sol. Cells* **2004**, *83*, 273.
(472) Yu, G.; Gao, J.; Hummelen, J. C.; Wudl, F.; Heeger, A. J. *Science* **1995**, *270*, 1789.
(473) Ma, W. L.; Yang, C. Y.; Gong, X.; Lee, K.; Heeger, A. J. *Adv. Funct. Mater.* **2005**, *15*, 1617.
(474) Reyes-Reyes, M.; Kim, K.; Carroll, D. L. *Appl. Phys. Lett.* **2005**, *87*, 083506.
(475) Kim, J. Y.; Lee, K.; Coates, N. E.; Moses, D.; Nguyen, T.-Q.; Dante, M.; Heeger, A. J. *Science* **2007**, *317*, 222.
(476) Hauch, J. A.; Schilinsky, P.; Choulis, S. A.; Childers, R.; Biele, M.; Brabec, C. J. *Sol. Energy Mater. Sol. Cells* **2008**, *92*, 727.
(477) Heeger, A. J. *J. Phys. Chem. B* **2001**, *105*, 8475.
(478) Sariciftci, N. S. *Prog. Quant. Electron.* **1995**, *19*, 131.
(479) Hwang, I.-W.; Moses, D.; Heeger, A. J. *J. Phys. Chem. C* **2008**, *112*, 4350.
(480) Moon, J. S.; Lee, J. K.; Cho, S. N.; Byun, J. Y.; Heeger, A. J. *Nano Lett.* **2009**, *9*, 230.
(481) Gunes, S.; Sariciftci, N. S. *Inorg. Chim. Acta* **2008**, *361*, 581.
(482) Wendy, U.; Huynh, X. P. A. P. A. *Adv. Mater.* **1999**, *11*, 923.
(483) Arici, E.; Hoppe, H.; Schaffler, F.; Meissner, D.; Malik, M. A.; Sariciftci, N. S. *Thin Solid Films* **2004**, *451*, 612.
(484) Beek, W. J. E.; Wienk, M. M.; Janssen, R. A. J. *Adv. Funct. Mater.* **2006**, *16*, 1112.
(485) Beek, W. J. E.; Wienk, M. M.; Janssen, R. A. J. *Adv. Mater.* **2004**, *16*, 1009.
(486) Greenham, N. C.; Peng, X.; Alivisatos, A. P. *Phys. Rev. B* **1996**, *54*, 17628.
(487) McDonald, S. A.; Konstantatos, G.; Zhang, S. G.; Cyr, P. W.; Klem, E. J. D.; Levina, L.; Sargent, E. H. *Nat. Mater.* **2005**, *4*, 138.
(488) Gunes, S.; Fritz, K. P.; Neugebauer, H.; Sariciftci, N. S.; Kumar, S.; Scholes, G. D. *Sol. Energy Mater. Sol. Cells* **2007**, *91*, 420.
(489) Maria, A.; Cyr, P. W.; Klern, E. J. D.; Levina, L.; Sargent, E. H. *Appl. Phys. Lett.* **2005**, *87*, 213112.
(490) Zhang, S.; Cyr, P. W.; McDonald, S. A.; Konstantatos, G.; Sargent, E. H. *Appl. Phys. Lett.* **2005**, *87*, 233101.
(491) Kim, S. J.; Kim, W. J.; Cartwright, A. N.; Prasad, P. N. *Appl. Phys. Lett.* **2008**, *92*, 191107.
(492) Cui, D. H.; Xu, J.; Zhu, T.; Paradee, G.; Ashok, S.; Gerhold, M. *Appl. Phys. Lett.* **2006**, *88*, 183111.
(493) Miller, A.; Mackinnon, A.; Weaire, D. *Solid State Phys.-Adv. Res. Appl.* **1981**, *36*, 119.
(494) Ramanathan, K.; Contreras, M. A.; Perkins, C. L.; Asher, S.; Hasoon, F. S.; Keane, J.; Young, D.; Romero, M.; Metzger, W.; Noufi, R.; Ward, J.; Duda, A. *Prog. Photovoltaics* **2003**, *11*, 225.
(495) Repins, I.; Contreras, M. A.; Egaas, B.; DeHart, C.; Scharf, J.; Perkins, C. L.; To, B.; Noufi, R. *Prog. Photovoltaics* **2008**, *16*, 235.
(496) Mitzi, D. B.; Yuan, M.; Liu, W.; Kellock, A. J.; Chey, S. J.; Deline, V.; Schrott, A. G. *Adv. Mater.* **2008**, *20*, 3657.
(497) Castro, S. L.; Bailey, S. G.; Raffaelle, R. P.; Banger, K. K.; Hepp, A. F. *J. Phys. Chem. B* **2004**, *108*, 12429.
(498) Banger, K. K.; Jin, M. H. C.; Harris, J. D.; Fanwick, P. E.; Hepp, A. F. *Inorg. Chem.* **2003**, *42*, 7713.
(499) Czekelius, C.; Hilgendorff, M.; Spanhel, L.; Bedja, I.; Lerch, M.; Muller, G.; Bloeck, U.; Su, D. S.; Giersig, M. *Adv. Mater.* **1999**, *11*, 643.
(500) Castro, S. L.; Bailey, S. G.; Raffaelle, R. P.; Banger, K. K.; Hepp, A. F. *Chem. Mater.* **2003**, *15*, 3142.
(501) Choi, S.-H.; Kim, E.-G.; Hyeon, T. *J. Am. Chem. Soc.* **2006**, *128*, 2520.
(502) Tang, J.; Hinds, S.; Kelley, S. O.; Sargent, E. H. *Chem. Mater.* **2008**, *20*, 6906.
(503) Panthani, M. G.; Akhavan, V.; Goodfellow, B.; Schmidtke, J. P.; Dunn, L.; Dodabalapur, A.; Barbara, P. F.; Korgel, B. A. *J. Am. Chem. Soc.* **2008**, *130*, 16770.
(504) Allen, P. M.; Bawendi, M. G. *J. Am. Chem. Soc.* **2008**, *130*, 9240.
(505) Sargent, E. H. *IEEE J. Select. Top. Quantum Electron.* **2008**, *14*, 1223.
(506) Klem, E. J. D.; MacNeil, D. D.; Levina, L.; Sargent, E. H. *Adv. Mater.* **2008**, *20*, 3433.
(507) Law, M.; Beard, M. C.; Choi, S.; Luther, J. M.; Hanna, M. C.; Nozik, A. J. *Nano Lett.* **2008**, *8*, 3904.
(508) Oregan, B.; Gratzel, M. *Nature* **1991**, *353*, 737.
(509) Gratzel, M. *J. Photochem. Photobiol., A: Chem.* **2004**, *164*, 3.
(510) Wang, P.; Zakeeruddin, S. M.; Humphry-Baker, R.; Gratzel, M. *Chem. Mater.* **2004**, *16*, 2694.
(511) Wang, P.; Zakeeruddin, S. M.; Moser, J.-E.; Gratzel, M. *J. Phys. Chem. B* **2003**, *107*, 13280.
(512) Bai, Y.; Cao, Y.; Zhang, J.; Wang, M.; Li, R.; Wang, P.; Zakeeruddin, S. M.; Gratzel, M. *Nat. Mater.* **2008**, *7*, 626.
(513) Tennakone, K.; Kumara, G.; Kottegoda, I. R. M.; Wijayantha, K. G. U.; Perera, V. P. S. *J. Phys. D: Appl. Phys.* **1998**, *31*, 1492.
(514) Schmidt-Mende, L.; Gratzel, M. *Thin Solid Films* **2006**, *500*, 296.
(515) Robel, I.; Subramanian, V.; Kuno, M.; Kamat, P. V. *J. Am. Chem. Soc.* **2006**, *128*, 2385.
(516) Peter, L. M.; Riley, D. J.; Tull, E. J.; Wijayantha, K. G. U. *Chem. Commun.* **2002**, 1030.
(517) Gerischer, H.; Lubke, M. *J. Electroanal. Chem.* **1986**, *204*, 225.
(518) Vogel, R.; Pohl, K.; Weller, H. *Chem. Phys. Lett.* **1990**, *174*, 241.
(519) Zaban, A.; Micic, O. I.; Gregg, B. A.; Nozik, A. J. *Langmuir* **1998**, *14*, 3153.
(520) Yu, P.; Zhu, K.; Norman, A. G.; Ferrere, S.; Frank, A. J.; Nozik, A. J. *J. Phys. Chem. B* **2006**, *110*, 25451.
(521) Vogel, R.; Hoyer, P.; Weller, H. *J. Phys. Chem.* **1994**, *98*, 3183.
(522) Plass, R.; Pelet, S.; Krueger, J.; Gratzel, M.; Bach, U. *J. Phys. Chem. B* **2002**, *106*, 7578.
(523) Peter, L. M.; Wijayantha, K. G. U.; Riley, D. J.; Waggett, J. P. *J. Phys. Chem. B* **2003**, *107*, 8378.
(524) Suarez, R.; Nair, P. K.; Kamat, P. V. *Langmuir* **1998**, *14*, 3236.
(525) Shockley, W.; Queisser, H. J. *J. Appl. Phys.* **1961**, *32*, 510.
(526) Wanlass, M. W.; Emery, K. A.; Gessert, T. A.; Horner, G. S.; Osterwald, C. R.; Coutts, T. J. *Sol. Cells* **1989**, 191.
(527) Ross, R. T.; Nozik, A. J. *J. Appl. Phys.* **1982**, *53*, 3813.
(528) Schaller, R. D.; Pietryga, J. M.; Goupalov, S. V.; Petruska, M. A.; Ivanov, S. A.; Klimov, V. I. *Phys. Rev. Lett.* **2005**, *95*, 196401.
(529) Klimov, V. I.; McBranch, D. W. *Phys. Rev. Lett.* **1998**, *80*, 4028.
(530) Efros, A. L.; Kharchenko, V. A.; Rosen, M. *Solid State Commun.* **1995**, *93*, 281.
(531) Xu, S.; Mikhailovsky, A. A.; Hollingsworth, J. A.; Klimov, V. I. *Phys. Rev. B* **2002**, *65*, 045319.
(532) Beard, R. J. E. *Laser Photon. Rev.* **2008**, *2*, 377.
(533) Guyot-Sionnest, P.; Wehrenberg, B.; Yu, D. *J. Chem. Phys.* **2005**, *123*, 074709.
(534) Harbold, J. M.; Du, H.; Krauss, T. D.; Cho, K. S.; Murray, C. B.; Wise, F. W. *Phys. Rev. B* **2005**, *72*, 195312.
(535) Conibeer, G. J.; Jiang, C. W.; Konig, D.; Shrestha, S.; Walsh, T.; Green, M. A. *Thin Solid Films* **2008**, *516*, 6968.
(536) Schaller, R. D.; Klimov, V. I. *Phys. Rev. Lett.* **2004**, *92*, 186601.
(537) Schaller, R. D.; Sykora, M.; Pietryga, J. M.; Klimov, V. I. *Nano Lett.* **2006**, *6*, 424.
(538) Ellingson, R. J.; Beard, M. C.; Johnson, J. C.; Yu, P. R.; Micic, O. I.; Nozik, A. J.; Shabaev, A.; Efros, A. L. *Nano Lett.* **2005**, *5*, 865.
(539) Schaller, R. D.; Petruska, M. A.; Klimov, V. I. *Appl. Phys. Lett.* **2005**, *87*, 253102.
(540) Pijpers, J. J. H.; Hendry, E.; Milder, M. T. W.; Fanciulli, R.; Savolainen, J.; Herek, J. L.; Vanmaekelbergh, D.; Ruhman, S.; Mocatta, D.; Oron, D.; Aharoni, A.; Banin, U.; Bonn, M. *J. Phys. Chem. C* **2007**, *111*, 4146.
(541) Luther, J. M.; Beard, M. C.; Song, Q.; Law, M.; Ellingson, R. J.; Nozik, A. J. *Nano Lett.* **2007**, *7*, 1779.
(542) Nair, G.; Bawendi, M. G. *Phys. Rev. B* **2007**, *76*, 081304.
(543) Nair, G.; Geyer, S. M.; Chang, L. Y.; Bawendi, M. G. *Phys. Rev. B* **2008**, *78*, 125325.

(544) Talapin, D. V.; Haubold, S.; Rogach, A. L.; Kornowski, A.; Haase, M.; Weller, H. *J. Phys. Chem. B* **2001**, *105*, 2260.
(545) Kim, D. W.; Jang, J.; Kim, H.; Cho, K.; Kim, S. *Thin Solid Films* **2008**, *516*, 7715.
(546) Kim, H.; Kim, D. W.; Cho, K.; Kim, S. *IEEE Electron Device Lett.* **2007**, *28*, 42.
(547) Horowitz, G. *Adv. Mater.* **1998**, *10*, 365.
(548) Katz, H. E.; Bao, Z. *J. Phys. Chem. B* **2000**, *104*, 671.
(549) Coropceanu, V.; Cornil, J.; da Silva Filho, D. A.; Olivier, Y.; Silbey, R.; Bredas, J.-L. *Chem. Rev.* **2007**, *107*, 926.
(550) Dodabalapur, A. *Mater. Today* **2004**, *7*, 56.
(551) Boudjouk, P.; Seidler, D. J.; Bahr, S. R.; McCarthy, G. J. *Chem. Mater.* **1994**, *6*, 2108.
(552) Li, M.; Schnablegger, H.; Mann, S. *Nature* **1999**, *402*, 393.
(553) Snow, E. S.; Novak, J. P.; Campbell, P. M.; Park, D. *Appl. Phys. Lett.* **2003**, *82*, 2145.
(554) Zhou, Y. X.; Gaur, A.; Hur, S. H.; Kocabas, C.; Meitl, M. A.; Shim, M.; Rogers, J. A. *Nano Lett.* **2004**, *4*, 2031.
(555) Bekyarova, E.; Itkis, M. E.; Cabrera, N.; Zhao, B.; Yu, A. P.; Gao, J. B.; Haddon, R. C. *J. Am. Chem. Soc.* **2005**, *127*, 5990.
(556) Talapin, D. V.; Black, C. T.; Kagan, C. R.; Shevchenko, E. V.; Afzali, A.; Murray, C. B. *J. Phys. Chem. C* **2007**, *111*, 13244.
(557) Kagan, C. R.; Mitzi, D. B.; Dimitrakopoulos, C. D. *Science* **1999**, *286*, 945.
(558) Kim, D. W.; Kim, T.; Banerjee, S. K. *IEEE Trans. Electron Devices* **2003**, *50*, 1823.
(559) Talapin, D. V., unpublished data.
(560) Beard, M. C.; Midgett, A. G.; Law, M.; Semonin, O. E.; Ellingson, R. J.; Nozik, A. J. *Nano Lett.* **2009**, *9*, 836.
(561) Lee, S.; Jeong, S.; Kim, D.; Park, B. K.; Moon, J. *Superlattices Microstruct.* **2007**, *42*, 361.
(562) Schneider, J. J.; Hoffmann, R. C.; Engstler, J.; Soffke, O.; Jaegermann, W.; Issanin, A.; Klyszcz, A. *Adv. Mater.* **2008**, *20*, 3383.
(563) Sun, B.; Sirringhaus, H. *J. Am. Chem. Soc.* **2006**, *128*, 16231.
(564) Lee, J. S.;Bodnarchuk, M.; Shevchenko, E. V.; Talapin, D. V., submitted for publication.
(565) Meijer, G. I. *Science* **2008**, *319*, 1625.
(566) Park, B. H.; Kang, B. S.; Bu, S. D.; Noh, T. W.; Lee, J.; Jo, W. *Nature* **1999**, *401*, 682.
(567) Sheikholeslami, A.; Gulak, P. G. *Proc. IEEE* **2000**, *88*, 667.
(568) Pirovano, A.; Lacaita, A. L.; Benvenuti, A.; Pellizzer, F.; Bez, R. *IEEE Trans. Electron Devices* **2004**, *51*, 452.
(569) Wuttig, M.; Yamada, N. *Nat. Mater.* **2007**, *6*, 824.
(570) Scott, J. C.; Bozano, L. D. *Adv. Mater.* **2007**, *19*, 1452.
(571) Sandip, T.; Farhan, R.; Hussein, H.; Allan, H.; Emmanuel, F. C.; Kevin, C. *Appl. Phys. Lett.* **1996**, *68*, 1377.
(572) Kapetanakis, E.; Normand, P.; Tsoukalas, D.; Beltsios, K.; Stoemenos, J.; Zhang, S.; van den Berg, J. *Appl. Phys. Lett.* **2000**, *77*, 3450.
(573) Takahashi, N.; Ishikuro, H.; Hiramoto, T. *Appl. Phys. Lett.* **2000**, *76*, 209.
(574) Kanoun, M.; Souifi, A.; Baron, T.; Mazen, F. *Appl. Phys. Lett.* **2004**, *84*, 5079.
(575) Duguay, S.; Grob, J. J.; Slaoui, A.; Le Gall, Y.; Amann-Liess, M. *J. Appl. Phys.* **2005**, *97*, 104330.
(576) Sun, S. H.; Murray, C. B. *J. Appl. Phys.* **1999**, *85*, 4325.
(577) Zhao, D. T.; Zhu, Y.; Liu, J. L. *Solid-State Electron.* **2006**, *50*, 268.
(578) Lee, J. J.; Kwong, D. L. *IEEE Trans. Electron Devices* **2005**, *52*, 507.
(579) King, Y. C.; King, T. J.; Hu, C. M. *IEEE Trans. Electron Devices* **2001**, *48*, 696.
(580) Zhang, L. H.; Koka, R.; Yuen, Y.; Lam, E. *IEEE Trans. Magn.* **1999**, *35*, 927.
(581) Grochowski, E.; Halem, R. D. *IBM Syst. J.* **2003**, *42*, 338.
(582) Sandip, T.; Farhan, R.; Kevin, C.; Leathen, S.; Hussein, H. *Appl. Phys. Lett.* **1996**, *69*, 1232.
(583) Yi, S.; Kenichi, S.; Hiroki, I.; Toshiro, H. *J. Appl. Phys.* **1998**, *84*, 2358.
(584) Garrido, B.; Cheylan, S.; Gonzalez-Varona, O.; Perez-Rodriguez, A.; Morante, J. R. *Appl. Phys. Lett.* **2003**, *82*, 4818.
(585) Lu, T. Z.; Alexe, M.; Scholz, R.; Talelaev, V.; Zacharias, M. *Appl. Phys. Lett.* **2005**, *87*, 202110.
(586) Park, B.; Cho, K.; Moon, B. M.; Kim, S. *Microelectron. Eng.* **2007**, *84*, 1627.
(587) Chan, K. C.; Lee, P. F.; Dai, J. Y. *Appl. Phys. Lett.* **2008**, *92*, 223105.
(588) Yun-Shan, L.; Ke-Chih, L.; Jyun-Yi, W.; Cheng-Hao, H.; Tai-Bor, W. *Appl. Phys. Lett.* **2008**, *93*, 132907.
(589) Liu, Z. T.; Lee, C.; Narayanan, V.; Pei, G.; Kan, E. C. *IEEE Trans. Electron Devices* **2002**, *49*, 1614.
(590) Hasler, P.; Lande, T. S. *IEEE Trans. Circuits Syst. Express Briefs* **2001**, *48*, 1.
(591) Liu, Z. T.; Lee, C.; Narayanan, V.; Pei, G.; Kan, E. C. *IEEE Trans. Electron Devices* **2002**, *49*, 1606.
(592) Tsoukalas, D.; Dimitrakis, P.; Kolliopoulou, S.; Normand, P. *Mater. Sci. Eng., B* **2005**, *124*, 93.
(593) Prakaipetch, P.; Yukiharu, U.; Takashi, F.; Atsushi, T.; Eiji, T.; Tsukasa, H.; Atsushi, S.; Sadayoshi, H. *Appl. Phys. Lett.* **2006**, *89*, 093502.
(594) Lombardo, S.; De Salvo, B.; Gerardi, C.; Baron, T. *Microelectron. Eng.* **2004**, *72*, 388.
(595) De Blauwe, J. *IEEE Trans. Nanotechnol.* **2002**, *1*, 72.
(596) Han, K.; Kim, I.; Shin, H. *IEEE Trans. Electron Devices* **2001**, *48*, 874.
(597) Lee, J. J.; Wang, X. G.; Bai, W. P.; Lu, N.; Kwong, D. L. *IEEE Trans. Electron Devices* **2003**, *50*, 2067.
(598) Rao, R. A.; Steimle, R. F.; Sadd, M.; Swift, C. T.; Hradsky, B.; Straub, S.; Merchant, T.; Stoker, M.; Anderson, S. G. H.; Rossow, M.; Yater, J.; Acred, B.; Harber, K.; Prinz, E. J.; White, B. E.; Muralidhar, R. *Solid-State Electron.* **2004**, *48*, 1463.
(599) Feng, T.; Yu, H. B.; Dicken, M.; Heath, J. R.; Atwater, H. A. *Appl. Phys. Lett.* **2005**, *86*, 033103.
(600) Muller, T.; Heinig, K. H.; Moller, W. *Appl. Phys. Lett.* **2002**, *81*, 3049.
(601) Li, X. G.; He, Y. Q.; Talukdar, S. S.; Swihart, M. T. *Langmuir* **2003**, *19*, 8490.
(602) Bonafos, C.; Carrada, M.; Cherkashin, N.; Coffin, H.; Chassaing, D.; Assayag, G. B.; Claverie, A.; Muller, T.; Heinig, K. H.; Perego, M.; Fanciulli, M.; Dimitrakis, P.; Normand, P. *J. Appl. Phys.* **2004**, *95*, 5696.
(603) Ohba, R.; Sugiyama, N.; Uchida, K.; Koga, J.; Toriumi, A. *IEEE Trans. Electron Devices* **2002**, *49*, 1392.
(604) Ammendola, G.; Vulpio, M.; Bileci, M.; Nastasi, N.; Gerardi, C.; Renna, G.; Crupi, I.; Nicotra, G.; Lombardo, S. *J. Vac. Sci. Technol., B* **2002**, *20*, 2075.
(605) Punchaipetch, P.; Ichikawa, K.; Uraoka, Y.; Fuyuki, T.; Tomyo, A.; Takahashi, E.; Hayashi, T. *J. Vac. Sci. Technol., B* **2006**, *24*, 1271.
(606) Lu, T. Z.; Alexe, M.; Scholz, R.; Talalaev, V.; Zhang, R. J.; Zacharias, M. *J. Appl. Phys.* **2006**, *100*, 014310.
(607) Lu, X. B.; Lee, P. F.; Dai, J. Y. *Appl. Phys. Lett.* **2005**, *86*, 203111.
(608) Shahrjerdi, D.; Garcia-Gutieffez, D. I.; Banerjee, S. K. *IEEE Electron Device Lett.* **2007**, *28*, 793.
(609) Liu, Z. C.; Xue, F. L.; Su, Y.; Lvov, Y. M.; Varahramyan, K. *IEEE Trans. Nanotechnol.* **2006**, *5*, 379.
(610) Lee, C. H.; Meteer, J.; Narayanan, V.; Kan, E. C. *J. Electron. Mater.* **2005**, *34*, 1.
(611) Chen, W. R.; Chang, T. C.; Liu, P. T.; Tu, C. H.; Chi, F. W.; Tsao, S. W.; Chang, C. Y. *Surf. Coat. Technol.* **2007**, *202*, 1292.
(612) Pavel, A. A.; Khan, M. A.; Kirawanich, P.; Islam, N. E. *Solid-State Electron.* **2008**, *52*, 1536.
(613) Hou, T. H.; Lee, C.; Narayanan, V.; Ganguly, U.; Kan, E. C. *IEEE Trans. Electron Devices* **2006**, *53*, 3095.
(614) Son, D. I.; Kim, J. H.; Park, D. H.; Choi, W. K.; Li, F.; Ham, J. H.; Kim, T. W. *Nanotechnology* **2008**, *19*, 055204.
(615) Li, F.; Son, D. I.; Kim, B. J.; Kim, T. W. *Appl. Phys. Lett.* **2008**, *93*, 021913.
(616) Li, F.; Cho, S. H.; Son, D. I.; Park, K. H.; Kim, T. W. *Appl. Phys. Lett.* **2008**, *92*, 102110.
(617) Li, F. S.; Son, D. I.; Cha, H. M.; Seo, S. M.; Kim, B. J.; Kim, H. J.; Jung, J. H.; Kim, T. W. *Appl. Phys. Lett.* **2007**, *90*, 222109.
(618) Li, F.; Son, D. I.; Seo, S. M.; Cha, H. M.; Kim, H. J.; Kim, B. J.; Jung, J. H.; Kim, T. W. *Appl. Phys. Lett.* **2007**, *91*, 122111.
(619) Lee, J. S.; Cho, J.; Lee, C.; Kim, I.; Park, J.; Kim, Y. M.; Shin, H.; Lee, J.; Caruso, F. *Nat. Nanotechnol.* **2007**, *2*, 790.
(620) Das, B. C.; Batabyal, S. K.; Pal, A. J. *Adv. Mater.* **2007**, *19*, 4172.
(621) Mohanta, K.; Majee, S. K.; Batabyal, S. K.; Pal, A. J. *J. Phys. Chem. B* **2006**, *110*, 18231.
(622) Park, B.; Cho, K.; Kim, H.; Kim, S. *Semicond. Sci. Technol.* **2006**, *21*, 975.
(623) Park, C. J.; Cho, K. H.; Yang, W. C.; Cho, H. Y.; Choi, S. H.; Elliman, R. G.; Han, J. H.; Kim, C. *Appl. Phys. Lett.* **2006**, *88*, 071916.
(624) Choi, H.; Choi, B. S.; Kim, T. W.; Jung, S. J.; Chang, M.; Lee, T.; Hwang, H. *Nanotechnology* **2008**, *19*, 305704.
(625) Lee, J. S.; Kim, Y. M.; Kwon, J. H.; Shin, H.; Sohn, B. H.; Lee, J. *Adv. Mater.* **2009**, *21*, 178.
(626) Liz-Marzan, L. M.; Mulvaney, P. *J. Phys. Chem. B* **2003**, *107*, 7312.
(627) Garcia-Santamaria, F.; Salgueirino-Maceira, V.; Lopez, C.; Liz-Marzan, L. M. *Langmuir* **2002**, *18*, 4519.
(628) Yang, L. M.; Ouyang, J.; He, J.; Liem, H. M.; Chu, C. W.; Prakash, A. *Organic Nonvolatile Memories*; Springer: London, 2005.
(629) Yang, Y.; Ouyang, J.; Ma, L. P.; Tseng, R. J. H.; Chu, C. W. *Adv. Funct. Mater.* **2006**, *16*, 1001.
(630) Jianyong, O.; Chih-Wei, C.; Douglas, S.; Yang, Y. *Appl. Phys. Lett.* **2005**, *86*, 123507.
(631) Das, B. C.; Pal, A. J. *Small* **2008**, *4*, 542.
(632) Lai, P. Y.; Chen, J. S. *Appl. Phys. Lett.* **2008**, *93*, 153305.

(633) Tseng, R. J.; Tsai, C.; Ma, L.; Ouyang, J.; Ozkan, C. S.; Yang, Y. *Nat. Nanotechnol.* **2006**, *1*, 72.
(634) Frank, V.; Stefan, C. J. M.; Rene, A. J. J. *Appl. Phys. Lett.* **2006**, *89*, 102103.
(635) Bozano, L. D.; Kean, B. W.; Beinhoff, M.; Carter, K. R.; Rice, P. M.; Scott, J. C. *Adv. Funct. Mater.* **2005**, *15*, 1933.
(636) Ouyang, J.; Chu, C.-W.; Szmanda, C. R.; Ma, L.; Yang, Y. *Nat. Mater.* **2004**, *3*, 918.
(637) Ankita, P.; Jianyong, O.; Jen-Lien, L.; Yang, Y. *J. Appl. Phys.* **2006**, *100*, 054309.
(638) Fischbein, M. D.; Drndic, M. *Appl. Phys. Lett.* **2005**, *86*, 193106.
(639) Li, F.; Son, D. I.; Ham, J. H.; Kim, B. J.; Jung, J. H.; Kim, T. W. *Appl. Phys. Lett.* **2007**, *91*, 162109.
(640) Ghosh, B.; Sahu, S.; Pal, A. J. *J. Phys. Chem. C* **2008**, *112*, 11290.
(641) Das, S.; Das, K.; Singha, R. K.; Dhar, A.; Ray, S. K. *Appl. Phys. Lett.* **2007**, *91*, 233118.
(642) Chappert, C.; Fert, A.; Van Dau, F. N. *Nat. Mater.* **2007**, *6*, 813.
(643) Terris, B. D.; Thomson, T. *J. Phys. D: Appl. Phys.* **2005**, *38*, R199.
(644) *Nanoscale Materials in Chemistry*; Klabunde, K. J., Ed.; John Wiley & Sons, Inc.: New York, Chichester, Weinheim, Brisbane, Singapore, Toronto, 2001.
(645) Teng, X. W.; Yang, H. *J. Am. Chem. Soc.* **2003**, *125*, 14559.
(646) Nguyen, H. L.; Howard, L. E. M.; Giblin, S. R.; Tanner, B. K.; Terry, I.; Hughes, A. K.; Ross, I. M.; Serres, A.; Burckstummer, H.; Evans, J. S. O. *J. Mater. Chem.* **2005**, *15*, 5136.
(647) Hansen, M. *Constitution of Binary Alloys*; McGraw-Hill: New York, 1958.
(648) Kang, S.; Harrell, J. W.; Nikles, D. E. *Nano Lett.* **2002**, *2*, 1033.
(649) Chen, M.; Kim, J.; Liu, J. P.; Fan, H.; Sun, S. *J. Am. Chem. Soc.* **2006**, *128*, 7132.
(650) Sales, B. C. *Science* **2002**, *295*, 1248.
(651) Chen, G.; Dresselhaus, M. S.; Dresselhaus, G.; Fleurial, J. P.; Caillat, T. *Int. Mater. Rev.* **2003**, *48*, 45.
(652) Majumdar, A. *Science* **2004**, *303*, 777.
(653) Snyder, G. J.; Toberer, E. S. *Nat. Mater.* **2008**, *7*, 105.
(654) Fujikane, M.; Kurosaki, K.; Muta, H.; Yamanaka, S. *J. Alloys Compd.* **2005**, *393*, 299.
(655) Mercouri, G.; Kanatzidis, S. D. M.; Hogan, T. P. *Chemistry, Physics, and Materials Science of Thermoelectric Materials: Beyond Bismuth Telluride*; Springer: New York, 2003.
(656) *Thermoelectrics Handbook: Macro to Nano*; Rowe, D. M., Ed.; CRC Press: Boca Raton, FL, 2006.
(657) Bell, L. E. *Science* **2008**, *321*, 1457.
(658) Vining, C. B. *Nat. Mater.* **2009**, *8*, 83.
(659) Muller, K. H. *J. Chem. Phys.* **2008**, *129*, 044708.
(660) Hicks, L. D.; Dresselhaus, M. S. *Phys. Rev. B* **1993**, *47*, 12727.
(661) Hicks, L. D.; Dresselhaus, M. S. *Phys. Rev. B* **1993**, *47*, 16631.
(662) Kittel, C. *Introduction to Solid State Physics*; Wiley & Sons: New York, 2005.
(663) Mahan, G. D.; Sofo, J. O. *Proc. Natl. Acad. Sci. U.S.A.* **1996**, *93*, 7436.
(664) Sun, X.; Zhang, Z.; Dresselhaus, M. S. *Appl. Phys. Lett.* **1999**, *74*, 4005.
(665) Lin, Y.-M.; Dresselhaus, M. S. *Phys. Rev. B* **2003**, *68*, 075304.
(666) Alexander, A. B.; Olga, L. L. *Appl. Phys. Lett.* **2003**, *82*, 415.
(667) Humphrey, T. E.; Linke, H. *Phys. Rev. Lett.* **2005**, *94*, 096601.
(668) Venkatasubramanian, R.; Siivola, E.; Colpitts, T.; O'Quinn, B. *Nature* **2001**, *413*, 597.
(669) Hsu, K. F.; Loo, S.; Guo, F.; Chen, W.; Dyck, J. S.; Uher, C.; Hogan, T.; Polychroniadis, E. K.; Kanatzidis, M. G. *Science* **2004**, *303*, 818.
(670) Boukai, A. I.; Bunimovich, Y.; Tahir-Kheli, J.; Yu, J.-K.; Goddard Iii, W. A.; Heath, J. R. *Nature* **2008**, *451*, 168.
(671) Hochbaum, A. I.; Chen, R.; Delgado, R. D.; Liang, W.; Garnett, E. C.; Najarian, M.; Majumdar, A.; Yang, P. *Nature* **2008**, *451*, 163.
(672) Pierre, F. P.; Poudeu, J. D. A.; Downey, A. D.; Short, J. L.; Hogan, T. P.; Kanatzidis, M. G. *Angew. Chem., Int. Ed.* **2006**, *45*, 3835.
(673) Poudel, B.; Hao, Q.; Ma, Y.; Lan, Y.; Minnich, A.; Yu, B.; Yan, X.; Wang, D.; Muto, A.; Vashaee, D.; Chen, X.; Liu, J.; Dresselhaus, M. S.; Chen, G.; Ren, Z. *Science* **2008**, *320*, 634.
(674) Franchi, S.; Trevisi, G.; Seravalli, L.; Frigeri, P. *Prog. Cryst. Growth Charact. Mater.* **2003**, *47*, 166.
(675) Wise, F. W. *Acc. Chem. Res.* **2000**, *33*, 773.
(676) Chen, G. *Nanoscale Energy Transport and Conversion*; Oxford: New York, 2005.
(677) Kim, W.; Wang, R.; Majumdar, A. *Nano Today* **2007**, *2*, 40.
(678) Wang, R. Y.; Segalman, R. A.; Majumdar, A. *Appl. Phys. Lett.* **2006**, *89*, 173113.
(679) Prasher, R. *Phys. Rev. B* **2006**, *74*, 165413.
(680) Kovalenko, M. V.; Spokoyny, B.; Lee, J.-S.; Scheele, M.; Weber, A.; Perera, S.; Landry, D.; Talapin, D. V. Submitted for publication.
(681) Heremans, J. P.; Thrush, C. M.; Morelli, D. T. *Phys. Rev. B* **2004**, *70*, 115334.
(682) Lee, J.; Sundar, V. C.; Heine, J. R.; Bawendi, M. G.; Jensen, K. F. *Adv. Mater.* **2000**, *12*, 1311.
(683) Pourret, A.; Guyot-Sionnest, P.; Elam, J. W. *Adv. Mater.* **2009**, *21*, 232.

CR900137K